ALMA MATER STUDIORUM
UNIVERSITÀ DI BOLOGNA

DOTTORATO DI RICERCA IN

FISICA

Ciclo 36°

Settore Concorsuale: 02/A1 - Fisica Sperimentale Delle Interazioni Fondamentali

Settore Scientifico Disciplinare: FIS/01 - Fisica Sperimentale

Measurement of ϕ-meson pair production in pp collisions at $\sqrt{s}$ = 5.02 TeV and 7 TeV with the ALICE experiment

Presentata da: Nicola Rubini

Coordinatore Dottorato
Alessandro Gabrielli

Supervisore
Roberto Preghenella
Co-supervisore
Silvia Arcelli

Esame finale anno 2024

University of Bologna

Abstract

School of Science
Department of Physics and Astronomy

Doctoral Degree

Measurement of ϕ-meson pair production in pp collisions at $\sqrt{s} = 5.02$ TeV and 7 TeV with the ALICE experiment

by Nicola RUBINI

The Quark-Gluon Plasma (QGP) has been studied extensively by many experiments in the last decades. One of the first proposed signatures for its existence was the enhancement of strange and multistrange hadrons, called Strangeness Enhancement (SE). SE is the enhancement of strange and multistrange production in heavy-ion collisions with respect to pp collisions, where no hot plasma is expected to be formed. This effect is responsible for the production of an enhancement of the yield of strange and multistrange hadrons relative to pions and is more pronounced in hadrons carrying more strangeness. As is the case for a number of observables previously associated with heavy-ion collisions, SE is now measured in pp collision events with a high multiplicity of charged particles in the final state. These new measurements hinting at high-density QCD phenomena happening in a class of pp collisions paved the way to a new vision where smaller collision systems such as pp and p–Pb were no longer regarded as baseline for the heavy-ion physics but rather a new frontier where precision measurements could be conducted to understand non-perturbative QCD phenomenology. The ϕ meson is then a probe of choice to study the strangeness hadronisation mechanisms and to help deepening our knowledge on the nature behind the SE phenomenon. Its hidden strangeness makes its yield only dependent on strangeness production and its phenomenological description differs significantly between models, which makes it an invaluable tool in discriminating underlying physics phenomena. The work reported in this thesis build on these grounds and it is based on a novel technique to measure the ϕ-meson pairs yield in pp collisions. The measurement of the ϕ-meson pairs is not only interesting in its own right, but also for its possibility to be combined with the inclusive ϕ-meson yield. This allows one to directly asses the second moment (variance) of the statistical distribution of ϕ-meson production, opening the way to new observables to compare to Monte Carlo predictions such as PYTHIA8 phenomenological model.

In the last chapter an R&D work on SiPMs detectors for the ePIC experiment at the EIC collider is presented.

Contents

Introduction

The presented manuscript describes the work I performed during my PhD.

The first chapter

The first chapter consist of a general overview of Quantum Chromodynamics (QCD) and hadron physics at high-energy colliders. It is an introductory overview of general concepts of collider physics. This is followed by an excursus on the most recent results on the Quark-Gluon Plasma. The main focus is on results from the ALICE Collaboration and on the emergence of QGP-reminiscent effects in small systems. At last, an introduction on the Lund String Model is carried out.

The second chapter

The second chapter is devoted to a general overview of the ALICE detector. A rundown of all sub-systems will be done with a brief description of their core concept and purpose. At last, a review of the most relevant practices for the analysis presented will be carried out.

The third chapter

The third chapter discusses the details of the analysis for the measurement of the ϕ-meson pair production measurement. The description will cover in detail all the methods and cross-checks that have been performed. A discussion on the results and Monte Carlo comparisons will be given.

The fourth chapter

The fourth chapter presents the work being carried out on the R&D on Silicon Photomultipliers (SiPMs) for their use in the dual Ring Cherenkov Imaging (dRICH) detector at the electron-proton-ion collider experiment (ePIC) at the electron-ion collider (EIC). The chapter also features a small introduction on the physics programme foreseen for the EIC and on the dRICH project.

Chapter 1

Quantum chromodynamics and hadron physics

Quantum Chromodynamics (QCD) is the theoretical framework that describes the strong force, which is one of the four fundamental forces of nature alongside the electromagnetic, weak, and gravitational interactions. The strong force is responsible for binding protons and neutrons together to form atomic nuclei and holding quarks and gluons together to form hadrons, such as protons and neutrons. QCD is a part of the Standard Model of particle physics, which describes the behaviour of elementary particles and their interactions. A summary of the particles in the Standard Model is shown in Figure 1.1.

QCD is a non abelian gauge theory based on the colour group SU(3)$_c$, the Special Unitary group in three complex dimensions. Its elements are the set of 3×3 unitary matrices with determinant one [2]. The theory has 8 degrees of freedom, since there are 9 linearly independent unitary complex matrices of which one has determinant -1, corresponding to 8 generators or independent directions in colour space. We can use the fundamental representation of eight traceless hermitian matrices, using i, j, k to refer to their rows and columns and $a, b, c, \ldots$ to refer to the generators themselves. These generators represent gluons in the colour space and the 3-vectors they act upon represent quarks in colour space.

The Lagrangian density of QCD is:

$$\mathcal{L} = \bar{\psi}_q^i (i\gamma^\mu)(D_\mu)_{ij}\psi_q^j - m_q \bar{\psi}_q^i \psi_{qi} - \frac{1}{4} F^a_{\mu\nu} F^{a\mu\nu} \tag{1.1}$$

where $\psi_q = (\psi_{qR}, \psi_{qG}, \psi_{qB})^T$ is the quark field and the i index runs through the colours, γ^μ is the Dirac matrix, indicating the interaction is vectorial in nature and m_q gives the possibility for quarks to be massive, for example through the Higgs mechanism. $F^a_{\mu\nu}$ is the gluon strength field with adjoint colour index a and D_μ is the covariant derivative in QCD:

$$(D_\mu)_{ij} = \delta_{ij}\partial_\mu - i g_s t^a_{ij} A^a_\mu \tag{1.2}$$

where g_s is the strong coupling ($g_s^2 = 4\pi\alpha_s$), A^a_μ is the gluon field and t^a_{ij} is proportional to the hermitian traceless Gell-Mann matrices of SU(3) with $t^a_{ij} = \frac{1}{2}\lambda^a_{ij}$.

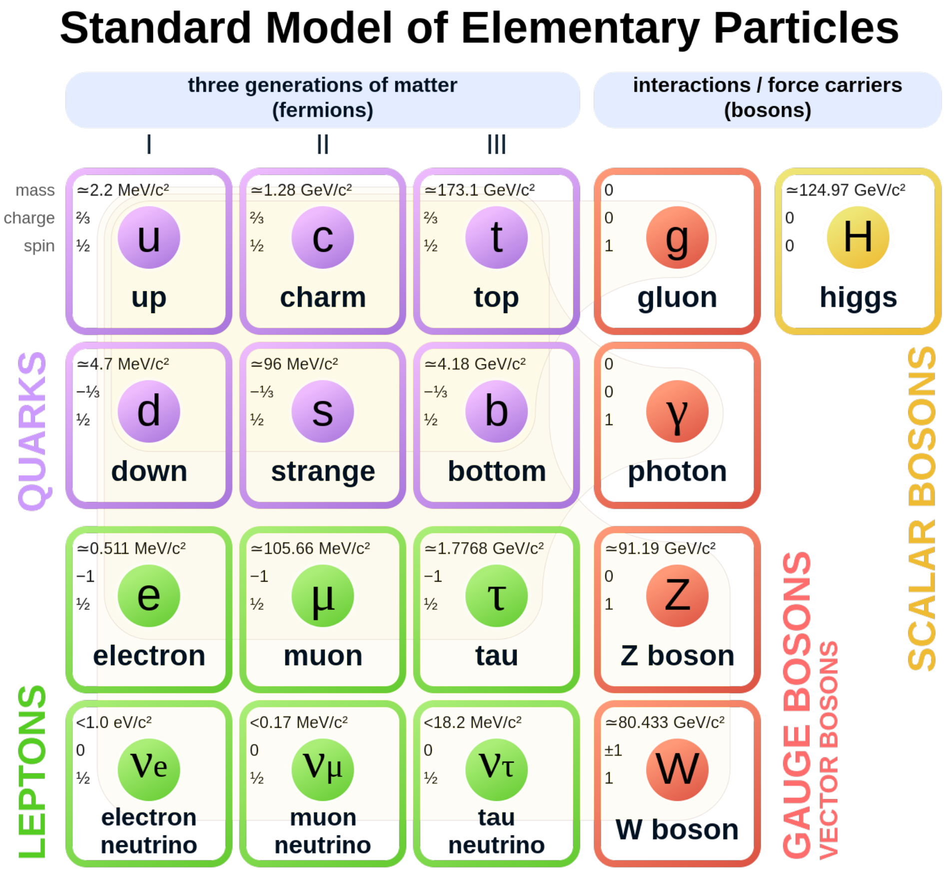

I	II	III		
≃2.2 MeV/c² ⅔ ½ u up	≃1.28 GeV/c² ⅔ ½ c charm	≃173.1 GeV/c² ⅔ ½ t top	0 0 1 g gluon	≃124.97 GeV/c² 0 0 H higgs
≃4.7 MeV/c² −⅓ ½ d down	≃96 MeV/c² −⅓ ½ s strange	≃4.18 GeV/c² −⅓ ½ b bottom	0 0 1 γ photon	
≃0.511 MeV/c² −1 ½ e electron	≃105.66 MeV/c² −1 ½ μ muon	≃1.7768 GeV/c² −1 ½ τ tau	≃91.19 GeV/c² 0 1 Z Z boson	
<1.0 eV/c² 0 ½ νe electron neutrino	<0.17 MeV/c² 0 ½ νμ muon neutrino	<18.2 MeV/c² 0 ½ ντ tau neutrino	≃80.433 GeV/c² ±1 1 W W boson	

FIGURE 1.1: Standard model of elementary particles: the 12 fundamental fermions and 5 fundamental bosons. Please note that the masses of certain particles are subject to periodic reevaluation by the scientific community. The values currently reflected in this graphic are as of 2019 and may have been adjusted since, please refer to [1] for latest values.

1.1 Strong Coupling

In first approximation, QCD is *scale invariant*: going to smaller scales continuously reproduce the same patterns, in a fashion similar to fractals[1]. This feature is called Bjørken scaling [2] and it would hold absolutely true if the QCD coupling constant was not running. In this simplified framework, the bremsstrahlung jets scaling depends only on dimensionless kinematic quantities such as scattering angles and ratios of energies and a measurement of a $10\,\mathrm{GeV}$ jets associated with an ordinary Z boson could be used as a direct prediction of the rate of $100\,\mathrm{GeV}$ jets that would be produced in association with a $900\,\mathrm{GeV}$ Z'[2] boson.

On top of this baseline behaviour, there is the running coupling contribution which is dependent on the absolute scale. The value of the strong coupling is usually specified by giving its value at the specific reference scale $Q^2 = M_Z^2$, from which

---

[1] A fractal is a geometric shape containing detailed structure at arbitrarily small scales, that have a strong similarity at any scale

[2] A hypothetical gauge bosons that arises from extensions of the electroweak symmetry of the Standard Model. They are named in analogy with the Standard Model W and Z bosons

we can obtain its value at any other scale by solving equation

$$\alpha_s(Q^2) = \alpha_s(M_Z^2)\frac{1}{1 + b_0'\alpha_s(M_Z^2)\ln\frac{Q^2}{M_Z^2} + \mathcal{O}(\alpha_s)} \approx \frac{1}{b_o \ln\frac{Q^2}{\Lambda^2}} \tag{1.3}$$

$$\lim_{Q^2\to\infty} \alpha_s(Q^2) = 0 \qquad \lim_{Q^2\to 0} \alpha_s(Q^2) = \infty \qquad \Lambda \approx 200\text{MeV} \tag{1.4}$$

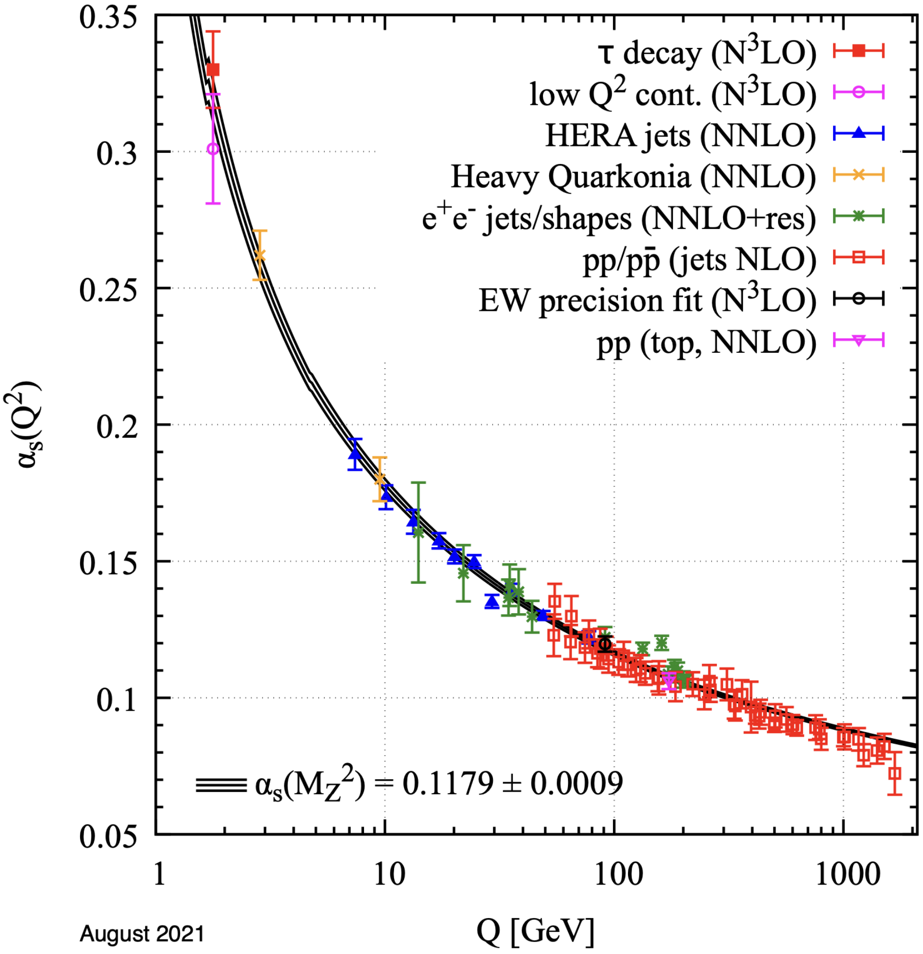

FIGURE 1.2: Summary of measurements of α_s as a function of the energy scale Q. The respective degree of QCD perturbation theory used in the extraction of α_s is indicated in brackets. Figure taken from [1].

Asymptotic freedom

What is inferred by Eq. 1.4 and seen in Figure 1.2 is that in the limit of very high energy the quarks are essentially free. This, in turn, means the perturbative approach will converge faster in the high energy range with respect to lower energies. Furthermore the jet shape will also vary with different energies.

Confinement

What is inferred by Eq. 1.4 is that the soft processes in QCD are not approachable by the perturbation theory, at least not completely, because of the high values of the coupling. Note that the divergence in the approximation is not reflective of a real divergence in the coupling itself, but rather of the approximation of it. The main take-away of this region is that the quarks are strongly bound together and one needs very high energies to disgregate hadrons.

1.1.1 Hard processes

Hard processes are defined as the ones happening at high energy scales, when $Q^2 \gg \Lambda_{\text{QCD}}$, where perturbative Quantum Field Theory (pQFT) can be applied. The starting point is the Matrix Elements that can be calculated to a fixed order (FO) in the strong coupling α_s . The Leading Order (LO) is by now a textbook exercise [3] and is highly automated by programs such as MadGraph [4].

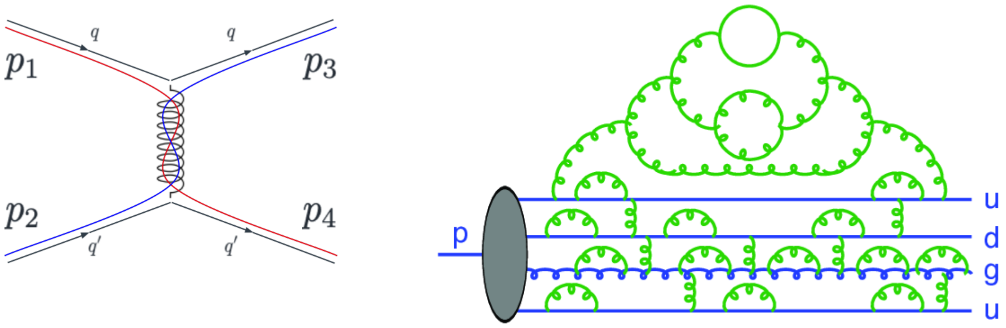

(A) Rutherford scattering of quarks in QCD, exemplifying the type of process that dominates the short-distance interaction cross section at hadron colliders. Figure taken from [2].

(B) Illustration of partonic fluctuations inside a proton beam. Figure taken from [5].

FIGURE 1.3

Starting with an example, on can look at the Rutherford scattering of two quarks via a t-channel gluon exchange (Fig. 1.3a), which is the most occurring process in hadron collisions. At LO the differential cross-section is:

$$qq' \to qq' : \frac{\mathrm{d}\sigma}{\mathrm{d}\hat{t}} = \frac{\pi}{\hat{s}^2}\frac{4}{9}\alpha_s^2\frac{\hat{s}^2+\hat{u}^2}{\hat{t}^2} \tag{1.5}$$

where we use the $2 \to 2$ Mandelstam variables:

$$\hat{s} = (p_1+p_2)^2 \tag{1.6}$$

$$\hat{t} = (p_3-p_1)^2 = -\hat{s}\tfrac{(1-\cos(\hat{\theta}))}{2} \tag{1.7}$$

$$\hat{u} = (p_4-p_1)^2 = -\hat{s}\tfrac{(1+\cos(\hat{\theta}))}{2} \tag{1.8}$$

As was previously stated, this cross section only takes into account the two interacting quarks. Many complications need to be taken into account: real-emission corrections, that can significantly affect the final state topology, loop factors or virtual corrections, affecting the normalisation of the cross-section, confinement and underlying event. These corrections are essentials to connect short-distance physics to the macro experiment where we have our measurements. In addition to perturbative calculation, a fundamental tool is factorisation.

Factorisation

Figure 1.3b gives a broad depiction of what goes on inside a proton in a beam. The internal structure is complex and time-dependent, with clouds of partons that are constantly being emitted and absorbed. This being the case, before calculating matrix elements one needs to address the hadronic substructure.

If the hadron is to remain intact, fluctuations within the parton must involve momentum transfers that lay within the confinement scale. Indeed, high-virtuality fluctuations are suppressed by powers of:

$$\frac{\alpha_s \, \Lambda^2}{|k|^2} \tag{1.9}$$

with k being the virtuality of the fluctuation and Λ the confinement scale ($\approx 200\,\mathrm{MeV}$). This implies most of the fluctuations happen over timescales of $\approx 1/\Lambda$. This is in spark contrast with respect to the timescale of the perturbative probe, such as the photon exchanged in the Deep Inelastic Scattering (DIS), which has $1/Q \ll 1/\Lambda$. The different timescale makes it so that the probe sees the hadron fluctuations as frozen in time, with a characteristic resolution of $\approx 1/Q$.

This is formalized by the factorization theorem, which expresses the independence of long-wavelength (soft) structure from the hard (short-distance) process. Firstly introduced in the context of DIS, it defines the cross-section as the convolution of a Parton Density Function (PDF), which can be measured, and a Partonic scattering Cross Section (PCS), which can be calculated using the perturbative approach. Denoting the fraction of the hadron momentum:

$$\vec{p_i} = x_i \vec{p}_h \tag{1.10}$$

Then the lepton-hadron cross section can be written as:

$$\sigma_{\ell h} = \sum_i \int_0^1 \mathrm{d}x_i \sum_f \int \mathrm{d}\Phi_f \, \underbrace{f_{i/h}(x_i, \mu_F^2)}_{\text{PDF}} \underbrace{\frac{\mathrm{d}\hat{\sigma}_{\ell i \to f}(x_i, \Phi_f, \mu_F^2)}{\mathrm{d}x_i \mathrm{d}\Phi_f}}_{\text{PCS}} \tag{1.11}$$

where i runs over all possible parton types in the incoming hadron and f enumerates all possible final states with Lorentz-invariant phase space Φ_f. PDFs, $f_{i/h}$, are usually unpredictable or hardly predictable by the theory and are inferred from data with fits over a large sample of data. They are used to describe the hadron sub-structure. PCSs, $\mathrm{d}\hat{\sigma}$, are usually truncated at the desired precision, using perturbative QCD. Factorisation Scale (μ_F^2) is an arbitrary parameter defining the energy range for the two processes. The general hadron-hadron process, we write the factorable cross section as:

$$\sigma_{h_1 h_2} = \sum_{i,j} \int_0^1 \mathrm{d}x_i \int_0^1 \mathrm{d}x_j \sum_f \int \mathrm{d}\Phi_f \, \underbrace{f_{i/h_1}(x_i, \mu_F^2) f_{j/h_2}(x_j, \mu_F^2)}_{\text{PDF}} \underbrace{\frac{\mathrm{d}\hat{\sigma}_{ij \to f}}{\mathrm{d}x_i \mathrm{d}x_j \mathrm{d}\Phi_f}}_{\text{PCS}} \tag{1.12}$$

1.1.2 Soft processes

Soft process is a term usually referred to all the non-perturbative QCD processes for which a strict calculation to a certain precision order cannot be done. One then usually resort to phenomenological models to describe them.

Parton density function

The parton density function, $f_{i/h}(x_i, \mu_F^2)$, represents the effective density of partons of type/flavor i, as a function of the momentum fraction x_i, when a hadron of type h is probed at the factorization scale μ_F. These functions belong to the non-perturbative regime and are not calculable a priori, even though a perturbative differential equation governing their evolution with μ_F can be obtained. This means that only the form of the PDFs has to be determined as a function of x at a single arbitrary scale μ_F.

1.2 Phase transition in QCD: The Quark-Gluon Plasma

One of the most relevant discoveries in QCD in the last decades is the existence of the Quark Gluon Plasma (QGP). This new state of matter is comprised of quarks and gluons that undergo de-confinement, a phenomenon for which the high energy density provides enough momentum to the constituents to have high-Q^2 collisions and essentially shield them from the strong binding into hadrons. A lot of evidence and results support the QGP hypothesis and study its characteristics, such as the temperature, the energy density, the dimension and also its effect on subsequent hadronisation.

1.2.1 Experimental evidence and characterisation of the QGP

A large plethora of evidence has been recorded by the ALICE collaboration on the existence and on the properties of the QGP. It is current understanding that the collision of heavy ions at LHC evolves as show in Figure 1.4, with the creation of the QGP a small fraction (<$1\,\mathrm{fm}/c$) of a second after the first interaction of the nuclei. In the following sections an overview of the state-of-the-art results on the QGP existence and its characteristic is outlined.

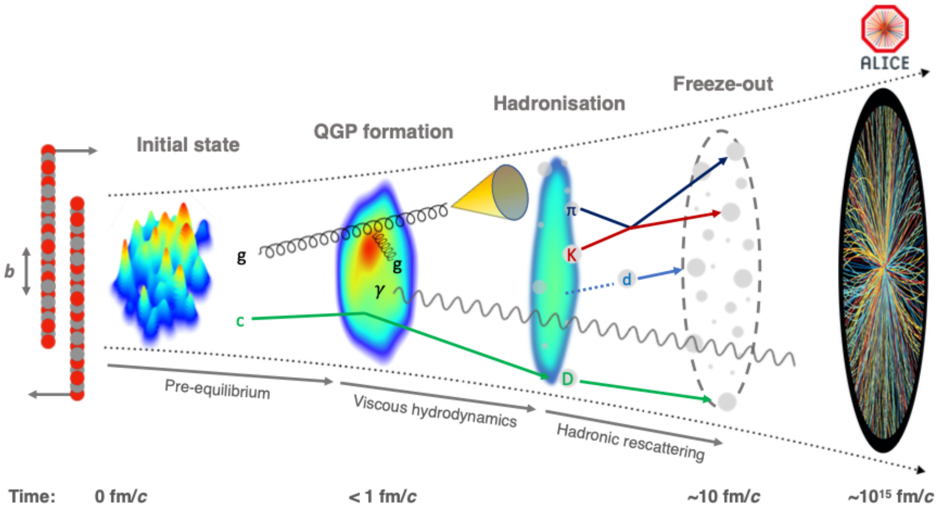

FIGURE 1.4: The evolution of a heavy-ion collision at LHC energies. The figure is taken from [6]

1.2.2 Macroscopic quantities and thermodynamics of QGP

We have claimed that the QGP does form in heavy ion collision at high energies. This occurs if, from lattice QCD theoretical calculations, the energy density exceeds a critical value of $\epsilon_c = 0.42 \pm 0.06\,\mathrm{GeV/fm^{-3}}$ [7] and the temperature reaches a value of $T_{\mathrm{pc}} \approx 157\,\mathrm{MeV}$ [7], slightly different depending on the calculations. The system then cools down and confinement kicks in. As in the rapid expansion of the fireball both the total energy and the entropy are expected to be approximately conserved, we can infer the quantities we are interested in from the final state with a good approximation. The initial state temperature is related to the final state charged hadrons multiplicity and the energy density to the transverse energy [6]. A selection based on the event centrality can indicate the initial energy concentration which in turn defines the charged final state multiplicity. The temperature and energy density can then be studied as a function of centrality. The chemical freeze-out phase is responsible for hadron production, but photons and leptons are emitted throughout the evolution of the fireball, giving indications on the evolution of the temperature. Lastly the system size and general properties can be studied by means of femtoscopy[3] and particle correlations.

Centrality evaluation

Centrality evaluation is an important tool to determine at least approximately the impact parameter b. It is usually expressed as percentile of the total hadronic cross-section, that is 0-5% indicates the 5% of most central events and 90-100% the 10% of the most peripheral events.

Charged particle density at mid-rapidity

This can be expressed as the charged multiplicity per unit of pseudorapidity $\mathrm{d}N_{\mathrm{ch}}/\mathrm{d}\eta$. If though this quantity differs significantly from pp to Pb–Pb central events, measurements can be compared by means of a normalisation to actual participants. We can define N_{part} as the number of nucleons in the nuclei that participate in an inelastic interaction (at least once) per collision. Then through $\langle \mathrm{d}N_{\mathrm{ch}}/\mathrm{d}\eta \rangle$ normalised to $\langle N_{\mathrm{part}} \rangle$ /2 a comparison is possible on similar grounds, trivially becoming unity in the case of a pp collision.

In Figure 1.5 the energy dependent evolution of the normalised charged particle multiplicty clearly shows a different trend for central nuclei collisions, that points to a more efficient energy use for hadron production in this system.

Initial energy density determination

To measure the Initial energy density we can make use of the "Bjorken-estimate" [26]:

$$\varepsilon_{\mathrm{Bj}}(\tau) = \frac{1}{S_{\mathrm{T}}\tau} \frac{\mathrm{d}E_{\mathrm{T}}}{\mathrm{d}y} \tag{1.13}$$

where $\mathrm{d}E_{\mathrm{T}}/\mathrm{d}y$ is the transverse energy $E_{\mathrm{T}} = \sqrt{p_T^2 + m^2}$ per unit of rapidity and S_{T} is the transverse size of the interaction region at the proper time τ. From the charged-particle multiplicity in pseudorapidity and assuming the charged-particle production in rapidity is a normal distribution, one can also extract a lower bound for the energy density times the proper time of the collision [23, 27, 28]:

$$\varepsilon_{\mathrm{LBj}}(\tau) = \frac{1}{S_{\mathrm{T}}} \frac{1}{f_{\mathrm{total}}} \sqrt{1 + a^2} \langle m \rangle \mathrm{d}N_{\mathrm{ch}}/\mathrm{d}y \tag{1.14}$$

where $\sqrt{1 + a^2}\langle m \rangle$ is the effective transverse mass, and f_{total} is the fraction of the charged out of all particles (roughly half) [29]. Here, a is the effective p_{T} $/m$ ratio extracted as part of the estimate. ALICE results on the energy density can be found in Figure 1.6.

---

[3] the technique of measuring short-range two-particle correlations as a function of relative momentum

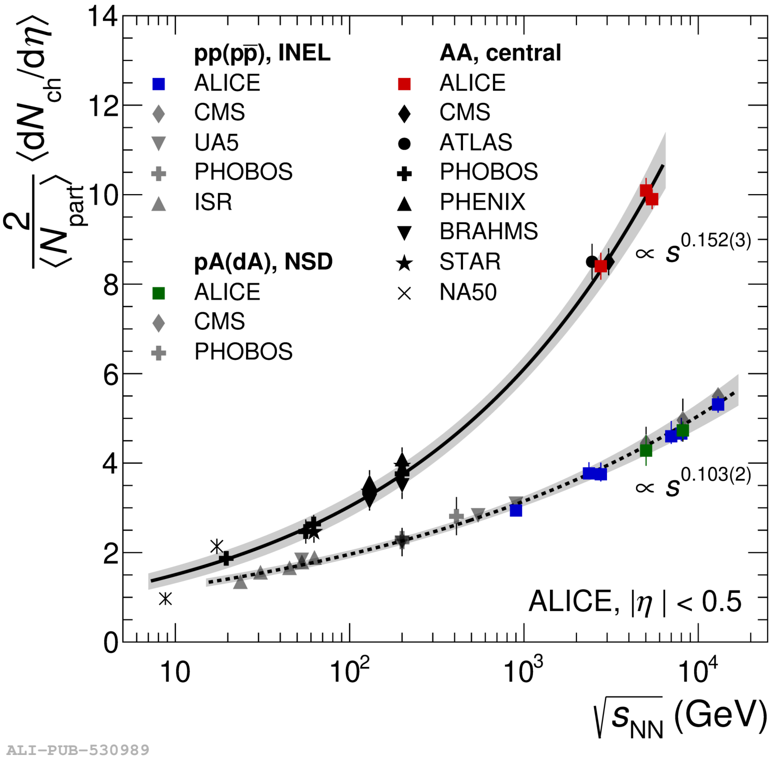

FIGURE 1.5: Collision energy dependence of the charged-particle pseudorapidity density at midrapidity ($|\eta| < 0.5$) normalised to the average number of participants, $\frac{2}{\langle N_{\mathrm{part}}\rangle}\langle \mathrm{d}N_{\mathrm{ch}}/\mathrm{d}\eta\rangle$. Data is from [8–25]. The figure is taken from [6]

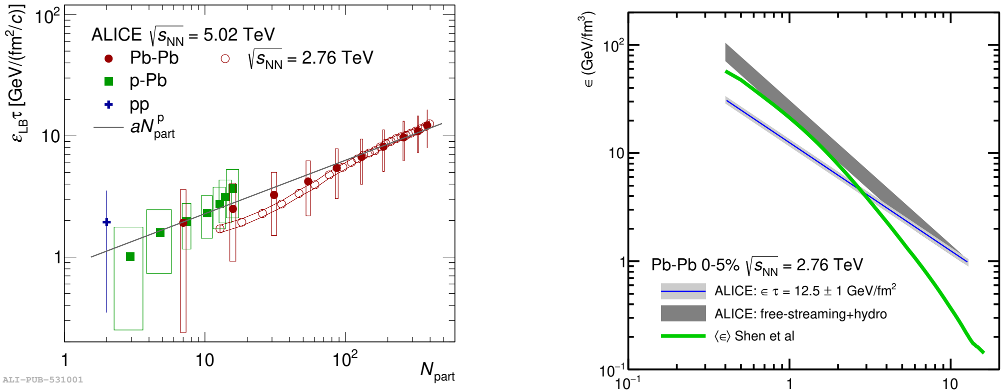

(A) Estimate of the lower bound for energy density times the formation time τ for different collision systems at $\sqrt{s_{\mathrm{NN}}} = 5.02$ TeV and 2.76 TeV, as a function of participating nucleons.

(B) Evolution of the average energy density as a function of the proper time of the system in hydrodynamic calculations.

FIGURE 1.6: Data is taken from [28–31]. The figure is taken from [6].

Temperature of the system

To measure the temperature of the QGP, one can rely on electromagnetic probes and heavy quarkonia produced in the initial hard scattering at the early stages of the collision. The quarkonia probe stems from the idea that the bound states produced in the early collision would propagate in a hot dense medium that would "melt" them, resulting in a suppression of their measured yield [32]. Electromagnetic probes are instead consisting of real and virtual photons, the latter studied by their di-lepton pair production. The present precision at the ALICE experiment only permits to study real photons as di-lepton measurements are not yet sensitive to possible thermal signals [33].

The present measurement for the QGP temperature makes us of the R_γ factor defined as:

$$R_\gamma = \frac{\gamma_{inc}}{\gamma_{dec}} \tag{1.15}$$

Where γ_{inc} refers to the inclusive photon invariant yield, γ_{dec} refers to the decay photon invariant yield. That is, R_γ is the excess of photons coming from the collision that are not produced by any hadron decay. As of the time of writing the consensus is that low p_T photons up to $3\,\mathrm{GeV}$ are dominated by thermal production, that approximately follow an exponential decay as $d^2N_{\gamma_\mathrm{dir}}/p_\mathrm{T}\ \mathrm{d}p_\mathrm{T}\ \mathrm{d}y \propto e^{-p_\mathrm{T}/T_\mathrm{eff}}$. Here T_eff represents the measured effective temperature, that needs model calculations taking into account for the evolution of the QGP medium as well as radial flow blue shift of photon spectra [34]. This correction has not yet been attempted. For central and semi-central Pb–Pb collisions, the fits lead to T_eff = (304 $\pm$ 41) MeV and T_eff = (407 $\pm$ 114) MeV. Further along the spectrum, above $5\,\mathrm{GeV}$ the dominant contribution becomes prompt photons, i.e. photons coming from the initial hard scatterings. In the high momentum tail the "jet-photon conversion"[4] phenomenon seems to take over, becoming the leading contribution.

Figure 1.7a shows a 2-6σ excess in the low p_T region of direct photons compatible with thermal photons from QGP. This result is interestingly in apparent contrast with Figure 1.7b that shows the photons do appear to have elliptic flow [5]. This contrast arises from the assumption that the photons are produced in the early stages of the QGP formation where still little flow is built up in the system. This tension in data interpretation is called the "direct photon puzzle".

Size and lifetime of the system

Femtoscopy is the main tool that allow us to measure the size and lifetime of the system. This technique measures momentum correlations at the kinetic freeze-out for two or more particles coming from a common source. The essence of the approach for two particles [43–45] is the equation:

$$C(k^*) = \mathcal{N}\frac{A(k^*)}{B(k^*)} \tag{1.16}$$

where $C(k^*)$ is the correlation function, $A(k^*)$ is the measured same-event distribution of particle pairs, $B(k^*)$ is the measured mixed-event distribution of particle pairs, $\mathcal{N}$ is the normalisation factor, k^* is the is the magnitude of the momentum of each of the particles in their pair rest frame.

This distribution is then fitted with a function that accounts for quantum statistics term for identical particles and a parameterisation which incorporates strong final-state interactions between the particles [46]. From this function one can calculate the radius of the emitting source, which is not necessarily equal to the total volume occupied by the system at the freeze-out temperature. This fit is performed

---

[4] high energy photons produced from energetic jets during their propagation through the QGP

[5] Anisotropic flow is quantified by studying the azimuthal distribution of particles emitted in the plane transverse to the beam direction. This is usually expressed in terms of a Fourier series in the azimuthal angle ϕ. The second Fourier coefficient, v_2, is usually referred to as elliptic flow.

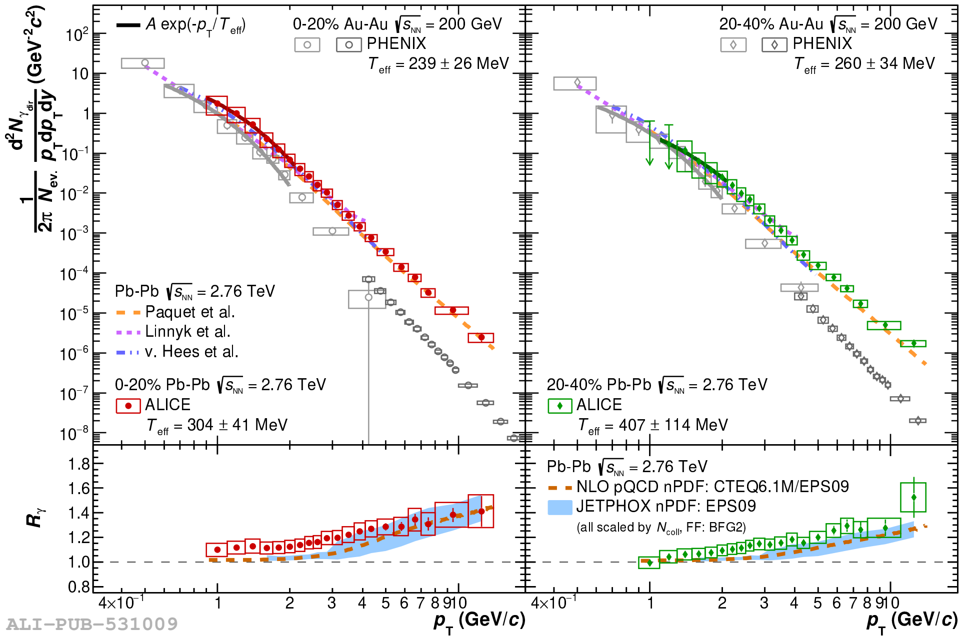

(A) Direct photons spectra. Slope of the exponential fit is corrected for pQCD contribution based off pp collisions for SPHENIX results. On the bottom is reported the R_γ direct photon excess.

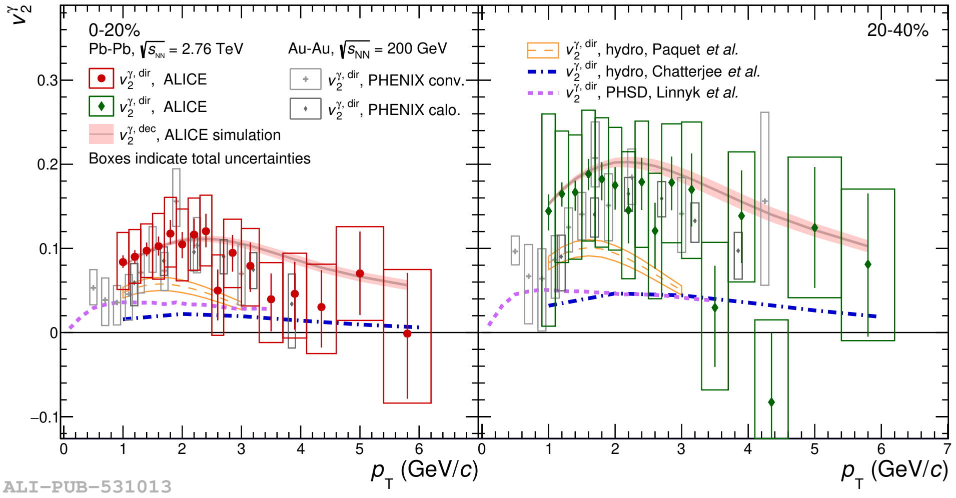

(B) Elliptic flow of direct photons. Model comparisons are from [35–37].

FIGURE 1.7: Data are for Pb–Pb collisions at $\sqrt{s_{NN}}$ = 2.76 TeV and 0.2 TeV [38–42]. Reported centrality classes are 0-20% (left) and 20-40% (right). Error bars and boxes represent the statistical and the total systematic uncertainty, respectively. The figure is taken from [6].

on correlations functions measured along the three axes of the difference between the particle pair momenta, giving a three-dimentional information about the source. The results for pions are reported in Figure 1.8a, assuming that they can be an indication for the whole system as they constitute 80% of all particles produced.

From the longitudinal radius of the source, the transverse mass and the kinetic freeze-out temperature one can also infer the decoupling time [47]. This information, measured again for the pions as a proxy for the whole system, is plotted in Figure 1.8b

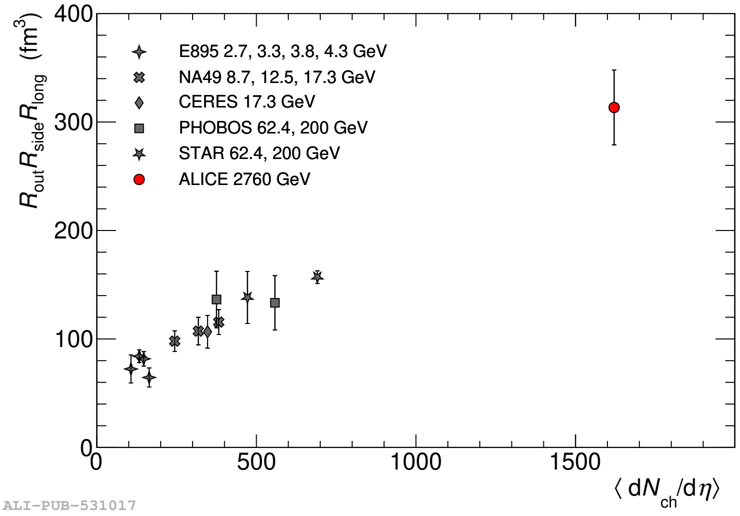

(A) Homogeneity volume, considering the pions radii at $\langle k_T \rangle$ = 0.3 GeV in 0-5% centrality events.

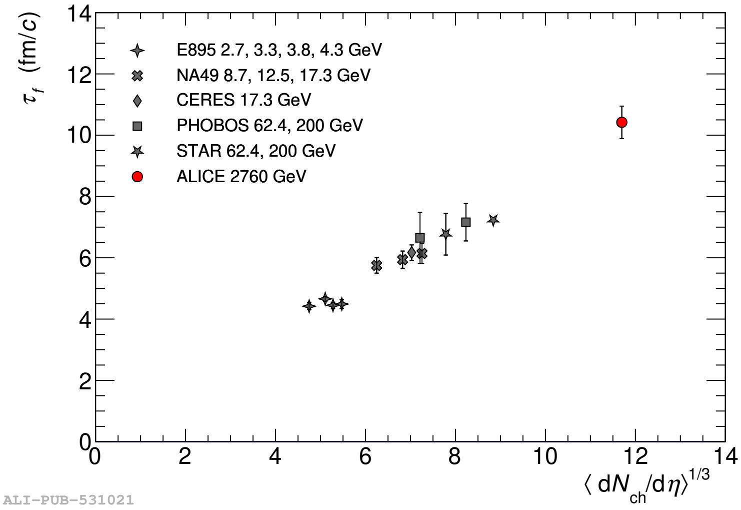

(B) Decoupling time considering the longitudinal pions radius at $\langle k_T \rangle$ = 0.3 GeV in 0-5% centrality events.

FIGURE 1.8: Data are for Au–Au and Pb–Pb collisions at $\sqrt{s_{NN}}$ = 2.76 TeV, 0.2 TeV and lower energies as reported [48–57]. Error bars represent the statistical and the total systematic uncertainty. The figure is taken from [6]

1.2.3 Hadronisation in the QGP

Hadronisation is the process by which the dense hot quark-gluon plasma becomes a hadron gas. This happens when the quarks and gluons start to experience smaller momentum transfers and the strong coupling strengthens: the phenomenon of confinement sets in. The critical point of energy density for the hadronisation to start is around $0.75\,\mathrm{GeV/fm^3}$ according to lattice-QCD calculations [7, 58]. This phenomenon falls under the umbrella of the Soft Processes for which one must resort to phenomenological models. These models include the statistical hadronisation models, the recombination model and many others. Most of the available models capture most of the key features of the hadron formation, despite missing many details.

After the hadronisation occurs, roughly 7-10 fm/c after the initial collision, the hadrons produced still interact with each other. This happens until the chemical freeze-out temperature is reached, after which inelastic collisions no longer happen.

This phase is still characterised by elastic collisions, mostly affecting resonances, that can undergo two main processes: regeneration and re-scattering, the former enhancing and the latter suppressing the measured resonance yields. On top of this effect, collective flow of particle can continue to build up, influencing all produced particles. This flow can be measured as a common directional shift of particle momentum distribution. These effects can persist up to the kinetic freeze-out, where all interaction stops, after $\approx 10\,\mathrm{fm}/c$.

These effects can be observed by measuring the yields of particles produced, differentiating by rapidity, momentum and/or azimuthal angle.

Resonances as a probe for the hadronic phase duration

Short- and long-lived resonances provide a useful probe for the measurement of the hadronic phase dynamics. The hadronic phase is defined as the window of time after the chemical freeze-out and before the kinetic freeze-out, that is when there are no loose quarks or gluons, having formed hadrons, and before hadrons stop interacting all together. This window can be of approximately 5-$10\,\mathrm{fm}/c$ and, depending on how long it actually last, the resonances measured yields are impacted by two main phenomena: re-scattering and regeneration. The former refers to the daughter particles of a decayed resonance elastically interacting with the hadron gas, modifying its momentum and thus effectively reducing the measured yield, which is relying on the invariant mass technique. The latter refers to the possibility for two hadron-gas particles to interact inelastically to form a new resonance, thus effectively enhancing the measured yield. Figure 1.9 shows a schematic representation of these processes. There has been no evidence of any effect compromising the shape or width of the invariant mass peak by these processes.

We can start by analysing a simple scenario of a sudden kinetic freeze-out: the yield of resonances mainly depends on their proper lifetime, the re-scattering cross section in the medium and on the time duration of the hadronic phase. Focusing on the latter we expect it to be longer for larger systems, i.e. central collisions and to study this phenomenon one can take the ratio of short- and long-lived resonances to particles with same or similar composition. We will analyse $\rho(770)^0$ (τ = $1.3\,\mathrm{fm}/c$, referred to as ρ), K$^*(892)^0$ (τ = $4.16\,\mathrm{fm}/c$, referred to as K*) , $\Lambda(1520)$ (τ = $12.6\,\mathrm{fm}/c$, referred to as Λ), $\phi(1020)$ (τ = $46.3\,\mathrm{fm}/c$, referred to as ϕ) [1]. We can now make use of their different interactions with the medium, to study the medium itself. In Figure 1.10a the p_T -integrated ratios are shown as a function of $\langle N_\mathrm{part}\rangle^{1/3}$ at $y \approx 0$, which is a proxy for the radial extent of the system.

The basic idea behind this analysis is that we expect the ratio of resonances to similar quark composition particles to be flat, when no re-scattering or regeneration occurs. To confirm this idea and to get a baseline measurement, we can take the ratio of a resonance with a lifetime greater than the hadronic phase ($\tau \gtrsim 20\,\mathrm{fm}/c$) to its more stable counterpart, like the ϕ meson to kaon shown in Figure 1.10a. The curve is flat and indeed the resonance reaches the end of the hadronic phase unscathed, making all the produced yield measurable. Along with it, we can see the behaviour of resonances with a lifetime in the order of or less than the hadronic phase ($\tau \lesssim 15\,\mathrm{fm}/c$), that is all others shown. Here, on the contrary, a suppression is seen with system size, indicating a dominating re-scattering effect that gets more pronounced for longer lived hadronic phases.

Assuming that regeneration effect is negligible in re-scaterring dominated resonances such as ρ, K* and Λ we can use an exponential fit to measure the hadronic phase lifetime. Defining the hadronic phase as the timespan between chemical and kinetic freeze-out ($\tau_{\mathrm{kin}} - \tau_{\mathrm{chem}}$) one can devise an exponential law such as $\mathrm{r}_{\mathrm{kin}} = \mathrm{r}_{\mathrm{chem}} \times e^{-(\tau_{\mathrm{kin}}-\tau_{\mathrm{chem}})/\tau_{\mathrm{res}}}$[59], where $\mathrm{r}_{\mathrm{kin}}$ is the ratio of resonance-to-stable-counterpart at the kinetic freeze-out, $\mathrm{r}_{\mathrm{chem}}$ is the same ratio at the chemical freezeout (reference is taken from pp collisions results), τ_{res} the proper lifetime of the resonance. The results of this calculation are reported in Figure 1.10b. A significant difference in the hadron phase duration can be seen from a resonance to another, with longer lived Λ experiencing a longer phase. This effect might be due to our approximation of negligible regeneration contribution. If regeneration is present, then we can suppose the measurement is sensitive to the timespan between the kinematic freeze-out and a delayed chemical freeze-out. The delayed chemical freeze-out would be defined as the average time of resonance formation, which would be influenced by later regeneration.

These last considerations, together with femtoscopy results suggesting [60, 61] a delay of 1.0 to $2.1\,\mathrm{fm}/c$ for the kaons, highlight how the picture described above is still too naive to account for the full picture and more research is required.

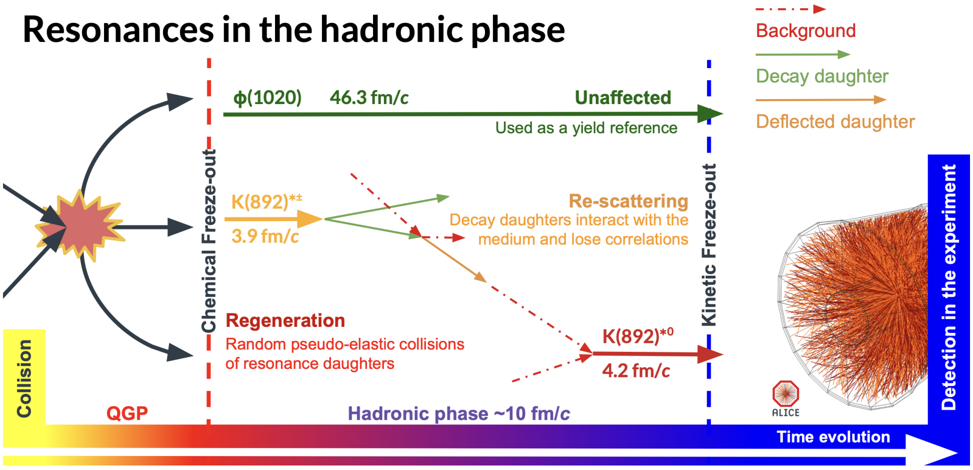

FIGURE 1.9: Schematic representation of the possible processes affecting the resonances measured yield. The resonances may be enhanced if the dominating effect is the regeneration, where inelastic random collisions generate new resonances, or suppressed if the dominating effect is the re-scattering, where at least one of the daughter particles elastically interact with the gas, losing the kinematic correlation to the other(s) daughter(s), making the invariant mass method unavailable to measure their yield.

Light-flavour hadron yields

Light flavour hadrons (made up of u-, d- and s-quarks) yields, light nuclei and hyper-nuclei, together with their anti-matter counterparts cover a large majority of the produced particles in high energy collisions. Their yields, measured by the ALICE collaboration at mid-rapidity, are reported is Figure 1.11 for Pb–Pb collisions at $\sqrt{s_{\mathrm{NN}}} = 2.76\ \mathrm{TeV}$. All the measurements are in good agreement with a statistical hadronisation model (SHM) picture, as can be seen by the comparison with thermal models such as THERMUS [73, 74], SHARE [75–78], Thermal-FIST [79, 80], and GSI-Heidelberg [81–83]. In a large fraction of the models the baryochemical potential has been set to zero as there is no evidence of asymmetry in matter-anti-matter production at LHC within uncertainties.

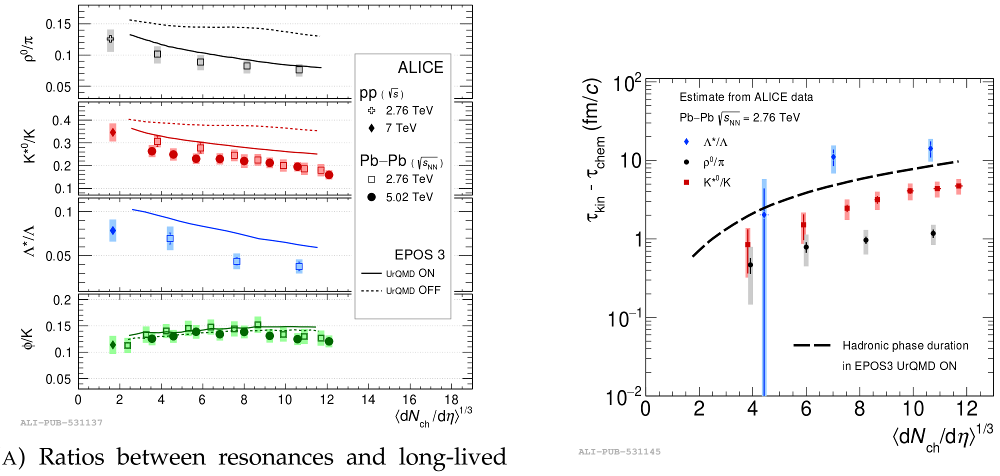

(A) Ratios between resonances and long-lived ground states at mid-rapidity in pp collisions at $\sqrt{s}$ = 2.76 TeV and 7 TeV [62–68] and in Pb–Pb collisions at $\sqrt{s_{\mathrm{NN}}}$ = 2.76 TeV and 5.02 TeV [59, 66, 67, 69–71] as a function of $\langle N_{\mathrm{part}}\rangle^{1/3}$. Model predictions are from EPOS3 with and without UrQMD [72].

(B) Duration of the hadronic phase, expressed as the time lapse from chemical to kinetic freeze-out as a function of $\langle N_{\mathrm{part}}\rangle^{1/3}$. The duration is calculated from the ρ, K* and Λ ratios in Pb–Pb collisions at $\sqrt{s_{\mathrm{NN}}}$ = 2.76 TeV, with the ρ to π ratio shifted by 0.1 for visibility.

FIGURE 1.10: Error bars and boxes represent the statistical and the total systematic uncertainty, respectively. The figure is taken from [6]

One of the less accurate predictions are protons, clearly showing an anomalously low measured yield, up to 25% lower than the expected yield. This has been called the "proton-yield anomaly". The causes of such a discrepancy are being investigated, although no definitive answer has been found. Some models could better predict their yield at the cost of increasing the chemical equilibrium temperature to 165 MeV [84].

From global fits a consistent chemical freeze-out temperature of $T_{\mathrm{chem}} \approx 156$ MeV is found, with a $\approx 1.5\%$ uncertainty. This values agrees with lattice QCD calculations that provide an estimate of the pseudo-critical point temperature of around $T_{\mathrm{pc}} \approx$ 156-158 MeV [7, 85] for the transition from the QGP to the hadron gas. The two quantities agree as the T_{pc} is the phase where multi-particle interactions are dominant, whereas the T_{chem} should be dominated by two-particle interactions and particles decay. This little interaction means the system fails to stay in equilibrium as the temperature drops, signaling the approaching hadronisation phase of the QGP. This value is a plateau that is reached when the $\sqrt{s_{\mathrm{NN}}}$ is above 20 GeV, whereas before we see a decrease in temperature proportional to the centre of mass energy.

The second important factor that can be measured through the global fit is the volume of the fireball for one unity of rapidity at the chemical freeze-out. Here models are much less in accordance: SHARE, Thermal-FIST, and GSI-Heidelberg report a volume of 4500 fm^3 whereas THERMUS gives a significantly larger number as it comprises an excluded-volume (Van-der-Waals like) correction [86].

Light-flavour particle spectra and ratios

The transverse momentum spectra of (anti-)pions, (anti-)kaons and (anti-)protons are shown in Figure 1.12, alongside the ratios of (anti-)protons to (anti-)pions (p/π) and of (anti-)protons to ϕ mesons (p/ϕ). The spectra are shown in central, peripheral Pb–Pb collisions and in pp collisions; a hardening of the spectra can be seen in the

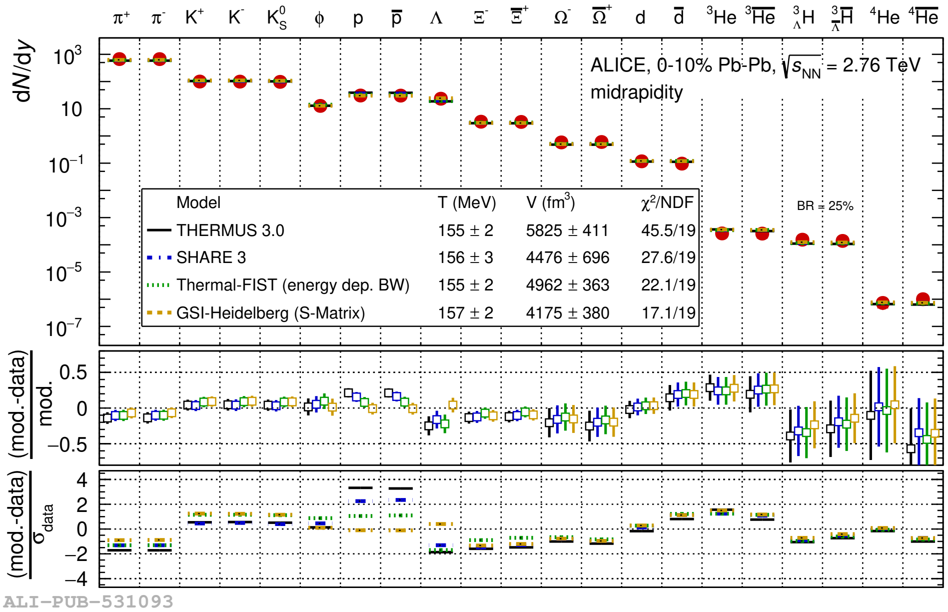

FIGURE 1.11: Particle yield at mid-rapidity for different hadron species and light nuclei [70, 71, 87–91] are compared to SHM fits from THERMUS [73, 74], SHARE[75–78], Thermal-FIST[79, 80], and GSI-Heidelberg [81–83]. The middle panel shows the relative difference between data and model, the bottom panel show the difference between data and model with respect to to the data uncertainty. The hypertriton yield is obtained through a theoretical 25% Branching Ratio in the ${}^{3}_{\Lambda}\mathrm{H} \to^{3} \mathrm{He}\pi^{-}$.

most central events.

Examining the p/π ratio, we notice a bump structure having a maximum of about 0.8 in the mid-momentum region, from roughly 1.5 to $8.0\,\mathrm{MeV}$. This phenomenon can be explained in terms of collective motion, where heavier particles are more boosted in momentum, and in terms of recombination being the dominant process. It is worth noting that the effect concerns a small fraction of pions (≈ 1.5%) and protons (≈ 7-20%), meaning the dependence on centrality of the p_{T} -integrated yield is mild. In fact the integrated yield only drops by 20% from head-on to peripheral collisions, suggesting the effect is mainly due to a re-distribution of hadrons in their transverse momentum spectrum [69, 83, 92, 93].

Further on, looking at the p/ϕ ratio, a greater insight can be gained. The proton and ϕ-meson masses are very similar, but with very different quark content. Their ratio in the low-p_{T} region ($< 6\,\mathrm{GeV}/c$) is mildly dependent for central events, as pointed out by the dark red curve, and show a more significant dependence for peripheral and small collision systems. This can be explained in the hydrodynamical picture [94, 95] by the fact the mass of the hadron is the main driver in the determination of the transverse momentum distributions. Going into smaller and smaller systems this behaviour is lost and a sharper dependence on momentum of the ratio is observed. In the high-p_{T} region the vacuum-like fragmentation picture takes up a more significant fraction of particle production in all cases, explaining why the results are compatible with each other for all systems [96].

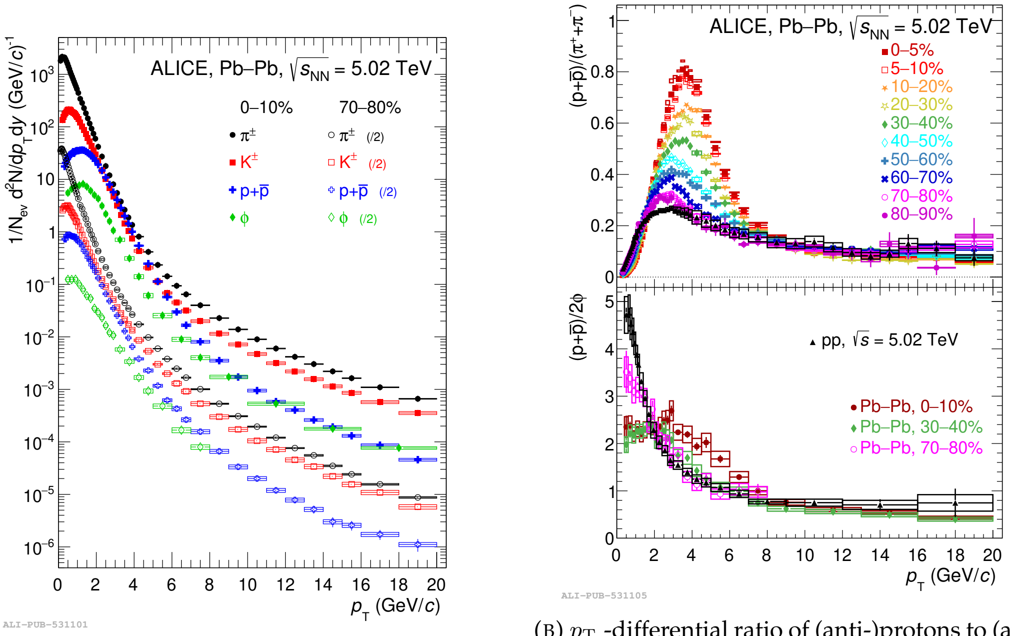

(A) $\pi^{\pm}$, $\mathrm{K}^{\pm}$, $\mathrm{p}+\overline{\mathrm{p}}$ p_{T} spectra in 0-10% (filled markers) and 70-80% (empty markers) centrality classes for Pb–Pb collisions at $\sqrt{s_{\mathrm{NN}}}$ = 5.02 TeV.

(B) p_{T} -differential ratio of (anti-)protons to (anti-)pions and ϕ-mesons in pp collisions at $\sqrt{s}$ = 5.02 TeV. The (anti-)protons to (anti-)pions ratio reports only the systematics uncertainties uncorrelated across centrality classes for visibility sake.

FIGURE 1.12: Data shown is from [59, 69]. Error bars and boxes represent the statistical and the total systematic uncertainty, respectively. The figure is taken from [6]

Strangeness enhancement in heavy-ion collisions

Strangeness enhancement was the first proposed signature of the QGP [97, 98] in the 1980s. The basic idea behind this phenomenon is that the hot and dense medium would favour the strange quark production, as it has relatively low mass its production is possibile via gluon splitting in thermal bath. As the strange quarks are produced, an equilibrium is reached as annihilation processes begin to balance the production.

One of the first and clear signature of strangeness enhancement, and consequently QGP formation, in heavy-ion collisions was reported by the NA35 Collaboration in July 1995 1.13. The ratio of Λ/p is reported as $\approx$ 1.4, with a fourfold increase with respect to smaller collision systems. The WA85 and WA94 focused on (anti-)hyperon ratios, measuring Ξ/Λ, shown in Figure 1.14. These results showed the hierarchy of the enhancement with the strangeness content.

As seen in the preceding sections, the start of LHC and ALICE in particular was a time of great advancement in the field. In one of the first reviews from the collaboration, in 2013, a summary of the then state-of-the-art findings on the strangeness enhancement is shown in Figure 1.15.

Turning to the present day, strange particles are still of particular interest. As can be seen in Figure 1.11 the various SHM models tend to underestimate the data points. One proposed solution is to set different hadronisation temperatures for strange quarks with respect to up and down quarks, based on lattice calculations the formers deconfinement temperature is slightly larger. This in turn implies a hierarchy in the hadronisation temperatures, having strange quarks with a

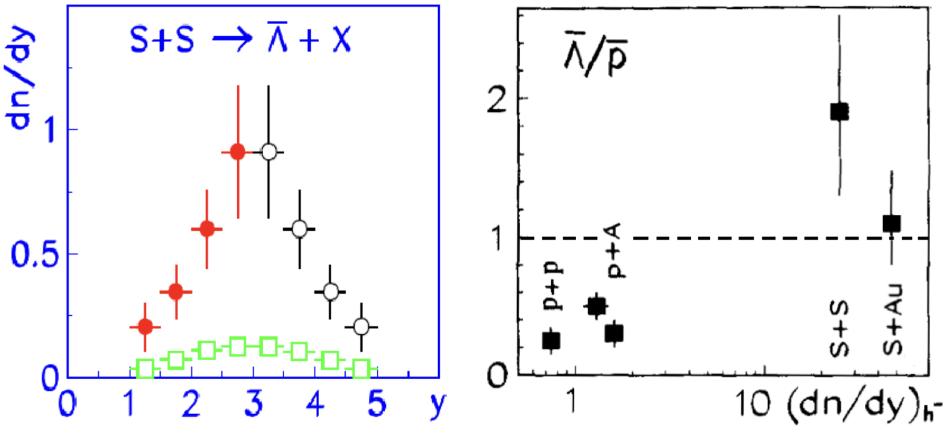

FIGURE 1.13: NA-35 antihyperon results for S-S collisions at $\sqrt{s_{\mathrm{NN}}} = 200$ GeV [99]. Figure taken from [98].

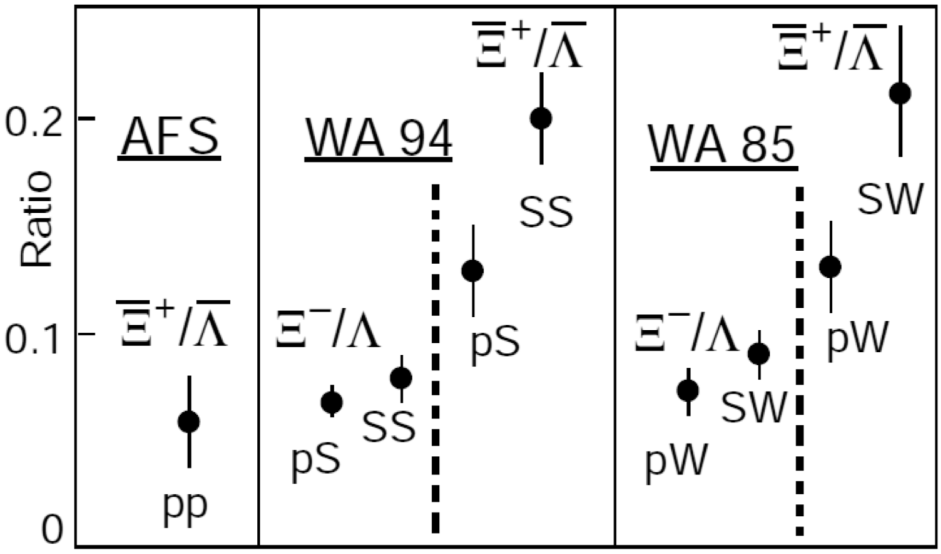

FIGURE 1.14: WA85 and WA94 (anti-)hyperon measurements for S-A collisions $\sqrt{s_{\mathrm{NN}}} = 200$ GeV [100]. Figure taken from [98].

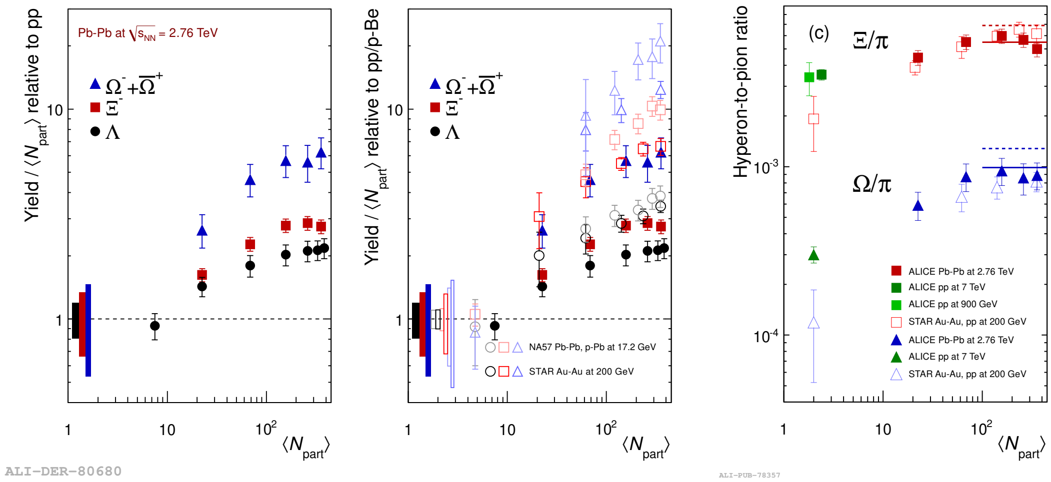

FIGURE 1.15: ALICE, RHIC and SPS results on Strangeness enhancement. Figure taken from [71].

$10-15\,\mathrm{MeV}$ higher characteristic temperature [101, 102]. This difference in temperature decreases with decreasing available energy, i.e. with increasing baryo-chemical potential. It is worth noting that not all the necessary correction have been yet applied to this approach, leaving some room for improvements to the theoretical predictions.

The production yields of strange and multi-strange particles at mid-rapidity in heavy-ion collisions are in general adequately described by the full-equilibrium SHM model which corresponds to the grand-canonical ensemble. For smaller collisions such as pp , the relative abundance of strange hadrons is instead treated with a canonical ensemble, introducing a correlation volume parameter to account for local conservation of the quantum number [103]. This approach then describes a strangeness suppression rather than an enhancement and explains the transition in terms of a passage from a canonical to a grand-canonical system. This description still falls short to an accurate prediction, as will be discussed in 1.3.

1.2.4 Partonic interactions in the QGP

This section focuses on some of the so-called hard probes for the existence of the QGP. That is, the interaction of particles produced in high-Q^2 initial collisions that are thus far from the equilibrium of the QGP. These particles undergo propagation in the QGP, giving rise to the possibility of using them as proxy to study in-medium interactions.

One of the most common ways to characterise this effect is the nuclear modification factor:

$$\mathrm{R}_{\mathrm{AA}}(p_{\mathrm{T}}) = \frac{1}{\langle T_{\mathrm{AA}}\rangle}\frac{\mathrm{d}N_{\mathrm{AA}}(p_{\mathrm{T}})/\mathrm{d}p_{\mathrm{T}}}{\mathrm{d}\sigma_{\mathrm{pp}}(p_{\mathrm{T}})/\mathrm{d}p_{\mathrm{T}}} \tag{1.17}$$

where $\langle T_{\mathrm{AA}}\rangle$ is the average nuclear overlap function, which is obtained dividing the average collisions number by the inelastic nucleon-nucleon cross section. The numerator of the second fraction then refers to the p_{T} -differential yield of a given particle and the denominator is the production cross section in pp collision. Then, we have a way to directly compare the production in A–A to the one in pp , rescaled by the average number of binary nucleon-nucleon collisions in the A–A system.

Heavy-quark diffusion

The study of heavy-quarkonia produced in the early stages of the collision can help us understand how they interact with the hot medium. Figure 1.16 shows the evolution with p_T of the R_{AA} and v_2 of prompt D-mesons in central and semi-central collisions. These results are consistent with previous results from both ALICE and CMS [104–108]. In the low- and mid-region of the p_T spectra the dominant process is expected to be the collisional interaction, which is consistent with the many models displayed based on quark transport in hydrodynamical expanding QGP.

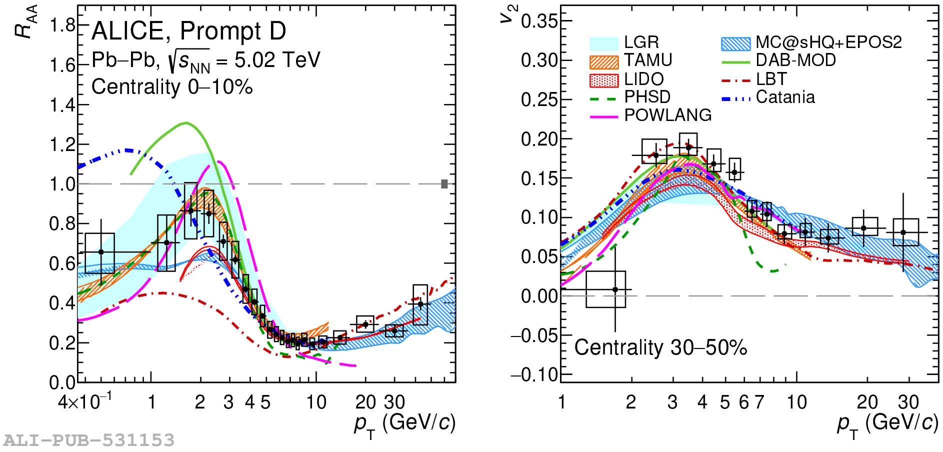

FIGURE 1.16: (right) D-meson production in Pb–Pb collisions at $\sqrt{s_{NN}}$ = 5.02 TeV [109, 110]. (Left) R_{AA} in 0-10% collisions; (right) v_2 in 30-50% collisions. Shown model calculations implement charm-quark transport in a hydrodynamically expanding QGP are: TAMU [111], LIDO [112], POWLANG [113–115], PHSD [116], MC@sHQ [117], Catania , LBT [118, 119], LGR [120], and DAB-MOD [121]. The figure is taken from [6]

Jet quenching

The phenomenon of jet quenching is the study of how the jets produced in the early stages of the collisions are modified after they traverse the hot QGP medium.

One of the most straightforward measurements that can be performed to assess this is the energy loss. Radiative energy loss is the expected dominant effect, responsible for the suppression of inclusive particle production in the high-p_T region, dominated by jets. An example of this effect is shown in Figure 1.17 via the aforementioned R_{AA} (Equation 1.17). It is clear by this picture that a relatively consistent result with the pp baseline (within 10%) is achieved for the p–Pb system, whereas going into Pb–Pb we see a suppression in high-p_T region (above $2\,\mathrm{GeV}/c$) of about 20% already in peripheral collisions (70-80%). For most central collisions (0-5%) we see a suppression of up to 85%.

This suppression is considered related to the energy loss for jets in the hot QGP medium. Other results can help have a clearer picture, such as shape and deflection.

1.2.5 Deconfinement in the QGP

Heavy quarkonia states of charmonium ($c\bar{c}$) and bottomonium ($b\bar{b}$) have been studied extensively since their discovery, a recent overview can be found in [123].

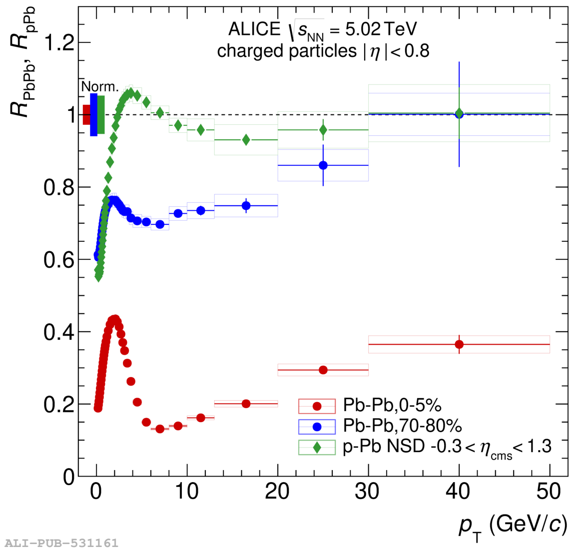

FIGURE 1.17: R_{AA} modification factor measured for p–Pb and central, peripheral Pb–Pb collisions. The figure is taken from [122].

The basic idea behind the interaction of quarkonia and QGP lies within the screening of colour charge in the deconfined medium, leading to a "melting" of the bound state [32]. Then, a connection from the quarkonia suppression to the temperature of the deconfined phase can be made [124]. The basic principle is that the binding energy, spanning from a few MeV to $1\,\mathrm{GeV}$, directly correlates to a dissociation temperature: in this picture analysing which states dissociate provides an estimate of the temperature created in the system. The temperature in heavy-ion collisions can in principle be varied by selecting on centrality.

The above considerations are strictly true for a static picture, with more complex interplay and effects arising in a more dynamic picture of production and evolution of quarkonia in a fireball. For example, indications of a regeneration effect have been measured together with an anisotropic suppression [125–130].

Charmonium

One of the main results on J/ψ suppression is shown in Figure 1.18a, where the R_{AA} factor as a function of charged multiplicity is measured. The latter can be considered a good proxy for collision centrality when considering the same system and energy. For different collision systems it is related to the initial energy density [26]. The measurements for the J/ψ go down to $0\,\mathrm{GeV}/c$, but a selection is performed to reject J/ψ coming from photo-production. The prominent result extracted from this is the onset of a regeneration effect for high multiplicity events at LHC, which are not seen in previous results.

In Figure 1.18b a rapidity dependent study from ALICE is shown. The two rapidity regions considered are $|y| < 0.9$ and $4 < y < 2.5$ from measured J/ψ in the e^+e^- and $\mu^+\mu^-$ channels respectively in central Pb–Pb collisions. The suppression effect does not seem to depend on the rapidity in the high p_{T} limit, whereas a significant suppression in forward production with respect to central yield is highlighted in the low-p_{T} region. Here, regeneration is indicated to be the main effect for this discrepancy. It is worth noting that the high-p_{T} limit reproduces the earlier findings on R_{AA} for charged hadrons. This picture is compatible with parton energy loss as a significant effect.

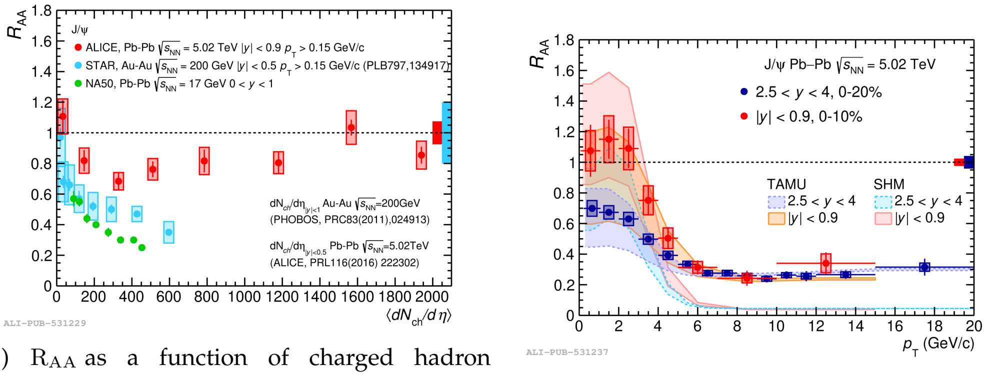

(A) R_{AA} as a function of charged hadron multiplicity for the J/ψ, selecting on p_T >0.15 GeV/c.

(B) R_{AA} as a function of p_T for central and forward rapidities with model comparison.

FIGURE 1.18: Data shown is from [131–134], p–Pb at $\sqrt{s_{NN}} = 5.02$ TeV, and models are from [135, 136]. Error bars and boxes represent the statistical and the total systematic uncertainty, respectively. The figure is taken from [6].

Bottonomium

A remarkable result that was discovered at LHC is that the bottonomium R_{AA} indicates a strong suppression already in semi-peripheral collisions, as shown in Figure 1.19, in a hierarchy dictated by their binding energies [124]. Generally, all models have an adequate description of the data points, although the large uncertainty may be covering possible discrepancies. TAMU is shown also with a small regeneration component, whereas all other models do not foresee such an effect. A large part of the bottonomium production in pp (30-50%) comes from feed-down contributions, which might point toward a suppression derived from the strong suppression of the excited states [137–139].

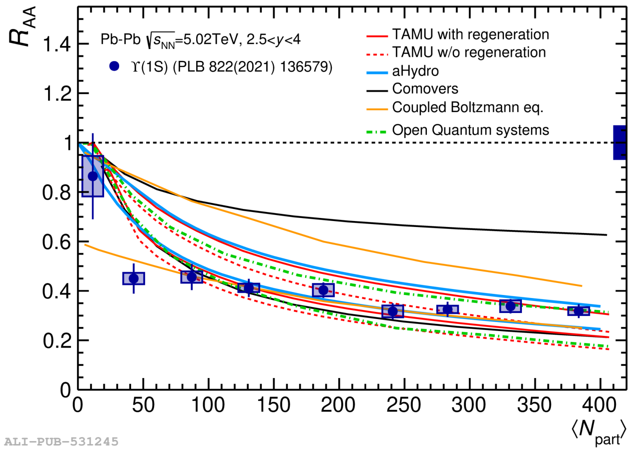

FIGURE 1.19: R_{AA} as a function of the average number of participating nucleons ($\langle N_{part} \rangle$) for ϒ(1S). Error bars and boxes represent the statistical and the total systematic uncertainty, respectively. Data is form [140], models are form [141–145], the two lines representing lower and upper limits of uncertainties. The figure is taken from [6].

1.3 High density QCD effects in small systems

The start of the last decade saw the widespread belief that pp and p–Pb collisions systems were to be regarded as some kind of baseline for heavy-ion collisions physics. This belief was thrown off by an ever increasing amount of evidence of high-density QCD phenomena in small collision systems. This can be seen in the historical excursus in Section 1.2.3. The data collected by the LHC even shows a number of pp collisions reach the multiplicities of peripheral Pb–Pb collisions. QGP reminiscent effects were found in this small system such as Strangeness Enhancement [63] and a double-ridge extended in pseudo-rapidity [146–149]. Then the question that arise from this is if the QGP is really forming in these collisions or not. If it is indeed creating, what mechanisms are responsible for providing sufficient energy density to produce it. The search for a better understanding of the reasons leading to these results has been since one of the main focus of the ALICE collaboration.

The results are mainly differential in multiplicity, with a selection performed similarly to what was done for centralities in Pb–Pb collisions; more information can be found in [150]. The event classification is a very important tool to disentangle the effects measured in the data and although most of the currently published results are using multiplicity, many new ways to characterise events are being explored as means to leverage different aspects of the collision dynamic. This is all part of the effort to shed a brighter light onto the new phenomena that emerge and to understand their origin. For example, the similar multiplicities seen for peripheral heavy-ion collisions and high-multiplicity pp collisions might be similar "on the surface" but coming from wildly different environments, energy densities, processes, etc.

1.3.1 Strangeness enhancement in small systems

A large plethora of results have been published by ALICE through the years in a large selection of systems (pp , p–Pb , Pb–Pb , Xe–Xe) and energies ($\sqrt{s_{\mathrm{NN}}} = 2.76$ TeV, $5.02\,\mathrm{TeV}$, $7\,\mathrm{TeV}$, $13\,\mathrm{TeV}$). An overview summary of such results can be found in Figure 1.20.

One striking observation is that all particles have an enhancement of production as a function of final state charged multiplicity in pp and p–Pb up to a plateau measured in Pb–Pb . More so is the case for strange particles, that show a behaviour known as strangeness enhancement: this phenomenon see a more exacerbated surge in particle yield for the strange sector with respect to the other non-strange mesons and baryons. The effect can be seen in the left panel of Figure 1.20 and it does, in fact, seem to be only driven by the final-state multiplicity, rather than on system size or beam energy.

Keeping in mind Figure 1.20 and turning our attention to Figure 1.21 a focus on strange particles is shown. Here one can notice how particles containing more strangeness are more enhanced than particles containing less strange content (See, for example, Ξ-baryons with respect to $\mathrm{K}^0_{\mathrm{s}}$). A special case has to be made about the ϕ-meson, as it is a bound state $s\bar{s}$: this makes the meson a probe of choice to understand the underlying mechanism of strangeness production and specifically for strangeness enhancement. As can be seen by the two model predictions shown in Figure 1.21a one can notice how the baseline tune (Monash 2013 and THERMUS SCE) both describe a rather flat behaviour, that have been adjusted with following updates to the models to better describe the published measurements. In the case of the Pythia model, rope hadronisation came into play, which is the topic of Section 1.4, whereas the Thermal model introduced a new factor γ_{s}, introducing local exact conservation of three conserved charges, allowing for a possibility of strangeness undersaturation [79, 151]. These results and subsequent additions show how important the ϕ-meson and in general the measurements of strangeness both in small and large collision system is to constrain theoretical models. These new findings perpetrated the novel idea to consider pp and p–Pb collisions as focus of renewed interest rather than an environment for baseline measurements for heavy-ion physics.

Turning our attention to Figure 1.21b one can notice that the enhancement of the ϕ meson can be assessed to be between 1 and 2 units of strangeness. This was particularly surprising in the Thermal description, where the strangeness suppression is expected to depend directly on the strangeness quantum number, which presumes the ϕ meson to behave as an $S = 0$ particle (hidden strangeness). In fact, also for Thermal-FIST γ_s CSM [79, 151], the prediction is still rather constant in multiplicity, with an enhancement for low multiplicities, in complete contrast with data points trends.

1.3.2 New proposed event classifiers

In an effort to provide a new way to explore high-multiplicity pp collisions, where similar behaviours to p–Pb and Pb–Pb collisions have been measured, a new event classifier has been devised. The basic idea is that the investigation of such similarities pushes toward the selection of high-multiplicity events, which skews the results toward events characterised by an abundance of jets and hard processes. Here, one wishes to then disentangle, among this class of events, which are closer to be hard-processes dominated and which are more keen on being soft-processes dominated. Among many others, we can see spherocity [158], transverse activity R_T [159] and effective energy [160].

Transverse activity

In Figure 1.22 a schematic representations of the basic idea of the classifier is shown. The transverse activity classifier (R_T) takes the ratio of the primary charged-particle multiplicity in the transverse region (N_T) obtained event-by-event to the average value ($\langle N_\mathrm{T}\rangle$) [161, 162]. It is defined as

$$R_\mathrm{T} = \frac{N_\mathrm{T}}{\langle N_\mathrm{T}\rangle} \tag{1.18}$$

The transverse region is defined taking the azimuthal difference of the incoming particle with respect to the leading particle, which is defined as the one having the highest p_T in the event.

In the small system context this new classifier can then help understand the properties of events with lower or higher contributions from the Underlying Event (UE). One can compare the results for low-UE events to the e^+e^- collision data (jet-universality) or to the high-UE to test the observation of non-trivial soft QCD dynamics [162–164]. This approach has also been used by ALICE in pp collisions at $\sqrt{s} = 13$ TeV [159].

Figure 1.23 shows the comparison of the R_T differential results from pp and Pb–Pb data, highlighting how the low-UE dominated environment of Pb–Pb collisions have a feeble dependence on the R_T selection, whereas the pp data show a strong autocorrelation with the R_T selection. This new method is an example of how novel techniques are being developed and employed on ALICE data to uncover new ways

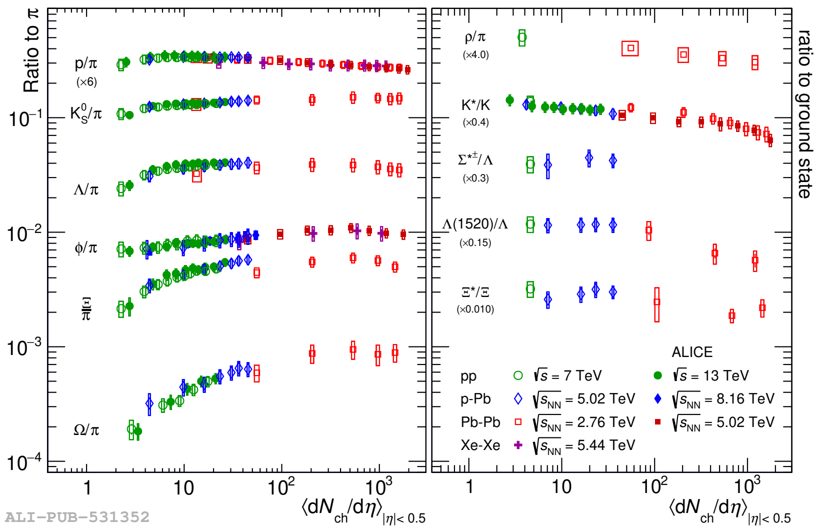

(A) Reference for pp system.

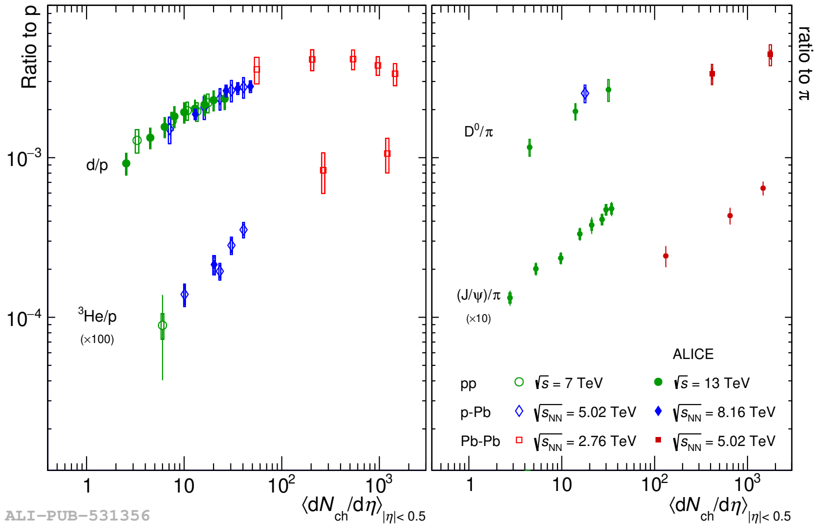

(B) Reference for Pb–Pb system.

FIGURE 1.20: Data is taken from [62–66, 68, 152–155]. All yields shown are measured at mid-rapidity, shown as a function of the event average multiplicity at mid-pseudorapidity. The error bars show the statistical uncertainty, whereas the empty and dark-shaded boxes show the total systematic uncertainty and the contribution uncorrelated across multiplicity bins, respectively. The figure is taken from [6].

to deepen our understanding of these new phenomena of high-density QCD in small systems.

Spherocity

In Figure 1.24 a schematic representations of the basic idea of the classifier is shown. The spherocity classifier (S_0) evaluates the level of "jettiness" of the event, defining UE-dominated events as opposed to jet-dominated events. It is defined as:

$$S_0^{p_T=1} = \frac{\pi^2}{4}\min_{\hat{n}}\left(\frac{\Sigma_i|\hat{p_T} \times \hat{n}|}{N_{\mathrm{trks}}}\right)^2 \tag{1.19}$$

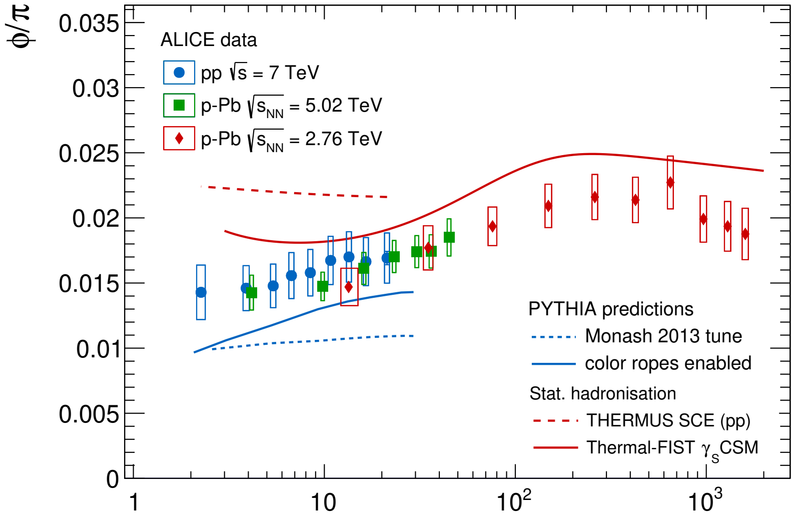

ALI-PUB-531364

(A) p_T -integrated yield at mid-rapidity of the ϕ meson as a function of final state charged particle multiplicity.

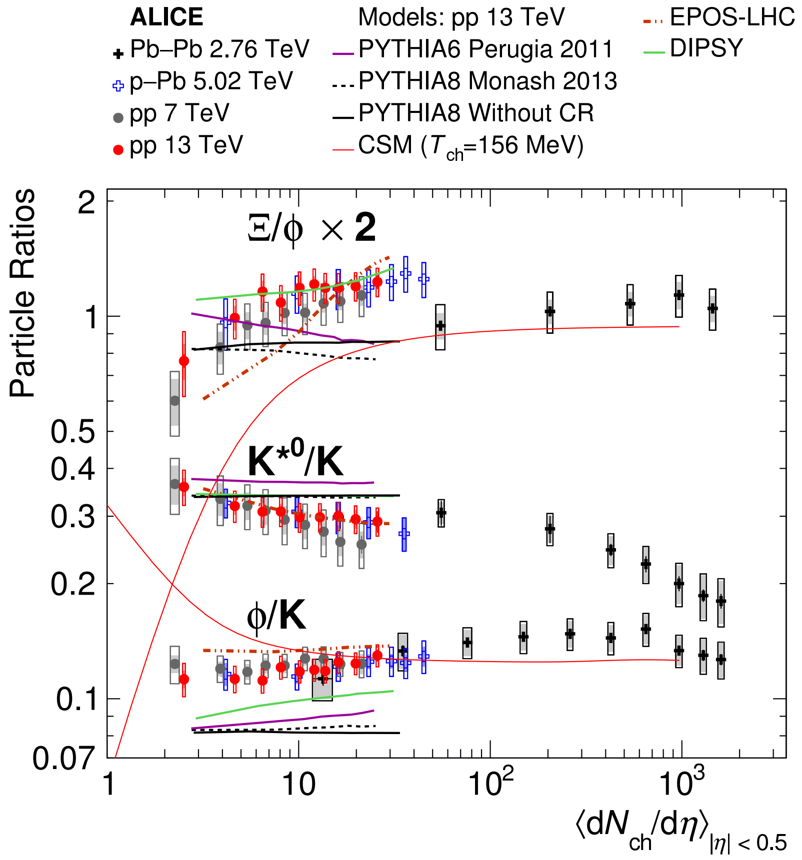

ALI-PUB-339048

(B) A selection of strange particle ratios for p_T -integrated yield at mid-rapidity as a function of final state charged particle multiplicity.

FIGURE 1.21: Curves are compared to theoretical models predictions for PYTHIA 8.2 (Monash 2013 Tune) [156], PYTHIA colour ropes model [157], THERMUS SCE [73], Thermal-Fist [79]. The figures are taken from [6] (1.21a) and [65] (1.21b).

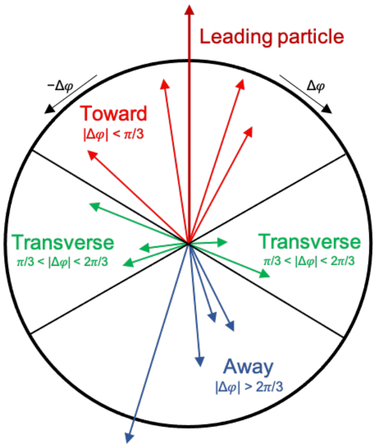

FIGURE 1.22: Schematic representation of the transverse activity classifier regions. The figure is taken from [165]

where $\hat{p_{\mathrm{T}}}$ refers to the p_{T} vector on the transverse plane, is a unit vector scanning the whole azimuthal angle, N_{trks} is the total number of tracks in the event. p_{T} =1 refers to the unweighted spherocity, meaning only the p_{T} direction in the transverse plane is considered. This new classifier come with a number of caveats that are extensively spoken of in [158].

In a similar fashion to the R_{T} selection, the goal is to select UE-derived physics from jet-derived physics. The main difference is that the R_{T} selection is on the transverse activity, with no requirement on the jet component, whereas the spherocity selects events based on the overall "shape" of the event.

The new results from ALICE show some very surprising behaviours such as the one shown in Figure 1.25. The p_{T} -integrated yield of the ϕ meson as a function of spherocity show a behaviour more similar to the non-strange hadrons rather than the strange ones. Another striking effect is that even though the PYTHIA models do not accurately predict the ϕ-meson yield and give significantly different predictions, the shown double ratios are consistent with model predictions, which are similar. This is an instance of what was discussed in the previous section, when a new classifier can shine a new light onto a phenomena, by highlighting mechanisms that were previously unaccessible and show how models behave in a more thorough comparison.

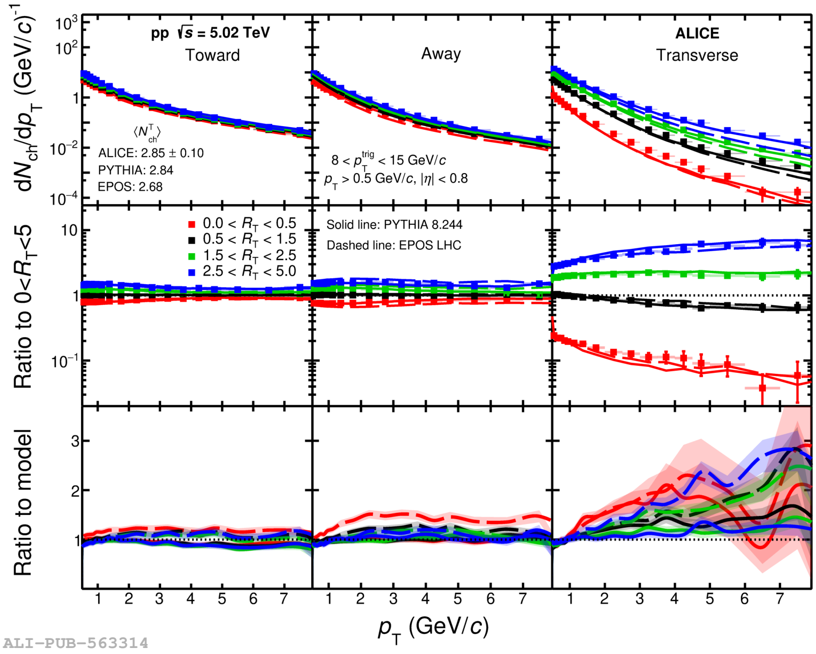

(A) Reference for pp system.

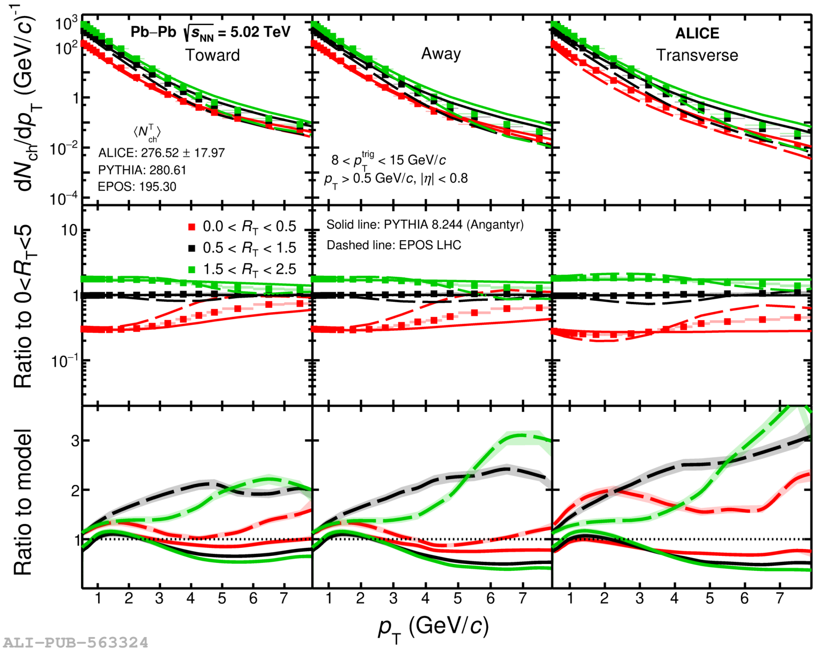

(B) Reference for Pb–Pb system.

FIGURE 1.23: Top panels show the p_T spectra of charged particles differentiated in different R_T regions as reported in Figure. Middle panels show the ratio of the spectra to the R_T integrated spectra. The boxes and bars represent the systematic and statistical uncertainties, respectively. Bottom panels show the ratio of the spectra to model predictions. Data points are compared to PYTHIA8 [156] and EPOS-LHC [166]. The shaded area represents the sum in quadrature of the systematic and statistical uncertainties. The figure and data is taken from [165] for both pp at $\sqrt{s} = 5$ TeV and Pb–Pb at $\sqrt{s_{NN}} = 5$ TeV.

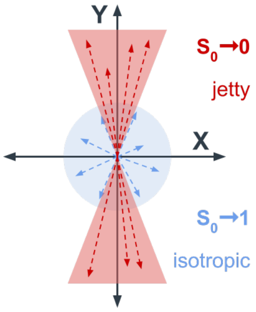

FIGURE 1.24: Schematic representation of the spherocity classifier.

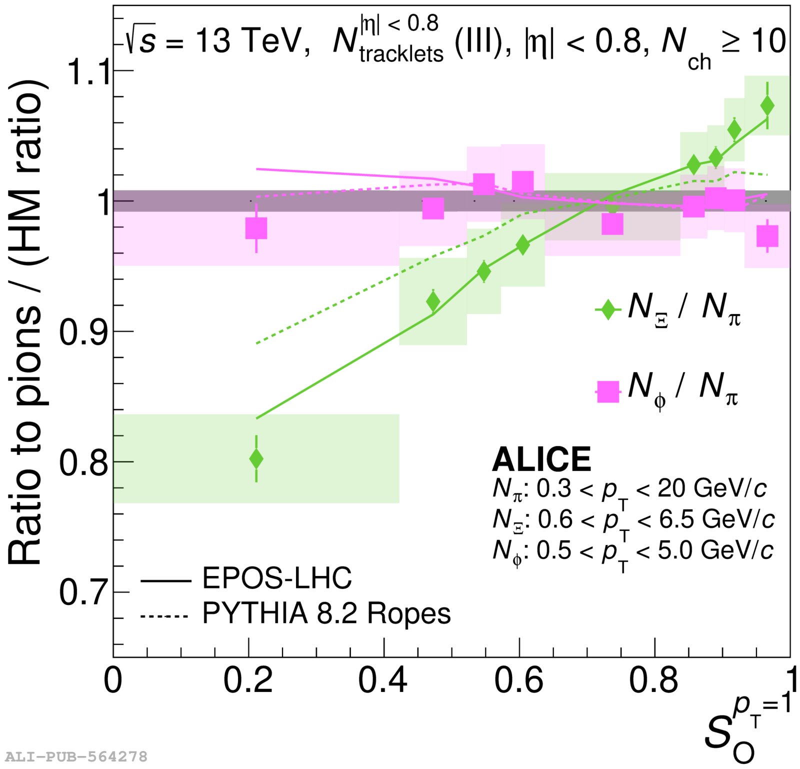

FIGURE 1.25: Schematic representation of the transverse activity classifier regions. The figure is taken from [158]

1.4 The Lund String Model

The Lund String Fragmentation Model [156] is based on a simple concept: the strong force creates a string between two quarks, that can eventually break generating new quarks on the loose ends.

The basic idea is that the linear strong potential between quarks will eventually store enough energy to produce a pair of $q\bar{q}$ if initial quarks are provided with sufficient energy. Their interaction can be modelled by a string between them, and their motion as a back-and-forth along their connecting axis. In this simple terms, the further they drift apart, the more energy will be stored in the string, if the energy is high enough a new pair of $q\bar{q}$ will be produced. That is the creation of $q\bar{q}$ and the subsequent creation of two strings is energetically favourable. This kind of approach can be made with a parametrisation of the strong potential as:

$$V_{QCD}(r) \approx -\frac{4}{3}\frac{\alpha_s}{r} + kr \tag{1.20}$$

Where $k \approx 1\,\mathrm{GeV/fm}$ and r is the distance between a quark and an antiquark, α_s is the strong coupling constant. One can see that kr is the dominant term.

As an example, if the oscillating quarks are $\overline{u}d$, a $s\overline{s}$ string breaking will result in the production of two kaons, if the string breaks twice and a double $s\overline{s}$ breaking occurs, two kaons and a ϕ meson are produced. In the case where the string breaks with a triple $s\overline{s}$ breaking, two kaons and two ϕ-mesons are produced.

The key to this phenomenological approach is the assumption of *jet universality*, the idea that the fundamental hadronisation process is unchanged from e^+e^- to pp collisions. Tuning on the "clean" events at LEP, the model is able to describe a large variety of events as a direct consequence of the assumption that the string tension, responsible for the string flavour-breaking probabilities, is constant.

The fragmentation, illustrated in Figure 1.26, is a process where all breaks are causally disconnected, giving the possibility to arbitrarily calculate the probability of fragmenting left to right or right to left:

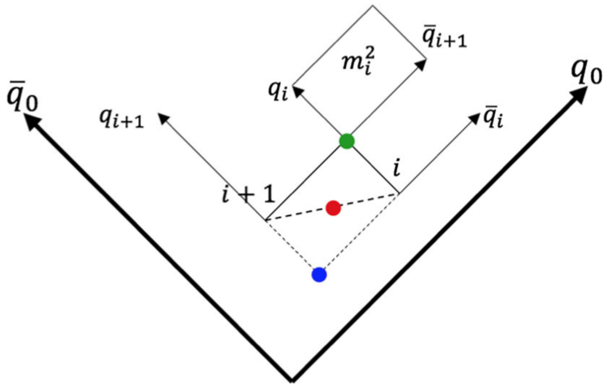

FIGURE 1.26: Hadron formation in a $q\overline{q}$ system. The blue, red and green dots represent the "early", "middle" and "late" definitions of hadron production points, respectively

$$f(z) = N\frac{(1-z)^a}{z}e^{-bm^2/z} \tag{1.21}$$

The equation above is referred to as the Lund symmetric fragmentation function, and is the only production mechanism for light quarks. a and b are parameters that can be tuned, z is the momentum fraction taken by the string end fragmenting, N is a normalisation constant, m is the mass of the fragmenting hadron. After the fragmentation, the quarks escape the strong field by tunnelling effects. These effects are responsible for the suppression of heavy quarks by this mechanism, as the tunnel probability is given by:

$$\lim_{m^2 \gg k/\pi} \mathrm{Prob}(m^2, p_T^2) \rightarrow \exp\Big(-\frac{\pi m_\perp^2}{k}\Big) = \exp\Big(-\frac{\pi m^2}{k}\Big)\exp\Big(-\frac{\pi p_\perp^2}{k}\Big) \tag{1.22}$$

Where m is the quark mass and p_{T} is its transverse momentum (with respect to the string). The result is a mass ordering in tunnel probability as $u\overline{u} : d\overline{d} \approx 1 : 1$, meaning the tunnel probability of a u quark is approximately equal to the one of a d quark. Conversely, $u\bar{u} : s\bar{s} \approx 1 : 0.3$ and $u\bar{u} : c\bar{c} \approx 1 : 10^{-11}$, where the last comparison show how the strong suppression effectively prohibits the production of heavy quarks in this process.

Colour reconnection

Colour reconnection is a way to rearrange the colour charges before the hadronisation phase starts. The process considers the leading colours strings and evaluates possible different colour configurations based on physical constraints.

Firstly, the string should be colour compatible as per the SU(3) colour rules from QCD. As an example, looking at Figure 1.27(a), this means that the left configuration has only a $1/9$ chance to transform in the right configuration based purely on colour considerations. Secondly, the causal contact between strings is tested in a simple space-time picture. Lastly, a string-length measure is used (λ) to decide if the transformation is actually favourable [167]. This measure roughly estimates how many hadrons will be produced by the string breakup [168].

Figure 1.27(a-b) shows the two possibile configurations for two colour dipoles. Figure 1.27(a) represents the picture (Colour dipole swing) where both dipoles exchange their colour connected partons, with a colour-related probability of $1/9$. Figure 1.27(b) shows the case for the creation of a Junction. In this case a new string piece is created connecting the two quarks quarks to the two anti-quarks on opposed ends. Even though the probability of simple colour considerations enhances to $1/3$, the λ-measure reduction is not very significant, so the configuration is likely to be suppressed. Figure 1.27(c) shows a new addition of a Three dipoles connection. The colour dependent probability is of $1/27$ and the result is two independent string systems of a (anti-)junction [168].

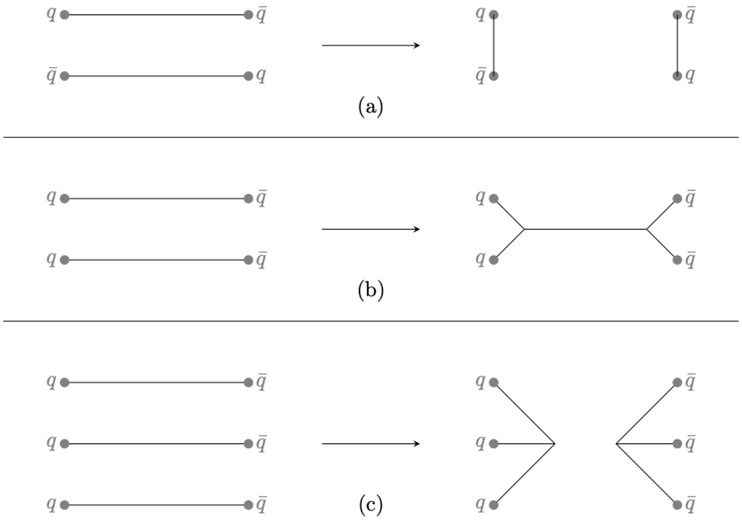

FIGURE 1.27: Two dipoles and three dipoles CR possibilities. For two dipoles, they can either have (a) a simple reconnection (a.k.a. a swing) or (b) a formation of a connected junction and anti-junction system. Three dipoles can form (c) disconnected junction and anti-junction systems. The figure is taken from [168]

Colour ropes

Colour ropes are formed from the interaction of colour charges in a limited area in transverse space acting coherently, assuming the total system is a colour singlet. Lattice calculation show that in such a situation if the endpoints charges correspond to a specific SU(3) multiplet, the tension of the rope is different than the string one [157].

To evaluate the differences introduced by this complication we can see its effects on the parameters a and b, and on new parameters we will introduce to quantify modifications.

$$k \mapsto \tilde{k} = hk \qquad \frac{n_s}{n_{u,d}} = \rho \mapsto \tilde{\rho} = \rho^{1/h} \qquad \frac{n_d}{n_q} = \xi \mapsto \tilde{\xi} = \tilde{\alpha}\beta\left(\frac{\xi}{\alpha\beta}\right)^{1/h} \tag{1.23}$$

Where $n_s, n_{u,d}, n_d, n_q$ are respectively the number of s quarks, u, d quarks, di-quarks and quarks produced by the string; k is the string tension and h its enhancement with respect to nominal value, α, β are di-quark production parameters.

The most interesting in the strangeness enhancement picture is ρ, the suppression of s quark production with respect to u, d quarks. To get visually a sense of how a change in the string tension could affect these parameters we can turn to Figure 1.28.

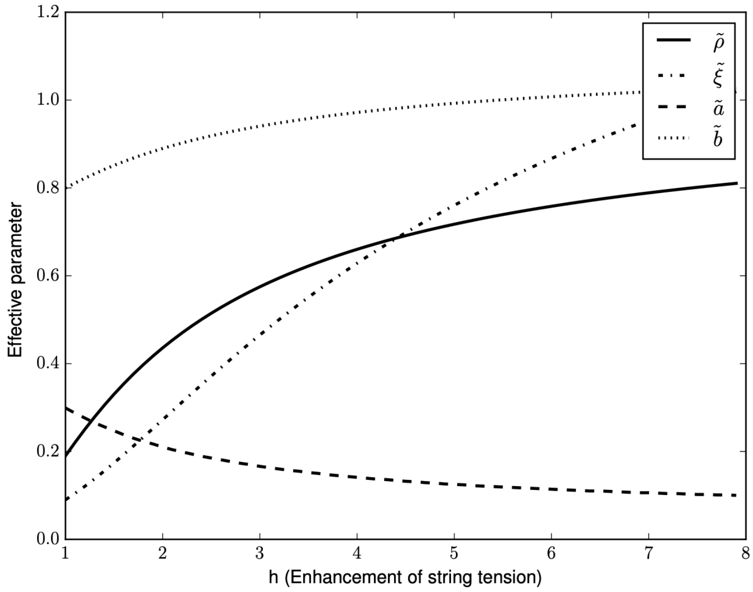

FIGURE 1.28: Effective parameters of the string model as a function of effective string tension. The parameters ρ and ξ control the strangeness content and baryonic content respectively, a and b are related to multiplicity. A modified string tension has a sizeable effect on ρ and ξ in particular. The range of h shown is much larger than relevant for pp collisions, which typically have h < 1.5. Larger values of h are, however, relevant for heavy ion collisions. The values of the parameters for h = 1 comes from a tune to LEP data.

This enhancement of string tension affects the final state multiplicity with a suppression of $\approx 5\%$ in high multiplicity pp collisions, and up to $15-20\%$ in heavy-ion collisions. It should be noted that in pp collisions the enhancement is in the order of

$h = 1.5$ and this value grows for heavy-ion collisions; $h = 1$ is the standard string tuned on the LEP data.

Chapter 2

A Large Ion Collider Experiment

A Large Ion Collider Experiment (ALICE) is an experiment at CERN[1], located at the interaction point 2 on the Large Hadron Collider (LHC) ring (Figure 2.1). The ALICE Collaboration aims to study the Quark Gluon Plasma (QGP), a state where quarks and gluons are no longer confined inside hadrons. This condition is thought to be the one in which the early universe was a few microseconds after the Big Bang [169]. We are currently in the middle of the Run3 data-taking campaign, started in March 2022, following Run1 and Run2 campaigns achieving a large plethora of groundbreaking results. One of the most intriguing being the emergence of QGP-like effects in smaller systems such as pp (proton-proton) and p–Pb (proton-lead). [63]. In the following sections a brief description of ALICE sub-detectors and their performance is carried out. In particular, a focus is put on the sub-systems and general techniques most used by the presented analysis.

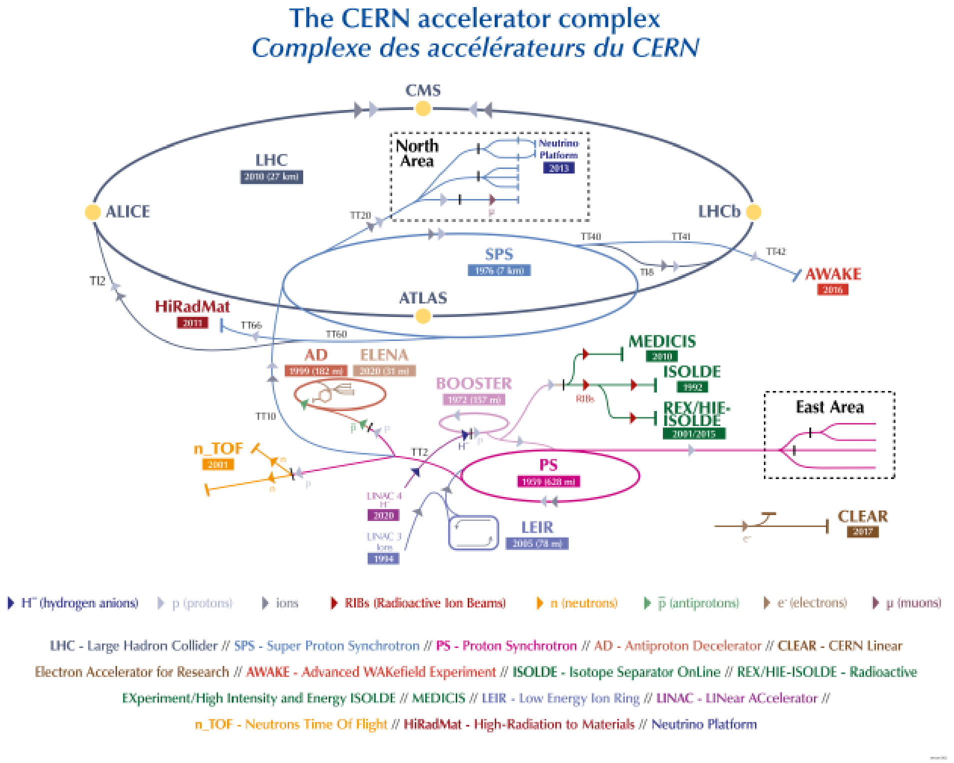

FIGURE 2.1: Overview of the CERN accelerator complex in February 2022. Figure taken from [170].

---

[1] Conseil Européen pour la Recherche Nucléaire

2.1 ALICE Sub-systems

The ALICE detector is a complex feat of engineering, combining many sub-systems each dedicated to a specific task. Its final goal is to describe the event final state in the most precise terms possible. The main areas of focus are Particle Identification (PID), tracking, i.e. a complete account of particle trajectories, and event related information such as multiplicity, centrality, event plane and many others.

The experiment develops in two directions: a cylindrical structure around the beam pipe, centred at the nominal interaction point, and a forward component (Fig. 2.2). Overall the experiment weighs around $10\,\mathrm{kt}$, occupying a volume of $16 \times 16 \times 26\,\mathrm{m}^3$. The cylindrical structure starts, from the beam pipe outward, with a layered structure of sub-detectors covering the full azimuthal angle as a core multipurpose detection system. On top of this core structure, more region focused detectors are positioned, covering only partially the transverse surface; these are usually aimed at dedicated physics. In addition to this central coverage, the detector also develops in the forward region. This is where the majority of detectors dedicated to event characterisation are situated, together with muon dedicated detection systems. Forward sub-systems are dedicated event luminosity, pile-up, effective energy measurements.

More specifically, Figure 2.3 shows how the central barrel is built. Starting from the beam pipe, we find:

1. Core central detectors covering the full azimuthal angle (Figure 2.3 and 2.2):
   (a) Inner Tracking System (ITS) devoted to measuring the vertex position and particle tracking
   (b) Time Projection Chamber (TPC) devoted to particle tracking and identification
   (c) Transition Radiation Detector (TRD) devoted to electron particle identification
   (d) Time Of Flight (TOF) devoted to hadrons and electrons particle identification
2. External detectors with partial azimuthal coverage (Figure 2.3 and 2.2):
   (a) ElectroMagnetic Calorimeter (EMCal) devoted to electrons, photons identification and jets reconstruction
   (b) Photons Spectrometer (PHOS) devoted to photons identification and jets reconstruction
   (c) High-Momentum Particle Identification Detector (HMPID) devoted to hadrons identification in high-p_{T} region and jets reconstruction
3. Forward detectors (Figure 2.2):
   (a) Forward Muon Spectrometer (FMS) devoted to muon tracking and identification
   (b) T0, V0, Forward Multiplicity Detector (FMD), Photon Multiplicity Detector (PMD), Zero Degree Calorimeters (ZDCs) devoted to triggers, multiplicity and centrality estimation, luminosity measurements.

All the core central barrel detectors are embedded in the L3 solenoid magnet which has maximum field of $0.5\,\mathrm{T}$. The Muon Spectrometer has its own dipole magnet, generating a field integral of B = $3\,\mathrm{T\,m}$. The magnetic field is used to curve charged particles and provide information on their momentum and charge.

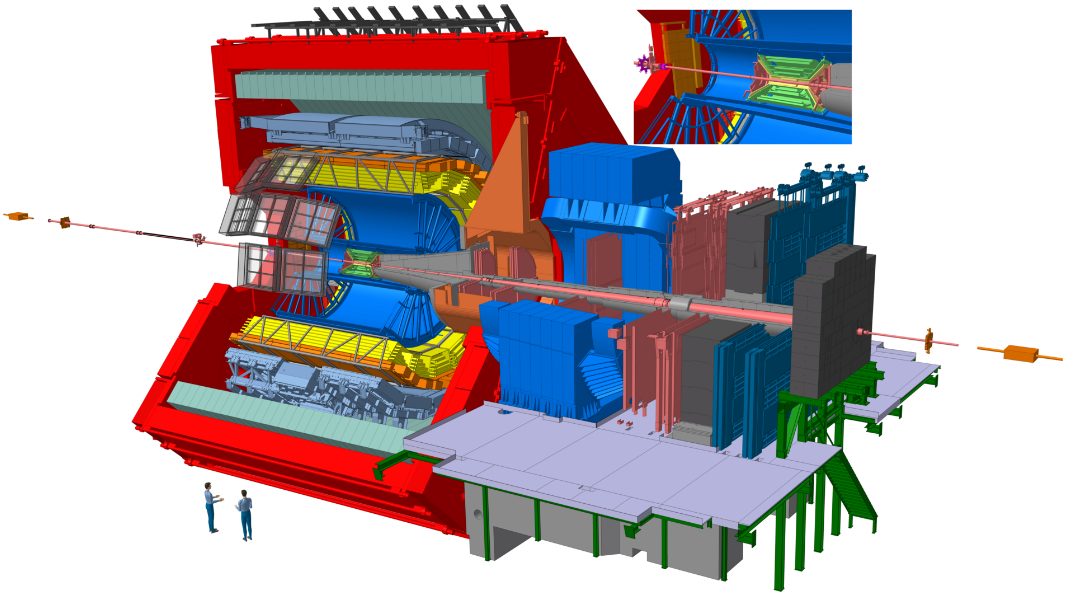

FIGURE 2.2: The ALICE detector schematic illustration in Run 1 and Run 2.

2.1.1 Inner Tracking System (ITS)

The Inner Tracking System serves the purpose of finding the primary vertex with a resolution below $100\,\mu\mathrm{m}$, together with secondary vertices from long-lived decays. Moreover, in Run 1 and 2 the ITS detector provided PID for charged particles below $200\,\mathrm{MeV}$, this is no longer the case in Run 3 where the detector was upgraded: the PID capability was lost in favour of a significant improvement in timing and position measurement. It also provides tracking for tracks outside the TPC coverage and improving momentum and angle resolution of the tracks that are matched in the TPC .

The detector consists in 6 layers of coaxial cylinders, completely wrapping the beam pipe, covering the pseudo-rapidity range $|\eta| \leq 0.9$ for all vertices within $\pm$ $5.3\,\mathrm{cm}$ of the nominal interaction point (Figure 2.3). The two inner layers consists of Silicon Pixel Detectors (SPD) and are situated at $\approx 6\,\mathrm{cm}$ from the interaction point, with the innermost being as close to the interaction point as engineeringly possible. The two outer layers consists of Silicon Strip Detectors (SSD) and are situated at $\approx$ $40\,\mathrm{cm}$ from the interaction point, as close to the TPC as engineeringly possible. The two intermediate layers consists of Silicon Drift Detectors (SDD) and are situated at $\approx 25\,\mathrm{cm}$ from the interaction point. The z-axis coverage increases going further from the beam pipe, to uphold the pseudo-rapidity coverage, from $\approx 14\,\mathrm{cm}$ to $\approx 50\,\mathrm{cm}$. The inner layers have a wider coverage up to $|\eta| \leq 1.98$ to provide continuous multiplicity measurement with the Forward Multiplicity Detector (FMD). The four outer layers are equipped with analogue readout to provide PID for very low momentum particles through the measurement of energy loss in silicon. A schematic view of the ITS for Run1 & 2 is shown in Figure 2.4.

The very low-momentum particles are affected by multiple scattering effects, which can interfere with tracking and vertexing measurements. In an effort to reduce to a minimum the impact of the detector contribution, as little material as possible has been put in the active region of the detector. Overall, a little less than 8% of a radiation length [171].

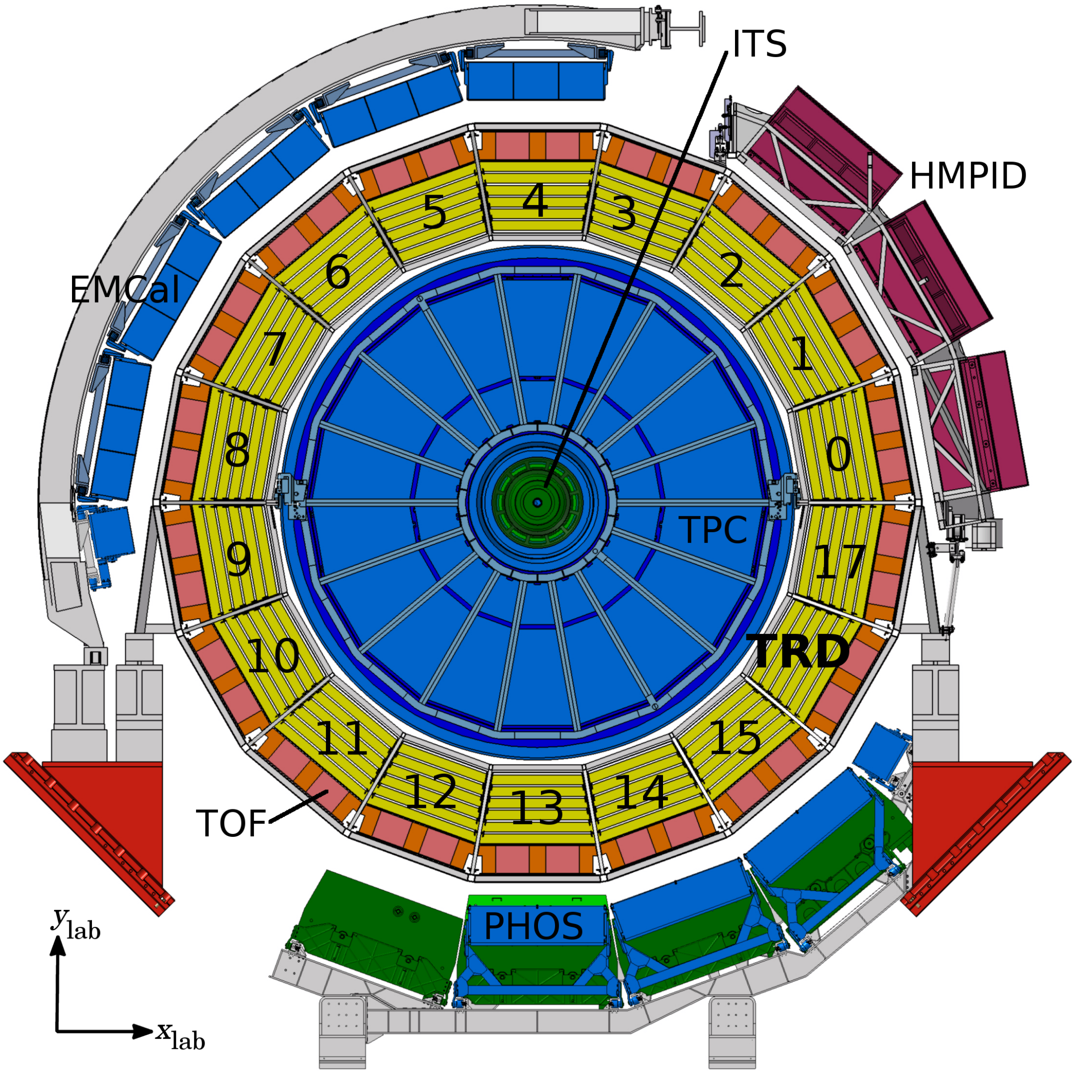

FIGURE 2.3: The ALICE central barrel structure.

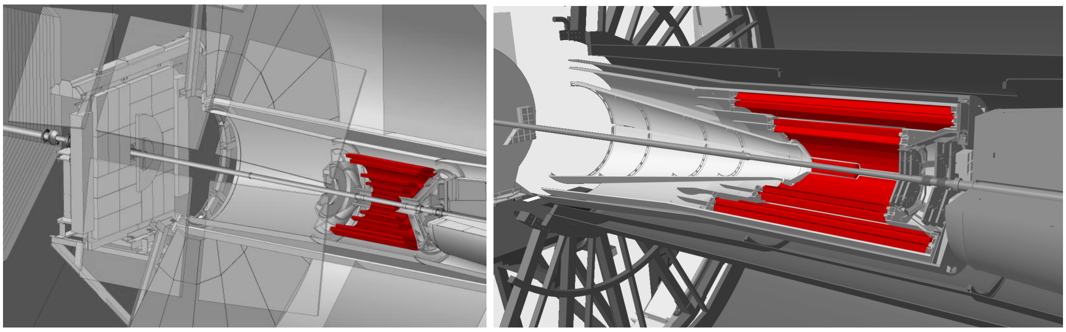

(A) ITS for the Run 1 and 2 campaigns.

(B) ITS for the Run 3 and 4 campaigns.

FIGURE 2.4: ITS for the Run 1, 2, 3 and 4 campaigns.

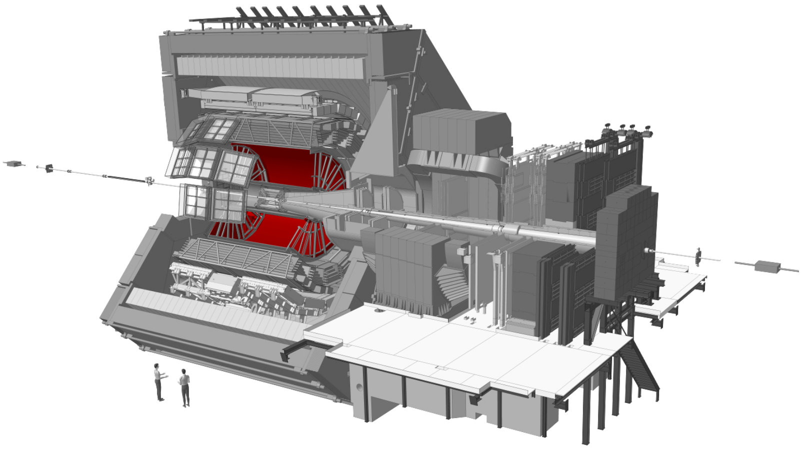

FIGURE 2.5: The TPC position inside the ALICE experiment, highlighted in red.

ITS Upgrade for Run 3 and 4 The new ITS for Run 3 & 4 has been designed to record Pb–Pb (lead-lead) data-taking at $50\,\mathrm{kHz}$ to increase the minimum-bias sample of a factor one hundred with respect to the data taken up to date, increase vertexing capabilities while maintaining low p_{T} PID capabilities.

These new goals are achieved through a number of factors:

1. Improving the impact parameter of a factor ≈ 4, thanks to three main changes:
    (a) The first layer of the detector has been brought closer to the interaction region, from $3.9\,\mathrm{cm}$ to $2.3\,\mathrm{cm}$.
    (b) The material budget has been decreased in the inner layers from 1.14% to 0.35% of a radiation length.
    (c) The pixel size has been reduced from $50\,\mathrm{\mu m}$ x $425\,\mathrm{\mu m}$ to $29.24\,\mathrm{\mu m}$ x $26.88\,\mathrm{\mu m}$.
2. The increased granularity of the detector will grant the tracking efficiency and the p_{T} resolution in low momenta tracks.
3. The readout rate will increase one hundred fold in Pb–Pb and two hundred fold in pp .

The main component for the new detector is the ALPIDE chip, a Monolithic Active Pixel Sensor (MAPS). The detector consists of 7 layers from $\approx 2.3\,\mathrm{cm}$ to $\approx 40\,\mathrm{cm}$, covering in the z-axis from $\approx 27\,\mathrm{cm}$ to $\approx 150\,\mathrm{cm}$ providing a $|\eta| \leq 1.22$ coverage [172].

2.1.2 Time Projection Chamber (TPC)

The Time Projection Chamber is the main tracking system for ALICE. It has a good momentum resolution in a very wide range, from $0.1\,\mathrm{GeV}/c$ up to $100\,\mathrm{GeV}/c$. Moreover it provides particle identification via energy loss in the gas volume.

The detector wraps around the ITS , filled with a gas mixture of Ne-Co_2 (90-10) and is highlighted in Figure 2.3. It covers the $|\eta| < 0.9$ pseudo-rapidity range for tracks matching outer detectors, i.e. traveling along the full radial dimension. The coverage increases up to $|\eta| < 1.5$ for tracks travelling a third of the radial dimension of the detector. Its active volume spans from $\approx 800\,\mathrm{cm}$ to $\approx 2500\,\mathrm{cm}$, $\approx 500\,\mathrm{cm}$ along the beam axis amounting to $\approx 90\,\mathrm{m}^3$ of active volume. In this volume a large electric

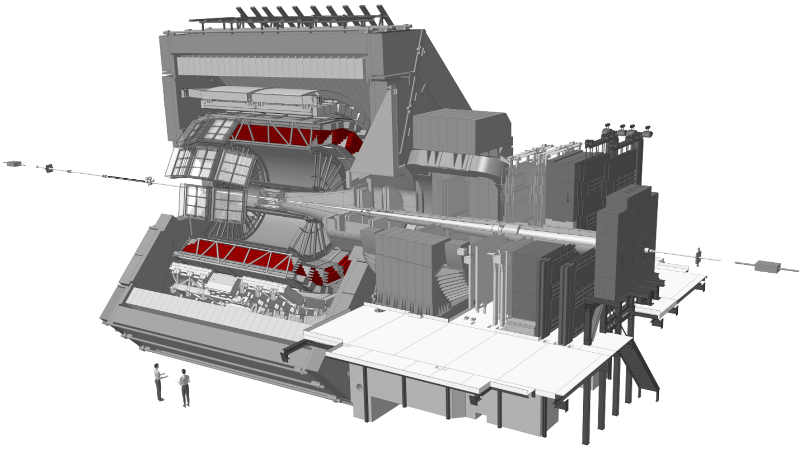

FIGURE 2.6: The TRD position inside the ALICE experiment, highlighted in red.

field is applied and ionisation produced by a charged particle is drifted up to 250 cm, half the TPC dimension, on either side of the central electrode. The then drifting charge finally hits a multi-wire proportional chambers on the end-caps, where the signal is read analogously to provide energy loss measurement and position of hit for tracking.

One of the most common distortion effects comes with the high multiplicity environment of Pb–Pb collisions. At such high-occupancy particle hits are very close together and may be difficult to discriminate. For these situations, other central barrel signals are combined to correct this effect. Moreover many concurrent ionisations may create local clusters of charge that may distort the electric field. This effect causes local electrical fields and subsequent drifts that may shift the position of final hits on the readout pads and the distortions have to be corrected offline. These effects increase the TPC energy loss resolution from 5% to 7% from pp collisions to Pb–Pb collisions [173].

TPC Upgrade for Run 3 and 4 The new TPC for Run 3 and 4 has been designed to withstand the new data-taking rate of 50 kHz, a sixteen fold increase from the previous 3 kHz trigger limitation. The previous limit was due to the gating grid, used to collect ions from the amplification region and prevent them from drifting back into the drift volume, where they would lead to substantial space-charge distortions of the drift field.

The high interaction rate defines the need to operate in continuous mode, mitigating the space-charge distortions to a maximum of 2% fractional ion back-flow. To achieve this, the upgraded TPC has replaced the multi-wire proportional chamber readout and now makes use of the Gas Electron Multiplier (GEM) detectors for the read-out planes. GEM detectors are Micro-Pattern Gas Detectors (MPGD), and thus have an intrinsically low ion back flow and their use will make the gating grid superfluous for the ion leakage control in the drift volume, thus allowing for a continuous data acquisition [174].

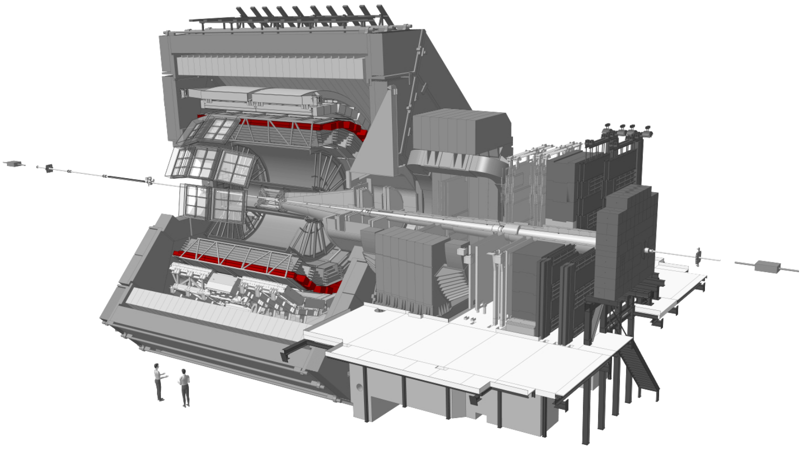

FIGURE 2.7: The TOF position inside the ALICE experiment, highlighted in red.

2.1.3 Transition Radiation Detector (TRD)

The Transition Radiation Detector (TRD) main purpose is electron identification via the pion hypothesis rejection above $1\,\mathrm{GeV}/c$, the upper limit of the TPC PID capabilities for electrons. Hits on the TRD are also used to improve tracking for particles matched to ITS -TPC tracks.

The TRD is positioned outside TPC outer layer (Figure 2.3). The principle of operation of the TRD is the Transition Radiation (TR), an Electro-Magnetic radiation released as the result of a charge speeding through a separation plane between two materials having different dielectric constants. For the radiation to be detected the particle relativistic γ factor should be about 1000, making it harder for any particle except for $e^{\pm}$ to reach this threshold. The detector structure alternates foils of polypropylene fibre mats of $3.2\,\mathrm{cm}$ and Rohacell foam sheets[2] of $0.8\,\mathrm{cm}$ to use as radiator. A multi-wire proportional chamber (MWPC) preceded by a drift region with a Xenon based gas mixture is positioned after the radiator to detect the TR generated by the incoming particle. A total of six layers are positioned.

2.1.4 Time of Flight Detector (TOF)

The Time of Flight detector (TOF) main purpose is to provide PID for charged particles at intermediate momenta, from $\approx 600\,\mathrm{MeV}/c$ to $\approx 5\,\mathrm{GeV}/c$. Hits on the TOF are also used to improve tracking for particles matched to ITS -TPC tracks. Moreover the TOF can also provide timing for the event and triggers for cosmic events and Ultra Peripheral Collisions (UPCs).

The TOF detector is layered on the outer bound of the TRD (Figure 2.3). The inner layer stands at $\approx 370\,\mathrm{cm}$ and the outer layer at $\approx 400\,\mathrm{cm}$ providing coverage at $|\eta| < 0.9$. It is made of 1593 glass Multi-gap Resistive Plate Chamber (MRPC) strip detectors, each with a sensitive area of $7.4{\times}120\,\mathrm{cm}$ for a total active area of $141\,\mathrm{m}^2$. Each MRPC is segmented into 96 readout pads of area $2.5{\times}3.5\,\mathrm{cm}^2$, for a total of over 150,000 channels [173].

The detector has an excellent efficiency of $\approx 99\%$. Combined with the geometrical acceptance and the tracking capabilities of ALICE the overall TOF efficiency is $\approx 80\%$ for p–Pb collisions.In Pb–Pb collisions, in the centrality range 0-70% the

---

[2] a closed-cell rigid foam based on polymethacrylimide (PMI) chemistry

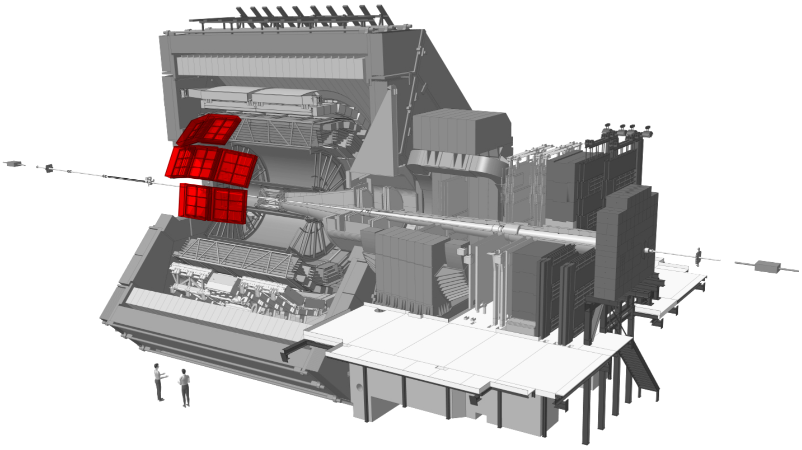

FIGURE 2.8: The HMPID position inside the ALICE experiment, highlighted in red.

overall TOF resolution is $80\,\mathrm{ps}$ for pions with a momentum around $1\,\mathrm{GeV}/c$.

The TOF also provides timing information on the single track, using the T0 signal as a start. The timing information is key, as every improvement of the time of flight resolution extends the momentum range where the separation power between species is acceptable (usually 3 or 5 σ). The event timing from the TOF is performed using a combination of all arrival times of the tracks, minimising the χ^2 for every mass hypothesis. This process is performed if at least three particles reach the TOF ; if over 30 reach it the resolution on the event timing can be as low as $30\,\mathrm{ps}$. This method proves useful when the T0 start signal is missing, if neither are available a standard time is used [175].

2.1.5 High-Momentum Particle Identification Detector (HMPID)

The High-Momentum Particle Identification Detector principle of operation is based on proximity focusing Ring Imaging Cherenkov (RICH), using C_6F_{14} ($n \approx 1.28$) as a radiator. The proximity focusing means that the cone of light is projected onto a photosensitive surface from a thin radiator, after a small gap, called the proximity gap, whereas in the focusing configuration the radiation is reflected by spherical mirrors. The radiation photons are detected using a Multi Wire Proportional Chamber (MWPC) with a CsI thin layer deposited onto its pad cathodes [176]. The detector provides a 3σ separation power for $\pi^{\pm}/\mathrm{K}^{\pm}$ up to $p_{\mathrm{T}} = 3\,\mathrm{GeV}/c$ and for $\mathrm{K}^{\pm}/\mathrm{p}$ up to $p_{\mathrm{T}} = 5\,\mathrm{GeV}/c$. The PID process requires information on the track extrapolated in the central barrel. When coupled with the other central barrel detectors, the HMPID has been used to extend the measurement of the transverse momentum distributions for π in the range $1.5\,\mathrm{GeV}/c < p_{\mathrm{T}} < 4\,\mathrm{GeV}/c$, for p in the range $1.5\,\mathrm{GeV}/c < p_{\mathrm{T}} < 6\,\mathrm{GeV}/c$, for deuteron in the range $3\,\mathrm{GeV}/c < p_{\mathrm{T}} < 8\,\mathrm{GeV}/c$ for the most central Pb–Pb collisions. The track matching efficiency with the TPC is roughly 5%, mostly due to the acceptance of roughly 5%.

2.1.6 Photon Spectrometer (PHOS)

The Photon Spectrometer (PHOS) is one of the two electromagnetic calorimeters of ALICE. Its main design goal is to measure spectra, collective flow and correlations of thermal and prompt direct photons, together with that of neutral mesons via their decay into photon pairs [177].

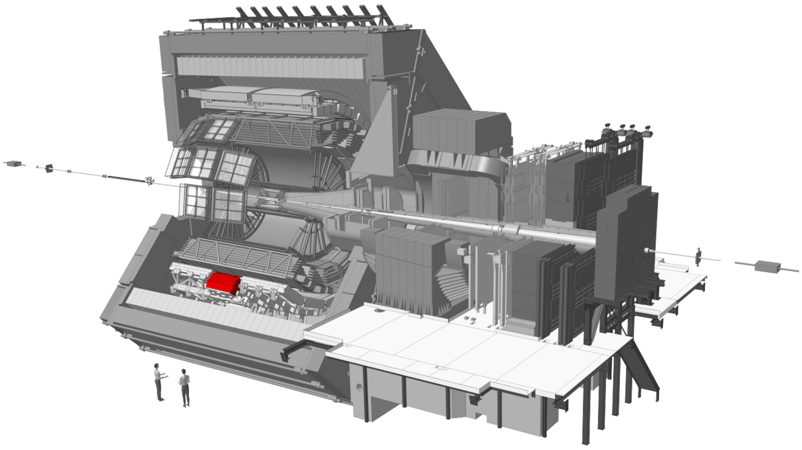

FIGURE 2.9: The PHOS position inside the ALICE experiment, highlighted in red.

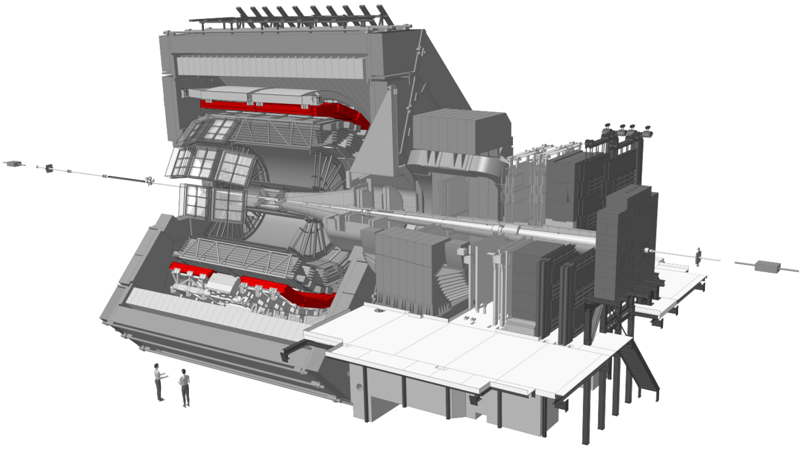

FIGURE 2.10: The EMCal position inside the ALICE experiment, highlighted in red.

The detector is a single arm, high-resolution electromagnetic calorimeter that identifies and measures electrons and photons in a wide range of transverse momentum. Currently it can cover from $100\,\mathrm{MeV}/c$ to $100\,\mathrm{GeV}/c$ at mid-rapidity and can provide a trigger for large energy deposits. TRD and TOF are designed to have an opening in front of the PHOS detector to provide a window with reduced material budget, below 0.2 X_0. The detector itself is divided into four modules located at a distance of $460\,\mathrm{cm}$ from the interaction point. It covers a $6\,\mathrm{m}^2$ area, spanning 70° in azimuthal angle and a quarter of pseudorapidity unit $|\eta| < 0.125$. The detection unit is a $22 \times 22 \times 180\,\mathrm{mm}^2$ of lead-tungstate crystal, $PbWO_4$ coupled to $5{\times}5\,\mathrm{mm}^2$ Hamamatsu Avalanche Photo Detectors (APDs). The detector is operated at -25 $^{\circ}\mathrm{C}$ to enhance the light yield.

2.1.7 ElectroMagnetic Calorimeter (EMCal)

The Electromagnetic Calorimeter (EMCal) is the second electromagnetic calorimeter of ALICE. The main design goal of the EMCal is to measure the electrons from the heavy-flavoured hadrons decay, electromagnetic components for jets and spectra of direct photons and neutral mesons. Moreover, it provides a dedicated trigger for jets

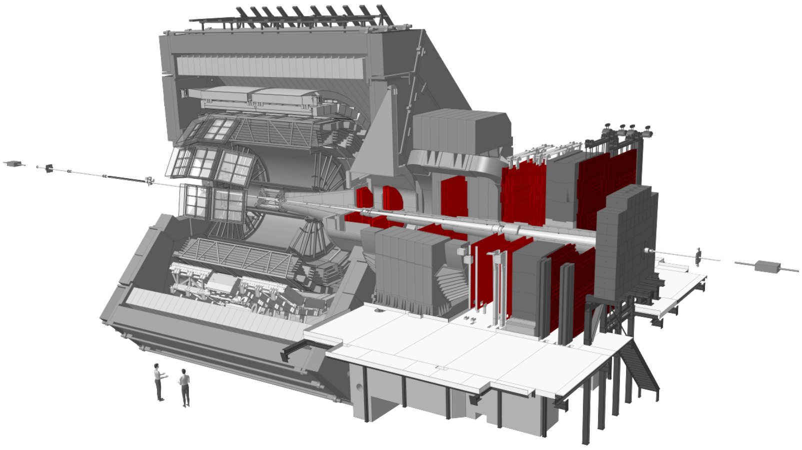

FIGURE 2.11: The FMS position inside the ALICE experiment, highlighted in red.

[178].

Structurally the EMCal is a sampling calorimeter with lead (Pb) as a stopper and a scintillator as active material, that transfers produced light in a wave-length shifting fibres. As seen in Fig. 2.3 the detector covers two different ranges in azimuthal angle, at a distance of $4.5\,\mathrm{m}$ from the beam pipe. The detector is divided in Supermodules and the installation had different phases, the last of which happened in 2014 with the addition of the Di-Jet Calorimeter (DCal) located opposite of the EMCal, which consists of Supermodules 12-19. The building block of the detector is a module composed of an optically isolated 2×2 matrix of towers, each covering a span of $\Delta\eta \times \Delta\varphi \approx 0.0143 \times 0.0143$. The orientation of towers is such that the incident angle with respect to a line originating from the interaction point is less than 2° in $\Delta\eta$ and 5° in $\Delta\varphi$. The layers in the towers are made of 76 foils of Pb $\approx 1.44\,\mathrm{mm}$ thick and 77 foils of scintillator $\approx 1.76\,\mathrm{mm}$ thick. Once canalised into the wavelength shifter fibres the light is collected in $5\times5\,\mathrm{mm}^2$ Hamamatsu Avalanche Photo Detectors (APDs).

2.1.8 Forward Muon Spectrometer

The main purpose of the Forward Muon Spectrometer is the study of quarkonia and low-mass vector meson production through their decays in $\mu^+\mu^-$ [179].

The detector starts with a block of absorber made of concrete and carbon, to minimise multiple scattering and energy loss, filtering all particles except muons, to clean the signal. The detector, positioned in the forward region, is also subject to possible background from the beam pipe, which is coated in tungsten, lead and stainless steel to shield it, either for particles emitted in the collision or showers produced in the shield. After the shield there are 5 stations of high-granularity tracking systems, each station having 2 detection planes of multi-wire proportional chambers with segmented cathode plane, called cathode pad chambers, providing a resolution greater than $100\,\mathrm{mm}$. The 5 stations are set-up to be 2 before, 2 after, and 1 inside a dipole magnet, positioned about $7\,\mathrm{m}$ from the interaction vertex, generating an integrated field of B = $3\,\mathrm{T\,m}$. After the tracking system, another filter block is placed followed by 4 Resistive Plate Chambers (RPC), divided in two stations, forming the Trigger system for the decay of heavy quark resonances. In fact the second filter is to stop low momentum muons coming from lighter particle decays.

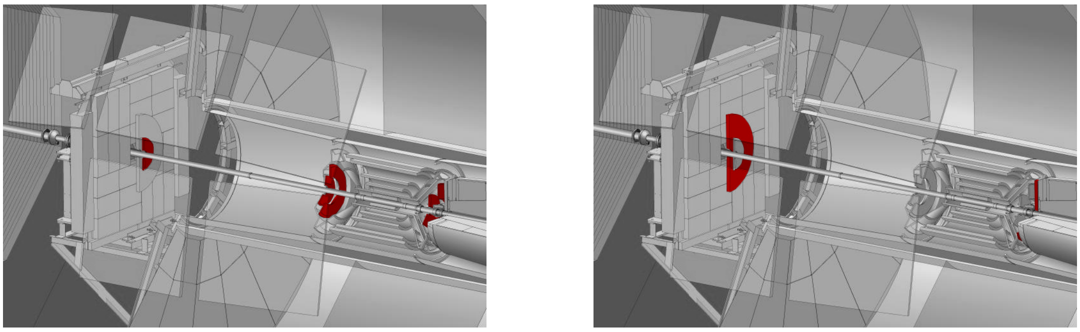

(A) Placement of the FMD

(B) Placement of the V0

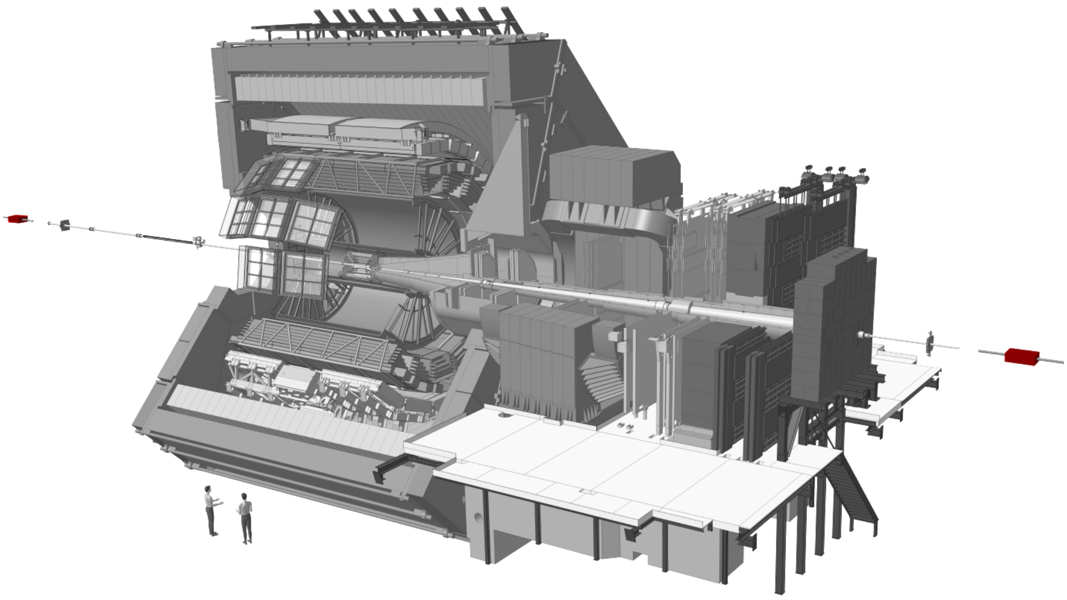

(C) Placement of the ZDC

FIGURE 2.12: Placement of some of the forward detectors

2.1.9 Other Forward Detectors

The other forward detectors are devoted to determine general information on the event, such as luminosity, centrality for heavy-ion collisions, timing of the interaction to be used by the TOF and many others. A graphic visualisation of some of their locations is made in Figure 2.12.

V0

The detector consists in scintillators counters, divided in two groups: V0A and V0C . The two detectors are set as close to the beam pipe as possibile, wrapping it, one closer to the nominal interaction point at a distance of $90\,\text{cm}$ (V0C) and the other outside the central barrel, at a distance of $340\,\text{cm}$ (V0A) in the opposite direction. They both have the same dimensions but given they are located asymmetrically from the interaction point they cover different pseudo-rapidity ranges: V0A covers $2.8 < \eta < 5.1$, whilst V0C covers $-3.7 < \eta < -1.7$.

Their main purpose is to evaluate the multiplicity of the event to generate a trigger on pp and heavy-ion collisions, in the latter giving information on the centrality of the event. During normal operations the detectors are run in AND mode and provide multiple triggers, most notably the Minimum Bias Trigger (MB) and the Multiplicity Trigger (MT).

T0

The detector consists in Cherenkov counters coupled with photomultipliers, divided in two groups: T0A and T0C. The two detectors are set as close to the beam pipe as possibile, one in proximity of the nominal interaction point at a distance of $72.2\,\mathrm{cm}$ (T0C) and the other outside the central barrel, at a distance of $375\,\mathrm{cm}$ (T0A) in the opposite direction. They both have the same dimensions, covering a little less than $40\,\mathrm{cm}^2$ transversally to the beam pipes, but given they are located asymmetrically from the interaction point they cover different pseudo-rapidity ranges: T0A covers $4.61 < \eta < 4.92$, whilst T0C covers $-3.28 < \eta < -2.97$.

Their goal is to give timing information on the event, setting the t_0, the real time of collision, for the TOF detector with a precision of $\approx 20\,\mathrm{ps}$ for heavy-ion collisions and $\approx 40\,\mathrm{ps}$ for pp collisions [175]. Their efficiency is 40% for minimum bias pp collisions, combining a 50% and 59% single efficiency, that escalates to roughly 100% for central heavy-ion collisions thanks to the high multiplicity.

FMD

The Forward Multiplicity Detector is a silicon strip detector with 51,200 strips arranged in 5 rings, covering the range $3.4 < \eta < 5.1$. It is placed around the beam pipe at small angles to extend the charged particle acceptance of ALICE into the forward regions, not covered by the central barrel detectors.

PMD

The Photon Multiplicity Detector is a Particle shower detector which measures the multiplicity and spatial distribution of photons produced in the collisions. It utilises as a first layer a veto detector to reject charged particles. Photons on the other hand pass through a converter, initiating an electromagnetic shower in a second detector layer where they produce large signals on several cells of its sensitive volume. Hadrons on the other hand normally affect only one cell and produce a signal representing minimum-ionizing particles.

ZDC

The ZDCs are calorimeters which detect the energy of the spectator nucleons, i.e. the nucleons that do not interact in the heavy-ion collision, in order to determine the overlap region of the two colliding nuclei. It is composed of four calorimeters, two to detect protons (ZP) and two to detect neutrons (ZN). They are located $115\,\mathrm{m}$ away from the interaction point on both sides, along the beam line. The ZN is placed at zero degree with respect to the LHC beam axis, between the two beam pipes. The ZP is positioned externally to the outgoing beam pipe. The spectator protons are separated from the ion beams by means of the dipole magnet D1. The ZDCs are "spaghetti calorimeters", made by a stack of heavy metal plates grooved to allocate a matrix of quartz fibres. Their principle of operation is based on the detection of Cherenkov light produced by the charged particles of the shower in the fibers.

2.1.10 Triggers

The triggers in ALICE are managed by the Central Trigger Processor (CTP) every machine cycle ($\approx 25\,\mathrm{ns}$). The decision is taken based upon the detector signals and information about the LHC bunch filling scheme. The bunch crossing mask informs the CTP about whether bunches are coming from the positive z side, the negative z side, both or neither. A list of all available triggers are listed in [150].

The main triggers used are the Minimum Bias class, and their requirements are:

MBor	signals in V0 and SPD
MBand	signals in V0A and V0C
MBZ	MB and signals in both ZDCs
SPI	n hits in SPD

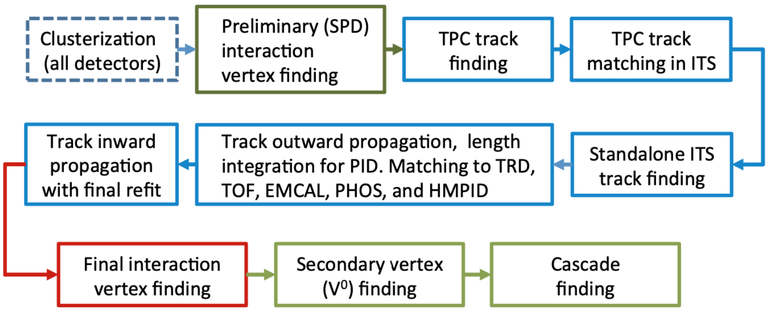

FIGURE 2.13: Event reconstruction flow. [150]

2.2 Central Barrel Tracking

Tracking is the process by which tracks and vertices (primary and secondary) are reconstructed to be used as particle trajectories with physically relevant attributes such as charge, momentum, etc. Firstly, data from detectors are separately clustered, associating positions, signal amplitudes, signal times, etc., and their associated errors.

2.2.1 Preliminary Interaction Vertex

Preliminary vertex finding uses the first two layers (SPD) of ITS: the two clusters in the layers are joint in tracklets, that are used as seeds that point toward a candidate, the candidate with most convergent tracklets is taken as preliminary vertex.

Presently pp collisions present the challenge of pile-up. For every bunch-crossing at the LHC, more than one pp collision could happen and thus the reconstruction needs to find all the primary vertices and assign them the tracks originating from them. The first method to do this is to loop through tracklets and try to assign them to found primary vertices until all track candidates have been associated to a vertex candidate. The second method, used when low-multiplicity prevents a satisfactory precision in vertex resolution, is to scan the z-coordinate of the points of closest approach (PCA) to look for a maximum.

2.2.2 Track reconstruction

The mechanism follows an inward-outward-inward scheme. The first step starts at the outer boundary of the TPC volume, where tracks are expected to be more resolved. In the TPC there are 159 tangential pad rows, giving a track the theoretical ability to leave as many clusters. The track seeds are first generated with two TPC clusters and the vertex, then three TPC clusters. The mechanism then propagates inward, adding to the track the cluster most suitable (i.e. most in trajectory) or none if the available ones are too far away (there is a cut on the distance from the track a cluster can have), not requiring a cluster must be uniquely used in a track. This makes it possible that the same track be reconstructed more than once: this problem is solved by an algorithm that checks overlap of tracks (25% to 50% same clusters used) and sort them by quality, discarding all but the the first. Only those tracks that have at least 20 clusters (out of maximum 159 possible) and that miss no more than 50% of the clusters expected for a given track position are accepted, passing these cuts mean the tracks are propagated further to the ITS . In this stage a first PID is performed based on the specific energy loss and a mass is provisionally assigned to the track.

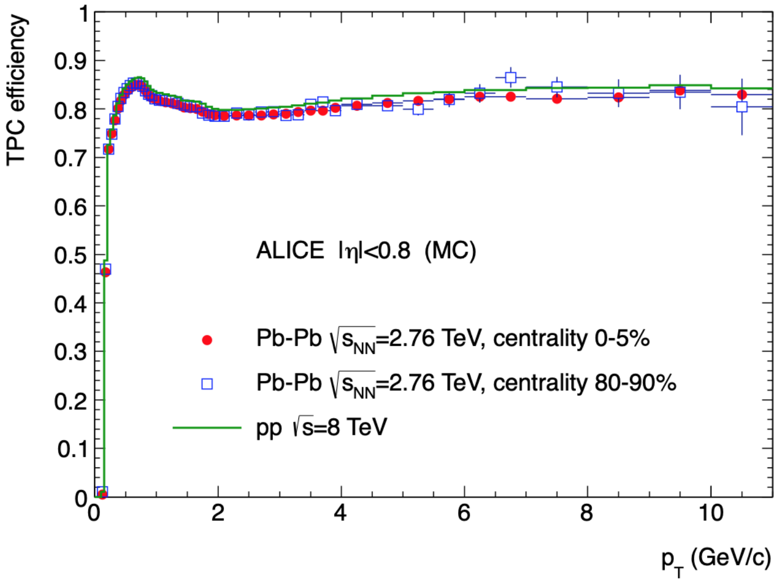

FIGURE 2.14: TPC track finding efficiency for primary particles in pp and Pb–Pb collisions (simulation). The efficiency does not depend on the detector occupancy. [150]

Continuing in the ITS , the propagation of the TPC tracks are used as seeds, updated at each layer with all clusters within a proximity range, saving each new fit as a new seed. If the track misses an expected hit on a layer, it is penalised on the χ^2, (the reduced χ^2) used to determine the track goodness. Once all the seeds have been found, a procedure similar to that performed on the TPC is carried-out, firstly constraining on the preliminary vertex, secondly losing this requirement. All the candiate tracks are sorted for quality, discarding all but the first, except when two different tracks share a cluster. In this case a resolution of this conflict is performed by searching for good alternatives among other candidates, if the conflict can't be resolved, the tracks are flagged as possibly mismatched. The final tracks are added to the TPC tracks in the reconstructed event. The efficiency of prolongation in the ITS for a track depends on the number of hits it has on the ITS itself: if only one hit is recorded an already very good ≈80% efficiency is achieved, whereas if two hits are present, the efficiency is even closer to unity at ≈95%. This efficiency slightly worsen in Pb–Pb collisions, as can be seen in Figure 2.15

One aspect to consider is the fall of reconstruction efficiency in the TPC for low transverse momentum (Fig. 2.14). The cut-off value is around 200 MeV/c for pions and 400 MeV/c for protons, and is caused by energy loss and multiple scattering in the detector material. This means a standalone ITS search for tracks is performed with those clusters not used to prolungate TPC tracks and account for these missing particles. The seeds are made using the vertex and the first three layers clusters, propagated in a similar fashion as for the TPC prolongation track searching. This procedure is able to find tracks down low to 80 MeV/c.

Once the ITS propagation is finished, all tracks are propagated up to their PCS to the preliminary vertex. From there the tracks are refitted using a Kalman filter in the outward direction using the clusters it was assigned. During this outward path all track properties are updated at each step, such as track length integral and time of flight expected for each particle species for use in the TOF detector for PID. The tracks are then propagated out of the TPC to the TOF , TRD , EMCal, PHOS, HMPID

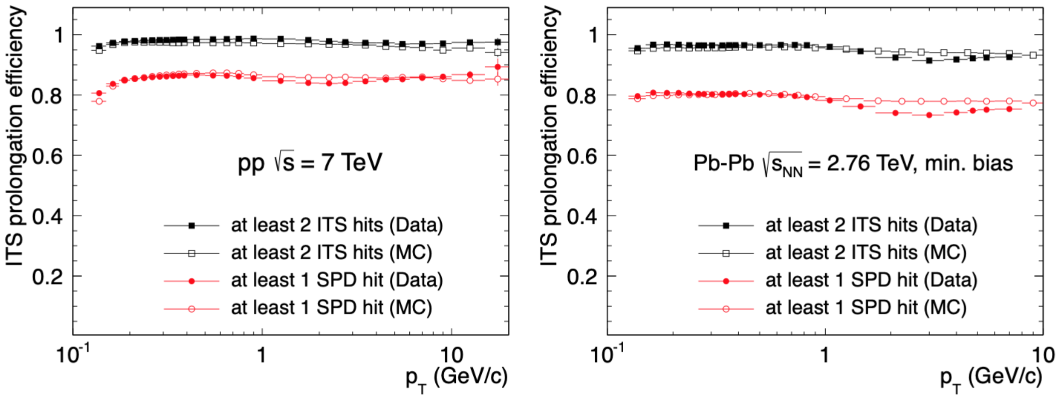

FIGURE 2.15: ITS-TPC matching efficiency vs. p_{T} for data and Monte Carlo for pp (left) and Pb–Pb (right) collisions [150].

and an attempt to match tracklets is made. These extensions are not used to update track information but are stored for PID purposes. Subsequently a new fit procedure is made starting from the outer radius of the TPC , determining the track's position, direction, inverse curvature, and ITS associated covariance matrix. This ends the procedure to find the tracks coming from the primary vertex. To suppress the presence of secondary tracks a cut on the distance of closest approach (DCA) of the track to the interaction vertex is made. This cut improves the already good primary tracks identification efficiency: taking the case of central Pb–Pb ad $\sqrt{s_{\mathrm{NN}}} = 2.76$ TeV not asking for a tight DCA results in an approximate 93% primary tracks in the sample, whereas the tight DCA requirement improves purity to as high as 98%, as shown in Figure 2.16.

The resolution of the measured momentum of a given particle is extracted form the covariance matrix of the track. As mentioned before, tracks can be reconstructed using the TPC standalone or combining it to the ITS . Track momentum resolution is expressed as the resolution on the inverse transverse momentum, related as:

$$\frac{\sigma_{p_{\mathrm{T}}}}{p_{\mathrm{T}}} = p_{\mathrm{T}}\sigma_{1/p_{\mathrm{T}}} \tag{2.1}$$

The performance of the ALICE apparatus in terms of inverse transverse momentum in various configurations is shown in Figure 2.17. A clear improvement is provided by constraining the tracks to the vertex, and to extend the TPC tracks to the ITS . On top of this, a deterioration of $\approx 10-15\%$ should be expected in central heavy ions collisions due to cluster overlap and fake clusters in tracks. Even thought the best configuration comprehend the ITS measurements, ITS acceptance has been reduced of about 25% for the years 2010/11 due to the unavailability of certain areas of the two innermost layers. A good approximation to its performance is provided by the TPC standalone constraining to the vertex up to 10 GeV/c, with a significant worsening at higher momenta.

2.2.3 Final primary and secondary vertices finding

The final vertex is found using fully reconstructed tracks in TPC and ITS , making a first elimination process to exclude outliers and weighting the track contributions to further prevent smearing from any remaining outliers. If the event has low multiplicity the nominal vertex position is added to the fit.

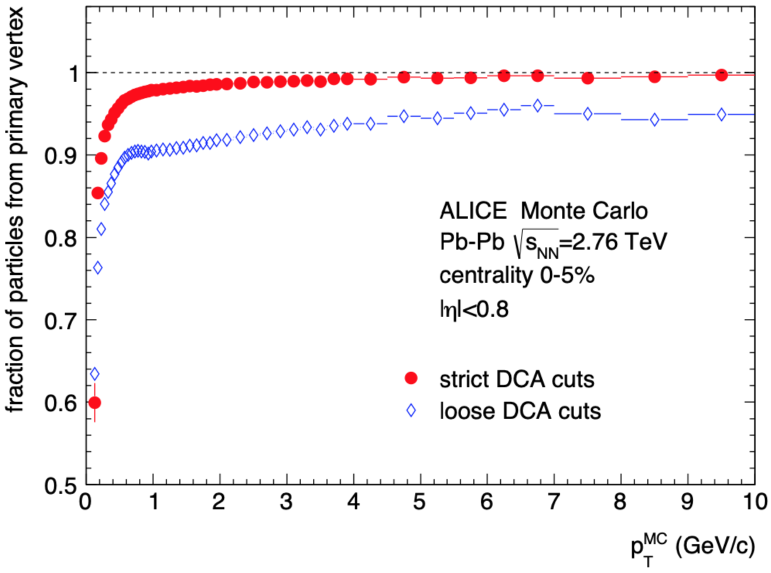

FIGURE 2.16: Fraction of reconstructed tracks coming from the primary interaction vertex. Two sets of cuts on the track distance of closest approach (d_0) to the primary vertex are shown: "loose" with $|d_{0,z}| < 3\,\mathrm{cm}$, $d_{0,xy} < 3\,\mathrm{cm}$ and "strict" with $|d_{0,z}| < 2\,\mathrm{cm}$, $d_{0,xy} < (0.0182 + 0.0350\,\mathrm{GeV}/c\,p_{\mathrm{T}}$) cm.[150]

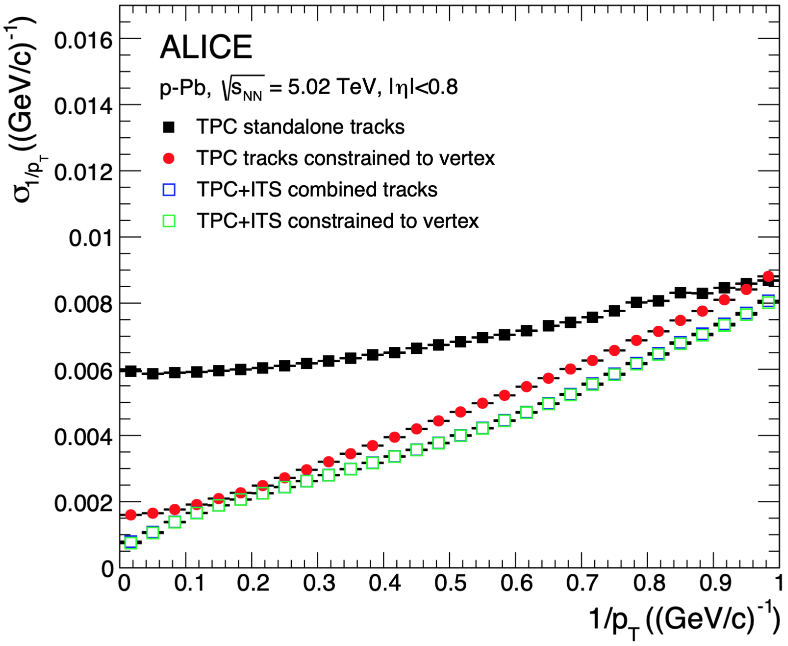

FIGURE 2.17: The p_{T} resolution for standalone TPC and ITS - TPC matched tracks with and without constraint to the vertex. The vertex constrain significantly improves the resolution of TPC standalone tracks. For ITS -TPC tracks, it has no effect (green and blue squares overlap).[150]

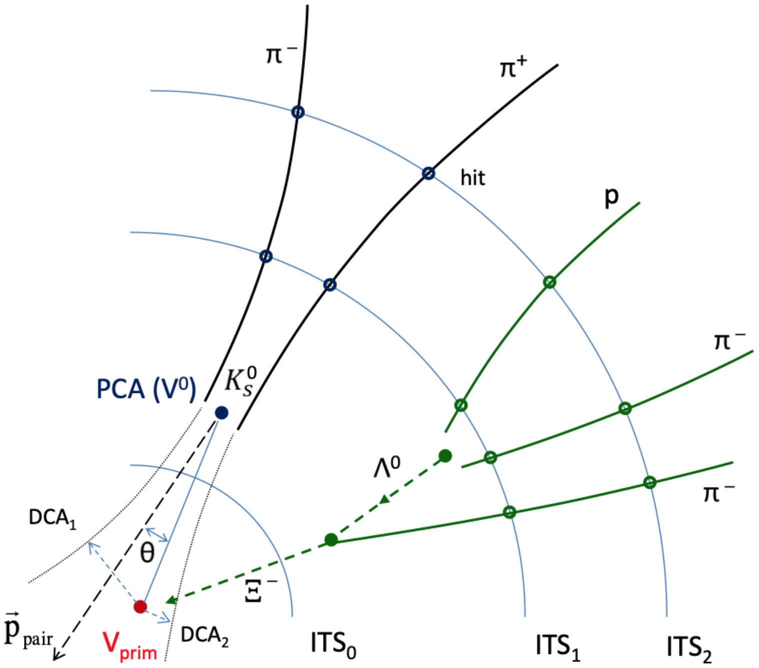

FIGURE 2.18: Secondary vertex reconstruction principle, with K_S^0 and Ξ^- decays shown as an example. For clarity, the decay points were placed between the first two ITS layers (radii are not to scale). The solid lines represent the reconstructed charged particle tracks, extrapolated to the secondary vertex candidates. Extrapolations to the primary vertex and auxiliary vectors are shown with dashed lines. [150]

After the primary vertex is pinned to final position and all possible tracks are found, the search for secondary vertices starts. Secondary vertices are the spatial points were short-lived particles decay producing either a deflection (kink) in the ongoing track (decay in one charged and neutral particles), a split in the ongoing track into multiple tracks (decay in two or more charged particles and, eventually, neutral particles) or the appearance of multiple tracks (decay of a neutral particle into charged ones). Firstly a pool of possible decay product tracks is determined requiring a DCA to the vertex over a threshold ($0.5\,\mathrm{mm}$ in pp and $1\,\mathrm{mm}$ in Pb–Pb). These tracks are then combined in the search of secondary vertices candidates (V0), which consists of pairs of unlike-sign tracks, relying on their mutual PCA. V0s are the secondary vertices that come from the decay of a neutral particle into charged ones. This starting set of candidates is then subjected to multiple cuts: (a) The distance between the tracks and the V0 candidate must be below $1.5\,\mathrm{cm}$; (b) PCA is requested to be closer to the interaction vertex than the innermost hit of either of the two tracks; (c) Taking as θ the angle between the straight line connecting the V0 to the Vertex and the total momentum of the two candidate tracks $\overrightarrow{p}_{\mathrm{pair}}$, cos($\theta$) must be over 0.9. This last requirement is relaxed if the candidate has a momentum below 1.5 GeV/c. A schematic illustration of secondary vertices search is shown in Figure 2.18.

2.3 Particle Identification (PID) in ALICE

The ALICE experiment, despite having a strong focus on heavy-ion collisions physics, is a general purpose experiment: this means that along with specific goals of studying established phenomena there is the will to explore previously unaccessible areas of high-energy physics, both in pp , p–Pb and Pb–Pb collisions. This wide range of goals requires an excellent capability of reconstructing the full event and most of all, assign a particle species to each track: that is the goal of the particle identification. To this end a wide range of detectors are devoted to various degree to the PID effort, a brief graphical summary is shown in Figure 2.19.

The PID is also of special interest for the presented analysis. The measurement will in fact heavily rely on kaon identification from the TOF and TPC detectors.

2.3.1 Charged Particles Identification

Most of our current technology is based on the understanding of electromagnetic interactions and phenomena, thus giving a somewhat privileged status to charged particles. Because of this status, a number of possible ways to detect charged particles have been developed and perfected over the years and the ALICE experiment is an instance where almost every possible identification method is employed.

The three main particle identification methods employed in ALICE are based on the measurement of energy loss through ionisation (ITS , TPC), time of flight (TOF) and Cherenkov Radiation emission (HMPID) and each of these specialises in a certain range of momentum and particle species.

Energy Loss

The method is based on the measurement of ionisation energy loss in a given medium. It can take many forms, in ALICE is notably ionisation in a gas mixture (TPC) and in silicon (ITS).

The basic principle is that a charged particle traversing a medium will ionise the material atoms, freeing an electron that can later be collected. The amount of electrons generated and the detector resolution is directly connected to the first ionisation energy, which is the energy that is required to be lost to ionise a material atom. The detector usually makes then use of high voltages to generate strong electric fields that drift the freed electrons onto instrumentation that can collect them, generating a change in voltage. The change in voltage is then recorded and constitute the signal.

The reference value for how much energy is lost by a given particle species with a given momentum in a given medium is calculated with the Bethe-Bloch equation of ionisation energy loss:

$$-\frac{\mathrm{d}E}{\mathrm{d}x} = 4\pi N_e r_e^2 m_e c^2 \frac{z^2}{\beta^2}\left(\ln\frac{2m_e c^2\beta^2\gamma^2}{I} - \beta^2 - \frac{\delta(\gamma)}{2}\right) \tag{2.2}$$

Where r_e,m_e are the electron classical radius and mass, c is the light speed, N_e is the mean electron density in the medium, β,γ are the relativistic factors of the particle, z is the particle charge, I is the mean excitation energy of the medium, $\delta(\gamma)$ is a high energy correction. For the sake of simplicity and convenience, ALICE uses a

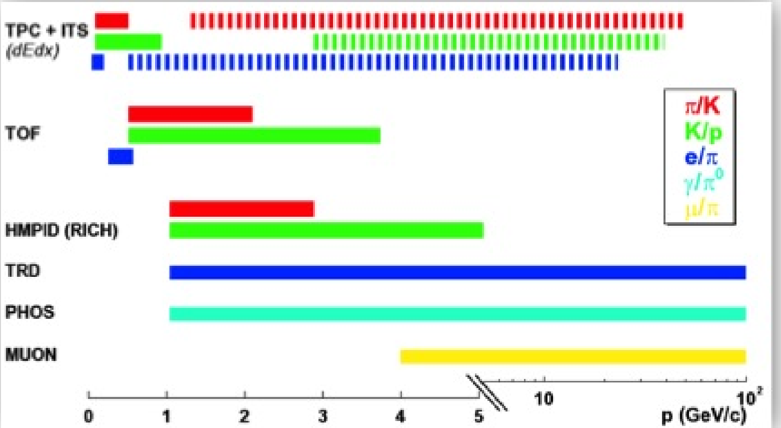

(A) Particle Identification momentum ranges for various detectors. The figure is taken from [150].

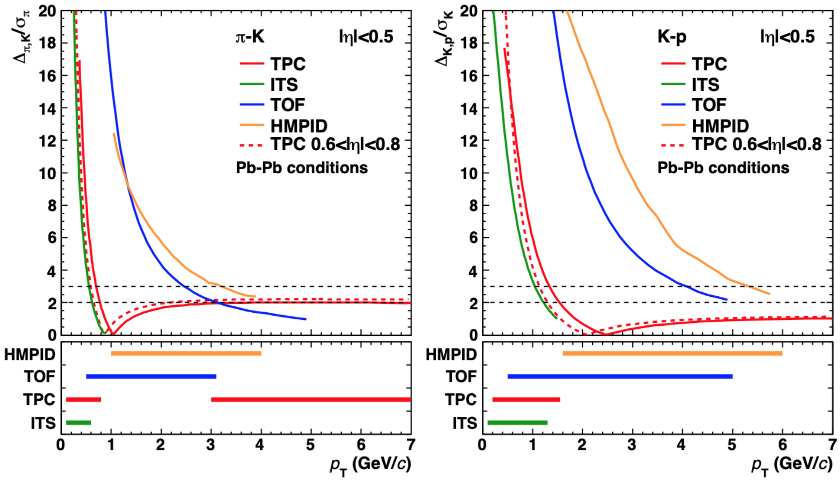

(B) Separation power of hadron identification in the ITS , TPC , TOF , and HMPID as a function of p_T at midrapidity. The left (right) panel shows the separation of pions and kaons (kaons and protons), expressed as the distance between the peaks divided by the resolution for the pion and the kaon, respectively, averaged over $-0.5 < \eta < 0.5$. For the TPC , an additional curve is shown in a narrower η region. The lower panels show the range over which the different ALICE detector systems have a separation power of more than 2σ. The figure is taken from [150].

FIGURE 2.19: Particle Identification momentum ranges for various detectors

different parametrisation:

$$f(\beta\gamma) = \frac{P_1}{\beta^{P_4}}\Big(P_2 - \beta^{P_4} - ln(P_3 - \frac{1}{(\beta\gamma)^{P_5}})\Big) \tag{2.3}$$

where P_{1-5} are fit parameters and β, γ the relativistic factors.

The idea is that the energy loss throughout the central barrel and specifically within the detector itself, in high-energy collisions, is negligible with respect to the particle energy. This is a reasonable assumption as the whole detector was designed and is upgraded according to a principle of minimum interaction: the material in the way of the particle is limited to the extent of the bare minimum for an efficient detection. Thus, the particle $\beta\gamma$ is unchanged and all measurements of energy loss should converge onto a single value for the $\beta\gamma$ prediction through the Bethe-Bloch equation. An advantage of this approach is also that the multiple-scattering effect and subsequent corrections are too at the bare minimum.

The energy loss given in Eq. 2.2 expresses the energy lost in a unit length: once the $\beta\gamma$ of the track has been measured, combining it to the energy loss will determine the most probable particle species. The curves shown in Figure 2.20 are those of a typical energy loss for single charge particles in the ITS and TPC . Despite being a very powerful tool for low momenta particles, as can be seen by the very clear separations in Fig. 2.20, the high momentum region presents more constraints. Indeed one can see that the relativistic rise, that is when the energy loss rises logarithmically over a certain threshold, makes the curves of different particles particularly similar. As can be inferred by Equation the ionisation depends both on the particle and on the medium. This effect is more pronounced for solid detectors such as the ITS , but less strict for gaseous detectors such as the TPC . This difference is evident in their energy loss measurements in Figure 2.20. The ITS has little room for separation over a few GeV/c, whilst the TPC can still achieve a good separation in the tens of GeV/c, see Fig. 2.19b.

ITS In the ITS only the outer four layers are able to provide information about energy loss. The cluster charge is normalised to the track length found from the final track fit parameters, to retrieve a value of dE/dx for each layer. These measurements are then combined: if all four layers are available a mean of the lowest two values is performed, if three layers are available a weighted mean of the lowest (weight 1) and second lowest (weight 1/2) is performed, called truncated mean. A plot of the results of this process is shown in Figure 2.20a.

TPC In the TPC a large variety of physical properties are measured: momentum, charge, energy loss. In the low momentum range, up to $1\,\mathrm{GeV}/c$, the PID can be performed on a track-by-track basis, whereas above that multi-gaussian fits can still statistically separate particles with long tracks (over 130 samples) and with the truncated mean method the dE/dx peak is a gaussian shape. The dE/dx precision is roughly $\approx 5\%$ (pp) to $\approx 6.5\%$ (central Pb–Pb) and this points to a reliable PID up to $\approx 20\,\mathrm{GeV}/c$. The main limitation is the statistical precision, giving way to possible future improvements that could expand the $20\,\mathrm{GeV}/c$ limit to $\approx 50\ \mathrm{GeV}/c$. A plot of the results of this process are plotted in Figure 2.20b

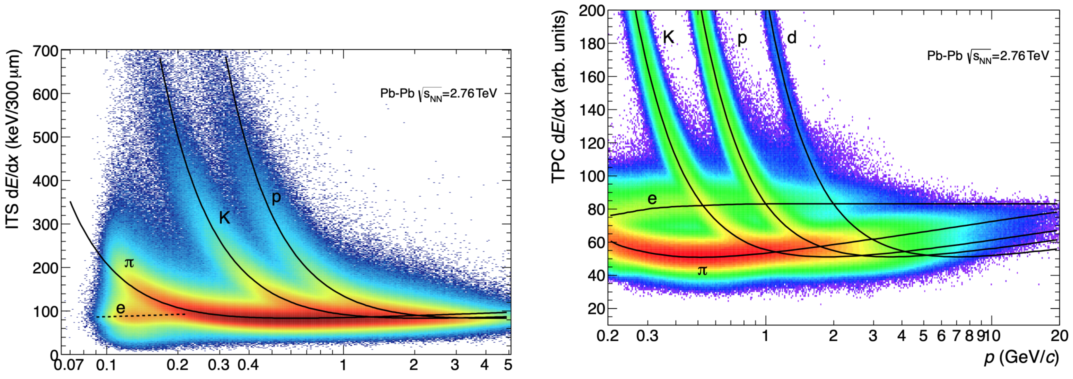

(A) Distribution of the energy-loss signal in the ITS as a function of momentum. Both the energy loss and momentum were measured by the ITS alone. The figure is taken from [150].

(B) Specific energy loss in the TPC vs. particle momentum in Pb–Pb collisions at $\sqrt{s_{NN}} = 2.76$ TeV. The lines show the parametrisations of the expected mean energy loss. The figure is taken from [150].

FIGURE 2.20: Particle Identification by energy loss in TPC and ITS

Time of Flight

This method of particle identification is based on the measurement of the particle velocity.

The basic principle is that, if the knowledge about the momentum is available, the particle mass can be recovered measuring its velocity. This in turn can be measured knowing the track length and the time of flight. The relativistic momentum can be expressed as $p = m\beta\gamma$, then the mass becomes:

$$m = \frac{p}{\beta\gamma} \tag{2.4}$$

where p is the momentum, β and γ are the relativistic factors.

TOF Detector

A plot of the measured β from TOF as a function of momentum is shown in Figure 2.21, where the separation power can be appreciated. The majority of the background comes from mismatching of tracks to TOF hits in the high multiplicity environment of Pb–Pb collisions, telling it is not related to the detector performance but rather to the track density. In fact for tracks above 1 GeV/c in central Pb–Pb collisions the TOF pad occupancy is $\approx 6.7\%$, which in turns produces a mismatch fraction of $\approx 6.7\%$.

Cherenkov Light

This method of particle identification is based on a threshold phenomenon of light emission in a medium.
The Cherenkov phenomenon happens when charged particles travel through a medium at velocities above the light speed in the medium itself: the result is a characteristic light emission in a specific direction. The emission happens with a typical distribution centred around a certain angle θ, defining a characteristic cone of light, related

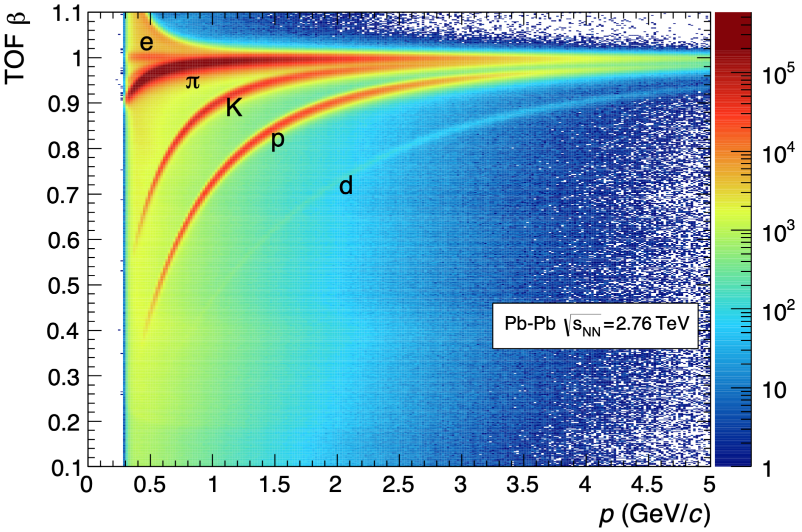

FIGURE 2.21: Distribution of β as measured by the TOF detector as a function of momentum for particles reaching the TOF in Pb–Pb interactions. The figure is taken from [150].

by the speed of the particle (β) and the refractive index of the medium (n) by:

$$\cos(\theta) = \frac{1}{n\beta} \tag{2.5}$$

The goal of the detector is then to determine the angle θ and combine it with the (known by construction) refractive index to find the particle speed. In the Ring Imaging Cherenkov this is made by having the particle cross a layer of medium and then collecting the resulting photons on a photodetection plane, placed at a given distance. The collected photons positions on the plane are then measured and a fit is performed to calculate the circle radius. The radius is then combined with the distance from the radiator to the screen to determine the angle θ.

HMPID

The detector is a collection of 7 identical proximity-focusing RICH modules, with a refractive index for the radiator of $n \approx 1.289$ at $175\,\mathrm{nm}$. The PID is performed track-by-track. The detector help in the PID effort is strongly suppressed by the geometrical acceptance: the matching ratio to the TPC tracks is roughly 5%, which is consistent with the acceptance of 5%.

A plot of the measured cherenkov angle of the HMPID as a function of momentum is shown in Figure 2.22.

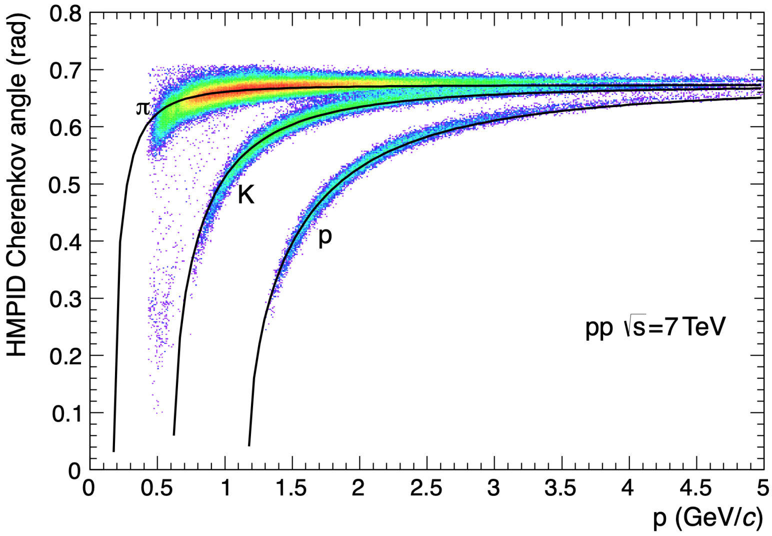

FIGURE 2.22: Particle Identification in the HMPID. The figure is taken from [150].

Chapter 3

Measurement of the ϕ-meson pair production

This chapter illustrates the methodology, the careful cross-checks and the results of the analysis performed for the measurement of the ϕ-meson pair production. In addition, an overview of the future prospects will be discussed with ideas for novel ways this measurement could help us improve our understanding of strangeness production in high-energy collisions and the hadronisation process.

3.1 Physics Motivation

Section 1 describes at length the numerous characteristics and results published about the QGP. One of the most interesting recent results consists in the emergence of high-density QCD reminiscent signals in small systems, most notably the discovery of Strangeness Enhancement in pp collisions [63].

These results point to a gradual enhancement as a function of multiplicity, rather than a threshold effect from pp to Pb–Pb collisions. Indeed relative yield of strange particles evolves as a function of the final state charged-particle multiplicity, which increases from pp to p–Pb and to Pb–Pb . This trend hints at some gradually onsetting phenomena which could be interpreted as the initial creation of a small droplets of QGP gradually becoming the thermalised QGP fireball that forms in heavy-ions collisions. These new possibile interpretations helped steering considerable efforts that led to the observation of other QGP reminiscent phenomena in small systems such as the ones discussed in Section 1.3.

The discussion in section 1.3.1 also revealed how the conversation quickly shifted to finding new ways to extract more information from available data and at that a popular way is to elaborate new event classifiers. The presented analysis is a step forward towards a more in depth characterisation of the production of strange particles and the understanding of the phenomenon of strangeness enhancement altogether. The path taken here is to extract more information about the particle production in each event, rather than extract a more general information in differently classified events. The new approach can then potentially be combined with new exciting classifiers to maximise the insight we can get from the data available to us.

In this context, the ϕ meson is a probe of choice: it is a bound state of $s\bar{s}$ quarks, which makes it strongly dependent on the strangeness production of the event. Moreover, it is a widely studied particle with already many results on its production, correlations with other particles and other physical quantities. It also has the advantage to be described quite differently among phenomenological models, which bestows it a critical advantage in model discrimination and tuning. A more detailed description will be given in section 3.11.

3.2 Data sample

The presented analysis uses both data from the LHC Run 1 (2009-2013) for pp collisions at $\sqrt{s} = 7$ TeV and Run 2 (2015-2018) for pp collisions at $\sqrt{s} = 5.02$ TeV. The event selection was performed using the Minimum Bias trigger for the inclusive analysis and the INEL>0 for the final state charged multiplicity analysis. The minimum bias trigger requires a signal on the V0A and on the V0C. The INEL>0 requires at least one charged particle in $|\eta| < 0.5$

After the trigger selection, a further selection on the vertex is performed. Two types of vertices can be used as selected vertex: SPD vertex, measured from the SPD tracklets, and tracking vertex, measured by extrapolating all reconstructed (primary) tracks in the interaction region to a single common origin. The following selections and cuts have been applied:

1. If the SPD vertex has not been reconstructed, the event is discarded. The SPD vertex is considered as the vertex candidate.
2. If the tracking vertex is available.
    (a) The tracking vertex is considered as the vertex candidate.
    (b) If the z coordinate of the two vertices are more than $0.5\,\mathrm{cm}$ apart, the event is discared.
3. If the vertex candidate z coordinate is farther than $10\,\mathrm{cm}$ from the nominal interaction point, the event is discarded.
4. The event is required to have a full DAQ reconstruction
5. The event should not be flagged as pile-up

After the selection is applied roughly 281 millions events are considered in pp collisions at $\sqrt{s} = 7$ TeV and 1.764 billions in pp collisions at $\sqrt{s} = 5.02$ TeV.

The Monte Carlo productions used for the efficiency calculations make use of the the PYTHIA generator [156, 180], PYTHIA6 for the $\sqrt{s} = 7$ TeV dataset and PHYTHIA8.2 for the $\sqrt{s} = 5.02$ TeV dataset.

3.3 Track Selection

In ALICE the ϕ meson is mainly reconstructed via invariant mass of leptons, in the forward and central region, and kaons, in the central region. Considering the branching ratios of these decays, about 1% for the former and 50% for the latter, the kaon decay channel was chosen. The main target of our selection effort is then primary charged kaons. First a quality cut is performed to have a pool of good primary tracks to use in the analysis, secondly a particle identification cut is applied in order to select those tracks that are compatible with the kaon hypotesis.

3.3.1 Track quality selection

First we review the quality cuts to identify primary tracks. We make use of the standard cuts for primary particles in ALICE[1]:

1. A minimum number of rows crossed in the TPC ($N_{cr,\mathrm{TPC}} \geq 70$)
2. A maximum χ^2 per cluster in the TPC ($\chi^2_{\mathrm{TPC}} < 4$)
3. Reject kink daughters
4. Require ITS refits[2]
5. Require TPC refits
6. Minimum number of clusters in SPD: 1
7. $|xy{-}\mathrm{DCA}| < 0.0182 + 0.0350/p_{\mathrm{T}}{}^{1.01}$ cm (7-σ cut)
8. A maximum χ^2 per TPC -constrained Global fit ($\chi^2_{CGI} < 36$)
9. $|z{-}\mathrm{DCA}| < 2\,\mathrm{cm}$.
10. A maximum χ^2 per cluster in the ITS ($\chi^2_{ITS} < 36$)

Where $z{-}\mathrm{DCA}$ is the component of the Distance of Closest Approach (DCA) of the track parallel to the beam pipe and $xy{-}\mathrm{DCA}$ is the perpendicular component. Although the standard cuts are used, the cuts a re-implemented in the analysis to provide full control for systematic uncertainty evaluation. In addition to these selections we add a cut in η, p_{T} for the kaons and rapidity for the ϕ-meson candidate:

1. charge of kaon candidate equal to 1
2. p_{T} of kaon candidate larger than $0.15\,\mathrm{GeV}$ ($\mathrm{p_T} \geq 0.15\,\mathrm{GeV}$)
3. η of kaon candidate in range [-0.8,0.8] ($|\eta| < 0.8$)
4. Reconstructed ϕ candidate in rapidity range [-0.5,0.5] ($|y| < 0.5$)

The first two are a requirement to select candidates within optimal detector acceptance and avoid distortions effect on the acceptance edges, the second one is a physical cut as the measurement is performed at mid-rapidity.

---

[1] We resort to the cuts implemented in DPG Track Filterbit 5 that incorporates the `GetStandardITSTPCTrackCuts2010()` selection on the tracks.

[2] A special refit in uncalibrated coordinates improves the track model entropy encoding [181]

3.3.2 PID Selection

Once the primary tracks are selected, we proceed to the particle identification using the TPC and TOF detectors, respectively measuring the energy loss and the time of flight of the particle. The selection is made using the $\sigma^{\mathrm{det}}_{\mathrm{kaons}}$ of the detector det, this quantity represents the difference between the measured signal ($\mathrm{S}^{\mathrm{det}}$) and the expected signal for a given mass hypothesis ($\mathrm{S}^{\mathrm{exp}}_{\mathrm{part}}$), normalised to the detector resolution ($\sigma_{\mathrm{det}}(\mathrm{part})$):

$$n\sigma^{\mathrm{det}}_{\mathrm{part}} = \frac{\mathrm{S}^{\mathrm{det}} - \mathrm{S}^{\mathrm{exp}}_{\mathrm{part}}}{\sigma_{\mathrm{det}}(\mathrm{part})} \tag{3.1}$$

$$n\sigma^{\mathrm{TPC}}_{\mathrm{kaons}} = \frac{\mathrm{S}^{\mathrm{TPC}} - \mathrm{S}^{\mathrm{exp}}_{\mathrm{kaons}}}{\sigma_{\mathrm{TPC}}(\mathrm{kaons})} \tag{3.2}$$

$$n\sigma^{\mathrm{TOF}}_{\mathrm{kaons}} = \frac{\mathrm{S}^{\mathrm{TOF}} - \mathrm{S}^{\mathrm{exp}}_{\mathrm{kaons}}}{\sigma_{\mathrm{TOF}}(\mathrm{kaons})} \tag{3.3}$$

It reflects the detector confidence for a given track being compatible with a given mass hypotesis. The selections used in the analysis are:

1. If the track does not match a TOF hit:

   $\left|n\sigma^{\mathrm{TPC}}_{\mathrm{kaons}}\right| < 3.0$ selection on TPC signal is performed (this is called TPC standalone)

2. If the track matches a TOF hit:

   $\left|n\sigma^{\mathrm{TPC}}_{\mathrm{kaons}}\right| < 5.0$ selection on TPC signal is performed

   and

   $\left|n\sigma^{\mathrm{TOF}}_{\mathrm{kaons}}\right| < 3.0$ selection on TOF signal (this is called TOF veto).

During the analysis quality checks, the presence of unexpected imperfections in the TPC calibration was discovered. The imperfection concerned the very low momentum region and was consistent with a shift of the expected value, effectively moving the mean of the distribution of up to -4 (from the expected 0), in the $\leq 0.28\,\mathrm{GeV}/c$ region, as can be seen in Figure 3.1b.

This unexpected behaviour would have heavily affected the low momentum measurements, as the standard cut would require to consider only tracks with the TPC standalone cut[3] $\left|n\sigma^{\mathrm{TPC}}_{\mathrm{kaons}}\right| < 3.0$, guaranteeing the exclusion of good kaons candidates. Moreover, moving our attention to Figure 3.1, the unexpected nature of this imperfection shows how the reconstruction efficiency × acceptance, driven by the Monte Carlo reconstruction, would underestimate the kaons loss. This altogether would affect considerably the low momentum PID selection performance.

To avoid the underestimation and signal rejection, the TPC selection is widened to $\left|\sigma^{\mathrm{TPC}}_{\mathrm{kaons}}\right| < 7.0$ for tracks having a $p_{\mathrm{T}} \leq 0.28\,\mathrm{GeV}$. Given this is an already wide selection, that involves a very small fraction of tracks, it will not be concerned by variations made to evaluate the systematic uncertainty. A more clear visualisation of the issue can be seen in Figure 3.5 middle-right panel.

---

[3] TOF contribution on PID start to be relevant at $\approx 0.8\,\mathrm{GeV}/c$

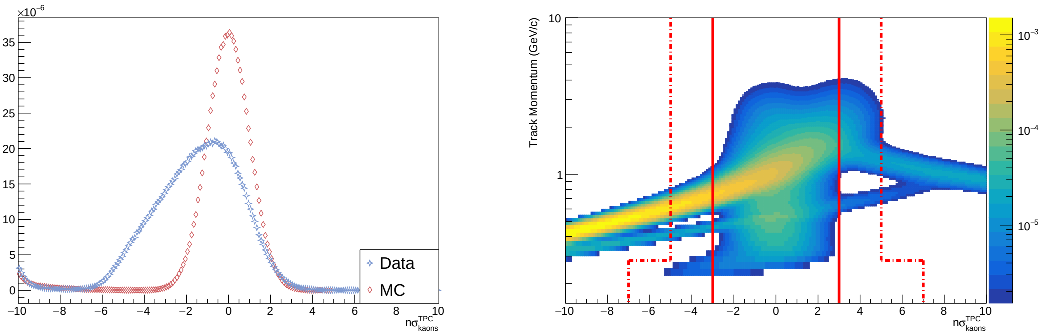

(A) Close up of problematic region ($p_{\mathrm{T}} \leq 0.28\,\mathrm{GeV}/c$) in the kaon identification signal for TPC . pp collision at $\sqrt{s}$ = 7 TeV dataset, arbitrary units of selected tracks normalised per the curve integral.

(B) TPC $\sigma^{\mathrm{TPC}}_{\mathrm{kaons}}$ as a function of particle momentum. pp collision at $\sqrt{s} = 7$ TeV dataset. 1

FIGURE 3.1: Unexpected imperfection in TPC PID predictions for kaons in pp collision at $\sqrt{s} = 7$ TeV.

3.3.3 Quality Assurance

To ensure a correct selection and a reliable reproduction of the data by the Monte Carlo simulation we can take a look at various distributions in both datasets. All distributions are intended after all quality and PID cuts, and represents the tracks used in the analysis. For the kinematic quantities pseudorapidity (η) and azimuthal angle (φ), the tracks are compared taking into account their electric charge, comparing positive and negative tracks separately. Figure 3.2 show such comparisons, highlighting how the Monte Carlo correctly reproduces data and how the track sign is not affecting the reproducibility goodness. The η distribution also provides a check on the track cut of $|\eta| < 0.8$ working properly. For the DCA distributions, the tracks are compared separating by their charge. The p_{T} distributions are examined for the p_{T} -dependent xy-DCA cut and inclusively for the inclusive z-DCA cut. Figure 3.3 shows the distributions, compared to the Monte Carlo, which provides again a way to check the goodness of the Monte Carlo to reproduce data. Together with that, the p_{T} distribution is reported for data only and compared instead to the nominal cuts performed. The distributions also provide a check on the $z-$DCA cut of $|z-\mathrm{DCA}| < 2\,\mathrm{cm}$ is working properly together with the $xy-$DCA p_{T} -dependent cut. For the PID selection, multiple checks are done as in Figures 3.4-3.5. First (Top panel), the signal from all tracks is recorded to check the resulting distribution in momentum is as expected. Then the signal from the kaons selected only is superimposed to check the selection is done properly both in TOF and TPC . Then (Central panel), the distribution for all tracks in N$\sigma^{\mathrm{DET}}_{\mathrm{kaons}}$ is plotted with a line depicting the cuts performed in the analysis to check we are correctly selecting the kaons. Lastly (Lower panel), we check the Monte Carlo simulation correctly reproduce the data by comparing the integral ($f_{n\sigma}$) within a nσ window (N$_{n\sigma}$) normalised to the integral that falls within 5σ (N$_{5\sigma}$).

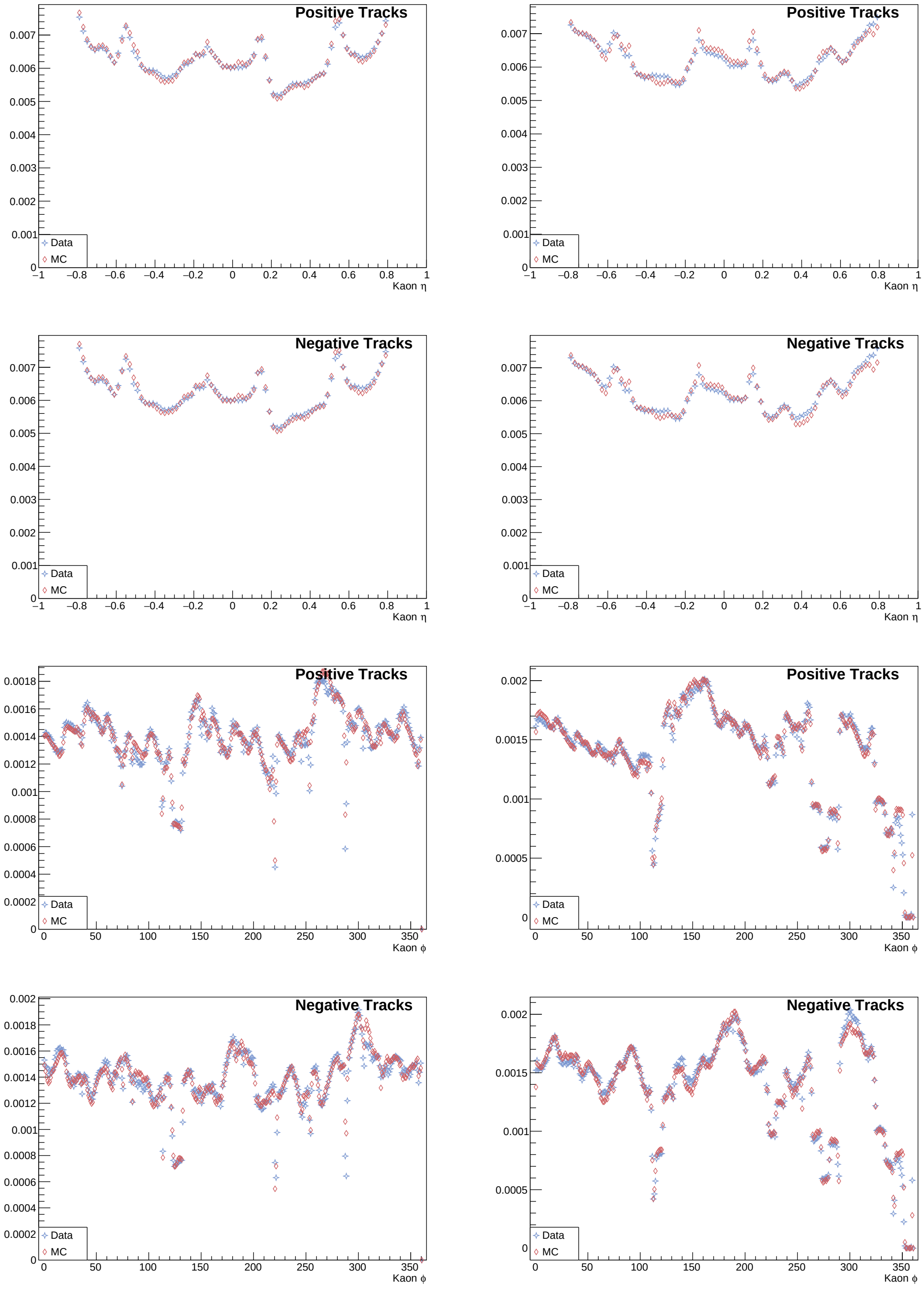

FIGURE 3.2: Comparison between data and Monte Carlo simulation for pseudorapidity (η) and azimuthal angle (φ) kaons candidate tracks distribution. On the left is the pp collision at $\sqrt{s} = 5.02$ TeV, on the right is the pp collision at $\sqrt{s} = 7$ TeV. The tracks are divided in positive and negative where stated and are reported in arbitrary units of selected tracks normalised per the curve integral.

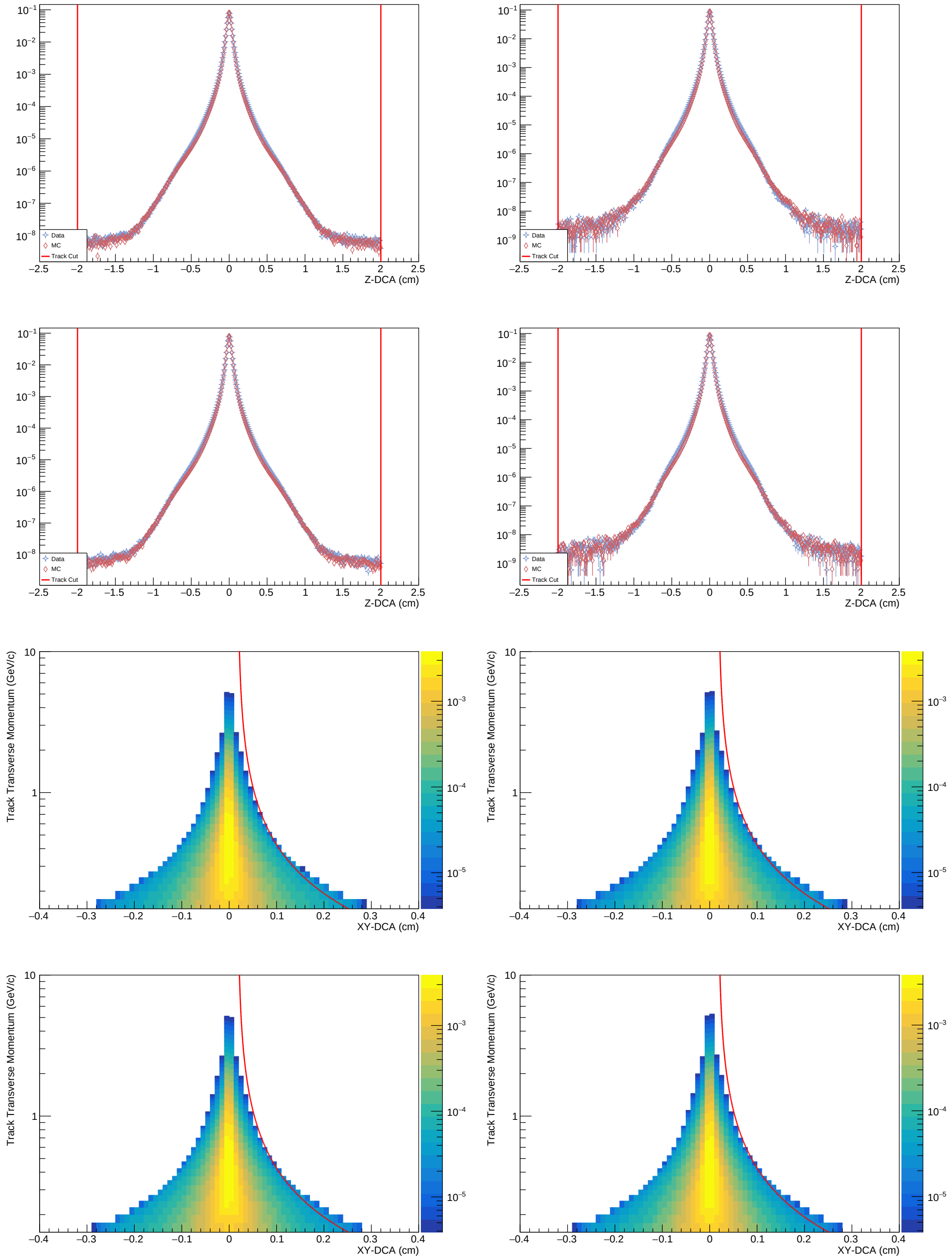

FIGURE 3.3: Comparison between data and Monte Carlo simulation for $xy-$DCA and $z-$DCA distribution. On the top panel are the cumulative distributions, on the bottom panel are the p_{T} dependent distribution. The red lines indicate the quality cut applied. For every two rows, the top one is the positive tracks and the bottom one is the negative tracks. On the left is the pp collision at $\sqrt{s} = 5.02$ TeV, on the right is the pp collision at $\sqrt{s} = 7$ TeV

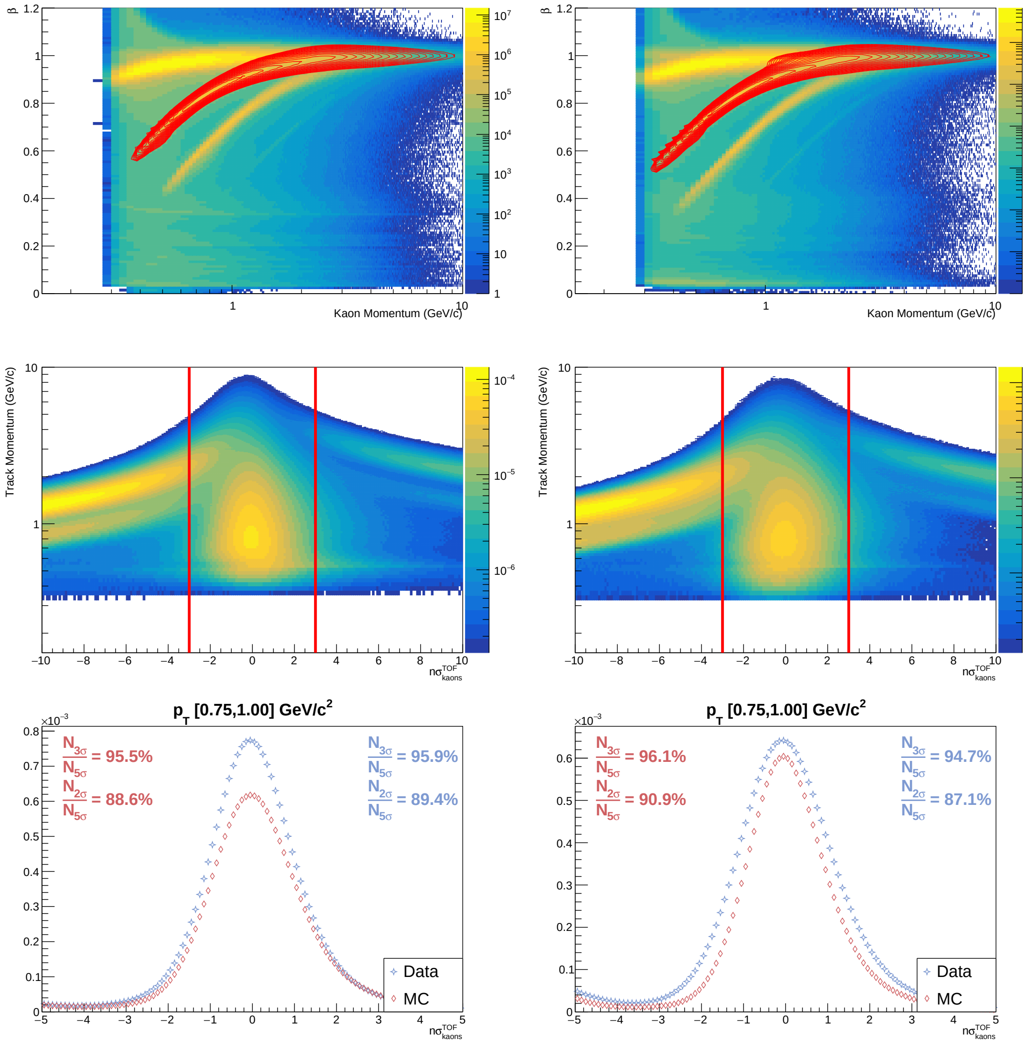

FIGURE 3.4: On the top panel there is highlighted the TOF (left) and TPC (right) signal selected for the kaons. On the central panel the σ_{kaons} of TOF (left) and TPC (right) for kaons as a function of transverse momentum. The red solid lines indicate the PID cut applied with the Standalone detector, the dashed red lines indicate the TOF -veto cut for the TPC . On the bottom panel the selection efficiency is checked against the Monte Carlo production. On the left is the pp collision at $\sqrt{s} = 5.02$ TeV, on the right is the pp collision at $\sqrt{s} = 7$ TeV.

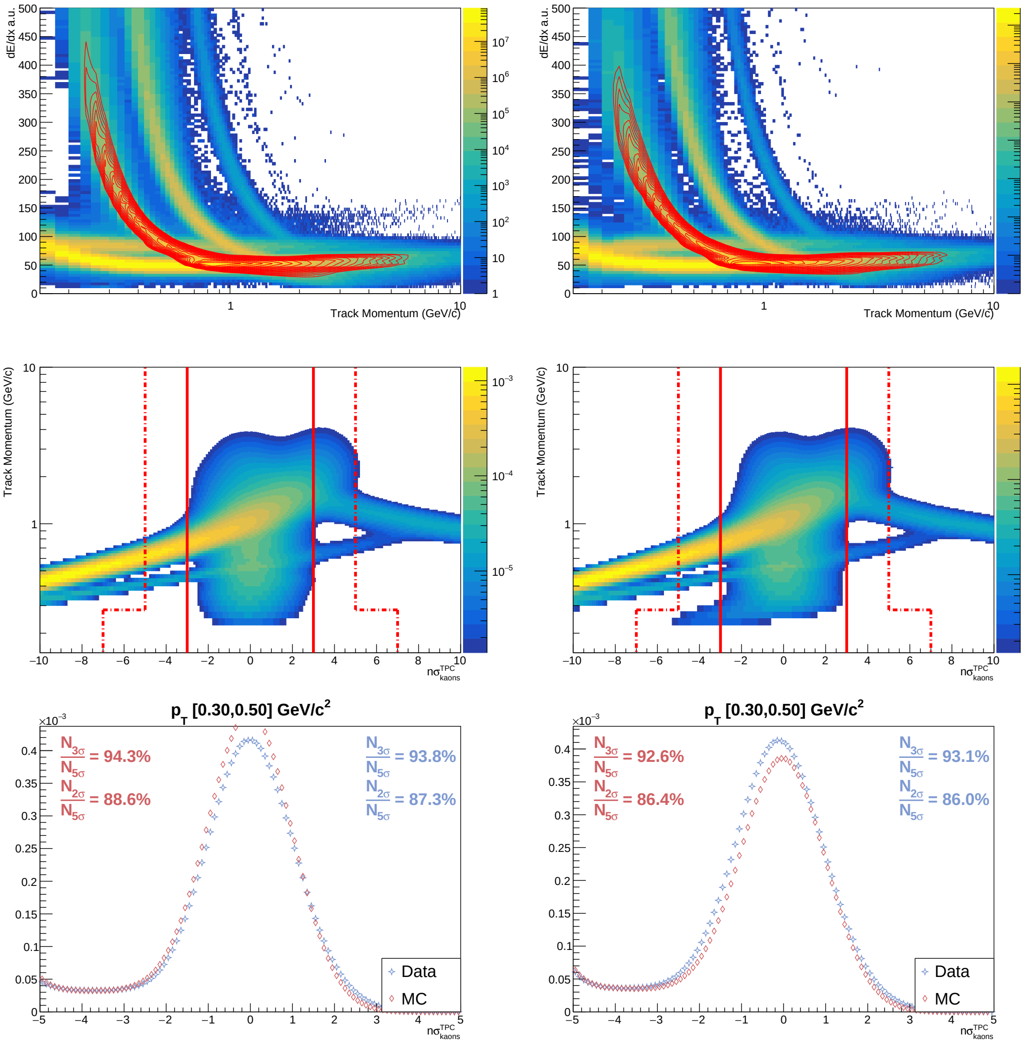

FIGURE 3.5: On the top panel there is highlighted the TOF (left) and TPC (right) signal selected for the kaons. On the central panel the σ_{kaons} of TOF (left) and TPC (right) for kaons as a function of transverse momentum. The red solid lines indicate the PID cut applied with the Standalone detector, the dashed red lines indicate the TOF - veto cut for the TPC . On the bottom panel the selection efficiency is checked against the Monte Carlo production. On the left is the pp collision at $\sqrt{s} = 5.02$ TeV, on the right is the pp collision at $\sqrt{s} = 7$ TeV

1D Analysis						2D Analysis		
Bin	Min	Max	Bin	Min	Max	Bin	Min	Max
1	0.4	0.6	11	1.6	1.8	1	0.4	0.9
2	0.6	0.7	12	1.8	2.0	2	0.9	1.2
3	0.7	0.8	13	2.0	2.4	3	1.2	1.4
4	0.8	0.9	14	2.4	2.8	4	1.4	1.7
5	0.9	1.0	15	2.8	3.2	5	1.7	2.0
6	1.0	1.1	16	3.2	3.6	6	2.0	2.5
7	1.1	1.2	17	3.6	4.0	7	2.5	4.0
8	1.2	1.3	18	4.0	5.0	8	4.0	8.0
9	1.3	1.4	19	5.0	6.0			
10	1.4	1.6	19	6.0	8.0			

TABLE 3.1: The p_{T} bins used in the analysis, all values are in GeV/c

3.4 Signal Extraction

The raw yield of the $\phi(1020)$ is measured via the invariant-mass reconstruction technique in the decay channel $\phi \to \mathrm{K}^-\mathrm{K}^+$. The yield of the $\phi(1020)$ pair is measured via a generalisation of the invariant-mass reconstruction technique in the same decay channel. The data samples used for the analysis are discussed in Section 3.2., the list of bins are listed in Table 3.1.

3.4.1 Extraction of ϕ meson

Charged kaons used in the analysis are requested to pass the selections on track and PID as described in sections 3.3 and 3.3.2. The invariant mass of the candidate is taken combining the quadri-momentum of selected tracks, after they are assigned the reference mass for charged kaons $493.677\,\mathrm{MeV}/c^2$[1]. The rapidity of the ϕ-meson candidate is requested to be within $|y| < 0.5$. For each event, all unlike sign pairs of kaons are used, generating a distribution with the signal on top of a combinatorial background.

For reasons that will become clear in the next section, we do not make use of the background subtraction technique. Instead the signal extraction is done through a 2-component fit, one to model the signal and one to model the background:

$$f_{\text{total}}(\mathrm{m}_{\mathrm{K}^\pm}) = A_{\text{sig}} f_{\text{sig}}(\mathrm{m}_{\mathrm{K}^\pm}) + A_{\text{bkg}} f_{\text{bkg}}(\mathrm{m}_{\mathrm{K}^\pm}) \tag{3.4}$$

where $\mathrm{m}_{\mathrm{K}^\pm}$ is the invariant mass of two opposite-sign kaon candidates.

Signal Component The signal component is modelled through a Voigtian function. This function is the convolution of the non-relativistic Breit-Wigner $f_{\text{BW}}(\mathrm{x};\mathrm{m},\Gamma)$ and a Gaussian $f_{\text{Gaus}}(\mathrm{x};\mu,\sigma)$:

$$f_{\text{Gaus}}(\mathrm{m}_{\mathrm{K}^\pm}) = \frac{1}{\sigma_\phi\sqrt{2\pi}} e^{\left(-\frac{\mathrm{m}^2_{\mathrm{K}^\pm}}{2\sigma^2_\phi}\right)} \tag{3.5}$$

$$f_{\text{BW}}(\mathrm{m}_{\mathrm{K}^\pm}) = \frac{1}{2\pi}\frac{\Gamma_\phi}{(\mathrm{m}_{\mathrm{K}^\pm} - \mathrm{m}_\phi)^2 + (\Gamma_\phi/2)^2} \tag{3.6}$$

$$f_{\text{sig}}(\mathrm{m}_{\mathrm{K}^\pm}) \equiv f_{\text{VG}}(\mathrm{m}_{\mathrm{K}^\pm}) = \int_{-\infty}^{+\infty} f_{\text{Gaus}}(\mathrm{m}'_{\mathrm{K}^\pm} - \mathrm{m}_{\mathrm{K}^\pm}) f_{\text{BW}}(\mathrm{m}'_{\mathrm{K}^\pm})\mathrm{d}\mathrm{m}'_{\mathrm{K}^\pm} \tag{3.7}$$

where Γ_ϕ is the ϕ-meson width, m_ϕ is the ϕ-meson mass, σ_ϕ is the invariant mass resolution.

Background Component The background component is modelled through a Čebyšëv polynomial of third degree:

$$f_{\mathrm{bkg}}(\mathrm{m}_{\mathrm{K}^\pm}) = \left[1 + c_1\left(\mathrm{m}_{\mathrm{K}^\pm}\right) + c_2\left(2\mathrm{m}^2_{\mathrm{K}^\pm} - 1\right) + c_3\left(4\mathrm{m}^3_{\mathrm{K}^\pm} - 3\mathrm{m}_{\mathrm{K}^\pm}\right)\right] \tag{3.8}$$

where c_i represent the power coefficient for the polynomial.

Integral Signal Loss The developed fit procedure has been designed to only return the number of ϕ mesons within the fit range. For this reason one has to correct to be able to obtain the total number of produced ϕ mesons, which are produced with invariant masses from the low mass limit to infinity. The low mass limit is $0.995\,\mathrm{GeV}/c^2$ and is the physical limit equivalent to the mass of the two daughter kaons produced at rest.. To recover the missing yield we use the width and mean from the fit to build a Breit-Wigner and use the Voigtian from the fit to integrate them from the low mass limit to infinity and compare this number to the integral over the measured range.

$$f_{\mathrm{miss}} = \frac{\int_{0.995}^{+\infty} f_{\mathrm{BW}}(\mathrm{m}_{\mathrm{K}^\pm}; \Gamma_\phi, \mathrm{m}_\phi)}{\int_{0.998}^{1.065} f_{\mathrm{BW}}(\mathrm{m}_{\mathrm{K}^\pm}; \Gamma_\phi, \mathrm{m}_\phi)} \approx 0.974 \tag{3.9}$$

or, alternatively

$$f_{\mathrm{miss}} = \frac{\int_{0.995}^{+\infty} f_{\mathrm{VG}}(\mathrm{m}_{\mathrm{K}^\pm}; \Gamma_\phi, \mathrm{m}_\phi, \sigma_\phi)}{\int_{0.998}^{1.065} f_{\mathrm{VG}}(\mathrm{m}_{\mathrm{K}^\pm}; \Gamma_\phi, \mathrm{m}_\phi, \sigma_\phi)} \approx 0.974 \tag{3.10}$$

Then, the corrected raw count is given as

$$\mathrm{N}^{raw} = \frac{S}{f_{\mathrm{miss}}} \tag{3.11}$$

Where S is the signal resulting from the fit.

This correction is performed for each p_{T} bin, simultaneously with the signal extraction itself. The standard correction is calculated using the Voigtian approach. The Breit-Wigner calculation is used as a cross-check.

3.4.2 Extraction of ϕ-meson pair

The 2D invariant mass extraction starts with the histogram filling. First, a pool of possible ϕ-meson candidates (a suitable $\mathrm{K}^-\mathrm{K}^+$pair) is created, the candidates are then paired if they share no kaon. For example, if the first ϕ-meson candidate is made from the kaons labeled 4 (positive) and 7 (negative) it will not be coupled to the pair made from the kaons labeled 6 (positive) and 7 (negative), as it would not be physical to have to assign the same kaon track as the daughter of two different phi meson decays. We use all combinations of kaon pairs, so for an event having kaons 1,2 (positive) and 3,4 (negative) we will use { [1; 3] [2; 4] }, { [2; 3] [1; 4] }. Other combinations are forbidden by the above argument.

We now have a list of ϕ-meson pairs that can be used to fill the invariant mass histogram. Care has to be taken to avoid double counting the ϕ-meson pairs when filling the histogram. For this reason, we introduced an arbitrary ordering in p_{T} for the

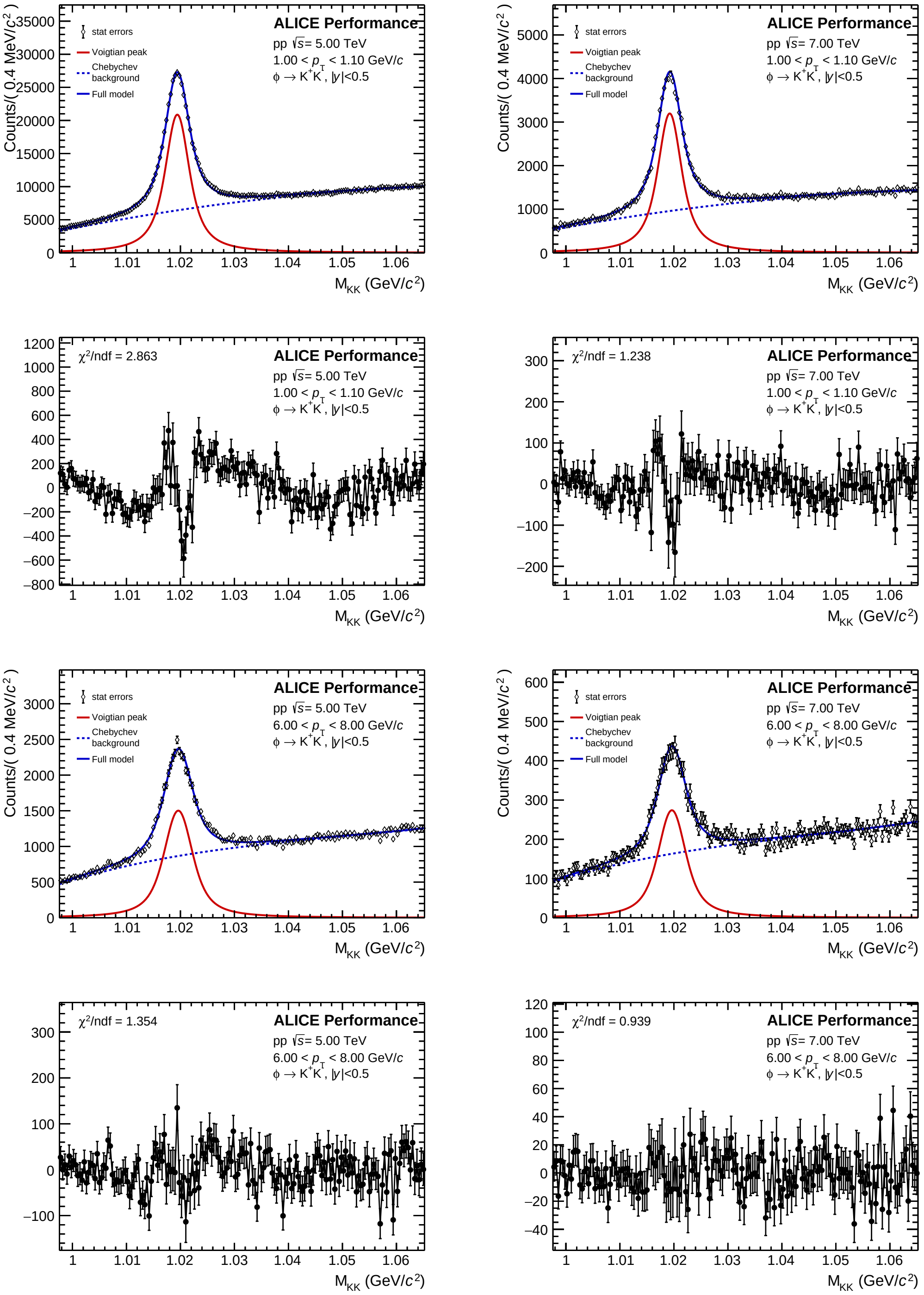

FIGURE 3.6: Example of the Fit results used to extract the yield of ϕ mesons in p_{T} bin [1.0,1.1] GeV (top) and [6.0,8.0] GeV. Highlighted in solid dark blue is the model, in dashed light blue the background and in solid red the signal. On the left is the pp collision at $\sqrt{s} = 5.02$ TeV, on the right is the pp collision at $\sqrt{s} = 7$ TeV

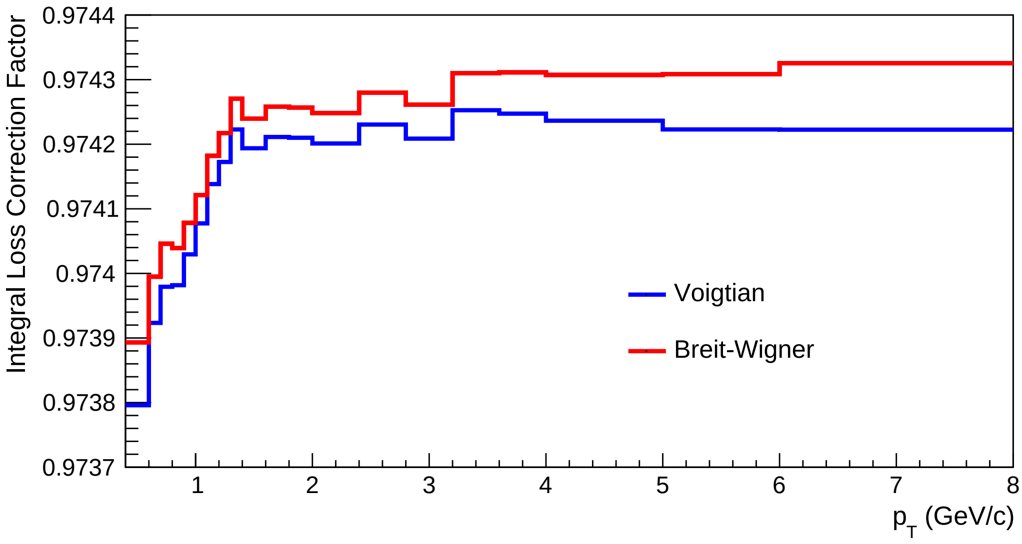

FIGURE 3.7: BW loss correction factor evaluated using the Voigtian or Breit-Wigner BW.

ϕ-meson candidates. Histogram filling is performed exclusively using pairs (ϕ_1,ϕ_2) when $p_{T1} < p_{T2}$, then the first member of the pair will define the x-coordinate and the second the y-coordinate. The pair will then be used to fill once the differential histograms corresponding to the chosen p_T bin combination. For example, for the p_T bins 2.0-2.5 and 4.0-8.0, [(2.0-2.5),(4.0-8.0)] w3ill be filled but not the opposite (but equivalent) [(4.0-8.0),(2.0-2.5)]. This ordering can be done on the basis of the 2D spectrum symmetry for opposite permutations of p_T bins. In fact it is easy to imagine that such ordering will leave half the spectrum unpopulated. As a consequence, only a fit on the upper half and diagonal of the spectrum is performed, assigning the results and errors to the conjugate bins.

Once the invariant-mass distribution is made, a procedure similar to the one discussed for the single ϕ meson is performed. A function is used to fit the distribution in order to extract the signal content. In this section, for the sake of clarity, the invariant masses of the paired ϕ-mesons will be referred to as $m_{\phi,i}$, where i is an index in [1,2]. We can start by developing the product of two invariant-mass distributions as a function of the two invariant masses:

$$f_{\text{total}}(m_{\phi,1})f_{\text{total}}(m_{\phi,2}) = \Big[f_{\text{sig}}(m_{\phi,1}) + f_{\text{bkg}}(m_{\phi,1})\Big]\Big[f_{\text{sig}}(m_{\phi,2}) + f_{\text{bkg}}(m_{\phi,2})\Big] \tag{3.12}$$

$$= f_{\text{sig}}(m_{\phi,1})f_{\text{sig}}(m_{\phi,2}) + \tag{3.13}$$

$$+ f_{\text{bkg}}(m_{\phi,1})f_{\text{sig}}(m_{\phi,2}) + f_{\text{sig}}(m_{\phi,1})f_{\text{bkg}}(m_{\phi,2})$$

$$+ f_{\text{bkg}}(m_{\phi,1})f_{\text{bkg}}(m_{\phi,2}) \tag{3.14}$$

Signal description The signal distribution can be modelled as:

$$f^{2D}_{\text{sig}}(m_{\phi,1}, m_{\phi,2}) = f_{\text{sig}}(m_{\phi,1})f_{\text{sig}}(m_{\phi,2}) \tag{3.15}$$

and only takes into account the component of Equation 3.13 that combines signal functions from both 1D models.

Background description The background distribution can be modelled as:

$$\begin{aligned} f^{\text{2D}}_{\text{bkg}}(\mathrm{m}_{\phi,1}, \mathrm{m}_{\phi,2}) &= C_{\text{sb}} f_{\text{sig}}(\mathrm{m}_{\phi,1}) f_{\text{bkg}}(\mathrm{m}_{\phi,2}) + \qquad (3.16)\\ &+ C_{\text{bs}} f_{\text{bkg}}(\mathrm{m}_{\phi,1}) f_{\text{sig}}(\mathrm{m}_{\phi,2}) + \qquad (3.17)\\ &+ C_{\text{bb}} f_{\text{bkg}}(\mathrm{m}_{\phi,1}) f_{\text{bkg}}(\mathrm{m}_{\phi,2}) \end{aligned}$$

and takes into account all the components of Equation 3.13 that combines at least one background function from either 1D model. C_{sb}, C_{bs} and C_{bb} are normalisation constants constrained to be positive for all terms.

Full model description From the above results we can define:

$$f^{\text{2D}}_{\text{total}}(\mathrm{m}_{\phi,1}, \mathrm{m}_{\phi,2}) = A^{\text{2D}}_{\text{sig}} f^{\text{2D}}_{\text{sig}}(\mathrm{m}_{\phi,1}, \mathrm{m}_{\phi,2}) + f^{\text{2D}}_{\text{bkg}}(\mathrm{m}_{\phi,1}, \mathrm{m}_{\phi,2}) \qquad (3.18)$$

as the full model function that is ultimately used to fit the invariant-mass distribution. It is worth noting that in the fit procedure not all parameters are free, as will be explained in the next paragraph.

Shape Evaluation The fitting function (Eq. 3.18) is a complex multi-parameter model which has three parameters for each single signal function ($\mathrm{m}_\phi, \Gamma_\phi, \sigma_\phi$) and five for each background function (c_i). On top of that, we must consider the four normalisation constants $A^{\text{2D}}_{\text{sig}}$, C_{sb}, C_{bs}, C_{bb}. This last addition brings the total free parameters to 16. However, a 2-dimensional fit is already a complicated endeavour and the large number of free parameters could result in non-converging results or large uncertainties. The results are then improved by constraining the parameters defining the shape of the background and signal shape $\mathrm{m}_\phi, \Gamma_\phi, \sigma_\phi$, c_i. The normalisation constants are, of course, not constrainable *a priori* and their evaluation is the result of the fitting effort. Our goal is then to constrain the parameters listed above.

Firstly, we can see that the combinatorial background is dependent on the transverse momentum interval we are examining, as can be appreciated in Figure 3.6. It is, in fact, a combination of unrelated kaons (with possible contaminations of other particles) that can have random or non-trivial correlations among them and an identical behaviour in the full p_{T} range is hardly possible. The implications of this observation are that we need to have a p_{T} dependent approach to measure the background parameters to assign their values and constrain them in the 2D fit.

Secondly, we turn our attention to the signal functions. Of the three parameters, only σ_ϕ, the detector invariant-mass resolution, is p_{T} dependent and its value is fixed based on Monte Carlo studies that will be explained in section 3.5.3. The mass and width of the ϕ meson are not expected to be sensitive to the measurement p_{T} range. Nevertheless, detector effects slightly shift the centre of the invariant mass peak, effectively shifting the ϕ-meson mass. For this reason, the width is fixed in all fits, 1D or 2D, and the mass is a free parameter.

In this scenario, we managed to fix four parameters ($\Gamma_{\phi,1}$, $\Gamma_{\phi,2}$, $\sigma_{\phi,1}$, $\sigma_{\phi,2}$), we know that four need to be free ($A^{\text{2D}}_{\text{sig}}$, C_{sb}, C_{bs}, C_{bb}) so we now need a way to constrain the remaining ones: this is done through a pre-fitting procedure that ought to be a function of the candidate p_{T} . All 2D invariant mass histograms are filled with combinations of ϕ-meson candidates in two given p_{T} ranges. We can then consider the invariant mass distribution of all ϕ-meson candidates in one given p_{T} range and fit it according to the f_{total} model. The fit results will yield values for all the missing parameters ($\mathrm{m}_\phi, \mathrm{c}_i$). These values can be used in the 2D fit as constants.

This procedure allows one to obtain the shapes of the ϕ-meson and of the background invariant mass distribution, hence leaving only the normalisation of the distributions as free parameters in the 2D invariant mass fit. A summary of the standard parameter values used is given in Table 3.3.

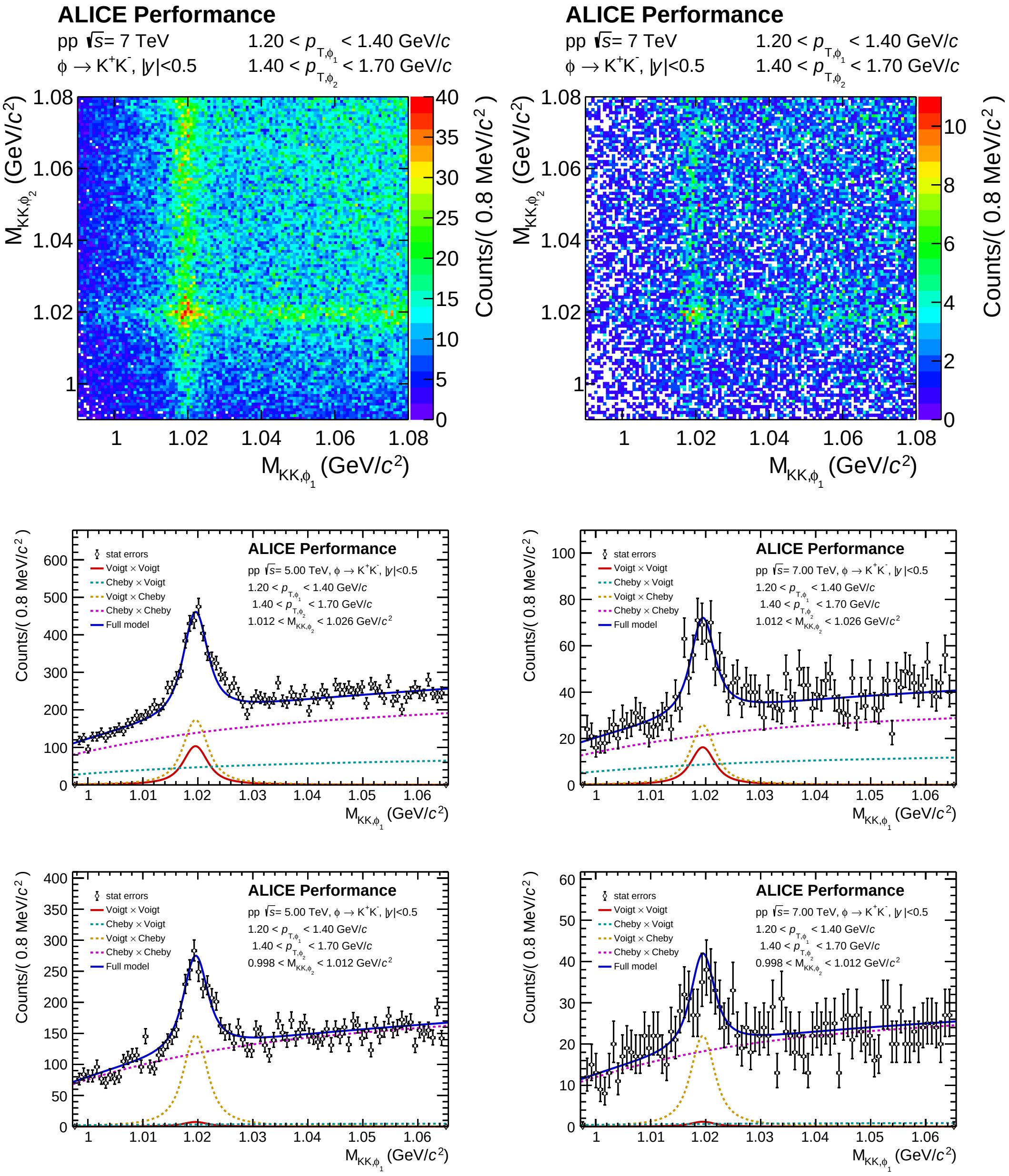

FIGURE 3.8: Example of the Fit results used to extract the yield of ϕ-meson pairs in p_{T} bin [1.2;1.4][1.4;1.7] GeV/c. Highlighted in solid dark blue is the model, in various dashed light blue shades the background components and in solid red the signal. Each columns represents a slice of the 2-Dimensional invariant mass distribution in intervals [0.998;1.012], [1.012;1.026] GeV/c^2 along the X-axis. On the left is the pp collision at $\sqrt{s} = 5.02$ TeV, on the right is the pp collision at $\sqrt{s} = 7$ TeV.

3.5 Simulation

A number of corrections have been carried out using the simulated dataset anchored[4] to the data used in this analysis. In particular, we used a general purpose Monte Carlo based on the PYTHIA [156, 180] event generator, using the GEANT3 [182] software to simulate particle transport in the experiment and interaction with the materials of the detector.

3.5.1 Efficiency × Acceptance

The Efficiency × Acceptance (ε) correction factor is p_{T} dependent and has been defined as:

$$\varepsilon(p_{\mathrm{T}}) = \frac{\mathrm{N}^{rec}}{\mathrm{N}^{gen}} \tag{3.19}$$

$\mathbf{N}^{rec}$ the number of reconstructed ϕ mesons after applying all track selection and particle identification cuts. Moreover it is required that the reconstructed rapidity is $|y_{rec}| < 0.5$. $\mathbf{N}^{gen}$ is the number of ϕ mesons that are generated in the Monte Carlo decaying in $\mathrm{K}^{-}\mathrm{K}^{+}$, of all the events that pass the quality cuts. Moreover it is required that the rapidity of the meson is $|y_{gen}| < 0.5$.

The 1D efficiency measured in the simulation can be seen in Figures 3.9-3.10. A check on the dependence of the efficiency on the multiplicity classes is also performed shown in Figures 3.11-3.12. The uncertainty in $\varepsilon(p_{\mathrm{T}})$ is calculated using the Binomial statistics approach described in [183]. The standard deviation in an efficiency ε = k/n, where the numerator k is a subset of the denominator n, is

$$\sigma_{\varepsilon}^{2} = \frac{\varepsilon(1-\varepsilon)}{n} \tag{3.20}$$

The statistical uncertainty σ_{ε} is added in quadrature with the statistical uncertainty of the uncorrected ϕ yield to give the total statistical uncertainty of the corrected ϕ yield. Its contribution is of similar magnitude with respect to the uncertainty from the signal extraction.

This efficiency can be trivially generalised for the ϕ-meson pair analysis. The numerator now requires that both ϕ mesons are reconstructed in mid-rapidity after applying all track selection and particle identification cuts, and the denominator represents the ϕ-meson pair participants both decay in $\mathrm{K}^{-}\mathrm{K}^{+}$. As we make no further assumption or requirement on the ϕ-meson pair than we would on two separate ϕ mesons, we do not expect any (anti-)correlation effects, nor we expected this efficiency to be any different than the square of the single ϕ meson. With this assumption in mind, we can define the ϕ-meson pair efficiency × acceptance as:

$$\varepsilon(p_{\mathrm{T}1}, p_{\mathrm{T}2}) = \varepsilon(p_{\mathrm{T}1})\varepsilon(p_{\mathrm{T}2}) \tag{3.21}$$

where $p_{\mathrm{T}i}$ represents the transverse momentum of the i-component of the pair. A comparison between the efficiency measured in the simulation (Eq. 3.19) generalised to the 2D case and the one derived from the 1D efficiency (Eq. 3.21) can be seen in Figure 3.13, 3.14. The two methods are equivalent within uncertainties, validating

---

[4] Anchored productions are done considering all the features of the detector at the time of data taking. It is used to calculate acceptance and efficiency as it reproduces closely the recorded detector behaviour, for example taking into account possible temporary dead zones or different gas mixtures.

our previous assumption, with the latter greatly improving the uncertainty propagated to the spectrum. For this reason, Eq. 3.21 is used as the efficiency correction for the 2D transverse momentum spectrum.

For the multiplicity analysis a similar assumption is made, for which the efficiency and acceptance correction should be independent of the multiplicity selection. The multiplicity selection indicates the event sample to analyse: this does not affect the acceptance and is not expected to have a significant impact on the detectors efficiency. A comparison to validate this assumption can be found in Figure **??**, where all the curves are compatible within uncertainty. The inclusive correction is taken as default as it significantly improves the uncertainty propagated to the spectra. Its contribution is slightly more than an order of magnitude lower with respect to the uncertainty from the signal extraction.

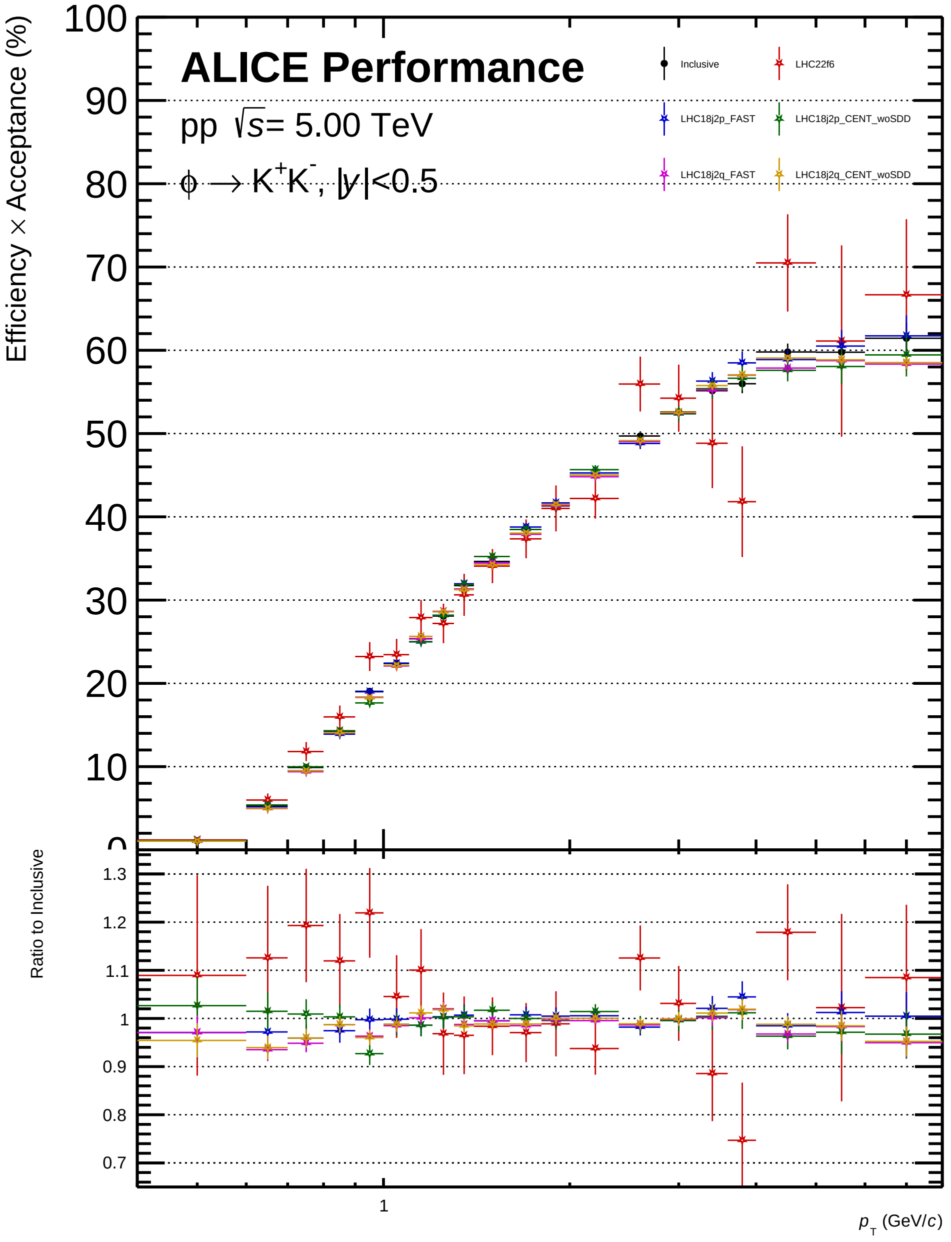

FIGURE 3.9: Efficiency × acceptance as a function of transverse momentum. The colours represent different periods of anchored Monte Carlo production as a test of homogeneity among productions.

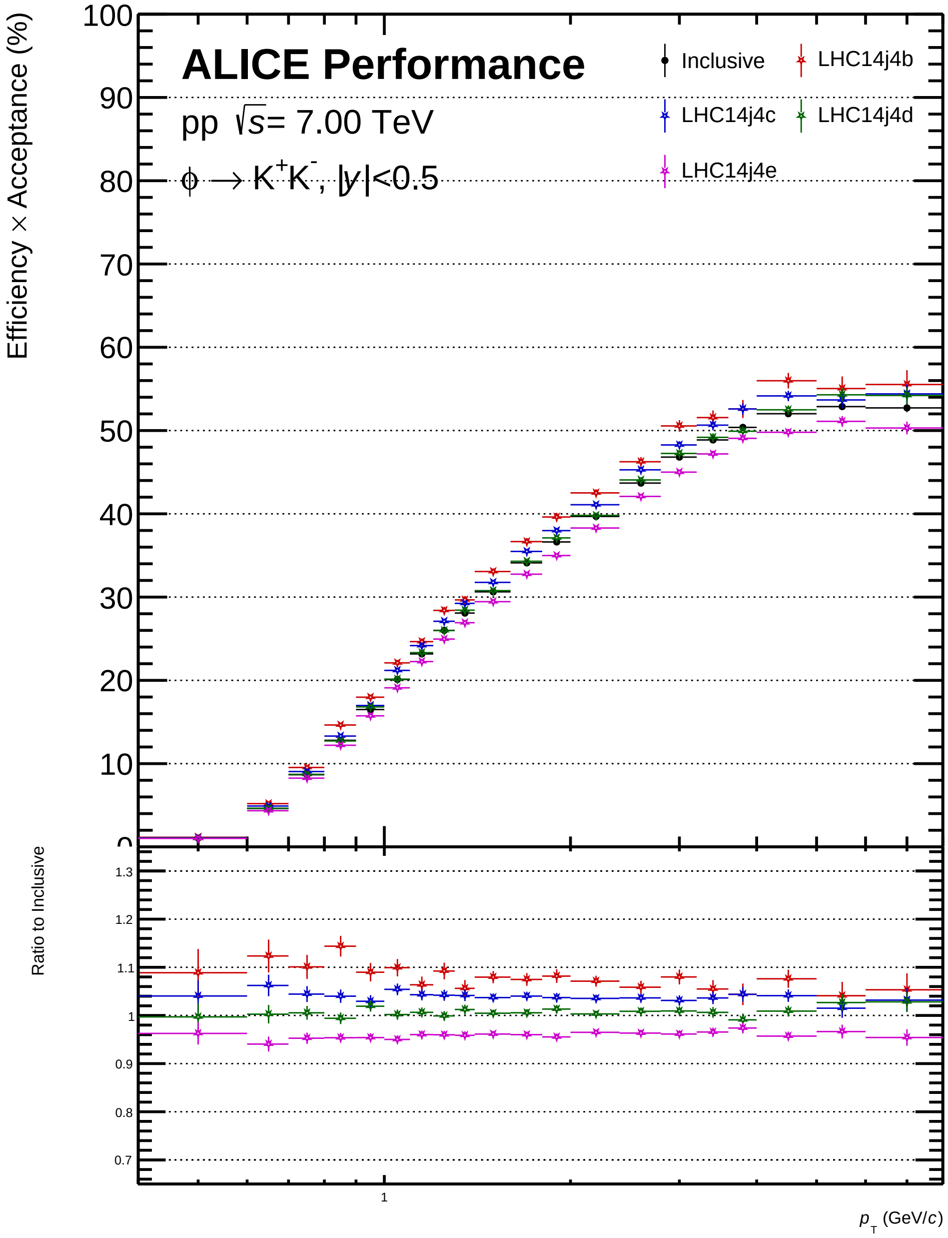

FIGURE 3.10: Efficiency × acceptance as a function of transverse momentum. The colours represent different periods of anchored Monte Carlo production as a test of homogeneity among productions.

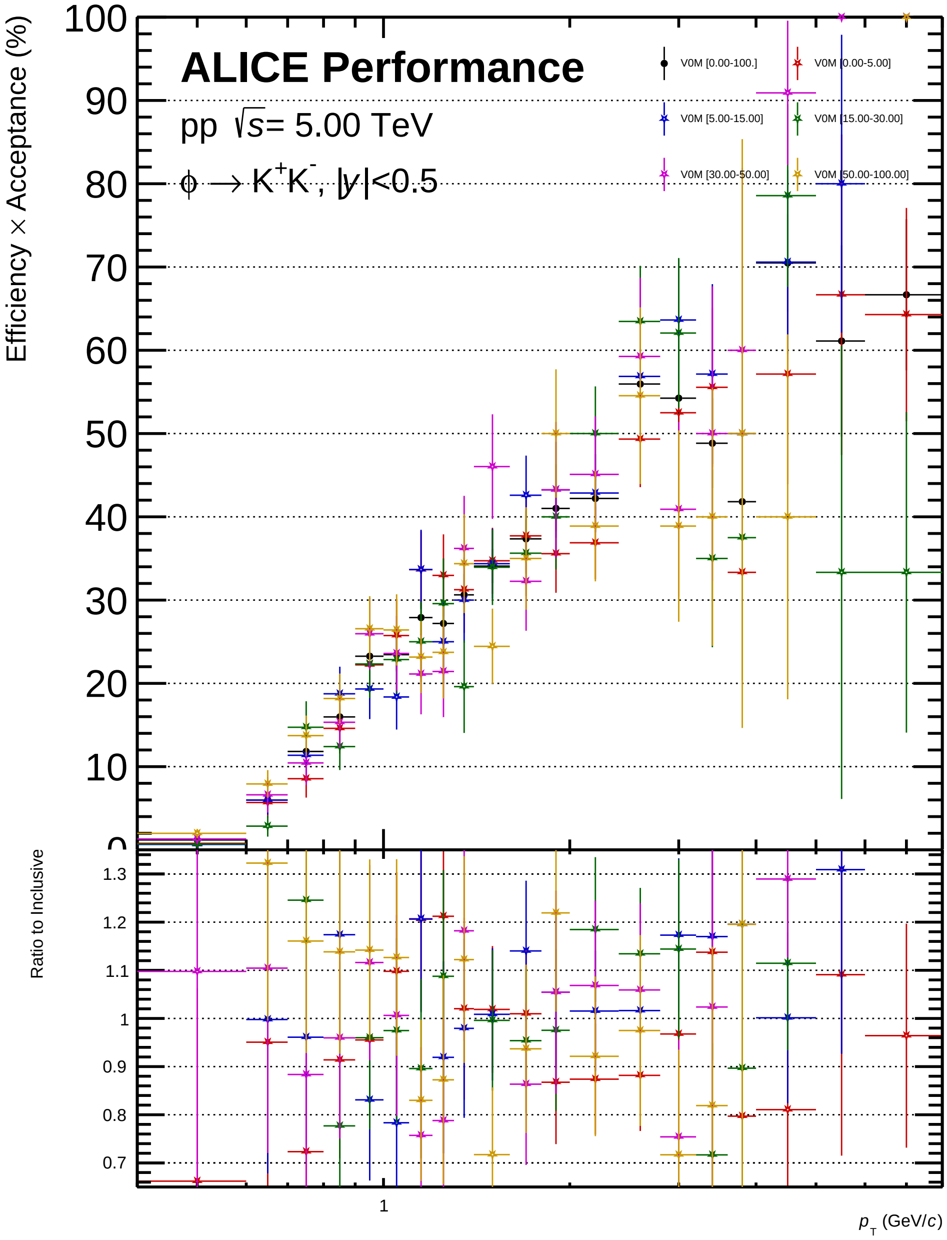

FIGURE 3.11: Efficiency × acceptance as a function of transverse momentum. The colours represent different multiplicity classe of V0M estimator as a test of homogeneity among classes.

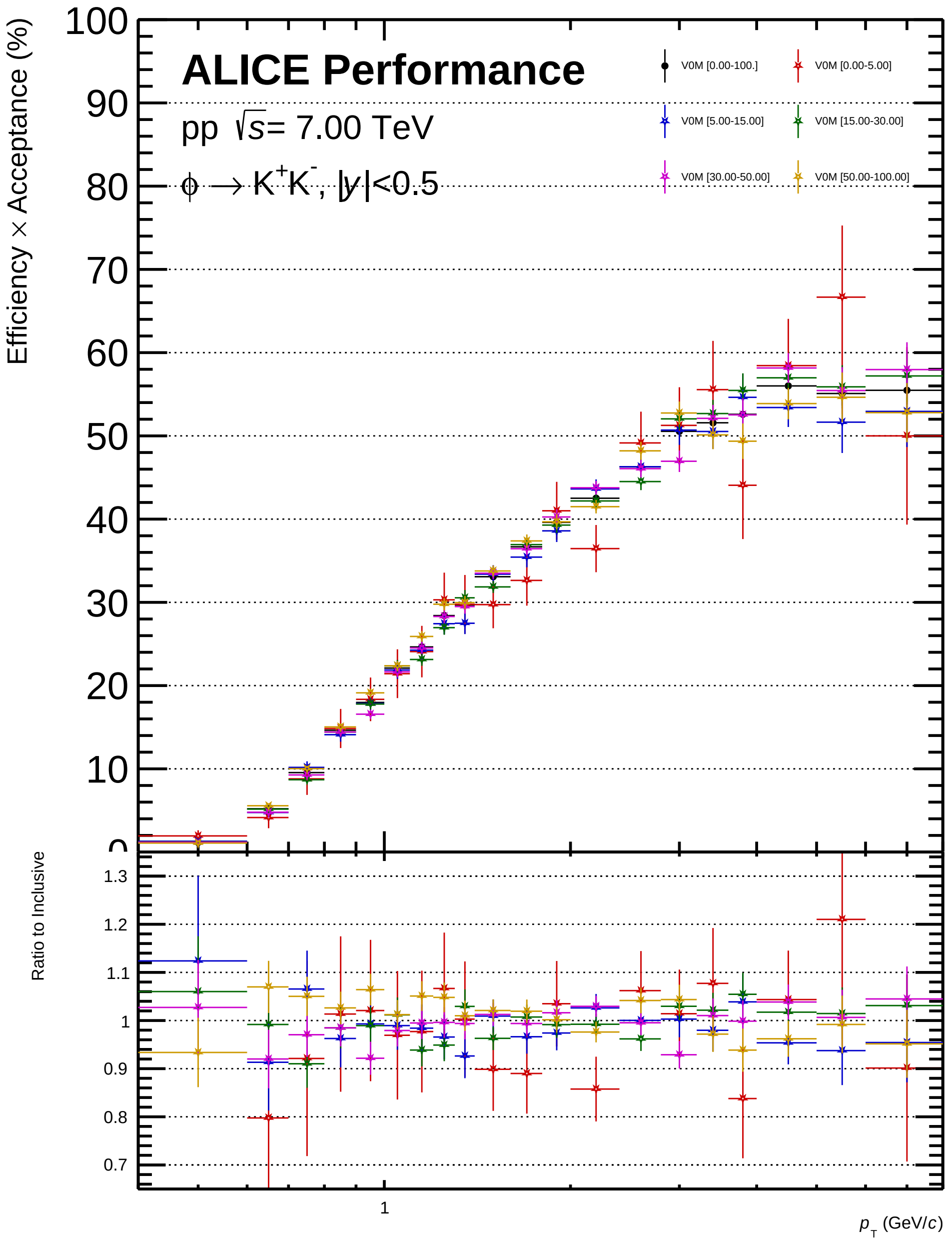

FIGURE 3.12: Efficiency × acceptance as a function of transverse momentum. The colours represent different multiplicity classe of V0M estimator as a test of homogeneity among classes.

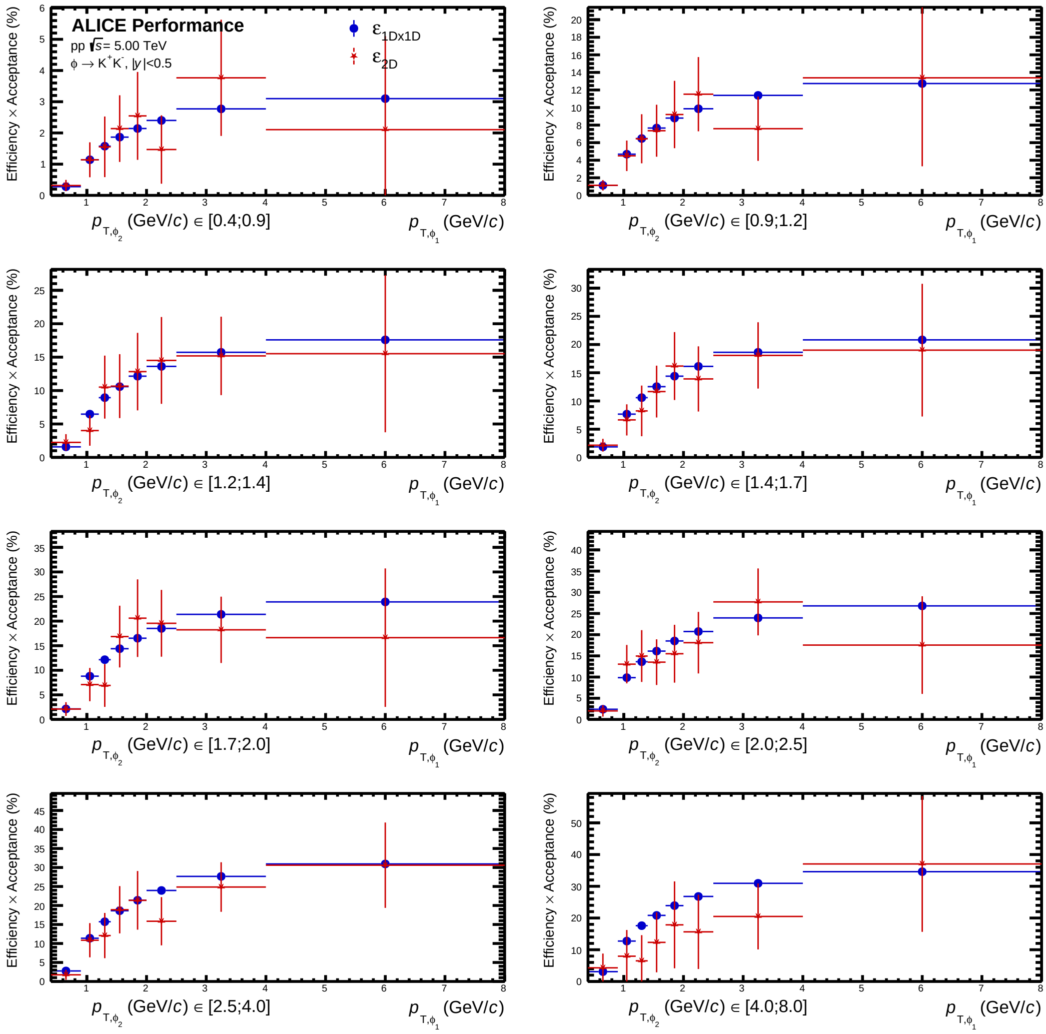

FIGURE 3.13: Efficiency × acceptance as a function of transverse momentum. The colours represent different periods of anchored Monte Carlo production as a test of homogeneity among productions.

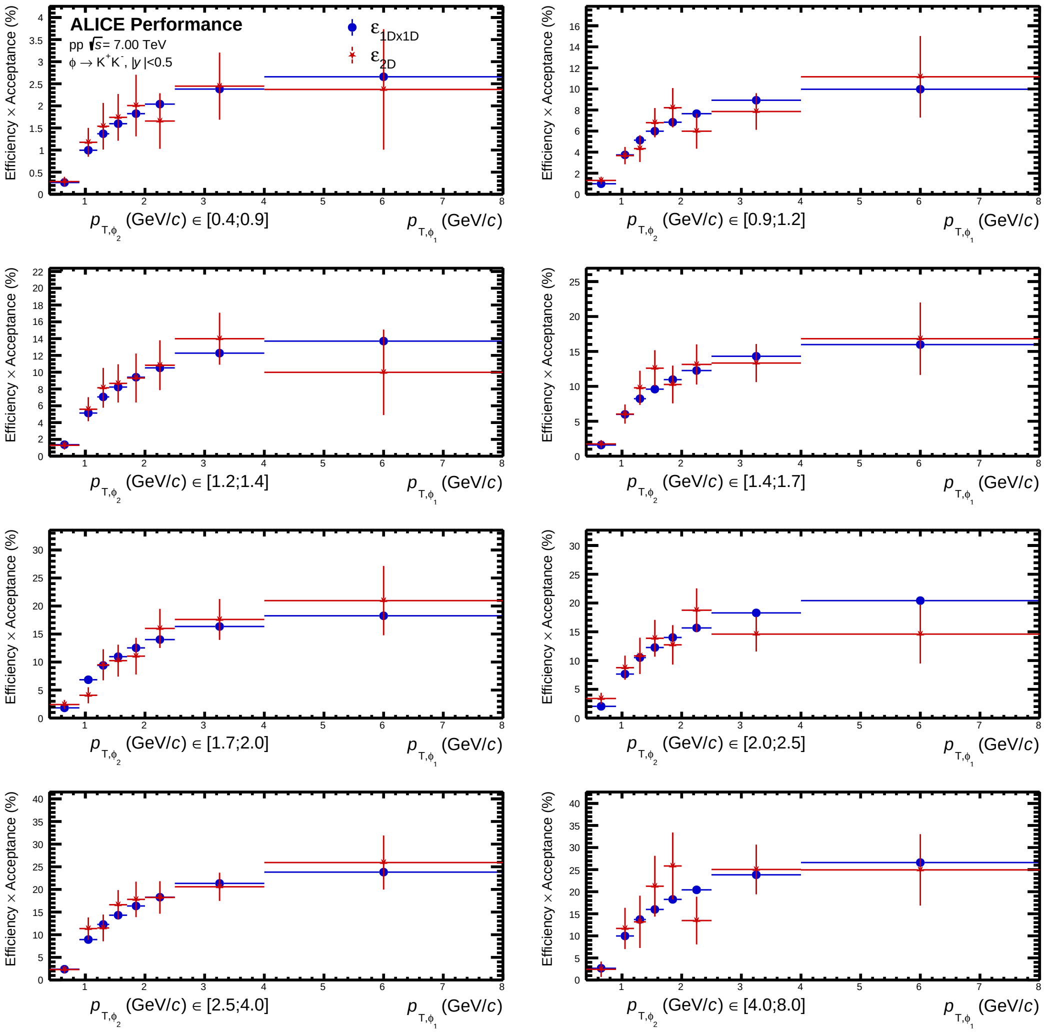

FIGURE 3.14: Efficiency × acceptance as a function of transverse momentum. The colours represent different periods of anchored Monte Carlo production as a test of homogeneity among productions.

3.5.2 Signal Loss

The Signal Loss correction (f_{SL}) takes into account the amount of ϕ mesons or ϕ-meson pairs lost due to the trigger selection, which selects only a part of the total inelastic interactions. In this section, all quantities are considered with a vertex within $|v_z| < 10\mathrm{cm}$. Furthermore, we are only considering ϕ mesons decaying in $\mathrm{K^-K^+}$generated at mid-rapidity $|y_{gen}| < 0.5$.

To understand the impact of the trigger selection, we devise the ratio:

$$f_{\mathrm{SL}}(p_{\mathrm{T}}) = \frac{\mathrm{N}^{gen*}}{\mathrm{N}^{gen}} - 1 \tag{3.22}$$

We already defined $\mathbf{N}^{gen}$ as the number of ϕ mesons that are generated in the Monte Carlo in events passing the quality cuts. $\mathbf{N}^{gen*}$ is then the number of ϕ mesons that are generated in the Monte Carlo in all events.

The f_{SL} is expected to be zero when no correction is present and greater than zero if a correction is needed. The correction is essentially the inverse of the trigger efficiency for ϕ mesons minus 1.

Figures 3.15-3.16 shows the signal loss correction for the 1D analysis whereas Figures 3.17-3.18 shows the Signal Loss correction for the 2D analysis. A comparison with 2D signal loss reconstruction from the 1D analysis, in a similar fashion to what was done in Eq. 3.21, is also shown. The estimation of signal lost, about 0.5-1% is low compared to the systematic uncertainty in the same low-p_{T} bins, of about 5-10% (Figg. 3.15-3.16-3.25). That being the case the correction is not considered.

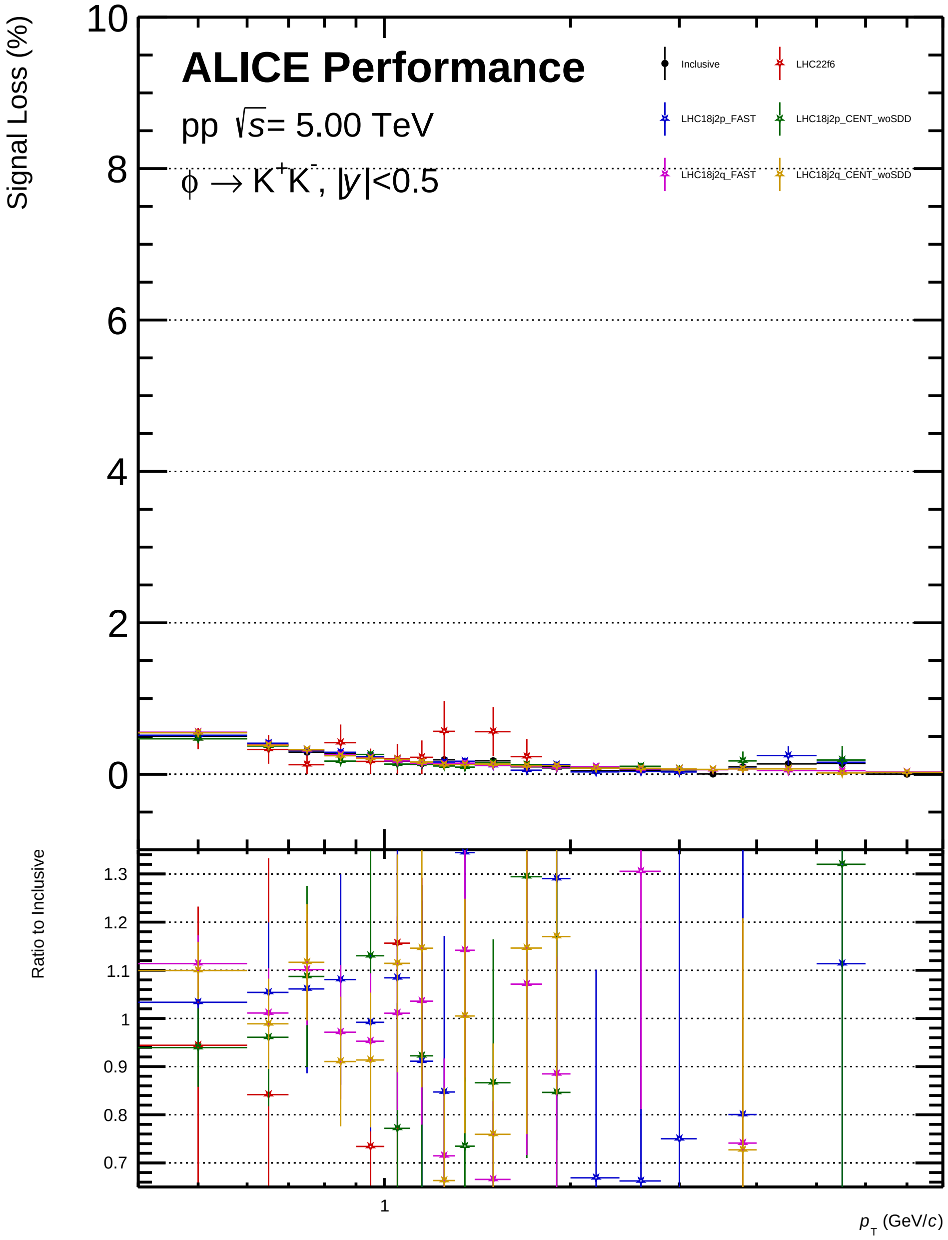

FIGURE 3.15: Signal loss as a function of transverse momentum. The colours represent different periods of anchored Monte Carlo production as a test of homogeneity among productions.

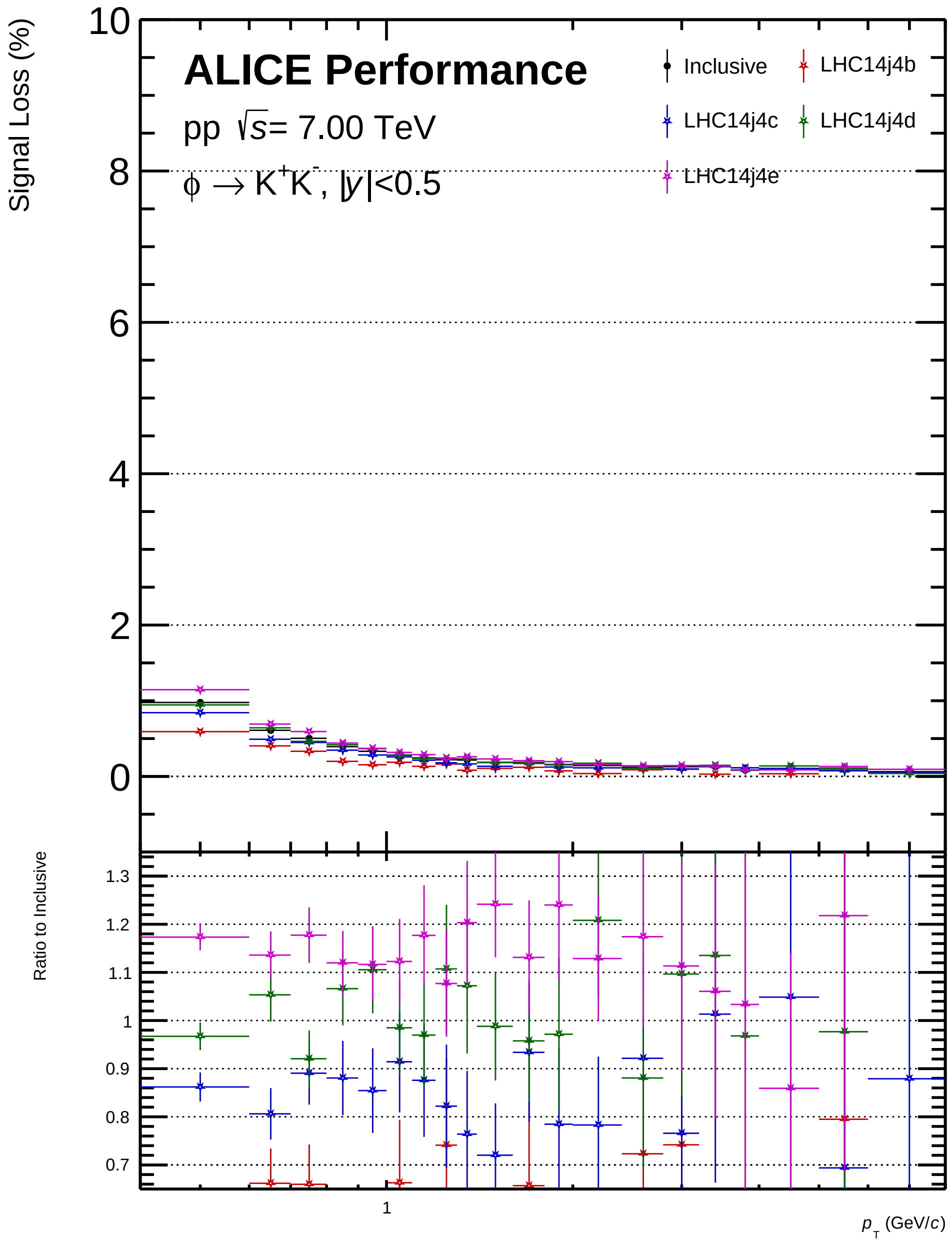

FIGURE 3.16: Signal loss as a function of transverse momentum. The colours represent different periods of anchored Monte Carlo production as a test of homogeneity among productions.

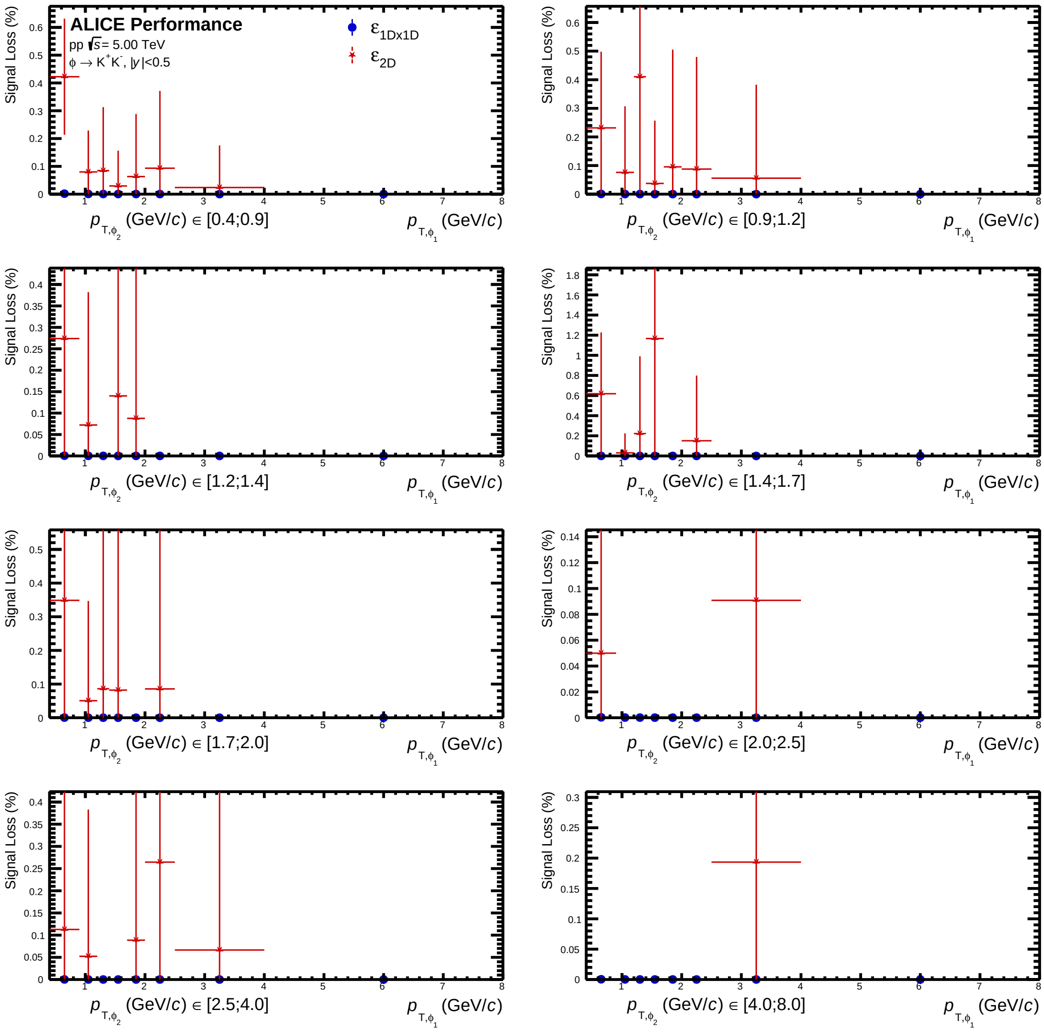

FIGURE 3.17: Signal loss as a function of transverse momentum. The colours represent different periods of anchored Monte Carlo production as a test of homogeneity among productions.

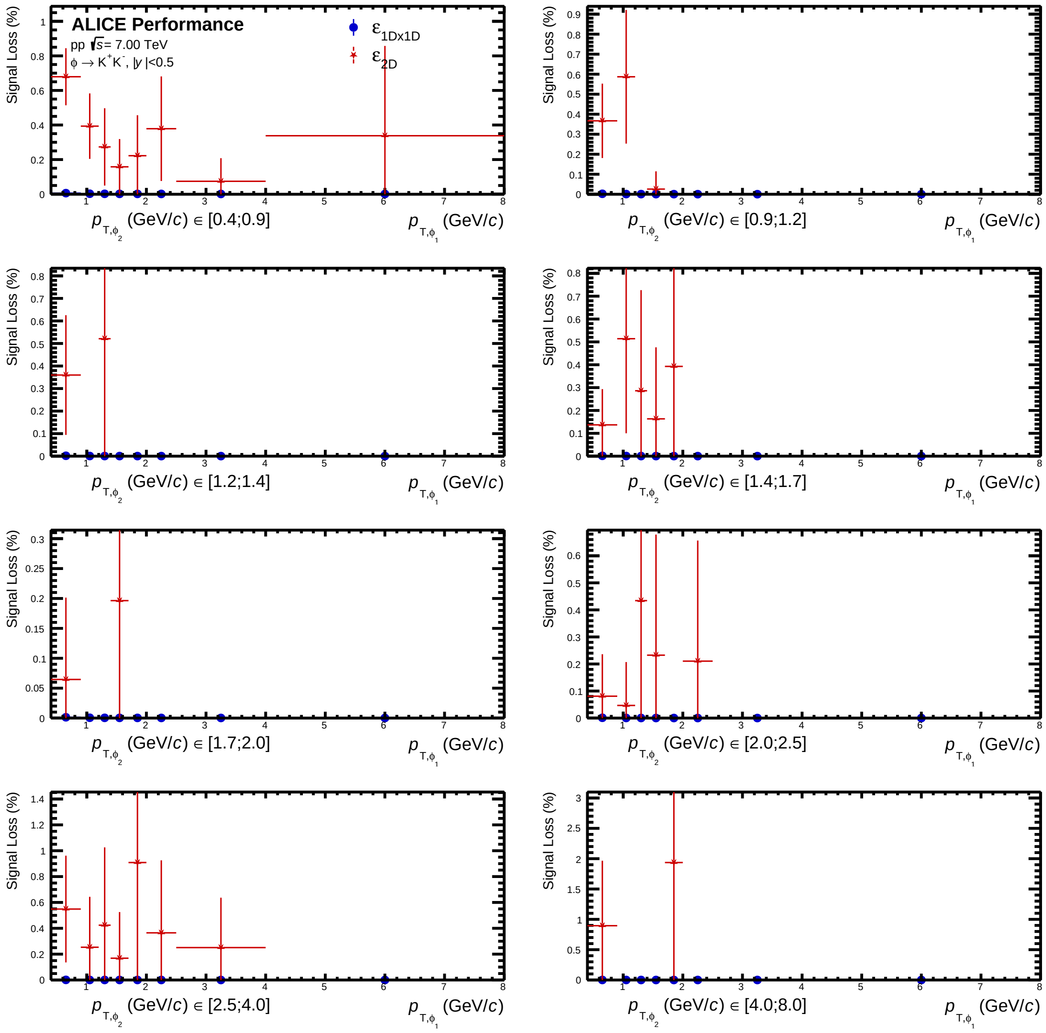

FIGURE 3.18: Signal loss as a function of transverse momentum. The colours represent different periods of anchored Monte Carlo production as a test of homogeneity among productions.

3.5.3 Mass resolution

A useful measurement that can be performed using the Monte Carlo reconstruction is the mass resolution. This quantity can be extracted from the distribution $\Delta \mathrm{m} = \mathrm{m_{rec}} - \mathrm{m_{gen}}$, where $\mathrm{m_{rec}}$ is the mass of the reconstructed ϕ-meson and $\mathrm{m_{gen}}$ is the mass of the generated ϕ-meson, and from the invariant-mass distribution of $\mathrm{m_{rec}}$. An example of such distributions can be seen in Figure 3.20.

These two distributions provide a number of ways to measure the mass resolution so as to fix this parameter in the signal extraction procedure. The three methods that will be considered in this analysis are:

- σ_h The resolution is extracted fitting a Voigtian function to the invariant mass distribution in the Monte Carlo dataset, fixing mass and width.[5]
- σ_c The resolution is taken as the RMS of the mass difference distribution truncated at 3σ
- σ_l The resolution is taken as the σ of the Gauss fit of the difference distribution truncated at 2σ

The results for these three methods are shown in Figure 3.20. The (σ_c) will be used as the default value, the others are used to evaluate the uncertainty on the resolution. The relative deviation of the variations can be seen in the bottom part of figure 3.20. Given the deviations are roughly constant on average and this behaviour is seen for both the low and high estimation we can take a constant 10% systematic error for the resolution, as a conservative approach.

---

[5] The width and mass are fixed to the value of a fit on the generated invariant mass. Moreover the mass is shifted through the p_{T} bins using the mean of the rec-true histogram.

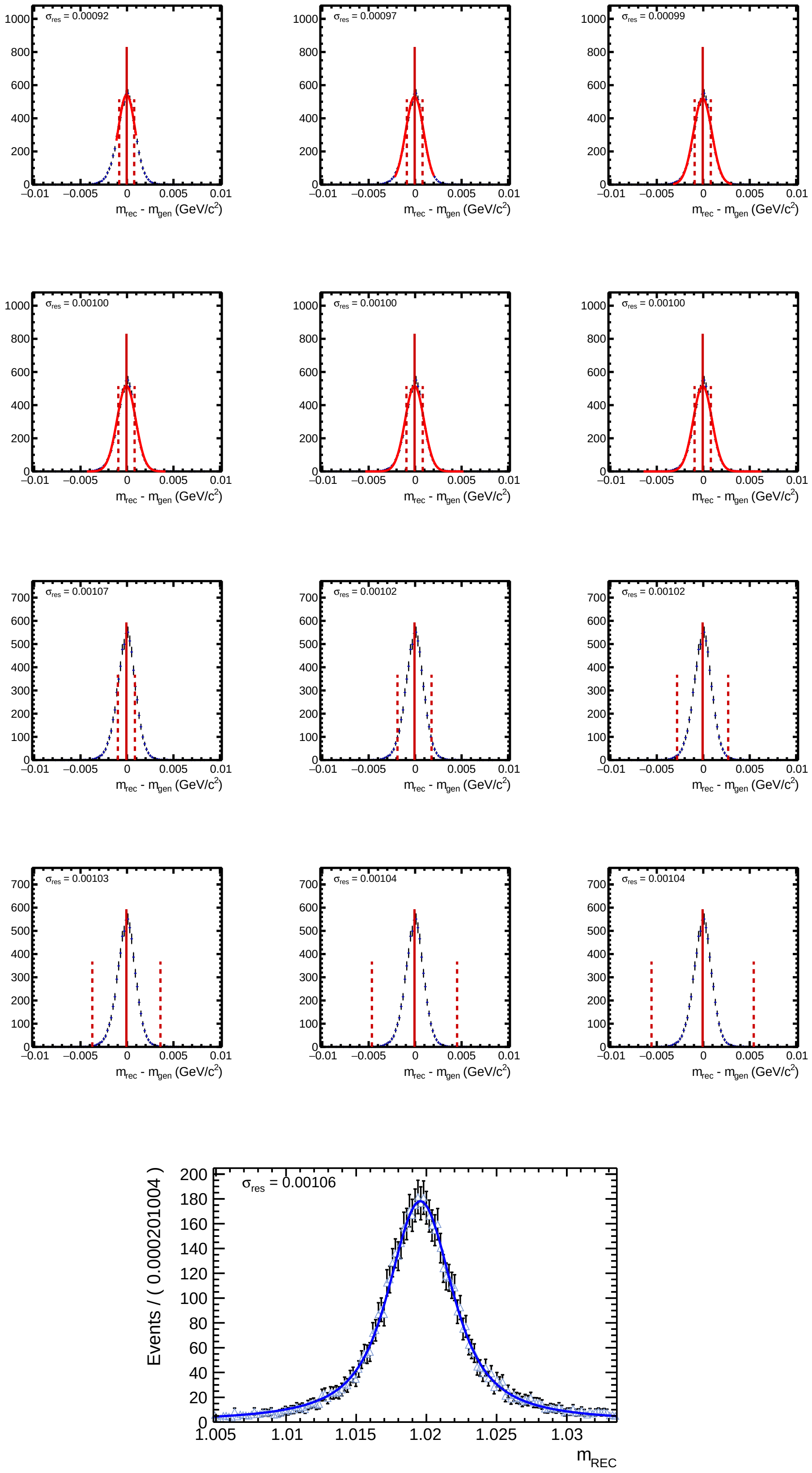

FIGURE 3.19: The invariant mass resolution measurement methods. (top) gaussian fit in all considered ranges, (middle) RMS within all considered ranges, (bottom) fit on (simulated) reconstructed invariant mass. pp collision at $\sqrt{s} = 5.02$ TeV.

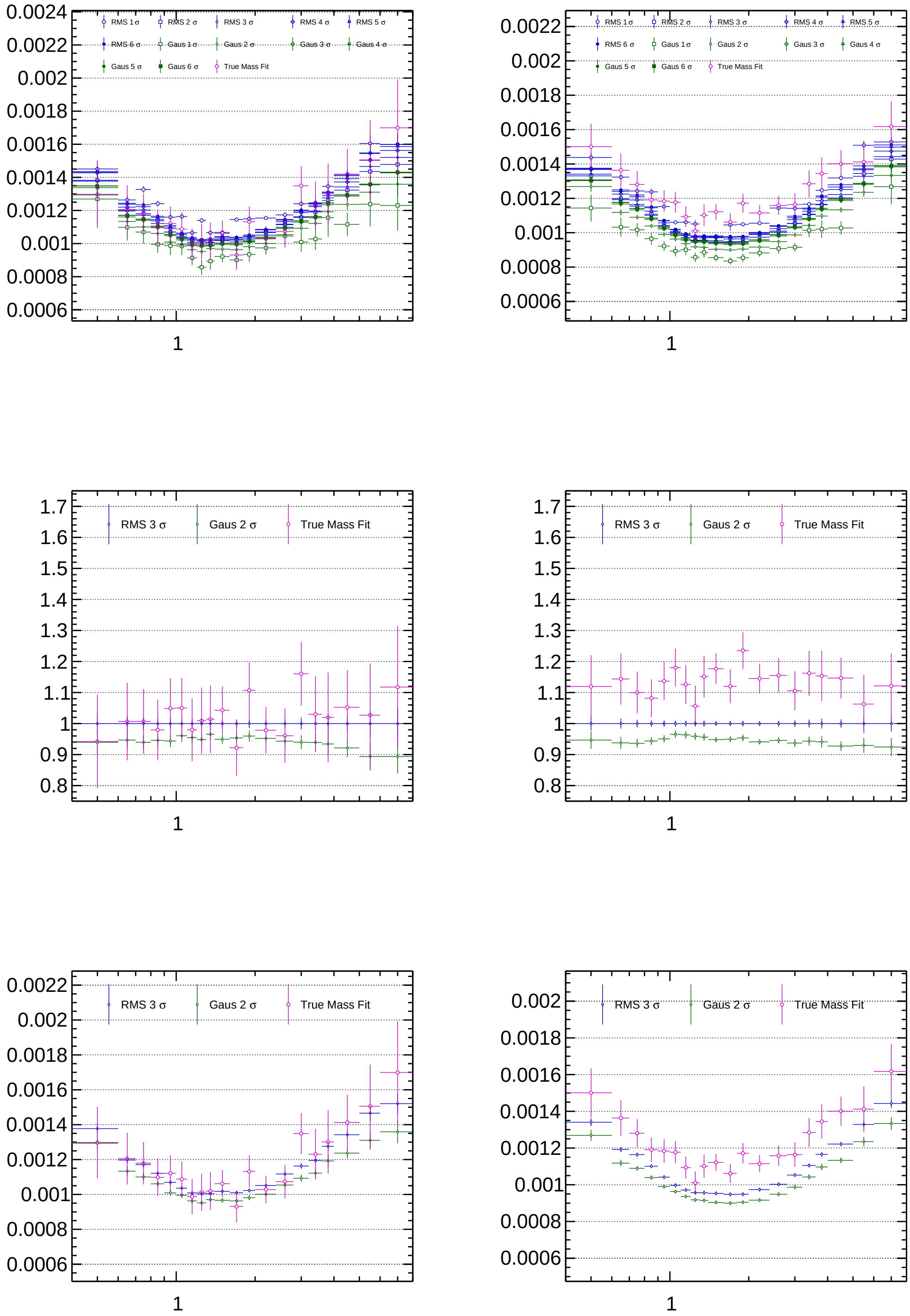

FIGURE 3.20: The invariant mass resolution as a function of transverse momentum in absolute terms with all variations (top), only considered variations (center) and normalised to default option (bottom). On the left is the pp collision at $\sqrt{s} = 5.02$ TeV, on the right is the pp collision at $\sqrt{s} = 7$ TeV.

3.6 Normalisation

After the signal extraction with the invariant mass technique we have now p_{T} spectra for both ϕ mesons and ϕ-meson pairs. On top of the mentioned Acceptance × Efficiency (ε) correction a number of other factors go into calculating the corrected spectra.

3.6.1 Inclusive analysis

The corrections applied to the p_{T} spectra for the 1D (Eq. 3.23) and for the 2D (Eq. 3.24) analysis are:

$$\frac{\mathrm{dN}^2_{\phi}}{\mathrm{d}p_{\mathrm{T}}\mathrm{d}y} = \frac{\mathrm{N}^{\mathrm{raw}}_{\phi}}{\Delta p_{\mathrm{T}}\Delta y}\frac{1}{\varepsilon(p_{\mathrm{T}})\mathrm{BR}}\frac{\varepsilon_{\mathrm{trg}}\varepsilon_{\mathrm{vtx}}}{\mathrm{N}_{\mathrm{evs}}} \tag{3.23}$$

$$\frac{\mathrm{dN}^3_{\phi\phi}}{\mathrm{d}p_{\mathrm{T}1}\mathrm{d}p_{\mathrm{T}2}\mathrm{d}y} = \frac{\mathrm{N}^{\mathrm{raw}}_{\phi\phi}}{\Delta p_{\mathrm{T}1}\Delta p_{\mathrm{T}2}\Delta y}\frac{1}{\varepsilon(p_{\mathrm{T}1},p_{\mathrm{T}2})\mathrm{BR}^2}\frac{\varepsilon_{\mathrm{trg}}\varepsilon_{\mathrm{vtx}}}{\mathrm{N}_{\mathrm{evs}}} \tag{3.24}$$

$\mathrm{N}^{\mathrm{raw}}_{\phi(\phi)}$ How many ϕ mesons (pairs) are found from the invariant mass fit, corrected for the integral signal loss (Sec. 3.4.1).

$p_{\mathrm{T}(i)}$ p_{T} (relative to the i-component of the pair)

$\Delta p_{\mathrm{T}(i)}$ p_{T} bin width (relative to the i-component of the pair)

Δy Rapidity bin width, in mid-rapidity is 1 ($-0.5 < y < 0.5$).

ε Efficiency × Acceptance correction (Sec. 3.5).

BR Branching ratio for the $\phi \rightarrow \mathrm{K}^-\mathrm{K}^+$decay (BR = 49.2 ± 0.5 %) [1].

$\varepsilon_{\mathrm{trg}}$ Trigger Efficiency [184–186]

$\sqrt{s} = 7$ TeV $\varepsilon_{\mathrm{trg}} = 85.2^{+6.2}_{-3.0}$ %

$\sqrt{s} = 5.02$ TeV $\varepsilon_{\mathrm{trg}} = 75.7 \pm 1.5\%$

$\varepsilon_{\mathrm{vtx}}$ Ratio between the number of triggered events not flagged as pileup and with complete DAQ and the number of events for which a good vertex was found, without the cut on the vertex position.

$\mathrm{N}_{\mathrm{evs}}$ Number of events after all selections.

3.6.2 Multiplicity analysis

The corrections applied to the p_{T} spectra for the 1D (Eq. 3.25) and for the 2D (Eq. 3.26) analysis are:

$$\frac{\mathrm{dN}^2_{\phi}}{\mathrm{d}p_{\mathrm{T}}\mathrm{d}y} = \frac{\mathrm{N}^{\mathrm{raw}}_{\phi}}{\Delta p_{\mathrm{T}}\Delta y}\frac{1}{\varepsilon(p_{\mathrm{T}})\mathrm{BR}}\frac{\varepsilon_{\mathrm{V0M}}}{\mathrm{N}_{\mathrm{evs}}|_{\mathrm{V0M}}} \tag{3.25}$$

$$\frac{\mathrm{dN}^3_{\phi\phi}}{\mathrm{d}p_{\mathrm{T}1}\mathrm{d}p_{\mathrm{T}2}\mathrm{d}y} = \frac{\mathrm{N}^{\mathrm{raw}}_{\phi\phi}}{\Delta p_{\mathrm{T}1}\Delta p_{\mathrm{T}2}\Delta y}\frac{1}{\varepsilon(p_{\mathrm{T}1},p_{\mathrm{T}2})\mathrm{BR}^2}\frac{\varepsilon_{\mathrm{V0M}}}{\mathrm{N}_{\mathrm{evs}}|_{\mathrm{V0M}}} \tag{3.26}$$

$\varepsilon_{\mathrm{V0M}}$ Number of events in the V0M class.

$N_{\mathrm{evs}}|_{\mathrm{V0M}}$ Efficiency of event selection in the V0M class [6].

All others are defined above.

---

[6] The selection in V0M takes the signal amplitude in the V0A and V0C and divides the events in percentiles, where the 0-1% are the 1% most central (high-multiplicity in pp) events and the 99-100% are the 1% most peripheral (low-multiplicity in pp) events

3.7 Signal Extrapolation

After the signal extraction procedure (Sec. 3.4) and subsequent corrections (Sec. 3.5 - 3.6) we are left with incomplete spectra for both ϕ meson and ϕ-meson pairs: the measurement is performed in the p_{T} range [0.40,8.0] GeV/c for both.

To have a full measurement of the yields, i.e. integrated over the full p_{T} range, we must extrapolate in the low and high p_{T} region. The extrapolation procedure is performed by fitting the full available spectrum with a given function and then integrating the function in the low-p_{T} ([0.0,0.4] GeV/c). The high-p_{T} ([8.00,+∞] GeV/c) contribution is negligible.

The presented analysis makes use of the Lévy-Tsallis function [187]. This function has been extensively used within the ALICE Collaboration [59, 65, 67, 155, 185, 188–190] and previously at RHIC [191]. The functional form describes the shape of the exponential spectra at low transverse momentum and the power law distributions at large p_{T} with an inverse slope parameter T and an exponent parameter n.

$$f_{\text{Lévy}} = \frac{\mathrm{dN}_{\phi}}{\mathrm{d}y}\frac{(n-1)(n-2)}{nT(nT+m(n-2))}p_{\mathrm{T}}\left(1+\frac{m_T-m}{nT}\right)^{-n} \tag{3.27}$$

m is the ϕ-meson mass.

m_T is the ϕ-meson transverse mass, defined as $\sqrt{m^2+p_{\mathrm{T}}^2}$.

T, n are the inverse slope parameter and the exponent parameter respectively

$\mathrm{dN}_{\phi}/\mathrm{d}y$ is the differential yield in rapidity unit.

In Table 3.2 a summary of the extrapolated yields for the inclusive ϕ meson and ϕ-meson pair for the pp at $\sqrt{s} = 7$ TeV is reported. The 1D analysis has approximately 14% of extrapolated yield, whereas the 2D case increases this fraction to 20%. In the pp at $\sqrt{s} = 5.02$ TeV inclusive and multiplicity dependent analysis the extrapolation fraction is comparable.

3.7.1 Uncertainty estimation

The uncertainty estimation of the extrapolated quantities consists in calculating the portion of uncertainty determined by the statistical or systematical fluctuations of data points. To this end, we resort to a numerical approach rather than a theoretical one. The spectrum is first considered with only the statistical (systematical) uncertainty. After, we generate a random value for each point, following a normal distribution with the point value as average and the point uncertainty as standard deviation. Every datapoint is then independently shifted by the calculated offset. The systematical (statistical) uncertainty is then combined for every point, meaning the spectrum now has the full uncertainty (square sum of statistical and systematical uncertainty). Now, the spectrum is ready for the extrapolation to be repeated. This mechanism is repeated a number of times (in this analysis 500 times) until the histogram containing the results of all repetitions of this procedure can now be used to assign the statistical (systematical) uncertainty to the extrapolated quantity.

There is an additional systematic uncertainty to apply on the measured extrapolated yield. In fact the choice of the Lévy-Tsallis function is arbitrary, and so a set of different functions is used to extrapolate the yield and used as a systematic uncertainty. Moreover, the fit range changes the extrapolated yield value, so different fit ranges are also considered.

The functions used for the systematic evaluation are taken from a pool of commonly used extrapolation functions [152]:

Lévy-Tsallis function fitted from $0.4\,\mathrm{GeV}/c$ up to 1.5, 2.0 and $4.0\,\mathrm{GeV}/c$

$$f_{\text{Lévy}} = \frac{\mathrm{dN}_{\phi}}{\mathrm{d}y}\frac{(n-1)(n-2)}{nT(nT+m(n-2))}p_{\mathrm{T}}\left(1+\frac{m_T-m}{nT}\right)^{-n} \tag{3.28}$$

$\mathbf{M_T}$-Exponential fitted from $0.4\,\mathrm{GeV}/c$ up to 1.5, 2.0 and $4.0\,\mathrm{GeV}/c$

$$f_{\text{Mexp}} = \frac{\mathrm{dN}_{\phi}}{\mathrm{d}y}p_{\mathrm{T}}\frac{\exp\left(\frac{m-m_{\mathrm{T}}}{\mathrm{T}}\right)}{\mathrm{T}\Big(\mathrm{T}+m\Big)} \tag{3.29}$$

Boltzmann fitted from $0.4\,\mathrm{GeV}/c$ up to 1.5, 2.0 and $4.0\,\mathrm{GeV}/c$

$$f_{\text{Boltz}} = \frac{\mathrm{dN}_{\phi}}{\mathrm{d}y}p_{\mathrm{T}}m_{\mathrm{T}}\frac{\exp\left(\frac{m-m_{\mathrm{T}}}{\mathrm{T}}\right)}{\mathrm{T}\Big(2\mathrm{T}^2+2m\mathrm{T}+m^2\Big)} \tag{3.30}$$

Bose-Einstein fitted from $0.4\,\mathrm{GeV}/c$ up to 1.5, 2.0 and $4.0\,\mathrm{GeV}/c$

$$f_{\text{B-E}} = \frac{\mathrm{dN}_{\phi}}{\mathrm{d}y}p_{\mathrm{T}}\frac{\exp\left(\frac{m}{\mathrm{T}}\right)-1}{\exp\left(\frac{m_{\mathrm{T}}}{\mathrm{T}}\right)-1} \tag{3.31}$$

The extrapolation uncertainty evaluation is shown in Figure 3.22.

3.7.2 Average transverse momentum

Average transverse momentum $\langle p_{\mathrm{T}}\rangle$ of the spectra is calculated as follows:

1. The $\langle p_{\mathrm{T}}\rangle$ of the un-measured region is calculated thorugh the chosen extrapolation function:

$$\mathrm{F} \equiv \int\limits_{0.0}^{0.4}\mathrm{f}(\mathrm{p_T})\mathrm{dp_T} \qquad \langle\mathrm{p_T}\rangle\Big|_{0.0}^{0.4} \equiv \frac{1}{\mathrm{F}}\int\limits_{0.0}^{0.4}\mathrm{f}(\mathrm{p_T})\mathrm{p_T}\mathrm{dp_T} \tag{3.32}$$

   where f is the function used for the extrapolation process, and p_{T} is the average transverse momentum.

2. The $\langle p_{\mathrm{T}}\rangle$ of the measured region is calculate through a weighted mean over the histogram bins:

$$\mathrm{I} \equiv \sum_{\mathrm{i}=1}^{\mathrm{n_{bins}}}\mathrm{H(i)W(i)} \qquad \langle\mathrm{p_T}\rangle\Big|_{0.4}^{8.0} \equiv \frac{1}{\mathrm{I}}\sum_{\mathrm{i}=1}^{\mathrm{n_{bins}}}\mathrm{H(i)W(i)C(i)} \tag{3.33}$$

   where i runs on all bins, H(i) is the i-bin content, W(i) is the i-bin width, C(i) is the i-bin center.

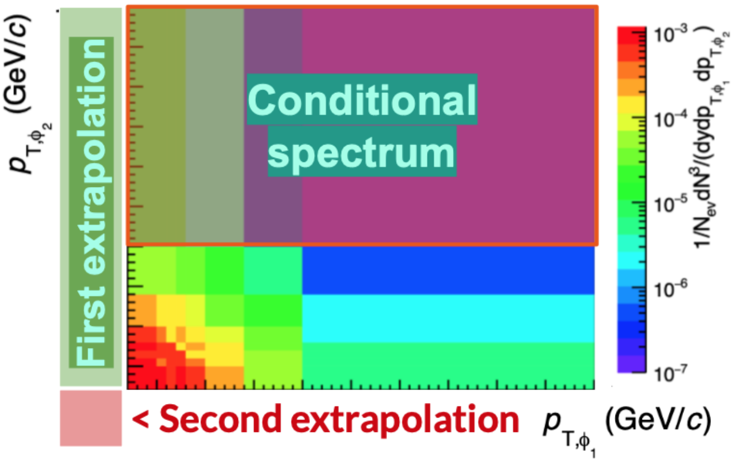

FIGURE 3.21: Schematic representation of the extrapolation methodology for the 2D ϕ-meson pair p_T spectrum.

3. The $\langle p_T \rangle$ of the two regions are averaged together, with the corresponding weight:

$$\langle p_T \rangle = \frac{\mathrm{F}\langle \mathrm{p_T} \rangle|_{0.0}^{0.4} + \mathrm{I}\langle \mathrm{p_T} \rangle|_{0.4}^{8.0}}{\mathrm{F} + \mathrm{I}} \tag{3.34}$$

3.7.3 Extrapolation of ϕ-meson yield

The extrapolation for the ϕ-meson yield is performed by fitting the full spectrum with a Lévy-Tsallis function and then integrating the function in the low-p_T ([0.0,0.4] GeV/c).

3.7.4 Extrapolation of ϕ-meson pairs yield

The extrapolation for the ϕ-meson pair spectrum is performed by slicing the 2-Dimensional p_T -spectrum in each p_T bin along one of the axes. These conditional spectra represent the p_T spectrum of a ϕ meson produced with another ϕ meson with a given p_T . One of these spectra is highlighted in the upper part of Fig. 3.21. Then the extrapolated yield measured in all these conditional spectra is combined to build a conditional spectrum for down to 0 p_T ϕ-mesons pairs, this is labeled as the first extrapolation. One can then see that, given the symmetry of the yield, the only range missing is the down to 0 p_T point for both ϕ-mesons, in our analysis [0.0,0.4,0.0,0.4] GeV/c. This is measured extrapolating the spectrum composed from the extrapolations of the measured yield.

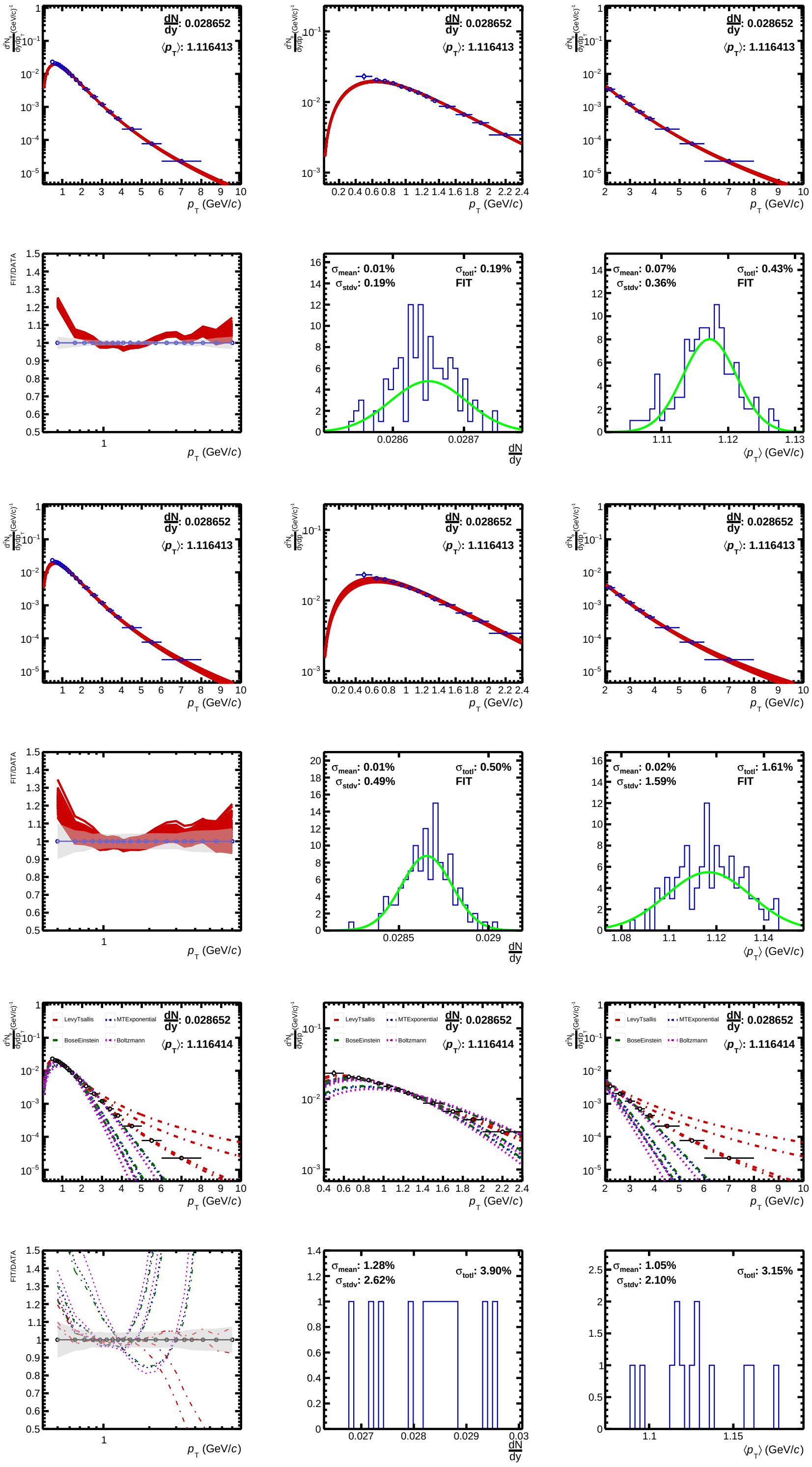

FIGURE 3.22: Summary of the extrapolation process uncertainty evaluation for the 1D spectrum. Statistical point fluctuations (top 2 rows), systematical point fluctuations (center 2 rows) and extrapolation systematics (bottom 2 rows). In each set of histograms there is the cumulative fits performed (top left) with a focus on low (top center) and high (top right) p_{T} regions and ratio to data (bottom left) with variations for yield (bottom center) and mean p_{T} (bottom right).

	$p_{T_{\phi_1}}$	dN_{full}/dy ($\times 10^3$)	dN_{ext}/dy ($\times 10^3$)	Fraction
1D	Full	32.121	4.465	13.9%
2D	[0.0;0.4]	0.958	0.128	13.4%
	[0.4;0.9]	1.839	0.210	11.4%
	[0.9;1.2]	1.573	0.197	12.5%
	[1.2;1.4]	1.066	0.130	12.2%
	[1.4;1.7]	1.070	0.141	13.2%
	[1.7;2.0]	0.706	0.090	12.8%
	[2.0;2.5]	0.414	0.047	11.3%
	[2.5;4.0]	0.140	0.013	9.3%
	[4.0;8.0]	0.016	0.001	8.5%
	Full	1.450	0.295	20.3%

TABLE 3.2: Summary of extrapolation fractions for each spectrum for the pp $\sqrt{s} = 7$ TeV.

3.8 Systematical uncertainties

Various classes of systematic uncertainties related to the presented measurement have been considered and are explained in details in the following sections. The classes that have been considered are:

1. Signal Extraction
2. PID Selection
3. Global Tracking Efficiency
4. Analysis Cuts
5. Material Budget
6. Hadronic Interaction
7. Branching Ratio
8. Signal Extrapolation

3.8.1 Uncertainty classes

Signal extraction, PID selection, track cuts

The signal extraction systematic represents the uncertainty related to the signal and background estimation of the fit on the invariant mass distributions. The PID selection systematic represents the uncertainty related to the PID selection performed to identify tracks as charged kaons. Track cuts systematic represents the error due to the quality cuts applied to the track.

The evaluation process for the systematic uncertainty is to repeat the full analysis on the different datasets (or fit parameters for the signal extraction case) and determine the extent by which the results differ from the standard case. The list of standard cuts, parameters and their variations for systematic checks are reported in Tables 3.3, 3.4 and 3.5.

	Default	**Shorthand**	**Variation**
Fit Range	[0.998 - 1.065]	RA	[0.996 - 1.059]
		RB	[0.996 - 1.062]
		RC	[0.996 - 1.065]
		RD	[0.996 - 1.068]
		RE	[0.996 - 1.071]
		RF	[0.998 - 1.059]
		RG	[0.998 - 1.062]
		RH	[0.998 - 1.068]
		RI	[0.998 - 1.071]
		RJ	[1.000 - 1.059]
		RK	[1.000 - 1.062]
		RL	[1.000 - 1.065]
		RM	[1.000 - 1.068]
		RN	[1.000 - 1.071]
ϕ-meson Mass	Free	N/A	Free
ϕ-meson Width	Fixed 4.249 MeV[1]	WDT	Free
Mass Resolution	Fixed	RSH	Fixed +10%
		RSL	Fixed −10%
Background shape	3°ebyv	DG2	2°ebyv
		DG4	4°ebyv
2D Background shape	Fixed	BKG	Free

TABLE 3.3: List of all Standard Fit conditions with the variations used to establish the systematic uncertainty with their shorthand notation.

	Default	**Shorthand**	**Variation**
Stand alone TPC	$3\sigma_{\text{kaons}}$	`PID1`	$+10\%$
		`PID2`	-10%
Vetoed TPC	$5\sigma_{\text{kaons}}$	`PID3`	$+10\%$
		`PID4`	-10%
TOF veto	$3\sigma_{\text{kaons}}$	`PID5`	$+10\%$
		`PID6`	-10%

TABLE 3.4: List of all Standard PID selections with the variation used to establish the systematic uncertainty

Global Tracking Efficiency, Branching Ratio and Normalisation

The global tracking efficiency represents the uncertainty on the TPC-ITS efficiency of track matching. It is listed as 4% per track in various publications for Run 1 data [64]. The uncertainty is evaluated as an overall 8% for the 1D spectrum and yield and as 16% for the 2D spectra and yield, as it is considered a normalisation uncertainty, that is coherently moving all points up or down by its magnitude. For the Run 2 data a p_{T} -dependent uncertainty is considered from previous analyses and is treated similarly to the material budget and hadronic interaction classes. Branching ratio is treated in a similar way, listed as 1% [1], and normalisation uncertainties are reported in 3.6.

The following discussion on the uncertainty is based on the pp collisions at $\sqrt{s} = 7$ TeV dataset, but it is extended to the pp collisions at $\sqrt{s} = 5.02$ TeV dataset, and will make use of the notation introduced in Section 3.10.

$\langle \mathrm{Y}_{\phi} \rangle$ The uncertainty is assigned directly to the yield:
8% for tracking, 1% for Branching Ratio, $^{+7.3}_{-3.5}\%$ for Normalisation.

$\langle \mathrm{Y}_{\phi\phi} \rangle$ The uncertainty is assigned directly to the yield:
16% for tracking, 2% for Branching Ratio, $^{+7.3}_{-3.5}\%$ for Normalisation.

$\langle \mathrm{Y}_{\phi\phi} \rangle / \langle \mathrm{Y}_{\phi} \rangle$ Several contributions cancel in the ratio: The tracking uncertainty over- (under-)estimate the particle yield. As the effect is the same at the numerator and denominator, the numerator 8% contribution is canceled out in the fraction. The assigned value is then the 8% left as per the denominator.
An equivalent argument can be made for the branching ratio, the assigned value is then 1%.
The normalisation is treated in the same fashion, canceling out completely as it corrects equally the numerator and denominator

$\langle \mathrm{Y}_{\phi\phi} \rangle / \langle \mathrm{Y}_{\phi} \rangle^2$ The elision above hold true again for this ratio, the considered uncertainties are: $^{+7.3}_{-3.5}\%$ for normalisation.

	Default	**Shorthand**	**Variation**
Maximum $\mathrm{DCA_z}$	2	TRK1	0.2
	2	TRK2	1.0
Maximum $\mathrm{DCA_{xy}}$	7σ 0.0182+0.0350/$\mathrm{p_T^{1.01}}$	TRK3	4σ
$\lvert V_z \rvert$	10 cm	TRK4	8 cm
Minimum TPC clusters	70	TRK5	80
	70	TRK6	100
Maximum χ^2_{TPC} per Cluster	4	TRK7	3
	4	TRK8	5
Maximum χ^2_{TPC} in Global Constrained	36	TRK9	32
	36	TRK10	40
Maximum χ^2_{TPC} per Cluster	4	TRK11	3
	4	TRK12	5
TPC and ITS refit	Required	N/A	Required
Reject Kink Daughter	Required	N/A	Required
1 Cluster in SPD	Required	N/A	Required

TABLE 3.5: List of all Standard Track Cuts conditions with the variation used to establish the systematic uncertainty

σ_ϕ, γ_ϕ The interplay of uncertainties for derived quantities is more complex. Here a numerical approach is taken, where the values of the yields are shifted coherently or not depending on the source, and the corresponding parameters are calculated with the new values. The RMS of the resulting distribution is taken as the related uncertainty.

Material Budget & Hadronic Interaction

Material budget systematic class represents how accurately we know the position and extent of material in the ALICE detector, whereas the hadronic interaction class represents how good the simulation of the interaction with the material of the detector is. Both these classes of uncertainty are negligible for the pp collision at $\sqrt{s} = 7$ TeV dataset [184, 185]. In this dataset the tracking (8-16%) and normalisation $(^{+7.3\%}_{-3.5\%})$ uncertainty are such that relatively small corrections (2-6%) are completely overshadowed and negligible. The pp collision at $\sqrt{s} = 5.02$ TeV dataset instead take the p_{T} -dependent values in [192].

The reported uncertainty is for kaons. The procedure to find the corresponding uncertainty for the ϕ-meson and for the ϕ-meson pair is to take advantage of a Monte Carlo production. The decay products of the ϕ meson(s) are singularly assigned the uncertainty based on their p_{T} . Then, the uncertainties of all daughters are linearly summed to provide the uncertainty associated to the starting ϕ meson(s). A profile histogram is then filled with a statistically significant number of decays to average the uncertainties for all possible decay kinematics. The resulting histogram is then taken as uncertainty to assign to the data points.

Regarding the procedure proposed in Section 3.8.3, as there is but one source of uncertainty, the histogram obtained by the process above is used to produce a number of fake sources. In a procedure reminiscent of the extrapolation uncertainty handling (refer to Section 3.7), the true data spectrum is randomised point-by-point based on the uncertainty under scrutiny. The new spectra are then treated as an independent source of systematics.

Signal Extrapolation

The discussion on the signal extrapolation is done in Section 3.7.

3.8.2 Uncertainty evaluation

Each class is made of a number of sources that will be evaluated as possible systematically relevant variations. To discriminate sources as systematically relevant or not, a Barlow check is performed (see next section). Then, all classes will be scrutinised for possible correlations or anti-correlations for inclusive yields or their combinations.

Barlow Check

The Barlow check is a test designed to discriminate a statistical fluctuation from a systematic variation. After repeating the full analysis with a systematic variation a number of times with as many different results, let us call them $y_i \pm \sigma_i$, one can compare them to the default measurement $y_c \pm \sigma_c$ defining the Barlow error as:

$$\Delta\sigma_i = \sqrt{|\sigma_i^2 - \sigma_c^2|} \tag{3.35}$$

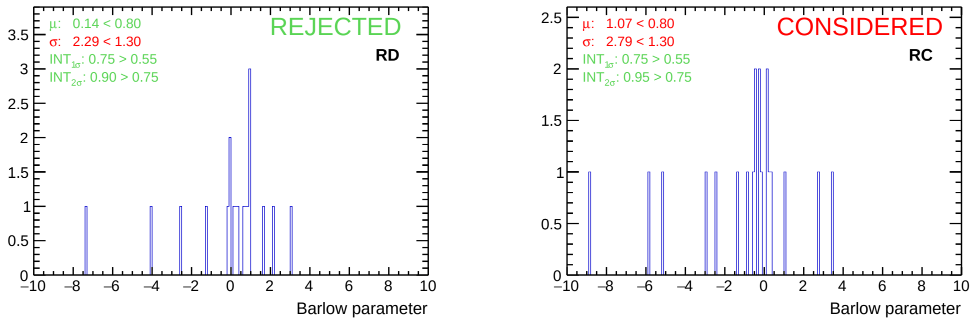

FIGURE 3.23: Example of a rejected Barlow parameter distribution (left) and an accepted Barlow parameter distribution (right) for the signal extraction systematic evaluation for the pp at $\sqrt{s} = 5.02$ TeV dataset. (see Table 3.3)

Using this error one can then define a Barlow parameter n_i defined as:

$$n_i = \frac{\Delta y_i}{\sqrt{|\sigma_i^2 - \sigma_c^2|}} = \frac{|y_i - y_c|}{\sqrt{|\sigma_i^2 - \sigma_c^2|}} \tag{3.36}$$

This parameter defines the fluctuation as within statistical uncertainty if $n_i \leq 1$, systematical otherwise. For each systematical variation the Barlow check is applied and a histogram is filled with the Barlow parameter n_i of all p_T bins. Then the source is scrutinised to determine whether it is a systematically significant variation. To discard the source as a systematical significant contribution the distribution we find should satisfy at least 3 of the following requirements:

$|\mu| \leq 0.80$ Mean of the distribution

$\sigma \leq 1.30$ Standard deviation of the distribution

$\mathrm{A}_{1\sigma} \geq 55\%$ Area within $\pm 1\sigma$

$\mathrm{A}_{2\sigma} \geq 75\%$ Area within $\pm 2\sigma$

For each p_T bin a histogram is filled with all the sources deemed systematical and the uncertainty is considered as the sum of the RMS and absolute value of the mean.

Inclusive yields, derived quantities uncertainties and mean p_T

The system described in Section 3.8.2 is working when evaluating the single bin uncertainty. This approach does not take into consideration the possible bin-by-bin correlations of the systematic classes. To this goal, a further study has been performed to determine the impact of such correlations on the total uncertainty.

The study consists in evaluating the yields for each variation source in each class if they pass the Barlow Check and are deemed systematical. Then a procedure similar to the one of the single p_T bin is performed: the ratio between the standard analysis quantity and the variation source quantity is evaluated, then the mean and RMS are assigned as overall systematical uncertainty:

$$\frac{Q_{\mathrm{STD}} - Q_{\mathrm{VAR}}}{Q_{\mathrm{STD}}} \tag{3.37}$$

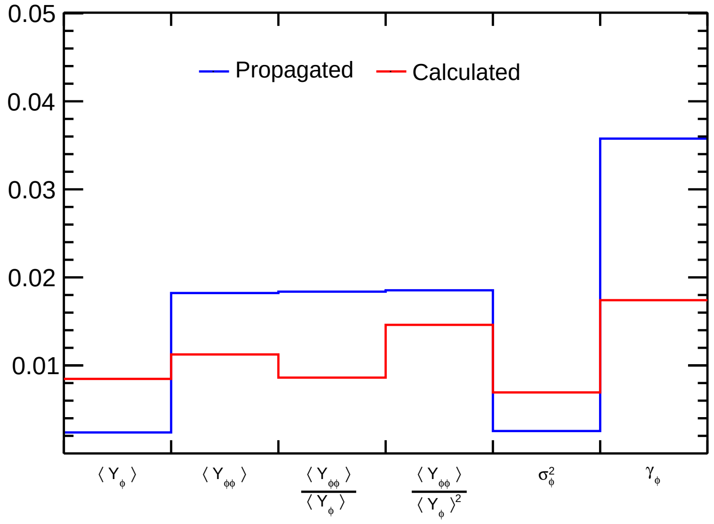

FIGURE 3.24: Example of a uncertainty propagation against calculation as described in Section 3.8.2 for the signal extraction systematic evaluation for the pp at $\sqrt{s} = 5.02$ TeV dataset. (see Table 3.3)

where Q_{STD} is the standard measurement for quantity Q, Q_{VAR} is the variation measurement for quantity Q.

The requirement for the passing of the Barlow check is performed separately on the 1D analysis and on the 2D analysis: for each, when a source is considered systematical it is used in this overall evaluation. When the quantity is measured combining the yields the requirement is that at least one of the two yields is systematically significant, then both are used to calculate Q_{VAR}. The Barlow check is also performed separately for the conditional $\langle p_{\mathrm{T}} \rangle$.

3.8.3 Total uncertainty

The total systematical uncertainty is given as the square sum of all systematic uncertainties. In the case of the spectra this operation is done in a bin-by-bin fashion. This means that all the uncertainties measured for each p_{T} bin are added quadratically. The results can be seen in Fig. 3.25, for the pp collision at $\sqrt{s} = 7$ TeV dataset a normalisation uncertainty of $^{+7.3\%}_{-3.5\%}$ must be added.

For the yields and derived quantities (refer to Section 3.10) the calculated systematical uncertainties are assigned and the total systematic uncertainty is the square sum of all classes.

The full systematic uncertainty for the yields and for the derived quantities can be seen in Fig. 3.25.

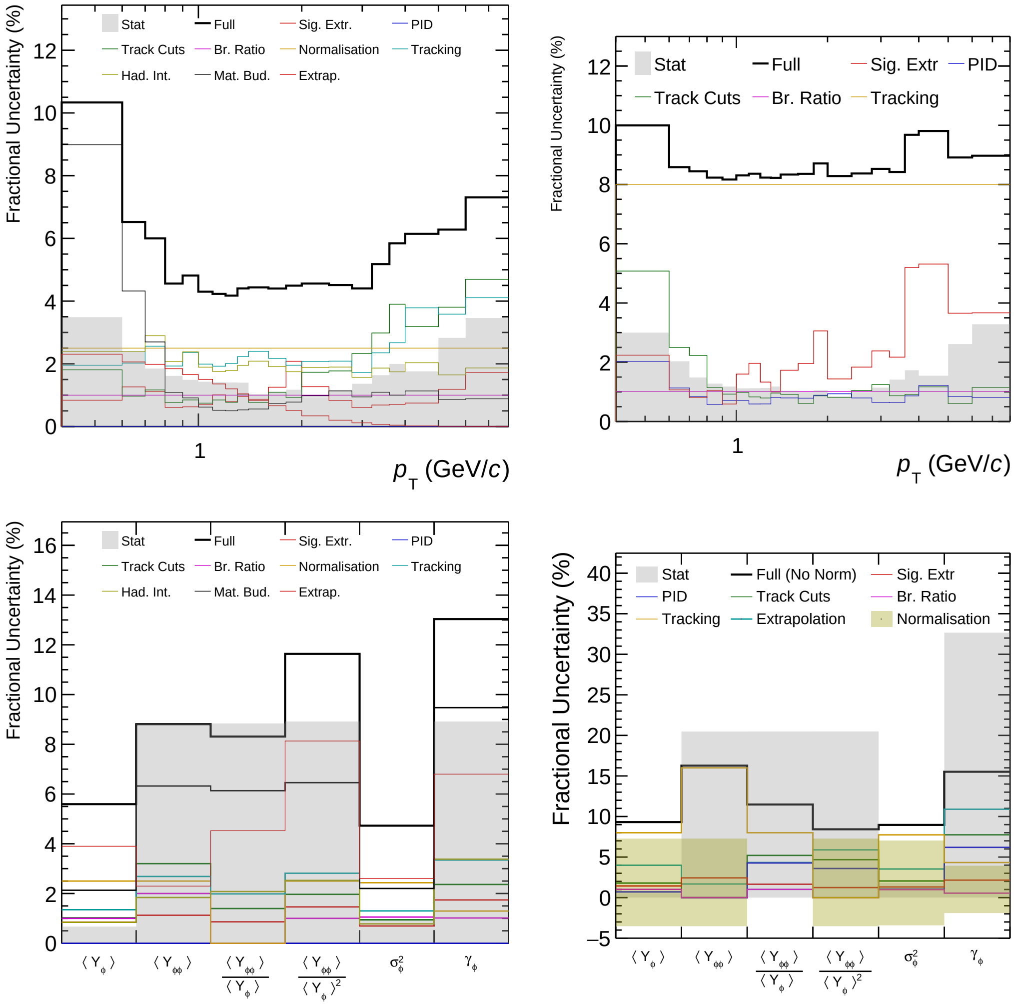

FIGURE 3.25: (top) final systematical uncertainties on the inclusive ϕ meson p_{T} sepctrum, (bottom) uncertainty on the final derived quantities (refer to Section 3.10). On the left is the pp collision at $\sqrt{s} = 5.02$ TeV, on the right is the pp collision at $\sqrt{s} = 7$ TeV. The negative values for the normalisation uncertainty in the $\sqrt{s} = 7$ TeV dataset is due to its asymmetric nature and shows the percentage of value over and below the central value of reference.

3.9 Consistency check

A consistency check have been carried out in an attempt to consolidate the analysis and the result. We refer to yields and derived quantities as discussed in section 3.10.

3.9.1 Volume fluctuation effect

The multiplicity selection on the V0M could lead to a bias called volume fluctuation [193, 194]. The problem comes from the experience in Pb–Pb collisions, where the selection of too large centrality bins could skew results because of borders effects in the selection. The effect is mitigated by selecting finer multiplicity bins, so the analysis is repeated in smaller V0M intervals. A reference on the intervals used can be found in Figure 3.27.

The first check was carried out on the anchored PYTHIA8 dataset analysing the distribution of the ϕ mesons produced in narrow (1%) and large (10%) multiplicity bins. The RMS of the distributions were then measured for both binning alternatives and the narrow bins were averaged, weighted by their events contributors, to compare to the large bins. This is shown in Figure 3.26a.

The second check was performed on data. The pp at $\sqrt{s} = 5.02$ TeV was used, measuring the yields in finer bins of V0M multiplicity. The γ_{ϕ} was chosen as a reference for the results as it is the most sensitive to the volume effect. The results are shown in Figure 3.26b.

Both these checks provide a clear indication that the volume effect is not an interference to our measurement, as all the shown results are compatible within statistical uncertainty.

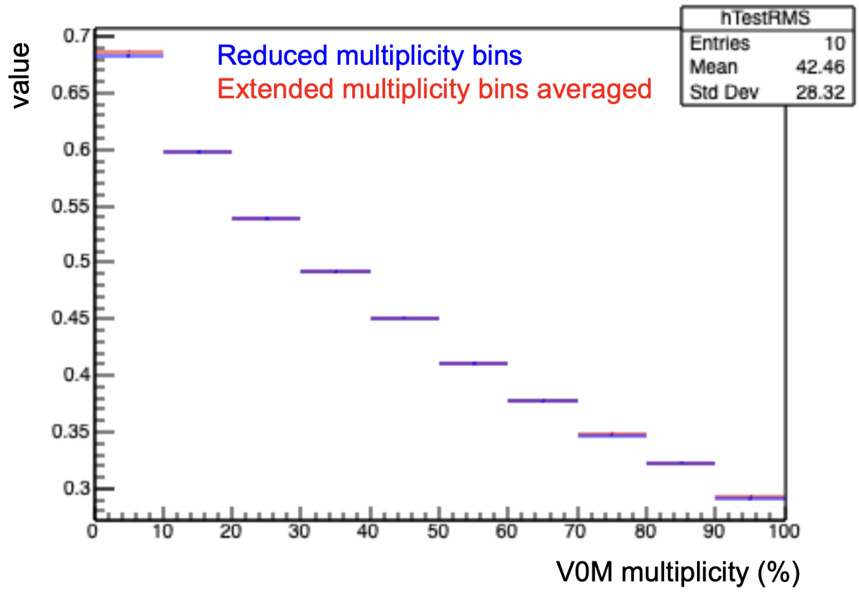

(A) Comparison of Monte Carlo calculated RMS of ϕ-meson porudction distribution in different V0M binnings.

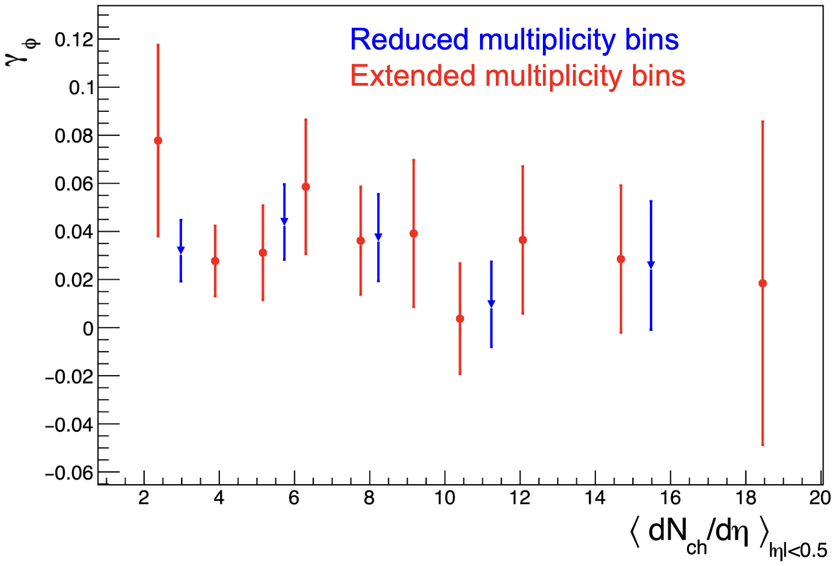

(B) γ_ϕ parameter as a function of charged particle final state multiplicity in two different multiplicity binning.

FIGURE 3.26: Summary of the volume effect check

3.10 Deducing the ϕ-meson production variance and new parameter γ_ϕ

The measurement to the ϕ-meson pair yield makes it possible to study the ϕ-meson production probability distribution in a new way. If we take a look at the definition of the inclusive productions:

$$\begin{aligned}
\langle \mathrm{Y}_{\phi} \rangle &\equiv \frac{\mathrm{d}N_{\phi}}{\mathrm{d}y} \qquad (3.38)\\
&= \Big(n_{1\phi} + 2n_{2\phi} + 3n_{3\phi} + \ldots \Big)\\
\langle \mathrm{Y}_{\phi\phi} \rangle &\equiv \frac{\mathrm{d}N_{\phi\phi}}{\mathrm{d}y} \qquad (3.39)\\
&= \Big(n_{2\phi} + 3n_{3\phi} + 6n_{4\phi} + \ldots \Big)\\
&\ldots\\
\langle \mathrm{Y}_{i\phi} \rangle &\equiv \sum_{k=0}^{\infty} \binom{k}{i} n_{k\phi} = \sum_{k=0}^{\infty} \frac{k!}{i!(k-i)!} n_{k\phi} \qquad (3.40)
\end{aligned}$$

where $\mathrm{d}N_{\phi}/\mathrm{d}y$ and $\mathrm{d}N_{\phi\phi}/\mathrm{d}y$ are the p_{T} -integrated yields of the ϕ meson and ϕ-meson pairs respectively, $n_{i\phi}$ is the probability of producing i ϕ mesons in a given event. The last equation is a generalisation of the p_{T} -integrated yield of an arbitrary ϕ-meson n-tuple.

We can now turn our attention to the ϕ-meson production probability distribution, and how the above defined quantities relate to the mean and variance of the distribution. It is straightforward to see that $\langle \mathrm{Y}_{\phi} \rangle$ represents the mean, whereas the variance needs a bit more thought:

$$\mu = \langle \mathrm{Y}_{\phi} \rangle \qquad \sigma^2 = \langle \mathrm{Y}_{\phi}^2 \rangle - \langle \mathrm{Y}_{\phi} \rangle^2 \qquad (3.41)$$

To calculate the variance we are missing $\langle \mathrm{Y}_{\phi}^2 \rangle$. Nevertheless, this factor can be derived by a combination of our measured yield:

$$\begin{aligned}
\langle \mathrm{Y}_{\phi\phi} \rangle &= \sum_{k=0}^{\infty} \frac{k(k-1)}{2} n_{k\phi} \qquad (3.42)\\
&= \frac{1}{2} \sum_{k=0}^{\infty} (k^2 - k) n_{k\phi} \qquad (3.43)\\
\langle \mathrm{Y}_{\phi\phi} \rangle &= \frac{1}{2} \langle \mathrm{Y}_{1\phi}^2 \rangle - \frac{1}{2} \langle \mathrm{Y}_{\phi} \rangle \qquad (3.44)
\end{aligned}$$

Therefore, from Equation 3.44, we can infer:

$$\langle \mathrm{Y}_{\phi}^2 \rangle = 2\langle \mathrm{Y}_{\phi\phi} \rangle + \langle \mathrm{Y}_{\phi} \rangle \qquad (3.45)$$

Then, the distribution variance can be expressed as:

$$\begin{aligned}
\sigma^2 &= \langle \mathrm{Y}_{\phi}^2 \rangle - \langle \mathrm{Y}_{\phi} \rangle^2 \qquad (3.46)\\
&= \Big(2\langle \mathrm{Y}_{\phi\phi} \rangle + \langle \mathrm{Y}_{\phi} \rangle \Big) - \langle \mathrm{Y}_{\phi} \rangle^2 \qquad (3.47)
\end{aligned}$$

If we wish to compare our results to a poissonian distribution, we can make use of the knowledge that in this distribution the mean and variance are equal. Then, their ratio minus one will be a parameter that can indicate if the production is poissonian (the parameter will take the value zero) or enhanced (the parameter will take positive values) or suppressed (the parameter will take negative values) with respect to this hypothesis. Following through with our idea we can see that:

$$\frac{\sigma^2}{\mu} - 1 = \frac{2\langle \mathrm{Y}_{\phi\phi}\rangle + \langle \mathrm{Y}_\phi\rangle - \langle \mathrm{Y}_\phi\rangle^2}{\langle \mathrm{Y}_\phi\rangle} - 1 \tag{3.48}$$

$$= \frac{2\langle \mathrm{Y}_{\phi\phi}\rangle}{\langle \mathrm{Y}_\phi\rangle} + 1 - \frac{\langle \mathrm{Y}_\phi\rangle^2}{\langle \mathrm{Y}_\phi\rangle} - 1 \tag{3.49}$$

$$= \frac{2\langle \mathrm{Y}_{\phi\phi}\rangle}{\langle \mathrm{Y}_\phi\rangle} - \langle \mathrm{Y}_\phi\rangle \tag{3.50}$$

$$\gamma_\phi \equiv \frac{2\langle \mathrm{Y}_{\phi\phi}\rangle}{\langle \mathrm{Y}_\phi\rangle} - \langle \mathrm{Y}_\phi\rangle \tag{3.51}$$

A second way to compare our results to a poissonian distribution is possible. We can start by rephrasing Eq. 3.44, after we can use the equalities in Eq. 3.41:

$$\langle \mathrm{Y}_{\phi\phi}\rangle = \frac{1}{2}\Big(\sigma_\phi^2 - \langle \mathrm{Y}_\phi\rangle + \langle \mathrm{Y}_\phi\rangle^2\Big) \tag{3.52}$$

$$= \frac{1}{2}\Big(\sigma_\phi^2 - \mu_\phi + \mu_\phi^2\Big) \tag{3.53}$$

At this point, reminding that variance and mean are equal in the poissonian, we can calculate the ratio:

$$\frac{\langle \mathrm{Y}_{\phi\phi}\rangle}{\langle \mathrm{Y}_\phi\rangle^2} = \frac{\frac{1}{2}(\sigma_\phi^2 - \mu_\phi + \mu_\phi^2)}{\mu_\phi^2} \tag{3.54}$$

$$= \frac{1}{2}\Big(\frac{\sigma_\phi^2}{\mu_\phi}\frac{1}{\mu_\phi} - \frac{\mu_\phi}{\mu_\phi}\frac{1}{\mu_\phi} + \frac{\mu_\phi^2}{\mu_\phi^2}\Big) \tag{3.55}$$

$$= \frac{1}{2}\Big(\frac{1}{\mu_\phi} - \frac{1}{\mu_\phi} + 1\Big) = \frac{1}{2} \tag{3.56}$$

$$\mathrm{R}_\phi \equiv \frac{\langle \mathrm{Y}_{\phi\phi}\rangle}{\langle \mathrm{Y}_\phi\rangle^2} \tag{3.57}$$

So our new parameter R_ϕ will be 1/2 for poissonian-distributed productions and else if not.

3.11 Results

In this section the final results of the analysis will be discussed. The plots will make use of the conditional classes outlined in Figure 3.27.

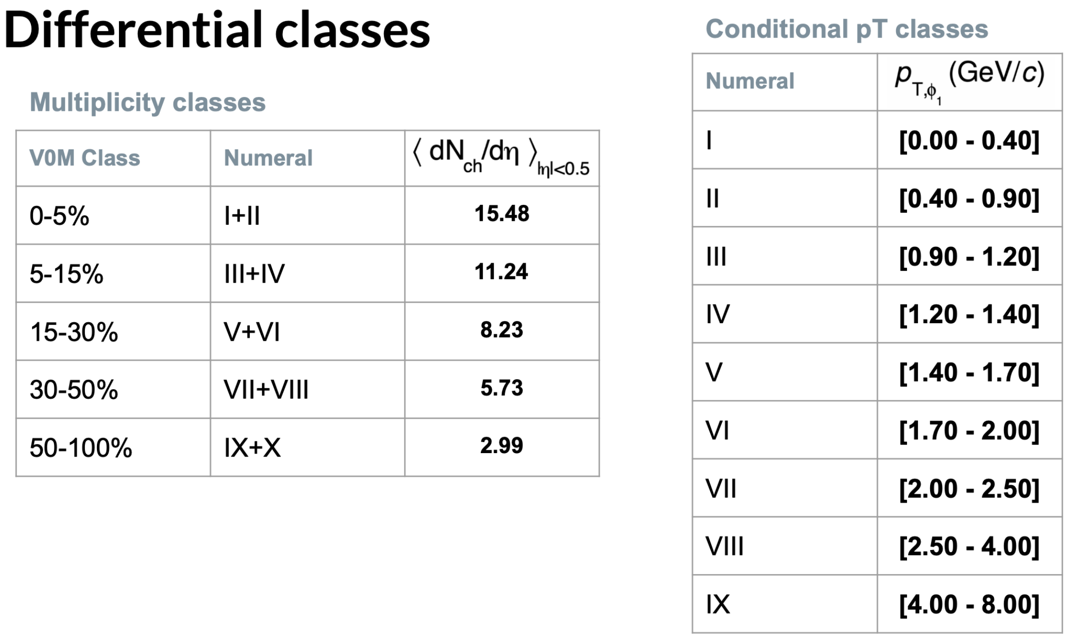

Differential classes

Multiplicity classes

V0M Class	Numeral	$\langle dN_{ch}/d\eta \rangle_{\lvert\eta\rvert<0.5}$
0-5%	I+II	**15.48**
5-15%	III+IV	**11.24**
15-30%	V+VI	**8.23**
30-50%	VII+VIII	**5.73**
50-100%	IX+X	**2.99**

Conditional pT classes

Numeral	p_{T,ϕ_1} (GeV/c)
I	**[0.00 - 0.40]**
II	**[0.40 - 0.90]**
III	**[0.90 - 1.20]**
IV	**[1.20 - 1.40]**
V	**[1.40 - 1.70]**
VI	**[1.70 - 2.00]**
VII	**[2.00 - 2.50]**
VIII	**[2.50 - 4.00]**
IX	**[4.00 - 8.00]**

FIGURE 3.27: Reference tables for differential classes.

3.11.1 The ϕ-meson conditional spectra and average transverse momentum

The ϕ meson conditional spectra for both pp collision at $\sqrt{s} = 7$ TeV and at $\sqrt{s} = 5.02$ TeV inclusive analysis is shown in Figure 3.28. The shown spectra are symmetric, so that every bin (e.g. bin (2,4)) has the same value and uncertainty as the conjugate (e.g. bin (4,2)).

The results presented show a similar behaviour for both measured energies, as can be seen by the comparison of Figg. 3.28a-3.28b. The p_{T} -differential conditional production of ϕ mesons show a hardening of the spectrum proportional to the p_{T} of the associated produced ϕ-meson. Indeed, the higher the p_{T} of the associated ϕ-meson, the harder the spectrum is. This is consistent with the average transverse momentum results shown in Figure 3.29 for both datasets. These results need further investigation, but hint at the possibility of a correlated production: (high-)low-p_{T} ϕ mesons are produced together with (high-)low-p_{T} ϕ mesons. A number of processes might be responsible for this behaviour, notably jet-production. The production of jets is expected to be dominated by colour strings, where the ϕ-meson correlated production is expected to be higher. In this scenario then the results would suggest a relevant jet-component for the ϕ-meson pair production.

The multiplicity dependent results do not have a high enough precision to draw any conclusion about the conditional spectra average transverse momentum evolution in multiplicity.

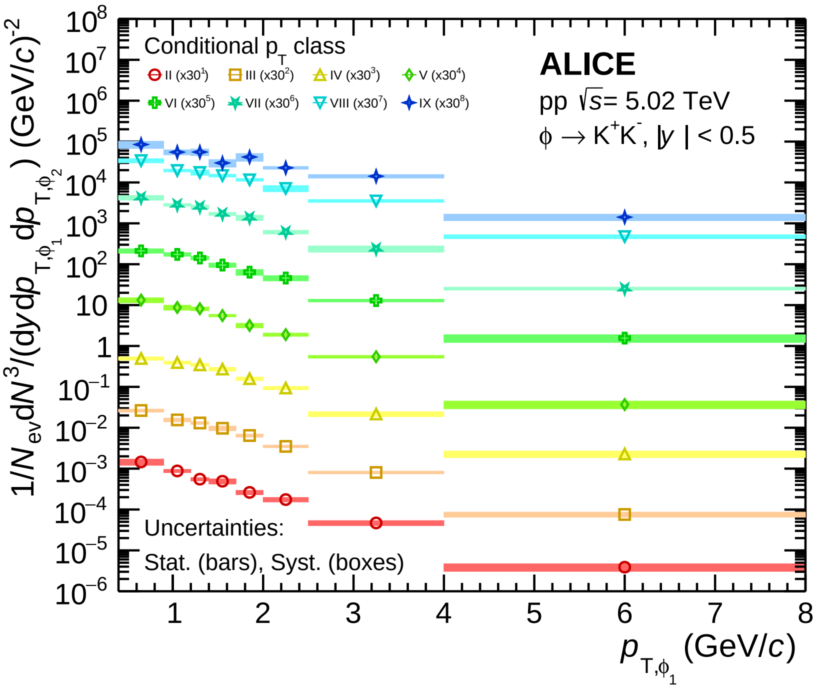

(A) Conditional p_{T} spectra. pp collision at $\sqrt{s} = 5.02$ TeV.

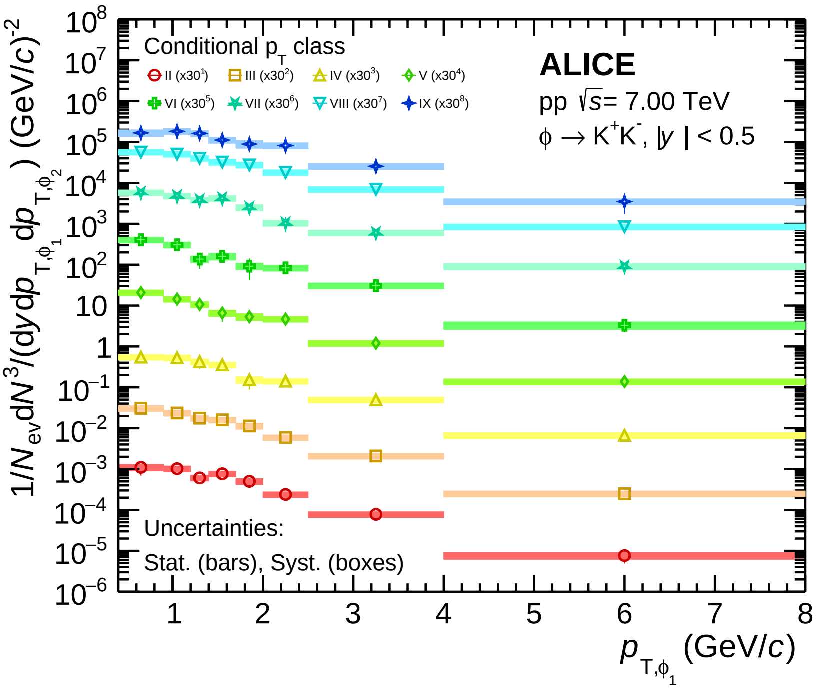

(B) Conditional p_{T} spectra. pp collision at $\sqrt{s} = 7$ TeV.

FIGURE 3.28: Conditional p_{T} spectra.

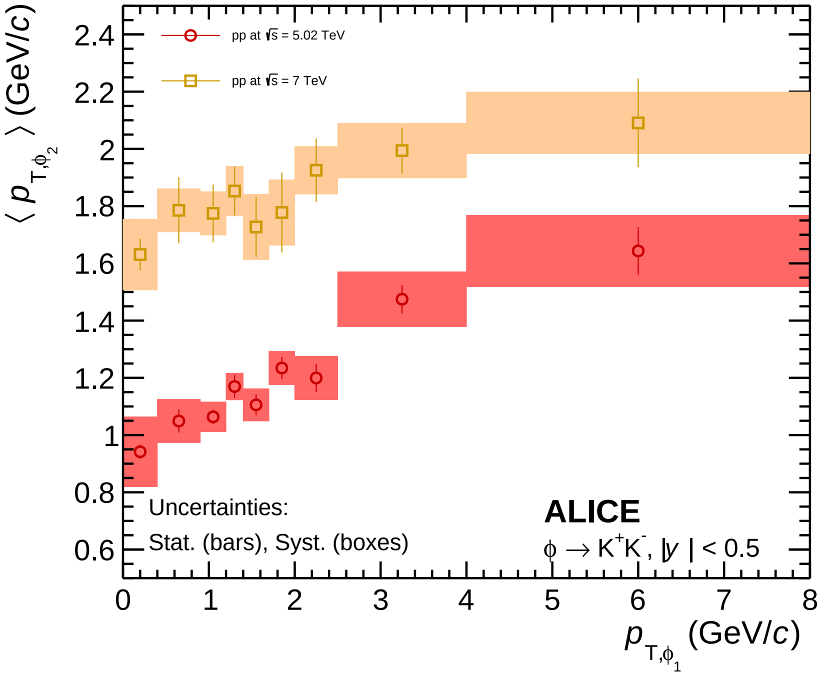

(A) Average p_T spectra. pp collision at $\sqrt{s}$ = 7 TeV and pp collision at $\sqrt{s}$ = 5.02 TeV.

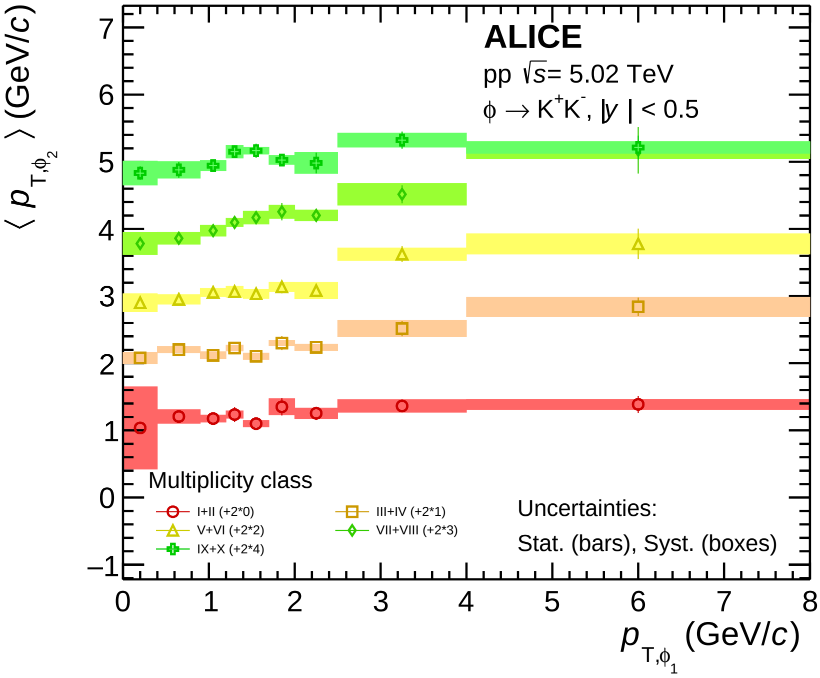

(B) Average p_T spectra as a function of multiplicity. pp collision at $\sqrt{s} = 5.02$ TeV.

FIGURE 3.29: Average p_T spectra.

3.11.2 The ϕ meson production probability results and comparison with Monte Carlo generators

The ϕ meson and ϕ-meson pair production are presented in Figure 3.30. The results for the inclusive ϕ meson production exhibit an approximately linear increase with increasing $\langle dN_{\mathrm{ch}}/d\eta\rangle_{|\eta|<0.5}$, this is a known behaviour [65]. The results for the inclusive ϕ-meson pair production hint at a quadratic increase with increasing $\langle dN_{\mathrm{ch}}/d\eta\rangle_{|\eta|<0.5}$, this is a novel observation. The Figure shows the PYTHIA8 predictions for the Monash 2013 tune [195] and the Monash tune with the addition of the Rope model [157] (refer to Section 1.4). It is worth noting that the predictions for both agree with the data as far as the multiplicity dependence is considered (both reproduce the linear and quadratic behaviour), but fail to reproduce the amount of ϕ mesons measured (both under predict the measured yield).

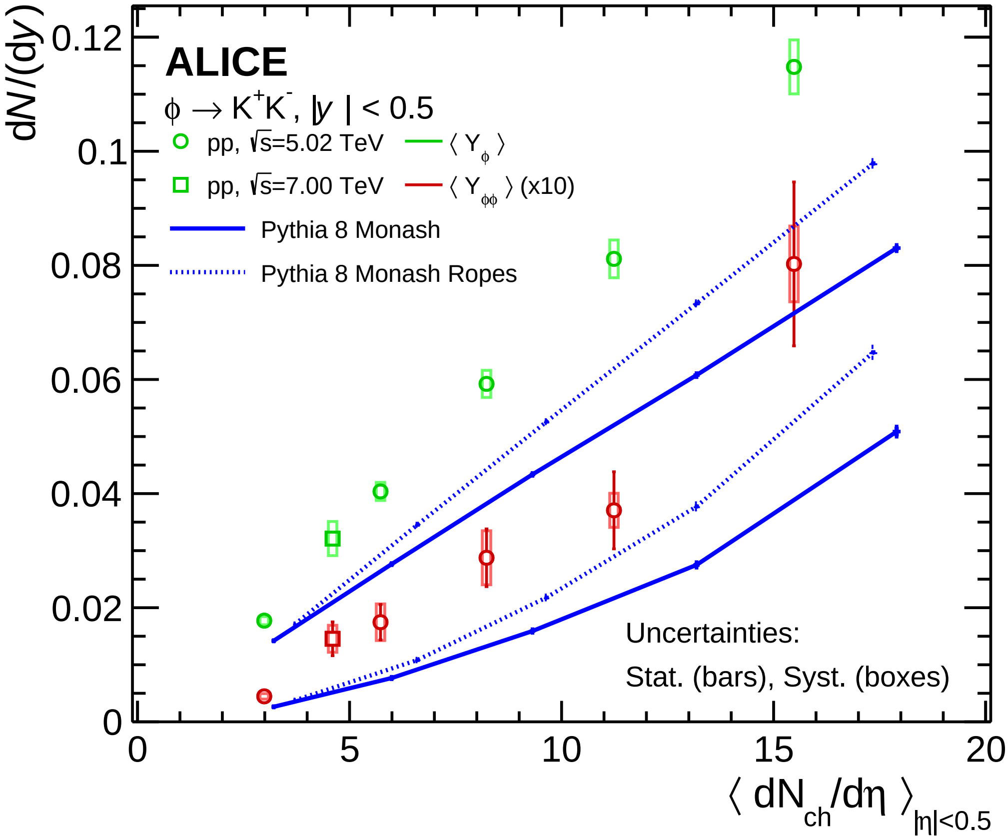

FIGURE 3.30: Yields of ϕ meson and ϕ-meson pairs as a function of multiplicity. pp collision at $\sqrt{s}$ = 7 TeV and pp collision at $\sqrt{s}$ = 5.02 TeV

Turning our attention to the production probability characterisation (refer to Section 3.10), we refer to Figure 3.31, where the newly introduced γ_ϕ (red points and line) and R_ϕ (green points and line) are shown as a function of final state charged multiplicity. Here the dashed lines signal the poissonian limit for both parameters.

R_ϕ shows a decreasing trend from low to high multiplicity events. This suggests that low multiplicity events have a larger excess with respect to the poissonian expectation. Both the PYTHIA tunes predictions show a similar behaviour and agree with the data points, although it should be noted that the uncertainties at play are quite large and might hide discrepancies.

γ_ϕ shows a rather constant behaviour with $\langle \mathrm{d}N_\mathrm{ch}/\mathrm{d}\eta\rangle_{|\eta|<0.5}$, which is again in agreement with both the PYTHIA tunes predictions. It shows an ≈ 3.5% deviation from a poissonian, for correlated production.

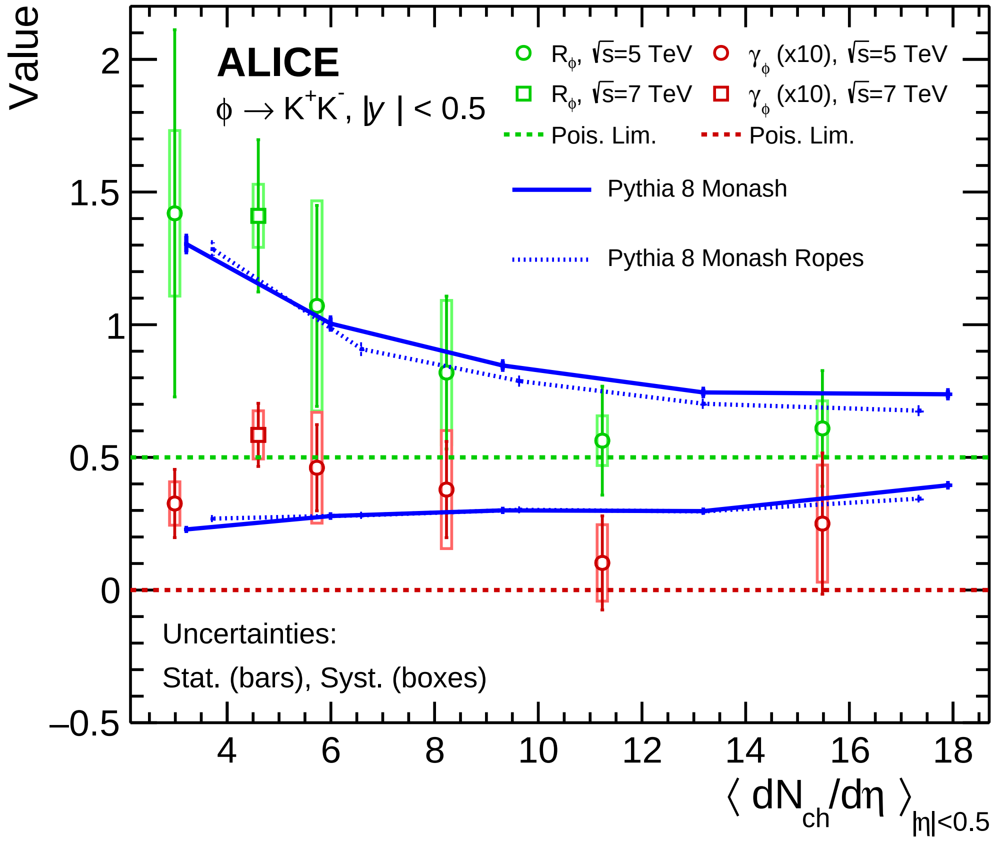

FIGURE 3.31: Values of γ_ϕ and R_ϕ as a function of multiplicity. pp collision at $\sqrt{s} = 7$ TeV and pp collision at $\sqrt{s} = 5.02$ TeV

These preliminary results suggest that the production of the ϕ meson is indeed enhanced with respect to the thermal production, which is associated with a poissonian distribution. In fact the excess exhibited by the PYTHIA predictions is expected in the Lund string picture. One can visualise this with the help of a naive approximation, shown in figure 3.32.

The thermal model describes a single source with a sea of de-confined quarks, where the probability of producing a pair of ϕ meson ($p_{\phi\phi}^{\mathrm{thermal}}$) is the square of the probability of producing a single ϕ meson ($p_{\phi\phi}^{\mathrm{thermal}} = (p_{\phi}^{\mathrm{thermal}})^2$).

In the Lund string model, a somewhat more complicated picture is described. The probability of producing a single ϕ meson (p_{ϕ}^{Lund}) depends on the square of the probability of the string to break into an $s\bar{s}$ pair ($p_{s\bar{s}}$), which results in $p_{\phi}^{\mathrm{Lund}} \propto p_{s\bar{s}}^2$. If another $s\bar{s}$ breaking occurs, then the probability of having two ϕ mesons ($p_{\phi\phi}^{\mathrm{Lund}}$) becomes $p_{\phi\phi}^{\mathrm{Lund}} \propto p_{s\bar{s}}^3$ (blue sketch). Of course there is also the possibility of having two strings, in which case the probability goes as in the Thermal picture $p_{\phi\phi}^{\mathrm{Lund}} \propto p_{s\bar{s}}^4 = (p_{\phi}^{\mathrm{Lund}})^2$ (orange sketch). Then we can expect that the low multiplicity selection is more sensitive to events with less strings, where the enhanced production is dominant, and the high multiplicity "drowns" this enhancement by having multiple sources.

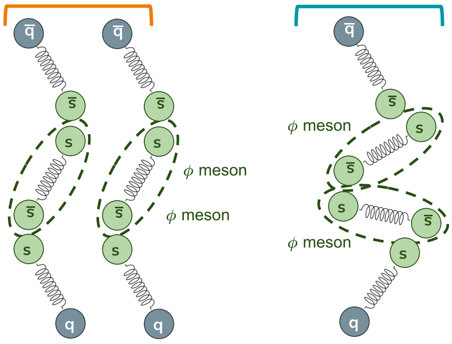

FIGURE 3.32: Schematical sketch for a naive picture for ϕ-meson production in the Lund string model.

3.11.3 Final thoughts and explored extensions

The author would like to stress the fact that the model predictions form the PYTHIA model, despite predicting quite different yields, are almost undistinguishable when compared with the production probability characterisation parameters γ_ϕ and R_ϕ, and most of all they fully agree to data within uncertainties. This is a very promising result that indicates that the novel approaches being put forward can have an impact in understanding the underlying mechanisms of hadronisation and can have an impact in model discrimination. This is in fact something reminiscent of the spherocity analysis (refer to 1.3.2), where the ϕ meson was poorly reproduced by PYTHIA based models when the yields were examined, but surprisingly predicted quite well the double ratios shown in Figure 1.25.

The downside of this measurement is the amount of data necessary to perform it with a satisfactory uncertainty. Indeed Run 1 data only allowed for the inclusive measurement to be performed and Run 2 data allowed for a limited differentiation. In this context the Run 3 data, which is greatly expanding the available data sample, is a very exciting opportunity to use the presented methods in combination to different event classifiers and to improve the now substantial uncertainty.

Explored extensions

As the pp collisions at $\sqrt{s} = 5.02$ TeV had enough statistics to allow for differentiation, a pilot study has been performed to understand the correlated production of the ϕ-meson pairs. A first attempt was performed by requiring the azimuthal angle difference between the candidates to be in a certain range. The results are shown in Figure 3.33, together with another pilot study of this novel measurement sensitivity to the string tension in the PYTHIA framework. The tension has been modified using the equations reported in the Rope model (ropes effectively modify the string tension), following the equation:

$$\tilde{k} = hk \tag{3.58}$$

where h represents the proportionality factor for which the string tension k has been scaled to the new effective string strength $\tilde{k}$. The pilot study was stopped to wait for the Run 3 wider dataset as the uncertainties were too large to draw any meaningful conclusions.

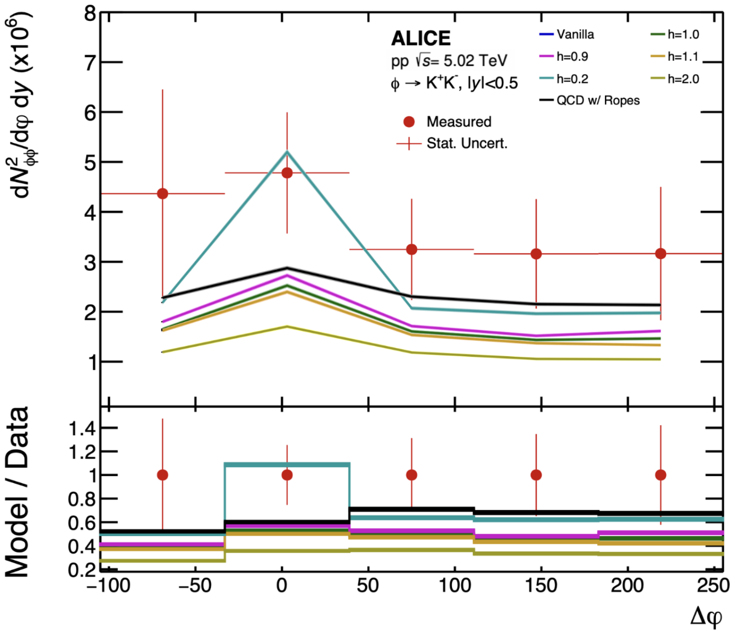

FIGURE 3.33: Yield of ϕ-meson pairs as a function of their azimuthal angle difference.

Chapter 4

Characterisation of SiPMs for the dRICH detector of the ePIC experiment at EIC

The Bologna ePIC group main effort is the characterisation of Silicon PhotoMultipliers (SiPMs) for single-photon applications in moderate radiation environment. The group also studies approaches to mitigate the radiation damage, most notably the use of high-temperature annealing cycles as a way to keep the dark count rates under control. These studies are aimed at the development of the dual-radiator Ring Imaging Cherenkov (dRICH) detector for the future electron-Proton/Ion Collider experiment (ePIC) at the Electron-Ion Collider (EIC).

4.1 Physics at EIC

The Electron-Ion Collider main goal is the investigation of the Quantum Chromodynamics via the Deep Inelastic Scattering (DIS). As a general purpose detector, many aspects will be investigated [196].

4.1.1 Global properties and parton structure of hadrons

Nucleon spin

Nucleon spin and mass are among the most important characteristics for any hadron. The spin of a nucleon can be decomposed as [197]:

$$\frac{1}{2} = \frac{1}{2}\Delta\Sigma(\mu) + \Delta G(\mu) + L_q(\mu) + L_g(\mu) \tag{4.1}$$

where we have the quark (gluon) contribution $\Delta\Sigma$ (ΔG) and their orbital angular momenta L_q (L_g). Each term of this equation depends on the re-normalisation scale μ, where scale dependence drops out upon summing over all contributions. Previously it was generally thought that the $\Delta\Sigma$ was the main contributor, whilst it has been uncovered in the 1980s that is not the case [198]. It is now established that only 25% of the proton spin is carried by quarks and a non-zero contribution of gluons[199, 200]. These numbers though have large uncertainties and EIC will step in, as these depend on the helicity parton distribution function, tackled by foreseen measurements. Presently the measured region span above 0.01 x, but EIC will not only extend this down to 10^{-4}, but it will also put constraints on angular momenta for both quark and gluons [196].

Nucleon mass

As the atom mass is almost exactly the sum of its constituents, electrons and nucleons, the mass of a nucleus is approximately the sum of its nucleons, protons and neutrons. Surprisingly, the mass of the proton is no longer in line with the sum of its valence quarks, that make up around a mere 1% of the total mass. While in a full QCD analysis the quark mass contribution to the nucleon mass is larger, studies show that the Higgs mechanism can only explain a small fraction of the nucleon mass. The bulk can be attributed to contributions from quark and gluon kinetic and potential energies. EIC will provide novel insights on the nucleons mass in QCD by means of quarkonium production close to the production threshold [196].

4.1.2 Multi-dimensional imaging of nucleons, nuclei and mesons

Imaging in position space: form factors and generalised parton distributions

Form factors and generalised parton distributions are fundamental tools to understand the structure of the strongly interacting system. Elastic electron scattering is a way to measure the electromagnetic form factors, the Dirac form factors F_1 and the Pauli form factor F_2. They are a linear combination of the electric and magnetic form factors and depend on the squared energy transfer to the target. In a nucleus they can be interpreted as the charge and magnetisation distributions whereas for the nucleon this interpretation is less clear due to relativistic corrections.

Generalised Parton Distributions (GPDs), which generalise the concept of ordinary PDFs [201], appear in the QCD description of hard exclusive processes like deep-virtual Compton scattering (DVCS) and meson production [202, 203]. The information they encapsulate is very precious as it carries information on the orbital angular momentum of partons as well as the distribution of pressure and shear forces inside a hadron [196].

Imaging in momentum space: transverse momentum dependent parton distributions

Transverse momentum dependent parton distributions are a more descriptive addition to traditional PDFs which only provide 1-dimensional images of the internal structure of hadrons. That is longitudinal information, whereas transverse momentum dependent parton distributions (TMDs) provide information about the distribution transverse to the hard process flow. The 8 gluon and 8 quark TMDs then provide a 3D image of the hadron in the transverse momentum space for a spin-$1/2$ hadron [204–207].

The inclusive DIS integrate over the TMDs contribution, so different processes must be explored to measure them. A starting point can be found in semi-inclusive DIS. It must be stressed that TMDs can also be studied via different final states in electron-nucleon collisions with di-hadrons or jets and, for instance, in reactions that are not lepton-induced such as the Drell-Yan process. The fact that TMDs can be measured via a large number of reactions adds to their significance [196].

4.1.3 The nucleus: a laboratory for QCD

Physics of non-linear colour fields and gluon saturation

The physics of non-linear colour fields and gluon saturation becomes relevant when we tackle DIS in hadronic collisions at high energy. The projectile interacts with a number of stacked nucleons, probing very strong colour fields at high energy and possibly leading to to the effect of saturation know as Colour Glass Condensate (CGC) [208]. This is a consequence of the rapid grow of gluon density in hadrons for low x collisions. Gluons are responsible for the vast majority of particle production in these type of collisions, as well as for the rise of the total cross-section. Scrutiny of non-linear gluon dynamics can help improve our insight into the strong interaction [196].

Nuclear PDFs

Nuclear PDFs (nPDFs) describe the behaviour of bound partons in the nucleus. They are assumed to be universal and are used in high energy experiments in the factorisation of the cross section in the same fashion as the PDFs are [209]. This knowledge is necessary to deepen our understanding of perturbative QCD in a nuclear medium and to better interpret the results from all collider experiments. They also prove useful in the understanding of QGP as its characterisation necessitates a thorough separation of initial and final state effects, which relies on nPDFs for electron-ion collisions. Moreover neutrino scattering experiments on nuclei require a very precise knowledge of nPDFs which in turn provide an impact on global proton PDFs.

Differences of PDFs and nPDFs are well established from deep-inelastic lepton-nucleus scattering data. These observations clearly argue with the naive picture of the nucleus as the simple superposition of its constituents and are in need of nuclear effects for a precise description. There are three effects in the x spectrum: shadowing in the low ($x < 0.1$) region, anti-shadowing in the mid ($0.1 < x < 0.3$) region and

EMC[1] in the high x region (x > 0.3) [211–213].

The understanding of these modification effects is a question actively pursued both in experiment and theory. There is a general idea on physical processes contributing to these effects that are dependent on the x-region under scrutiny, however no consensus has been reached on their exact nature. The dependency on nuclear size, impact parameter, x for these effects come from fits to the existing data and are not derived from first principle calculations. In spark contrast with the available free-proton PDFs, nPDFs are lacking a broad kinematic coverage and beam species in the available data. In this context the EIC will help widen this dataset [196].

Particle propagation through matter and transport properties of nuclei

Particle propagation through matter and transport properties of nuclei will be another focus of the EIC. In addition to further the knowledge on nPDFs, the modification of partons traversing both hot and cold nuclear matter will be under study. The energy loss is expected in both hot (QGP) and cold QCD matter through gluon radiation and collisional scattering losses. Specifically, the detector proposal has strong reconstruction capabilities that can help reduce significantly the role of nPDFs modifications in the measurements, making them almost only sensitive to final state effects. The jets undergoing medium effects are subject to a broadening of the transverse profile that is sensitive to the gluon radiation and its angular dependence [196].

4.1.4 Understanding hadronisation

Parton fragmentation

Parton fragmentation is part of many current models through the factorisation theorem: the perturbative component of the cross section is calculated using stat-of-the-art theoretical calculation programs such as MadGraph, whereas the non-perturbative component is encoded in the so-called fragmentation function (FF). The latter describe how the parton transforms to the colour-neutral hadron that is then detected in our experiments. These FFs will greatly benefit from the high luminosity measurements that are foreseen at EIC that will include light-meson fragmentation, polarisation fragmentation studies and di-hadron fragmentation. Moreover the EIC will also have the advantage of colliding many different species of nuclei enabling the study of FFs in the nuclear medium and is set to provide the cleanest understanding yet from QCD of the energy loss of energetic partons traversing a nuclear medium, as measured via reconstructed leading jets [196].

Jets and their sub-structure

Jets and their sub-structure will be an important tool at the EIC. Jets help deep scrutiny of hadronisation process through, among others, jet substructure that offers the possibility to study both the process of fragmentation, or parton radiation patterns, and hadronisation, or the formation of the parton shower into bound state hadrons. The jets will make possible the measurement of transverse-momentum FFs both polarised and unpolarised. Moreover heavy-flavoured tagging in electron-ion collisions will help provide useful measurements in parton-nuclear-medium interactions that could be sensitive to both fragmentation and hadronisation modifications.

---

[1] This effect was first observed in 1983 at CERN by the European Muon Collaboration [210], hence the name "EMC effect". It is the observed x-dependence of the PDFs and nPDFs ratio in disagreement with existing theoretical predictions.

The relatively low momenta of reconstructed jets could also help the jet splitting function measurements [196].

Production mechanism for quarkonia

Production mechanism for quarkonia are in a unique position to give insights on both perturbative and non-perturbative hadronisation, with the addition of in-nuclear-matter hadronisation for nuclear beam configurations [196].

4.2 PID with the dRICH at EIC

The physics goals of the EIC detector needs to cover a large area of momentum and pseudorapidity, of which a third will be covered by the dual-radiator Ring Imaging Cherenkov (dRICH), that takes advantages of two radiators with different refraction indices to cover a large momentum range from $\approx 2\,\mathrm{GeV}/c$ to $\approx 50\,\mathrm{GeV}/c$ in π/K separation at 3σ (Figure 4.1). The dRICH solution is compact and cost effective, having a combination of gas (C_2F_6) and aerogel with refractive indices of ≈ 1.0008 and ≈ 1.02 respectively. For the light readout, a surface of $\approx 3\,\mathrm{m}^2$ will be paved with 3x3 mm^2 sensors for a total of roughly 300k channel that must provide single-photon detection inside a high intensity magnetic field of around $1\,\mathrm{T}$. The sensors will be placed outside the detector acceptance, six spherical mirrors will convey the light emitted by the particles traversing the radiators onto the photodetector surface, as shown in Figg. 4.2a-4.2b [214].

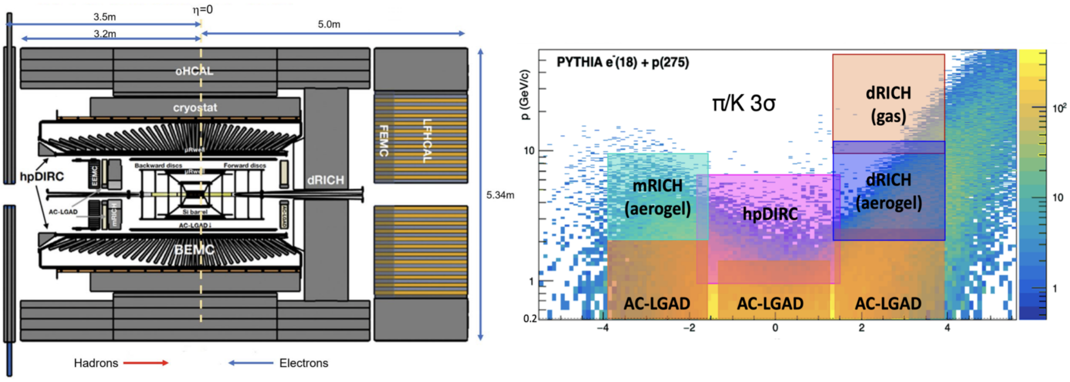

FIGURE 4.1: (left) overview of ePIC detector and (right) dRICH PID coverage

For this purpose, SiPMs are an excellent choice as they provide many of the specifications required: they are sensitive to single photons, they are insensitive to magnetic fields and can provide excellent timing (Section 4.3). The main drawback will be the medium radiation impact expected where the photosensors are located (Figure 4.7) will be a challenge as the SiPMs will need recursive treatment to recover at least partially their performance after damage.

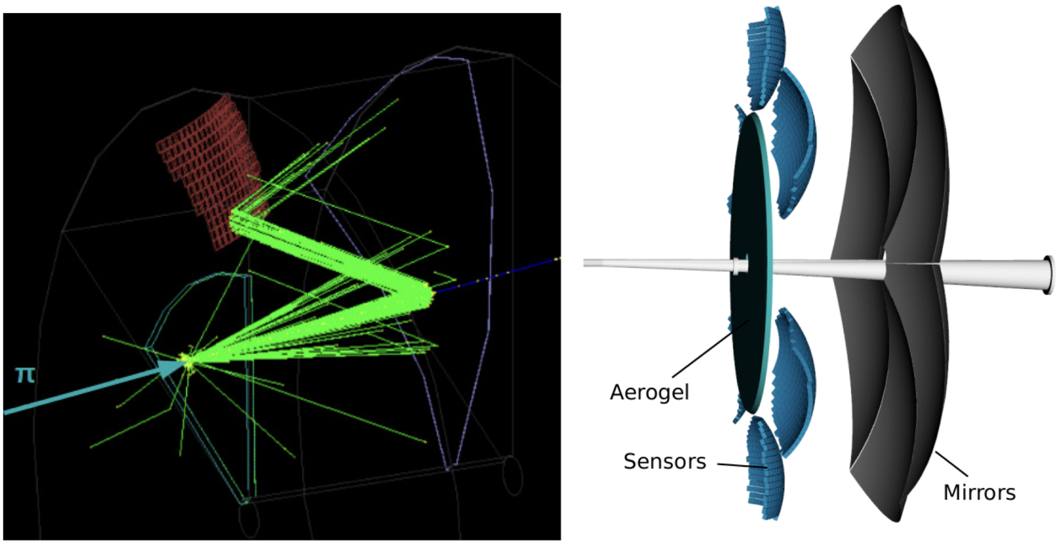

(A) Simulation of a π (light blue) emitting cherenkov light in the dRICH prototype, highlighted in bright green are the light rays that are reflected by the mirrors (dark blue) onto the photosensors (red)

(B) Visualisation of the dRICH structure

FIGURE 4.2: dRICH structure and simulated ray-tracing of cherenkov radiation.

4.3 Silicon PhotoMultipliers

Silicon Photomultipliers (SiPMs) are part of the fast growing group of silicon detectors. SiPMs can absorb incoming photons by exciting an electron to the conduction band. The absorption efficiency and depth depends on the incoming ray characteristics such as wavelength, of which a wide range is absorbed within a few $10\,\mu\mathrm{m}$ [215]. They are praised for their many advantages over conventional photo detectors such as excellent timing [216–219], compact design and single photon detection efficiency. Moreover they are insensitive to magnetic fields [220], which makes them a fitting choice for the application in high energy physics experiments.

Their main drawback is their radiation sensitivity [215]: we can define the recevied fluence of equivalent to $1\text{-MeV}/\mathrm{cm}^2$ neutron as $\mathrm{n_{eq}}$. Then a low dose would be less than $\approx 10^{10}\mathrm{n_{eq}}$, a moderate does would be $\approx 10^{11}\mathrm{n_{eq}}$ and a high does would be above $\approx 10^{12}\mathrm{n_{eq}}$. As an indication of the effects of radiation damage, one can consider that a fluence of $\approx 10^{9-10}\mathrm{n_{eq}}$ can already compromise the ability of single photon counting at room temperature of the SiPM [215]. This is due to the increase of the Dark Count Rate (DCR, see section) background that can disrupt the baseline in medium and high fluencies. One of the most promising ways the DCR can be reduced after radiation damage is the annealing procedure [221, 222].

4.3.1 Principle of operation

The silicon photodiode is based on a p-n junction, that is a volume of silicon that has been doped with atoms that provide electron donors (n) and a volume that has been doped with atoms that provides electron receivers (p) (Figure 4.3). Doping is the intentional introduction of impurities into an intrinsic semiconductor for the purpose of modulating its electrical, optical and structural properties. The doped material is referred to as an extrinsic semiconductor. The level of doping is considered *light* or *low* (*heavy* or *high*) when in the order of one dopant atom for 100 million (10 thousands) silicon atoms.

Typical dopants for silicon are [223]:

- p-donors, typically elements with 5 valence electrons
  - Phosphorus (P)
  - Arsenic (As)
  - Antimony (Sb)
- n-donors, with one less valence electron
  - Boron (B)
  - Aluminum (Al)
  - Gallium (Ga)
  - Indium (In)

Both n-doped and p-doped silicons are still neutral when separated, when they are joined together electrons and holes cross the junction via thermal diffusion. Electrons leaving the n-doped area are accepted in the p-doped region and will leave the donors behind as uncovered positive space charges. A positive space charge acts on the electrons that moved to the p-region and, thus creating a potential. The movement stops when the energy required for thermal diffusion becomes smaller than the space charge potential that has evolved between the two regions. Right at the junction between the two doped areas, a region free of mobile charge carriers is formed. It is called depletion region [223]. Whenever a photon is absorbed, a hole-electron pair is formed in the silicon: if a reverse bias is applied the now created holes (electrons) will move toward the anode (cathode) and this results in the creation of a net flow of current.

In the case of the SiPMS, the photodiode is put in a sufficiently high field to result in Geiger discharge upon photon absorption, thus the photodiode is a Single Photon Avalanche Diode (SPAD). The voltage required to reach this regime is called the breakdown voltage (V_{bd}). The Geiger discharge is a phenomenon in which the electron gains sufficient kinetic energy from the high electric field to produce secondary ionisation that in turn produces secondary ionisation and so on, generating an avalanche of electrons (holes). This avalanche forces the silicon to the point of being conductive, effectively amplifying the initial pair into a macroscopic flow of current which is the signal. To restore the SiPM ability to detect a photon, the current is halted by the mean of a quenching resistor (R_q) made in polysilicon or aluminium connected to the SPAD. This limits the current drawn and lowers the breakdown voltage seen by the diode, eventually applying a voltage below the V_{bd}, effectively switching it off. After the quench, the effective voltage applied rises back to the nominal applied value, making the SPAD ready to detect a new incoming photon. It is worth noting that this single SPAD cannot discriminate how many photons are responsible for initiating the avalanche.

The lack of proportionality is overcome by integrating large arrays of independent SPAD connected in parallel into a sensor, each with their own quench resistor, referred to as microcells. Now, the single SPAD firing will let current flow until fully quenched and lastly recover the nominal voltage, ready to be fired again: in this process all other microcells stay ready to fire in parallel. A usual SiPM has between a hundred and several thousands microcells that together contribute to the full signal.

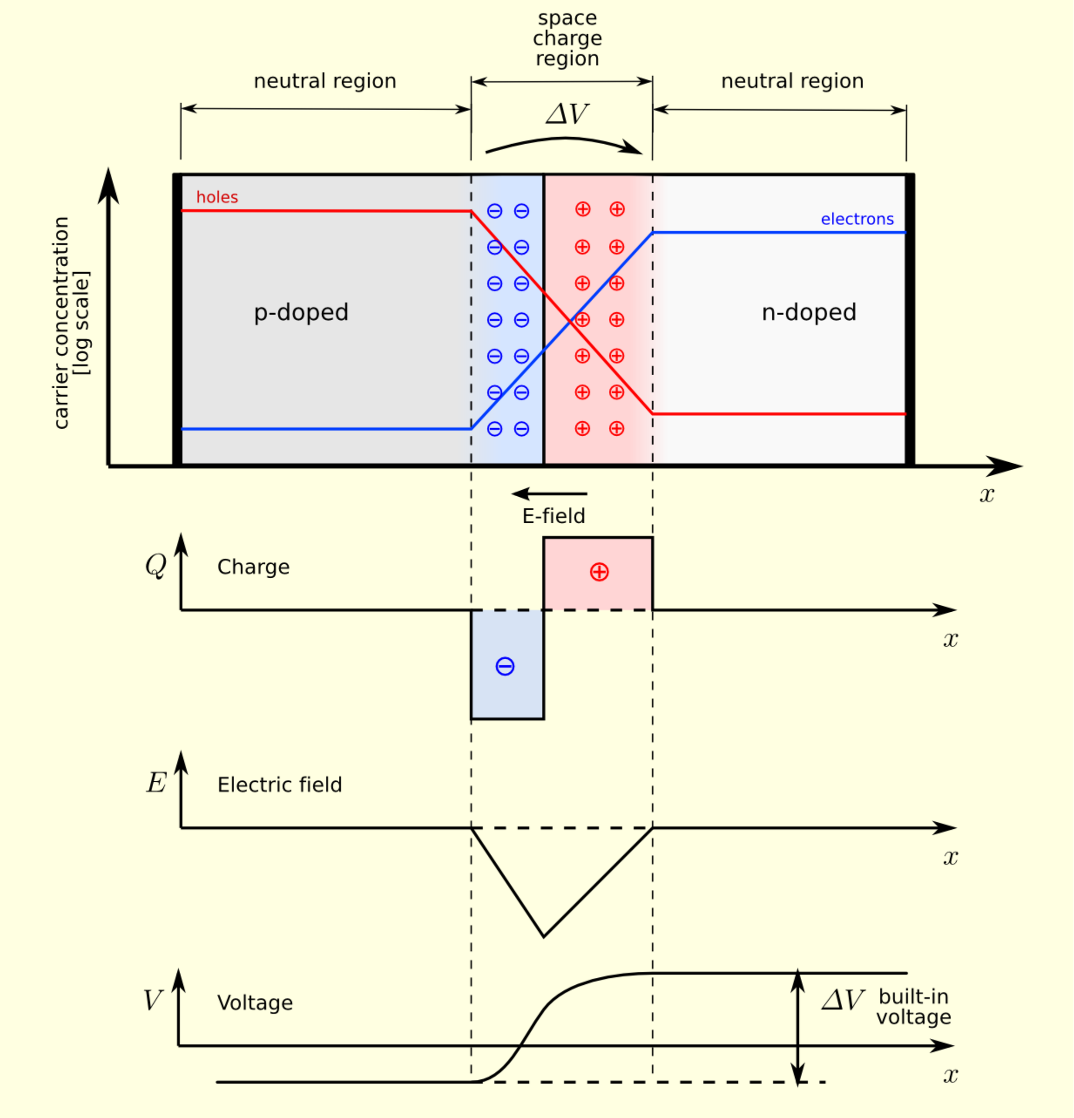

FIGURE 4.3: A PN junction in thermal equilibrium with zero bias voltage applied. Electron and hole concentrations are reported respectively with blue and red lines. Gray regions are charge neutral. Light red zone is positively charged. Light blue zone is negatively charged. Under the junction, plots for the charge density, the electric field and the voltage are reported. Note that the image depicts the red depletion region in the N-doped material going deeper (with a greater area) than the blue depletion region in the P-doped material, which is explained by a higher N-doped density. Figure taken from [224].

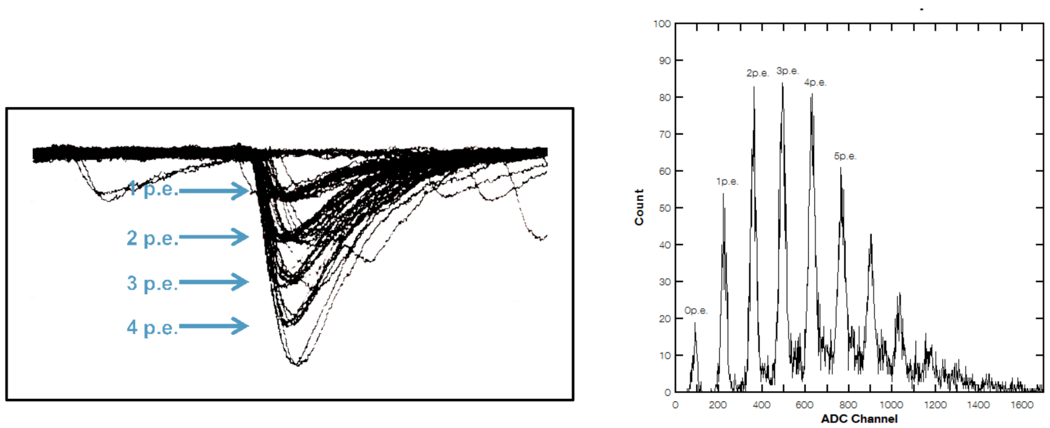

(A) Oscilloscope Shot Showing the Discrete Nature of the SiPM Output when Illuminated by Brief Pulses of Low-level Light

(B) Photoelectron Spectrum of the SiPM, Achieved using Brief, Low-level Light Pulses, such as those from Figure 4.4a

FIGURE 4.4: Figures taken from [225]

Combined they give a quasi-analog output that carries information on the incoming photon flux. Information is quantised in the characteristic signal (example in Figure 4.4a) and in the integrated charge plot, the so-called finger plot (example in Figure 4.4b).

Defining characteristics of the SiPM are the dynamic range and linearity. The dynamic range is defined as the optical signal range over which the sensor provides a useful output. The sensor has a linear response at lower photon fluxes, but as the number of incident photons increases the sensor output becomes non-linear. This deviation from linearity is linked to the total number of microcells in the sensor: more microcells result in a larger dynamic range. Therefore, for a given sensor size, smaller microcells will result in a larger dynamic range than larger microcells. A general rule of thumb to maintain an approximately linear response, is to match the maximum expected power to 70% of the SiPM range.

Another characteristic of SiPMs is the so-called fill factor. The fill factor refers to the percentage of surface area that is sensitive and able to detect light. This is derived by the need to isolate microcells both electrically and optically. Then these boundaries are not sensitive to incoming light, reducing acceptance. Fill factor can go up to 80% for larger cell sizes, with smaller cells having a lower fill factor that can go as low as 25%.

Despite the many advantages, they also have two main drawbacks that are especially of concern in high energy physics applications. Due to the nature of the microcell, being a carefully crafted layer of silicon with a target doping concentration, incoming non-ionising radiation make displacements in the lattice that will result in disruptions of the energy levels of the electrons. This makes these devices particularly susceptible to radiation damage. This will be the topic of sec. 4.3.4. On top of that, being highly sensitive detectors they suffer from high level of noise at room temperature.

4.3.2 Performance parameters

The SiPMs can be characterised with a few main components that describe most of their behaviour. By measuring these quantities one can fully characterise the sensor and understand its response to light signals.

Breakdown voltage and overvoltage

The breakdown voltage is the voltage necessary to allow Geiger avalanches in the silicon. Strictly related is the overvoltage ($\mathrm{V_{over}}$), how much voltage is applied ($\mathrm{V_{bias}}$) above this breakdown threshold ($\mathrm{V_{over}} = \mathrm{V_{bias}} - \mathrm{V_{bd}}$). Finding the Breakdown Voltage has its challenges as it relies on finding the start of the steep increase in current as a function of the applied voltage. This is done in a current-voltage plot (I-V) and can be performed in many ways [226]. The optimal value of operation for the overvoltage is given in the datasheet for the detector and is usually around 10-15% of the $\mathrm{V_{bd}}$, but no more than 4-5 V.

The $\mathrm{V_{bd}}$ is sensitive to temperature, usually shifting linearly by a few tens of mV per °C. Temperature also affects dark current, so a measurement at a higher temperature or in a light filled environment could yield a better result, as the increase after the $\mathrm{V_{bd}}$ is steeper and more accurately measurable. The radiation damage, on the contrary, has been proven not to affect the breakdown voltage below $\approx 10^{12}$ $\mathrm{n_{eq}}$ threshold [215].

Gain

The gain (G) is defined as the amount of charge created by each detected photon and is the same for all microcells. The gain of the microcell, hence of the sensor, is defined as the ratio of the charge integrated in the signal waveform and the elementary charge. This can be measured knowing the microcell capacitance, the applied $\mathrm{V_{over}}$ and the elementary charge as follows:

$$\mathrm{G} = \frac{C \times \mathrm{V_{over}}}{q} \tag{4.2}$$

Gain can also be measured by using the quantised signal (Figure 4.4a). We have seen how the signal is quantised from one to n photons detected. Then, the difference between a single photon peak and a two-photon peak will give the charge integrated on the single microcell.

At constant overvoltage, that is correcting for the shift in breakdown voltage due to temperature, the Gain does not depend on the temperature. The Gain also does not depend on the radiation level received up to medium-level radiation of $\approx 10^{12}$ $\mathrm{n_{eq}}$ [215].

Photon Detection Efficiency (PDE)

The photon detection efficiency refers to the probability of a photon to be detected when hitting the sensor surface. The first factor that comes into play is the fill factor, defining the geometrical acceptance. The second effect that needs to be taken into account is the quantum efficiency, defined as the probability for a photon to generate an electron-hole pair. The quantum efficiency depends on the light wavelength, different SiPMs are used for different applications depending on the spectrum of the expected light. Electrons are more efficient at producing an avalanche, so the overall chance of detecting the photon is higher if the e^--hole is produced in the p-layer. This is because the electron then needs to travel a longer distance, enhancing its probability of producing an avalanche. It is then straightforward that n-on-p sensors are more sensitive to longer wavelengths (longer mean free path) and p-on-n sensors are more sensitive to shorter wavelengths (shorter mean free path) [225].

The Photon Detection Efficiency does not depend on the temperature. The PDE also does not depend on the radiation level received up to medium-level radiation.

4.3.3 Main sources of noise

Dark Count Rate (DCR)

Dark Count Rate (DCR) is the production of signals that are not derived by incident photons. These signals are indistinguishable from photon induced signals, posing as a significant noise source for single photons detections. They are mainly due to thermal production of electrons and holes in the sensitive volume of the detector and their main drivers are overvoltage, active area and temperature.

This effect is usually quoted as a frequency of false hits (Hz) or frequency per unit area ($\mathrm{Hz/mm^2}$) and can be measured with a simple counting system setting a threshold at roughly half the peak of single photon signal. The measurement should be performed in a dark environment to exclude light detection contributions to the DCR. It is directly related to Dark Current, which is the charge integrated result of DCR.

At constant overvoltage the DCR shows a strong dependence on temperature, roughly doubling per each 5-10 °C increase. DCR increase is also the main drawback of radiation damage, possibly dealing with frequency increased of several orders of magnitude in irradiated sensors [215].

Optical cross-talk

Optical cross-talk is a phenomenon by which the firing of a microcell also generates a signal in a neighbouring cell. This, for example, can come from the emission of a photon by an accelerated carrier in the primary avalanche. The photons emitted are in the near infrared region (NIR) which gives them roughly an emission rate of 10^{-5} NIR photons per electron crossing the junction. After being emitted, the photons can either generate an avalache in an adjacent microcell right away (a) or be reflect in the window (b) or in the silicon substrate (c) as shown in Figure 4.5a

In general by cross-talk it is intended the probability of an avalanche firing a second microcell and can result in two, three or even more cells firing simultaneously. This effect can be measured analysing the signals of the SiPM in complete darkness, where all signals are thermally produced and no 2-photons signals are expected. In this setting, a threshold scan can be performed and a plot with plateaus will show when there is a crossing between photon peaks. By measuring the rates of single and 2-photons once can derive the cross-talk probability [215].

Afterpulsing

Afterpulsing is a phenomenon by which the carrier can be trapped in a silicon defect, delaying its drift to the cathode (anode) up to a few ns. When the carriers are released they have a small probability of generating a new avalanche: if the delay is short it occurs during the recovery time of the microcell and tends to have negligible impact as the microcell is not fully charged, if the delay is longer it can impact measurements, especially if the rate is high.

This effect can be measured analysing the time difference distribution of consecutive DCR signals.

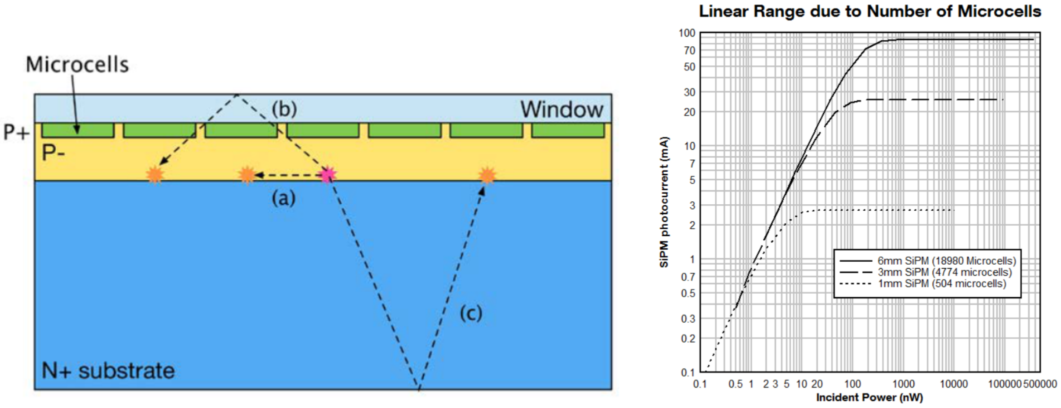

(A) An Illustration of the Various Ways in which Secondary Photons can Travel to Neighbouring Microcells to Cause Optical Crosstalk

(B) The SiPM Photocurrent as a Function of Incident Power on a Log‚àílog Scale. The SiPM Maintains a Linear Response at Higher Levels of Incident Light when there are more Microcells

FIGURE 4.5: Figures taken from [215]

4.3.4 Radiation damage

Silicon Photomultipliers rely on carefully crafted doping of silicon and engineering of silicon and insulating layers and thus are particularly sensitive to radiation that disrupts the silicon lattice, introduces defects or distorts doping. The two main categories of radiation damage are Bulk damage due to Non Ionizing Energy Loss (NIEL), and surface damage due to Ionizing Energy Loss (IEL) [215].

NIEL Damage

NIEL Damage primarily comes from high energy particles such as protons, photons and neutrons which can displace a silicon atom from their lattice site creating defects and leaving gaps. The minimum energy for such an effect is $\approx\ 25\,\mathrm{eV}$ and the first displaced atom is referred to as the Primary Knock-on Atom (PKA). When the PKA energy is above $\approx 1\,\mathrm{keV}$ it can displace in turn additional atoms, forming clusters of defects, and if the energy is above $\approx 12\,\mathrm{keV}$ multiple-cluster defects can be form. A simple hypothesis for the description of the damage is that the radiation damage is proportional to the non-ionizing energy loss of the penetrating particles (radiation) and this energy loss is again proportional to the energy used to dislocate lattice atoms (displacement energy). This of course does not take into account many other possible effects such as annealing, atom transformation, etc. but it is accurate enough for practical purposes. However, different effects (leakage current, doping concentration, charge collection efficiency) require different NIEL coefficients to describe their scaling as a function of fluence. The damage functions for various particle types and energies are discussed in [227]. It provides a hardness factor k for each particle type, allowing to compare the damage efficiency of radiation sources with different particles and energy spectra $\Phi(E)$.

The main effect of the radiation damage is the creation of energy levels that interferes with the proper working of the sensor. On a new sensor, the energy gap between valence and conduction band is $\approx 1.12\,\mathrm{eV}$ (E_g), depending on what energy levels the damage introduces, a variety of effects may arise (Figure 4.6a):

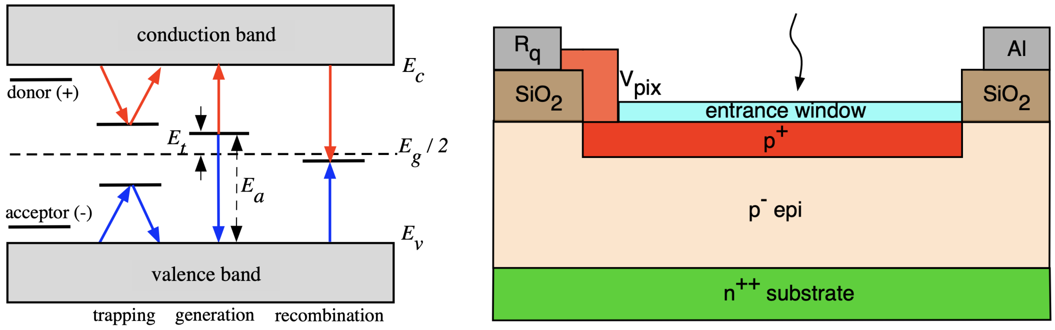

(A) An Illustration of the Various Ways in which Secondary Photons can Travel to Neighbouring Microcells to Cause Optical Crosstalk

(B) Schematic crosssection of a possible single pixels blue sensitive SiPM. The poly-silicon quenching resistor Rq and the Al-contact line are isolated from the silicon via a SiO_2 layer. A typical anti-reflecting coating material used for the entrance window is Si_3N_4.

FIGURE 4.6: Figures taken from [215]

- **Increase of leakage current** comes from the introduction of levels roughly halfway through the bands ($E_g/2 \approx 0.56\,\mathrm{eV}$) that facilitates the thermal excitation of carriers.

- **Decrease of signal** comes from levels closer to the bands which traps the carriers. If the trapping is not close enough to the bands, the de-trapping time can be long enough for the carrier not to contribute to the signal. Moreover this late de-trapping increases afterpulsing.

- **Change of effective doping energy** Depending on their occupation, defect states contribute to the effective doping, and thus to the electric field in the amplification region. The occupation depends on the density of free charge carriers, on the dark current, and on the distance of the defect state from the band gap. In addition, the radiation removes dopant atoms by nuclear interactions. These effects have an impact on the depletion region and the breakdown voltage.

IEL Damage

The ionisation damage in the sensors is mainly limited to window defects. Photons under $300\,\mathrm{keV}$ are below the bulk damage threshold and provide only surface damage [228].

The introduction of window defects can generate surface currents below the breakdown voltage, that might reach the amplification region contributing to DCR, depending on the sensor configuration.

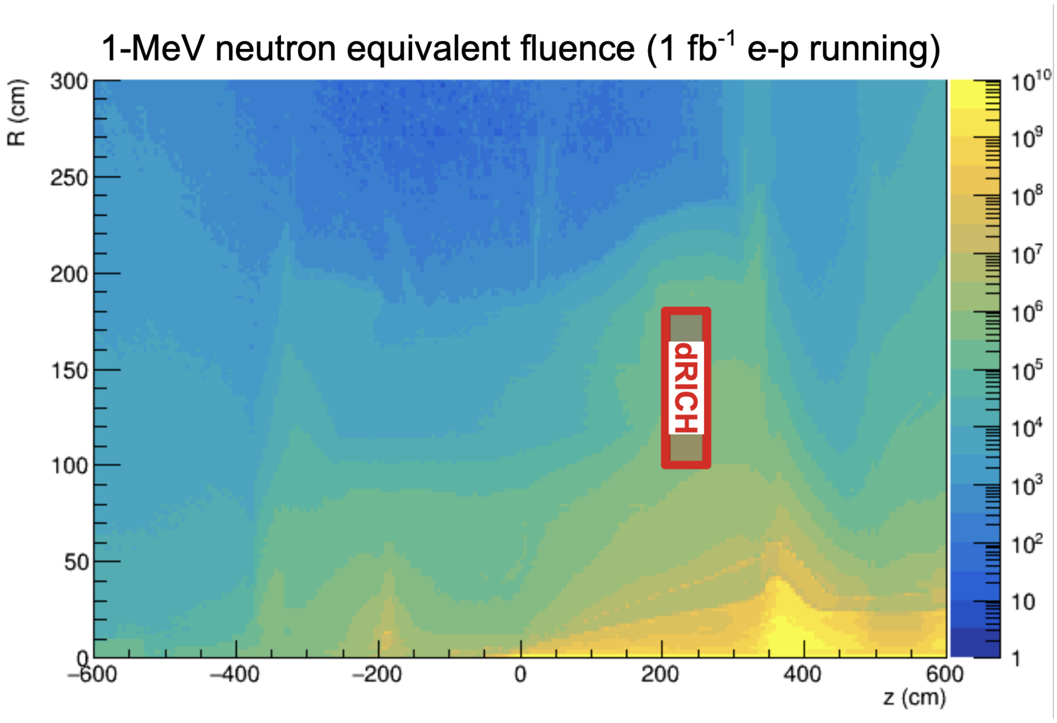

FIGURE 4.7: Pythia simulation of e-p events to evaluate the radiation fluence in the ePIC detector with highlighted the position of the dRICH sensors.

4.4 Characterisation of radiation damage and recovery through annealing of SiPMs in a dRICH prototype

The efforts of the EIC group in Bologna are devoted to the study of the radiation damage in SiPMs and their usability for Cherenkov imaging application up to fluences of 10^{11} $\mathrm{n_{eq}}$.

Figure 4.7 show the expected fluence in the ePIC detector per each fb^{-1} of luminosity, which highlights a moderately irradiated emplacement for the dRICH light sensors. The average expected radiation is $\approx 4{\cdot}10^5$ $\mathrm{n_{eq}}$ fb^{-1}, with a maximum of $\approx 10^6$ $\mathrm{n_{eq}}$ fb^{-1}. If we consider a safety factor 10, the maximum fluence becomes $\approx$ 10^7 $\mathrm{n_{eq}}$ fb^{-1}. The luminosity requirements for the key physics goals is $10\,\mathrm{fb}^{-1}$ per each configuration of energy and polarisation, which translates in an expected $\approx 10^9$ $\mathrm{n_{eq}}$ radiation that the sensors need to withstand. Including in the forecast the requirements for the nucleon imaging programme the expected fluence is increased of another factor 10 to $\approx 10^{10}$ $\mathrm{n_{eq}}$ to integrate a total of $100\,\mathrm{fb}^{-1}$ of data. Lastly, if one considers the expected 10-12 years of operation, a grand total of $1000\,\mathrm{fb}^{-1}$ of data is expected, meaning a lifetime total of $\approx 10^{11}$ $\mathrm{n_{eq}}$, which is the goal.

Considering the number of channels, the performance limit that is required for a fruitful datataking is $300\,\mathrm{kHz/mm^2}$, which corresponds to 10 hits of noise per sector in a $500\,\mathrm{ps}$ window. This target can be achieved through a number of ways by which the DCR can be reduced, such as temperature, timing and annealing procedures.

Figure 4.8 shows how the performance of a SiPM sensor could degrade if no intervention is done, if recurrent online annealing is performed and if a recurrent online annealing is followed by a more aggressive oven annealing off-site.

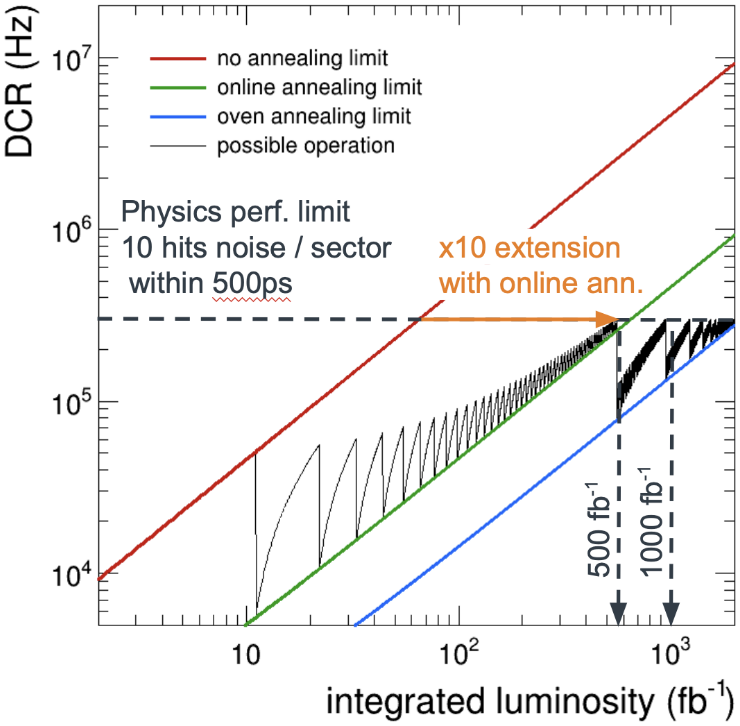

FIGURE 4.8: Expected degradation of SiPMs performance for various cases. The no-annealing, online annealing and oven annealing limits are reported, compared to physics performance limits as a function of integrated luminosity.

4.4.1 Tested sensors

A list of tested sensors can be found in Table **??**. Custom carriers boards have been designed to host the SiPMs under test, arranged in a matrix of 4x8 of 3x3 mm^2 sensors (Figure 4.12a). The board was carefully designed to withstand annealing and irradiation procedures for the tests together with having a form factor that is usable for imaging in beam tests. All boards were carrying two types of sensors as reported in Table **??**, the boards provided by Fondazione Bruno Kessler (FBK) carried 4x6 sensors due to the size of the sensors' window. The HAMA1, HAMA2, FBK, SENSL boards have been used in the 2021 and 2022 campaigns, after the preliminary results of these R&D efforts, the HAMA3 boards have been designed for the 2023 campaign.

A number of boards have been irradiated to different levels of radiation fluence.

4.4.2 Characterisation and annealing at SiLab

A new facility has been set-up in Bologna by the local branch of National Institute for Nuclear Physics (INFN), called the Silicon Laboratory (SiLab), where researchers working on Silicon detectors can work together to build a common know-how and exchange results.

In the context of this newborn facility, through the years a number of instrumentations and equipments have been adopted to build a fully operational laboratory that can swiftly and reliably characterise SiPMs, together with multiple annealing stations. We presently can anneal boards in three ways.

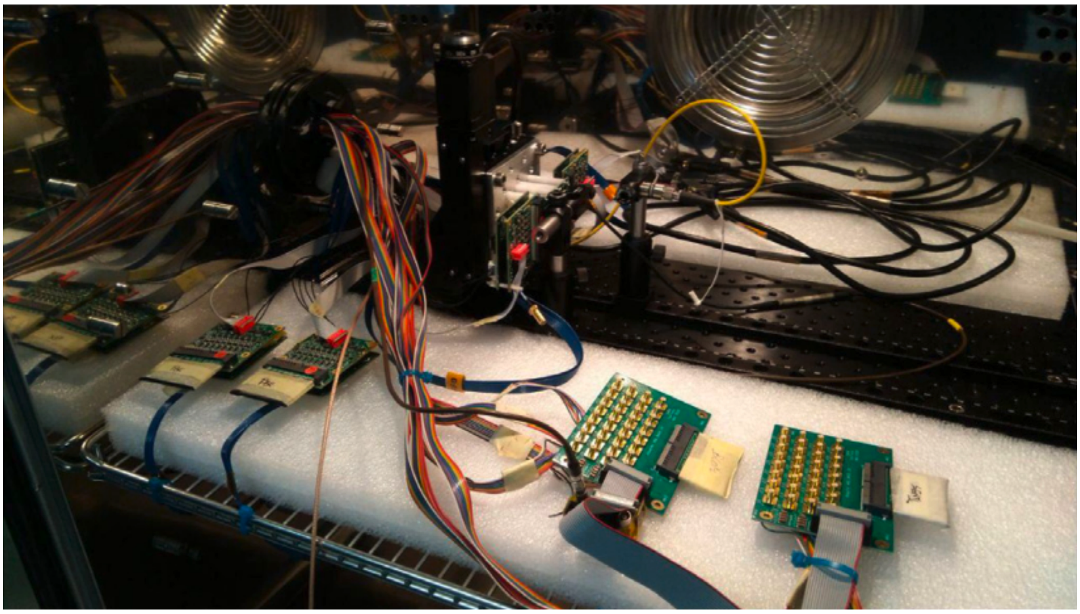

FIGURE 4.9: Characterisation stations inside the climatic chamber. (Left) The DCR setup with ALCOR chip readout (Right) the I-V setup with a multiplexer attached to a Keithley multimeter.

Characterisation at SiLab

Characterisation at SiLab is performed in a climatic chamber with controlled temperature and humidity levels. The chamber is continuously flowed with dry air that has a dew point of 203 K (−70 °C) to avoid humidity to frost on the electronics when operating in sub-zero temperatures. Inside the chamber four parallel stations are present, two for DCR measurements and two for I-V measurements, which are the two main ways we use to characterise the sensors. A photo of such setup can be seen in Figure 4.9

DCR measurements are taken with a full functioning readout chain relying on the ALCOR ASIC chip [229] that is programmed and read by a Xilinx Kintex-7 FPGA KC705 evaluation board controlled by a Linux PC.

I-V measurements are taken with a multiplexer attached to a Keithley 2450 source meter. All of the measurements are fully automated by bash scripts on a Linux PC dedicated to DAQ procedures. The automation includes temperature changes, measurements and QA plots sent at all steps via e-mail to all operators.

Characterisation on the go

Characterisation on the go is performed by the so-called AirBox (Figure 4.10), a prototype relying on external dry air supply to avoid frost at subzero temperatures. The temperature control is provided by a humidity and temperature sensor in the box, together with a temperature sensor on the SiPMs to control the operational temperature and dew point. Peltier cells provide local temperature drops down to ≈243 K (≈−30 °C) depending on external temperature. This solution was devised to involve other institutes willing to participate in the characterisation efforts without necessarily investing large amounts of money, the box costing under 1’000€.

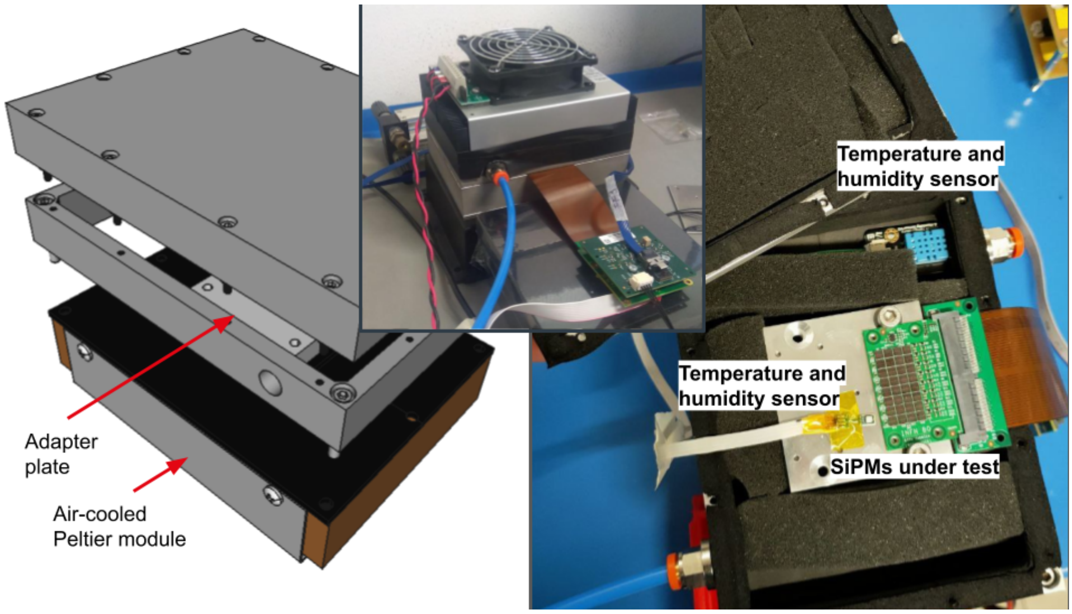

FIGURE 4.10: Schematics and photos of the AirBox on–the-go characterisation device.

Oven annealing

Oven annealing is performed by placing boards in a timed oven. This is the most invasive procedure as it requires long periods of time (≈ days, weeks) and thermalisation time (≈ 1 day) at the end of the cycle.

Forward annealing

Forward annealing is taking advantage of the thermal power dissipation by large currents flowing in the sensor while in forward mode, when the sensor essentially behaves as a diode in series with the parallel of the quenching resistor. By the means of a thermal camera[2] we control the power delivered to attain a stable temperature, by the mean of a PID[3] system.

Reverse annealing

Reverse annealing is performed essentially switching the sensors on, delivering a voltage above the V_{bd} and shining a bright light onto the SiPMs to have a large current flow. This essentially does a similar effect as the forward case. The temperature is also monitored by a FLIR thermal camera to avoid drifts that may severely damage the sensor. The temperature monitor is of utmost importance as above 200 °C the sensor and soldering could get compromised.

Online and Offline annealing

Online and Offline annealing are the two technique that are under investigation. Online annealing is performed without unmounting the sensors from the detector. Offline annealing is more effective but requires the sensors to be unplugged from the detector.

---

[2] In the stable configuration we are using a FLIR A400

[3] Proportional-Integral-Derivative controller

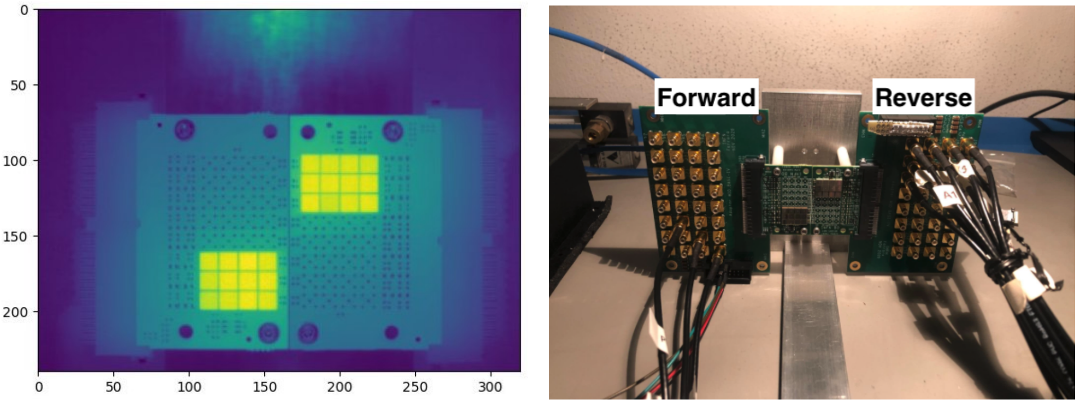

(A) SiPM boards undergoing Forward/Reverse annealing as seen by the thermal camera.

(B) SiPM boards on the annealing system, on the left the forward setup and on the right the reverse setup.

FIGURE 4.11: Forward/Reverse annealing setup as seen by an observer and by the thermal camera.

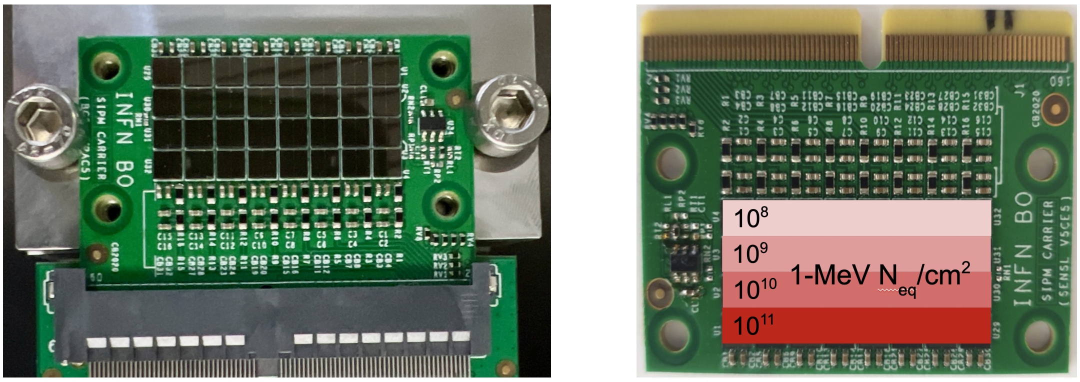

(A) SiPM custom carrier board

(B) Schematic representation of the levels of irradiation of one board for the 2021 campaign.

FIGURE 4.12

4.4.3 Irradiation at TIFPA and LNL

Irradiation campaigs have been undertaken at Trento Institute for Fundamental Physics and Applications (TIFPA) for proton damage and at Legnaro National Laboratories (LNL) for neutron damage research.

4.4.4 2021 Campaign: analysis of different irradiation levels and light response

The first campaign of irradiation took place at the TIFPA facility. The main objective was to have a first look at the radiation damage on the selected sensors: HAMA1, HAMA2, FBK, SENSL. These were mounted on carriers such as the one shown in Fig. 4.12a and irradiated as shown in 4.12b.

ID	Name	Target curve	Description
01	Linear fitting	I	Intercept of linear fit to the baseline and linear fit to the exponential rise
02	Parabolic fitting	I	Intercept of linear fit to the baseline and parabolic fit to the exponential rise
03	Exponential fitting	I	Intercept of linear fit to the baseline and $(x - x_0)^a$ fit to the exponential rise
04	Tangent	$\ln(\mathrm{I})$	Intercept of linear fit to the baseline and linear fit to the exponential rise
11	Relative derivative	$\frac{\mathrm{d}}{\mathrm{dV}}\ln(\mathrm{I}) = \frac{\mathrm{I}'}{\mathrm{I}}$	Take the curve maximum
12	Inverse relative derivative	$\left(\frac{\mathrm{d}}{\mathrm{dV}}\ln(\mathrm{I})\right)^{-1} = \frac{\mathrm{I}}{\mathrm{I}'}$	Fit linearly the rise and measure the intercept with the x-axis
21	Second derivative	$\frac{\mathrm{d}^2}{\mathrm{d}^2\mathrm{V}}\ln(\mathrm{I})$	Take the curve maximum
31	Second derivative	$\frac{\mathrm{d}^3}{\mathrm{d}^3\mathrm{V}}\ln(\mathrm{I})$	Take the curve maximum
101	Tangent	DCR	Intercept of linear fit to the baseline and linear fit to the exponential rise

TABLE 4.1: List of V_{bd} measurement methods implemented in the analysis code. Expanded from the methods listed in [230].

Characterisation of radiation damage

The characterisation consisted in measuring IV curves and DCR with the ALCOR chip, but the process was more tedious as the automation was not yet available in the SiLab. The first results were aimed at understanding how to treat the data, namely to start measuring basic quantities such as V_{bd}. We then developed a number of ways to measure the breakdown voltage, such as the ones listed in Table 4.1, mainly taken from [230]. From now on the methods are going to referred to by their ID.

The first set of sensors that were analysed were the FBK. An example of the analysed IV-curves can be seen in Figure 4.13. The V_{bd} was measured using the method 03 for all sensors. Each board had 8 sensors at the same level of irradiation, with 4 of the same kind. In this case we have 4 FBK NUV-HD-CHK sensors and 4 FBK NUV-HD-RH (See Tab. **??**).

First we examine the effect of the radiation on the V_{bd}. As we have seen so far, this is a crucial quantity for the correct operation of the sensors in the experiment. In fact, the overvoltage largely defines the detector response to light. It is thus not ideal that the V_{bd} could change as a result of the radiation damage. To this end and analysis of the breakdown voltage as a function of irradiation levels is shown in Figure

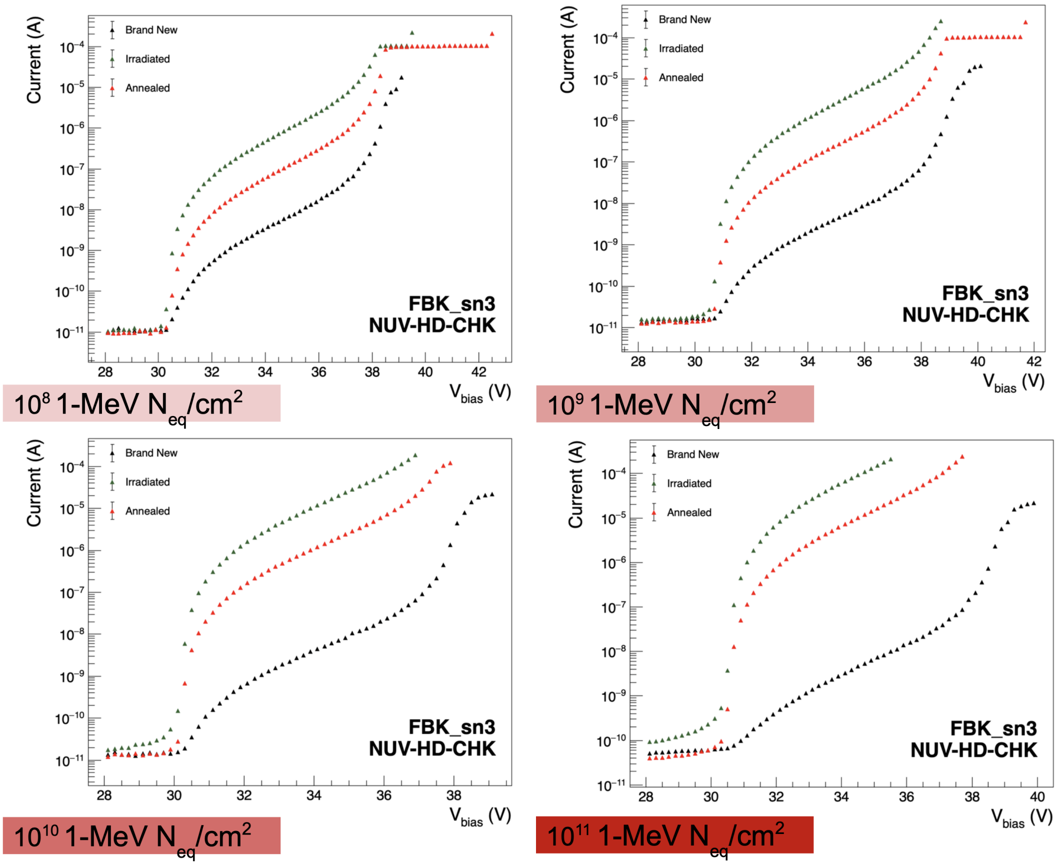

FIGURE 4.13: IV-curves of one FBK NUV-HD-CHK sensor as brand new (black), irradiated (green) and after subsequent annealing (red). The level of irradiation is reported on the figure.

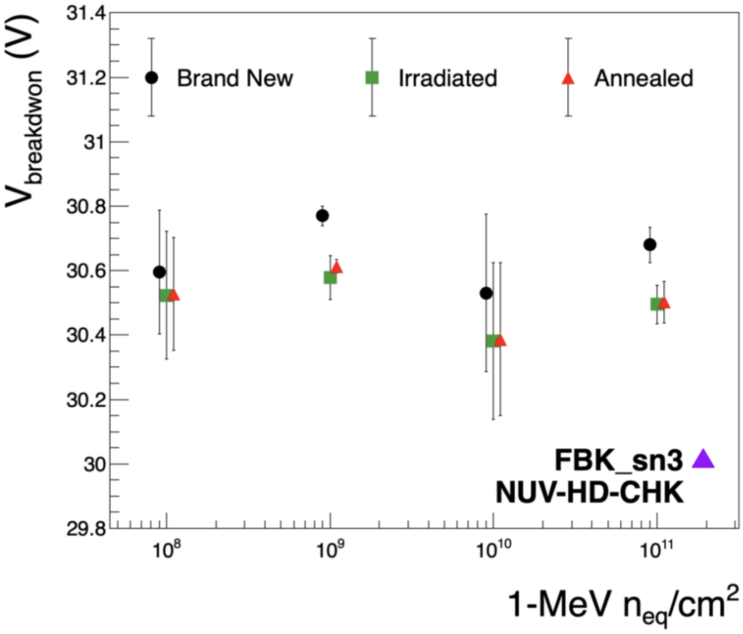

FIGURE 4.14: Measured V_{bd} of the FBK-HD-CHK sensors as a function of the radiation delivered. Error bars represent the RMS of the sample.

4.14. The general trend is that irradiation and annealing do not seem to consistently affect the V_{bd}. It is worth noting that the y-scale is very limited, spanning $1.6\,V$ in total, so the fluctuations are all within $0.4\,V$, consistent with the RMS of new sensors in the most spread case scenarios reported here (See new sensors of 10^8 n_{eq} and 10^{10} n_{eq}). This result is consistent with state-of-the-art knowledge [215].

After we have established the stability of V_{bd} with radiation, we can take a look at the background noise levels, together with the potential recovery with the oven annealing technique. Figure 4.15 shows the dark current measured as a function of the radiation received by the sensor. The measurements were performed at a fixed overvoltage of V_{over} $=3\,V$ and at a fixed temperature of T = $-30\,°C$. This was our first promising result of a significant performance recovery by the means of the annealing technique.

Afterward, a broader study was performed on all sensors with a more aggressive annealing. The results are shown in Figure 4.16. We can see that the softer (a little less time at a lower temperature) annealing shown in Figure 4.15 recovers halfway between a factor 10 and a factor 100, whereas a more aggressive annealing shown in Figure 4.16 recovers a factor 100 in dark current.

Characterisation of light response

A second line of R&D was the development of a testing station for the sensor light response. A first attempt was done at the start of 2022 by analysing the HAMA1 (See Tab. **??**) boards. This was also the subject of a bachelor degree thesis, where a more detailed description is given [231]. The setup schematics is shown in Figure 4.17. The setup was based on a green LED light of $\approx 1\,mm^2$ pulsed by a custom function generator, set to send impulses at a given frequency. Then, the sensor rate was measured when the LED was off (Rate off) and when it was on (Rate on). The

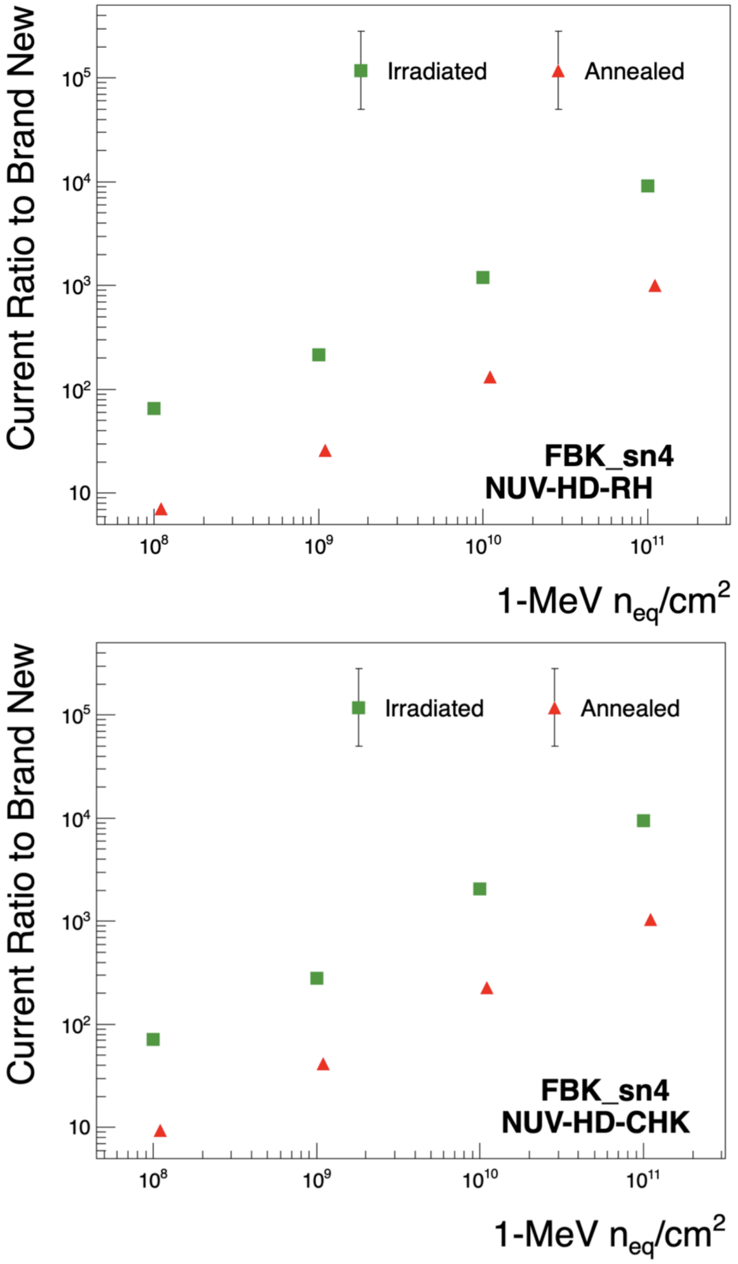

FIGURE 4.15: Measured current ratio to brand new sensor of the FBK-HD-CHK/RH sensors as a function of the radiation delivered. Error bars represent the statistical uncertainty. The measurements are taken at T = $-30\,^{\circ}$C. The annealing was done at $100\,^{\circ}$C for 24h and then at $125\,^{\circ}$C for 168h.

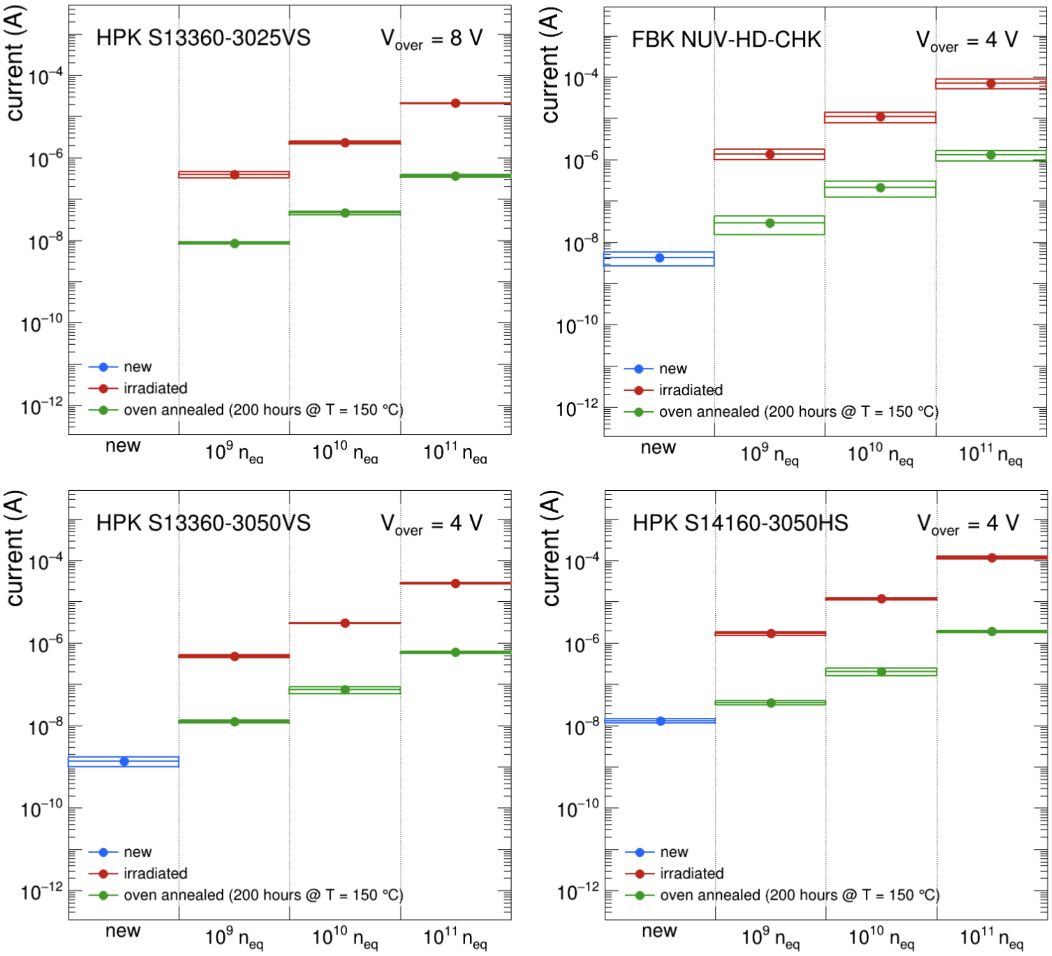

FIGURE 4.16: Measured dark current for a selection of sensors as a function of the radiation delivered. Error bars represent the statistical uncertainty. The measurements are taken at $V_{\text{over}} = 3\,\text{V}$ and at $T = -30\,^{\circ}\text{C}$.

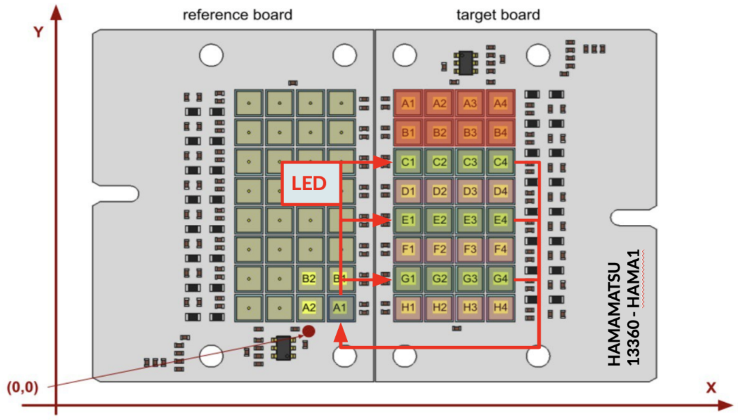

FIGURE 4.17: Schematic representation of the light test setup. The left carrier has 4 sensors that are devoted to calibration, the right sensor has a full board and is the Device Under Test (DUT). Limitations on the available instrumentation of the time made the A and B rows unaccessibles. The protocol for the measurement starts at the reference sensor A1 to evaluate any possible systematic variations. Then, it proceeds to move to the first reachable sensor, C1. Afterwards all the row is measured, before stopping back to the reference A1 and start again on the next row, E. The measurements go every two rows as each alternate row is mounted with one or another of the 2 sensors mounted on the board.

difference of (Rate on - off) is then taking as a proxy for the light detection efficiency, when normalised to the pulser set frequency (100 kHz).

Figure 4.18 shown on top the stability measurements performed at the start of 2022. The measurements were repeated in different days to test the system stability. In the bottom panel the measurements of light detection pseudo-efficiency are reported for the HAMA1 sensors. The setup, although preliminary, was already showing promising results of stable and consistent measurements.

4.4.5 2022 Campaign: test of repeated and new online annealing, calibration of ALCOR fine tune

The second campaign of irradiation took place at the TIFPA facility. The main objective was to study more accurately the power of annealing recovery of sensor performance towards possible applications of in-situ annealing in the final experiment. New ways to anneal were tested, such as the online annealing in forward current. The selected sensors were HAMA1, HAMA2, FBK, SENSL.

Characterisation of repeated annealing

The main topic for the 2022 campaign was to understand the effects of alternated irradiation and annealing cycles. To this end, a series of irradiation shots (10^9 $\mathrm{n_{eq}}$) were performed at TIFPA with proton beams, alternated with annealing cycles in oven of 150h at 150 °C. The results are shown in Figure 4.19.

The first result was that the damage is not fully recovered. We remind that the oven annealing represents, up to the time of writing, the most effective recovery, likely setting an absolute lower bound for the background reduction. The annealing restores up to 97% of the performance when considering the new detector with

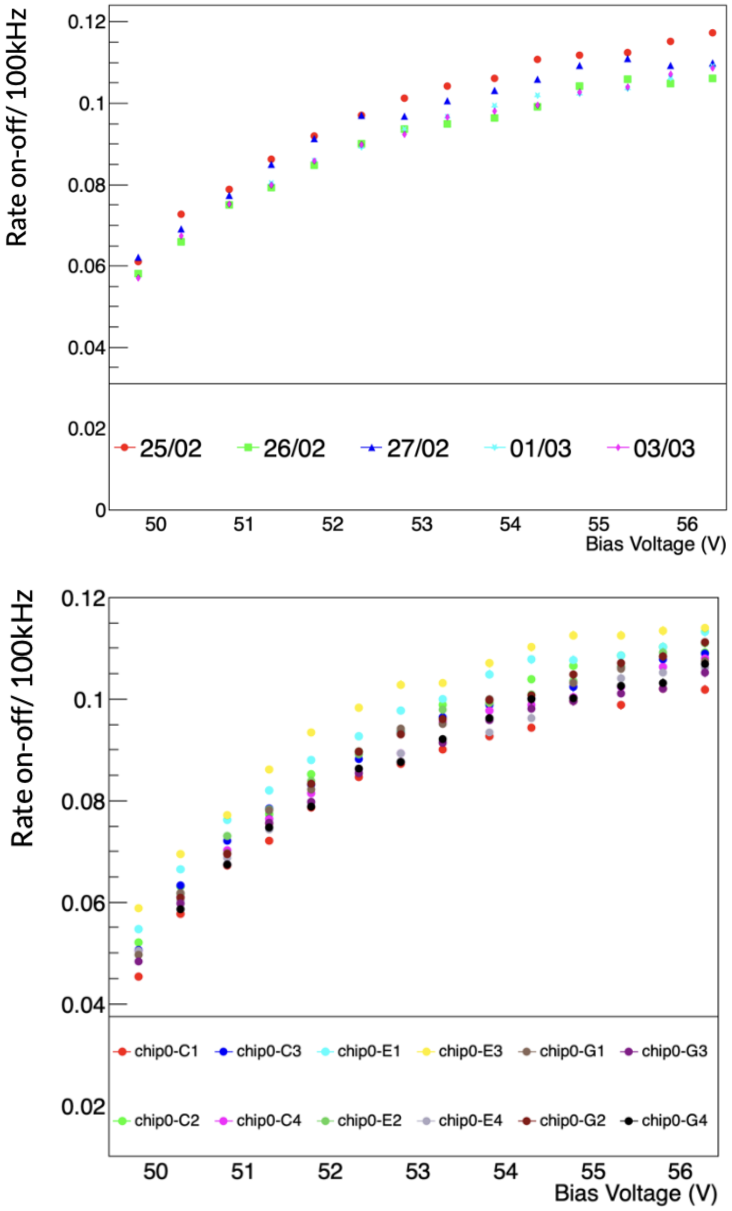

FIGURE 4.18: Pseudo light efficiency measurement for the HAMA1 sensor. (top) stability measurement (bottom) measurement of each sensor

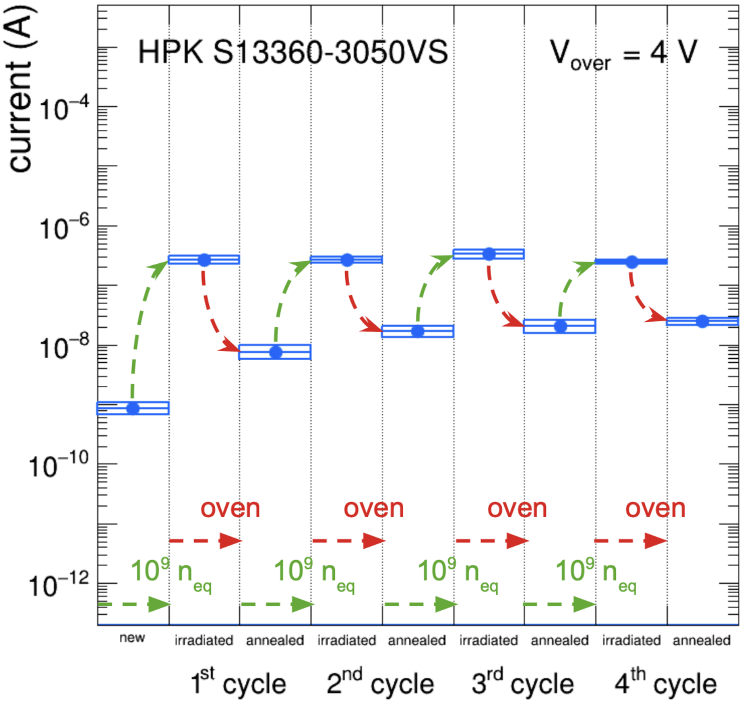

FIGURE 4.19: The performance degradation and recovery of the HPK S13360-3050VS in each cycle of alternating irradiation and annealing.

respect to the first irradiation session. This ≈ 15 kHz residual background build-up can be appreciated in Figure 4.19.

Characterisation of online annealing

The online annealing test consisted in an alternating pattern similar to the one described in Section 4.4.5. The sensors where first irradiated with a 2×10^8 $\mathrm{n_{eq}}$, then it was subjected to 1800 s annealing using the online procedure. In the online procedure the sensor was forward biased gradually until the temperature reached 175 °C. We reached around 10 V with a 100 mA for a total of about 1 W power delivered. The cycle was repeated 5 times to integrate the same level of radiation, 10^9 $\mathrm{n_{eq}}$ as the reference annealed sensor.

The results shown on the left of Figure 4.20 are that the recovery achieved is of a factor 10, that is an order of magnitude less than the oven annealing could achieve (Figure 4.16). Nevertheless this is a very promising result, as damage recovery is not the only aspect we are interested in: despite having less leverage for recovery, online annealing provides an approach that in principle does not require the sensors to be unmounted from the experiment. As a consequence of this very useful feature, the *in situ* approach also has the possibility to be performed with a high frequency during the EIC accelerator machine down time.

ALCOR fine tune calibration

This topic was also the subject of a master thesis, a more detailed description of the procedure and analysis can be found in [232]. The ALCOR chip used for the readout of the SiPMs works with a clock frequency of 320 MHz. To achieve a resolution smaller than the clock cycle (≈ 3 ns), an analog interpolation system is implemented. Every TDC has a *fine tune* information that needs calibration to become a *clock phase*,

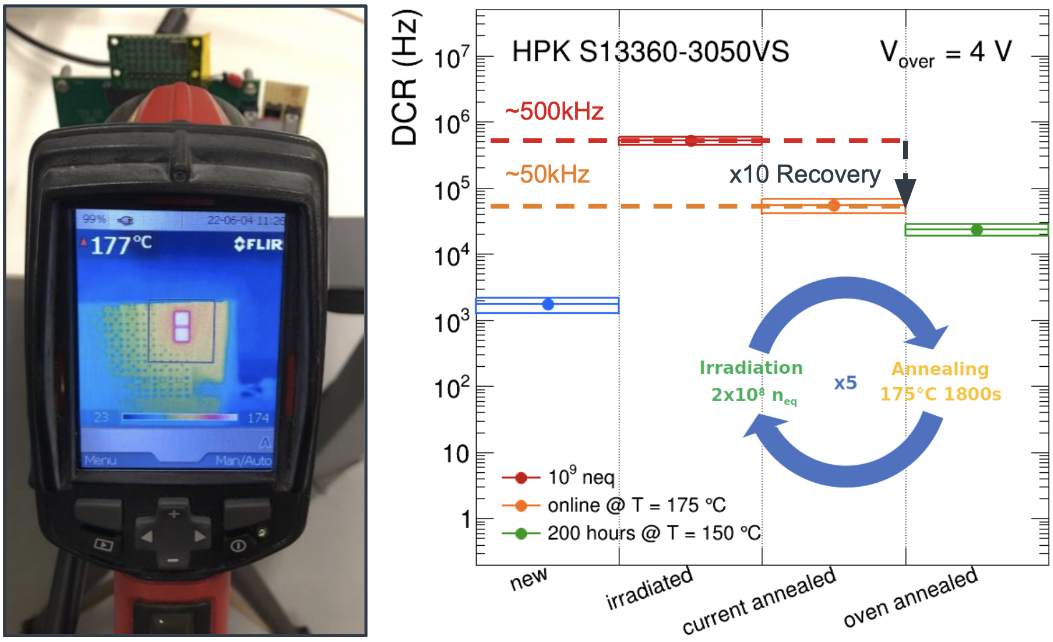

FIGURE 4.20: (left) monitoring of the sensor temperature during the online annealing procedure, (right) results of the repeated online annealing and irradiation alternation.

which can be converted in a fine correction for the hit time.

The reference time system is composed of two plastic scintillators read by two 32-sensors 4×8 matrices. The reference time signal requires all 64 sensors firing simultaneously, and the time average for the two scintillators is computed. The two trigger times are then compared and are valid if they fall within a 5 ns window. The final reference time is then taken as the average of the trigger times.

The first step is the calculation of the phase, performed via a formula that is given by ALCOR experts:

$$\mathrm{IF} = \max(\mathrm{fine}) - \min(\mathrm{fine}) \tag{4.3}$$

$$\mathrm{CUT} = \frac{\min(\mathrm{fine}) + \max(\mathrm{fine})}{2} \tag{4.4}$$

$$\mathrm{phase} = \begin{cases} \mathrm{fine} < \mathrm{CUT} & (\mathrm{fine} - \min(\mathrm{fine}))/\mathrm{IF} \\ \mathrm{fine} > \mathrm{CUT} & (\mathrm{fine} - \min(\mathrm{fine}))/\mathrm{IF} - 1 \end{cases} \tag{4.5}$$

Then, the phase is subtracted to the hit time once it is converted to ns. This procedure is applied to all sensors read by ALCOR and was developed to analyse the data from the 2022 test beam. In Figure 4.21 top panel the min and max for a single TDC is measured by fitting the TDC fine distribution. The fit is highlighted in red, a custom function was used to account for border effects:

$$f = \mathrm{N}\left[\exp\left(\frac{x - \min}{\sigma_{\min}}\right) + 1\right]^{-1}\left[\exp\left(\frac{x - \max}{\sigma_{\max}}\right) + 1\right]^{-1} \tag{4.6}$$

where N is a normalisation factor, $\min$ ($\max$) is the distribution lower (higher) bound for values of fine, $\sigma_{\min}$ ($\sigma_{\max}$) is the width of the rising (falling) region for the curve. This first step improved the single hit time resolution down to (≈ 50 ps).

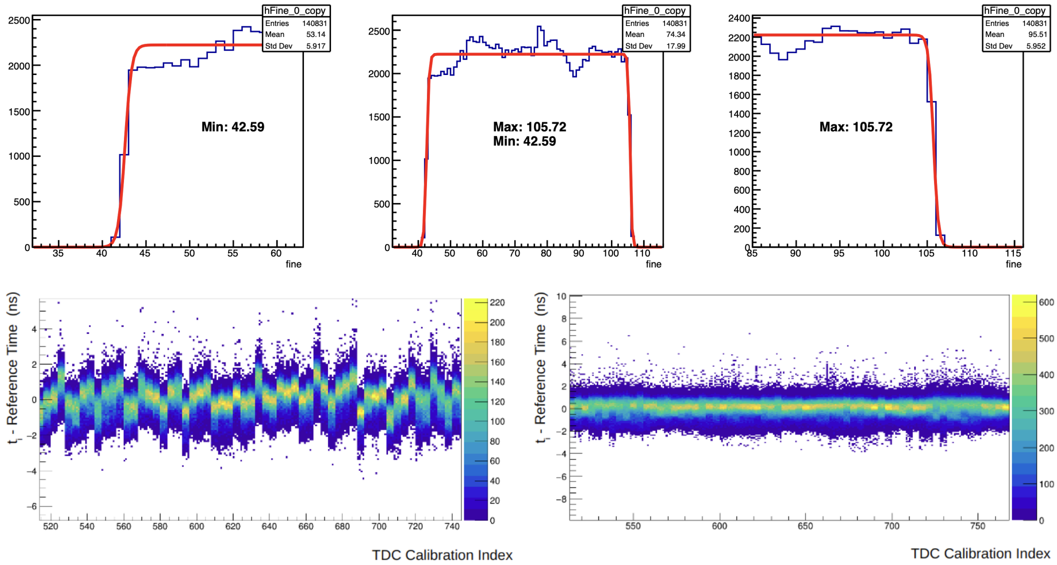

FIGURE 4.21: (top) evaluation of minimum and maximum of the fine parameter distribution for a TDC. (bottom left) time difference between the trigger time and the hit time for all timing TDCs, (bottom right) time difference between the trigger time and the hit time for all timing TDCs, after calibration. Figures taken from [232].

In an attempt to enhance the timing resolution of the system, a second calibration was performed on the readout of the timing sensors. The correction involved the synchronisation of all timing TDCs. The idea is that within the circuitry some delays arise, for example, from different length of connections. The delays are then a nuisance that smear the overall time resolution for the timing system. To get rid of the smearing, a recursive calibration is devised: the difference between the calibrated time of the single timing TDC and of the calibrated reference time is calculated for all hits, for all TDCs. This is shown in Figure 4.21 bottom left panel. The mean of the distributions are then taken as $\mathrm{offset}^{(0)}$ parameters and are added to the new calibrated phase ($\mathrm{phase}_{\mathrm{T}}^{(0)}$) as:

$$\mathrm{phase}_{\mathrm{T}}^{(0)} \equiv \mathrm{phase} - \mathrm{offset}^{(0)} \tag{4.7}$$

independent of the fine value. The first correction then affects the value of the reference time itself, as we are correcting the timing TDCs, so it is re-calculated and the new values for $\mathrm{offset}^{(1)}$ are summed to the phase:

$$\mathrm{phase}_{\mathrm{T}}^{(\mathrm{i}+1)} = \mathrm{phase}_{\mathrm{T}}^{(\mathrm{i})} - \mathrm{offset}^{(\mathrm{i}+1)} \tag{4.8}$$

The effect of this procedure can be appreciated in Figure 4.21 bottom right panel. The offset calibration yielded, if any, an improvement that could not be appreciated with the current statistical uncertainty. Further investigation is required to understand the full picture.

The overall timing resolution measured was $\approx 125\,\mathrm{ps}$ for the timing system and $\approx 500\,\mathrm{ps}$ for the imaging system [232].

4.4.6 2023 Campaign & ongoing activities: proton energy scan, neutron damage, laser timing

The third campaign of irradiation took place at the TIFPA facility (proton irradiation) and Legnaro National Laboratories (neutron irradiation). The main objective was to study the radiation damage of neutrons compared to proton and to deepen our understanding of proton damage through a variety of different approaches of both irradiation and annealing procedures. On the irradiation side, a proton scan in energy was performed to understand the radiation damage as a function of incoming particle energy. On the annealing side different types of annealing and different times of exposure were analysed.

A comprehensive list of all available boards in the current campaign is listed in Table 4.2 together with its intended purpose.

Fraction of damage

The fraction of damage (f_d) is a quantity devised to represent the damage recovery of an arbitrary sensor. The quantity relates to the sensor performance: the degradation after an arbitrary level of irradiation and recovery after an arbitrary annealing procedure. It is defined as:

$$f_\mathrm{d}(\mathrm{V_{bias}}) = \frac{\mathrm{I}^{(\mathrm{t_{ann}},\mathrm{T_{ann}})}_{\mathrm{dark}}(\mathrm{V_{bias}}) - \mathrm{I}^{(\mathrm{new})}_{\mathrm{dark}}(\mathrm{V_{bias}})}{\mathrm{I}^{(\mathrm{irr})}_{\mathrm{dark}}(\mathrm{V_{bias}}) - \mathrm{I}^{(\mathrm{new})}_{\mathrm{dark}}(\mathrm{V_{bias}})} \tag{4.9}$$

where $\mathrm{I}^{(\mathrm{new})}_{\mathrm{dark}}$ is the measured current at $\mathrm{V_{bias}}$ when the sensor is new, $\mathrm{I}^{(\mathrm{irr})}_{\mathrm{dark}}$ is the measured current at $\mathrm{V_{bias}}$ when the sensor is irradiated, $\mathrm{I}^{(\mathrm{t_{ann}},\mathrm{T_{ann}})}_{\mathrm{dark}}$ is the measured current at $\mathrm{V_{bias}}$ when the sensor is annealed for a time t_ann and at a temperature T_ann. $\mathrm{I}^{(\mathrm{t_{ann}},\mathrm{T_{ann}})}_{\mathrm{dark}}$ could also be measured after repeated annealing sessions of different duration and at different temperatures. This is an approach that stems from the fact that the radiation damage is mostly additive, thus the DCR increase will be on top of the baseline of the new sensor. In this picture, a fraction damage of zero would mean complete recovery, with DCR levels of the same order of the new sensor. In principle, a negative value would mean an improvement of the background levels with respect to the out-of-the-box SiPM.

As the evidence suggests the existence of a lower limit for the fraction of damage reduction, we can define the maximum recovery as:

$$\mathrm{R_d}(\mathrm{V_{bias}}) = 1 - \max_{\mathrm{t_{ann}},\mathrm{T_{ann}}} \Big(\mathrm{f_d}(\mathrm{V_{bias}}; \mathrm{t_{ann}}, \mathrm{T_{ann}})\Big) \tag{4.10}$$

where we take the maximum possible reduction over any amount of time and temperature.

Online annealing: forward and reverse bias

The online annealing, done in forward and reverse mode (Sections 4.4.2-4.4.2) was explored in a wide range of annealing time and temperatures. The results are shown in Figure 4.22. Specifically the results related to the forward annealing are plotted in the left panel and those related to the reverse annealing are plotted on the right panel. The gold curves refer to oven annealed sensors.

The general trend for both curves is a gradual recovery in time. At first glance, the overall speed of recovery is significantly different: after the first cycle of 27 h

Proton irradiation at TIFPA

Serial #	Irradiation	Beam current (nA)	Time (s)	Fluence	Notes
1	Standard	14	120	$1{\times}10^9 n_{eq}$	Laser timing
2	Standard	14	120	$1{\times}10^9 n_{eq}$	Offline ann.
3	Standard	14	120	$1{\times}10^9 n_{eq}$	Off. prev. ann.
4	Standard	14	120	$1{\times}10^9 n_{eq}$	Off. prev. ann.
5	Energy Scan	14	130	$1{\times}10^9 p$	$k = 1.11$
6	Energy Scan	14	130	$1{\times}10^9 p$	$k = 1.5$
8	Energy Scan	14	130	$1{\times}10^9 p$	$k = 2.0$
9	Energy Scan	14	130	$1{\times}10^9 p$	$k = 2.5$
10	Energy Scan	14	130	$1{\times}10^9 p$	$k = 3.0$
11	Online x10	2	82	$1{\times}10^8 n_{eq}$	On. Forward ann.
12	Online x10	2	82	$1{\times}10^8 n_{eq}$	On. Reverse ann.
13	Standard	14	120	$1{\times}10^9 n_{eq}$	Off. Forward ann.
14	Standard	14	120	$1{\times}10^9 n_{eq}$	Off. Reverse ann.
15	Standard	14	120	$1{\times}10^9 n_{eq}$	Infrared Lamp
16	Standard	14	120	$1{\times}10^9 n_{eq}$	Irr. Spare

Neutron irradiation at LNL

Serial #	Irradiation	Distance (cm)	Charge (mC)	Fluence	Notes
19	Standard	25	7.6	$1{\times}10^{10} n_{eq}$	Offline ann.
20	Standard	30	1.03	$5{\times}10^9 n_{eq}$	Offline ann.
21	Standard	35	1.03	$1{\times}10^9 n_{eq}$	Off. Fwd. ann. @150 °C
22	Standard	35	1.03	$1{\times}10^9 n_{eq}$	Off. Fwd. ann. @175 °C
23	Standard	35	1.03	$1{\times}10^9 n_{eq}$	Infrared lamp
24	Standard	35	1.03	$1{\times}10^9 n_{eq}$	Irr. Spare

In-stock spares

7	-	-	-	-	New Spare
17	-	-	-	-	New Spare
18	-	-	-	-	New Spare
25	-	-	-	-	New Spare
26	-	-	-	-	New Spare
27	-	-	-	-	New Spare
28	-	-	-	-	New Spare
29	-	-	-	-	New Spare
30	-	-	-	-	New Spare
31	-	-	-	-	New Spare
32	-	-	-	-	New Spare
33	-	-	-	-	New Spare
34	-	-	-	-	New Spare

TABLE 4.2: HAMA3 boards that have undergone many different irradiations and subsequent treatments.

at 100 °C the forward method recovered close to 75% of the fraction of damage, whereas the reverse stop shy of 60%. At the second cycle of 27 h at 125 °C the forward method recovered close to 83% of the fraction of damage, whereas the reverse catches up to 75%. In the third cycle of 350 h at 150 °C we see that the forward method already recovered ≈ 97%, comparable to a similar recovery with the oven method (600 h at 150 °C). The reverse method still lags behind at ≈ 94%. For both forward and reverse, the last annealing session of 100 h at 175 °C do not seem to have a noticeable impact, where in the reverse case we might see a slight improvement at first and then a worsening of the fraction of damage recovery for the last measurement.

The presented results suggest a number of very interesting results:

- **Forward annealing versus reverse annealing**
  Forward annealing show in general a quicker recovery and in general a better performance. The maximum fraction of damage recovered was ≈ 3% larger in the same time span and overall shows more stability (no final out-of-trend point).

- **Forward annealing versus oven annealing (Fraction of damage recovery)**
  Forward annealing show a limit in line with the oven annealing one, which is thought to be the value for R_d. This is consistent with the flat behaviour of the data points in the 175 °C, in which the sensor is insensitive to the treatment.

- **Forward annealing versus oven annealing (Time of recovery)**
  Even though the comparison at 150 °C was not completely on equal grounds, the general trend can give us precious insights. Indeed, the forward annealed sensors had integrated 27 h at 100 °C and 27 h at 125 °C of annealing treatment before being administered the 350 h session at 150 °C, for a total of 404 h. This being said, the same level of recovery was reached after 600 h at the same temperature in the oven case. One could then postulate that the speed of recovery of the Forward method is equal if not faster than the oven annealing (See Section 4.4.6).

In light of these results, the forward annealing is a strong candidate for the *in situ* annealing solution of damage recovery. The level of fraction damage reduction is maximal (≈ 97%) and the sensor has a stable behaviour for additional annealing treatment.

Neutron damage annealing

Neutron irradiation has been done at the same level of proton irradiation, at $10^9\ \mathrm{n_{eq}}$. They are compared to the forward annealing of proton irradiated sensors in Figure 4.23. The coloured points (blue, green, yellow, red) represent the forward annealing, proton irradiate sensors of Figure 4.22 left panel. The gold curves represent the forward annealing of neutron irradiated sensors at the reported temperatures. The empty black points represent the oven annealing of neutron irradiated sensors at the reported temperatures. The present section will always refer to the gold and empty black curves, unless specified otherwise. This is an ongoing investigation, only partial and preliminary conclusions will be drawn.

The general trend of all the curves is a slow exponential decrease of the fraction of damage, after an initial quick recovery. The first point, representing 10 min, establishes the magnitude of the first large reduction: approximately 80% for the forward annealing at 175 °C, 70% for the forward and 55% for the oven annealing at 150 °C.

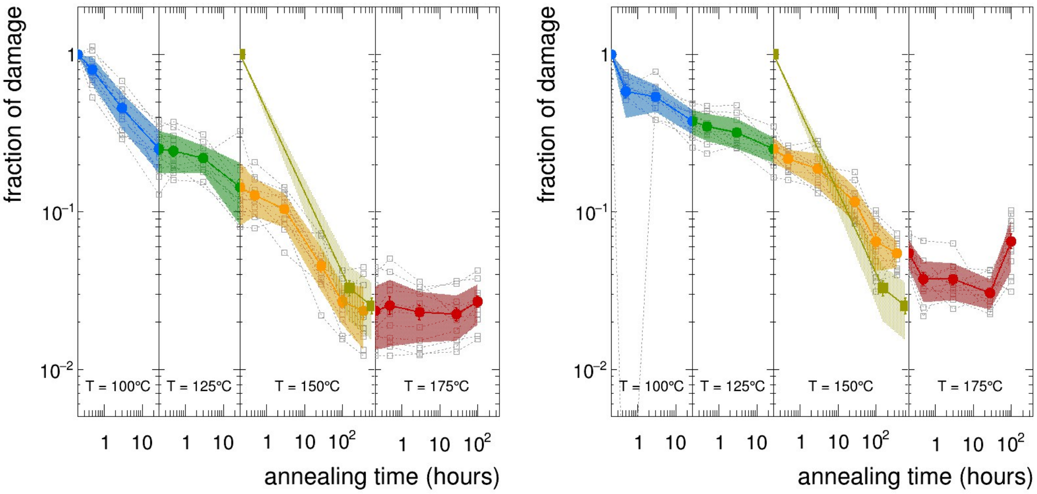

FIGURE 4.22: Fraction of damage as a function of annealing time and temperature. (blue, green, yellow, red) (left) Forward annealing, (right) Reverse annealing, the empty light grey square represent the values for the single sensor. (gold) oven annealing.

After this, the trend is qualitatively similar for all curves and is a slow decrease. The forward annealing at 175 °C is the steepest, reaching R_d (97% of recovery) in a record 10 h. This is the fastest recovery recorded up to date. The second fastest is the forward annealing, followed by the oven annealing at 150 °C. The annealing campaign is still ongoing and the results are partial, but trends already suggest a convergence to R_d for both methods at roughly the times seen in protons, 350 h and 600 h. The presented partial results already suggest a number of very interesting preliminary results:

- **Forward annealing in protons versus forward annealing in neutrons (Initial recovery boost and temperature dependence of recovery rate)**
  The initial recovery boost is a new feature in the context of the time dependence of the fraction of damage reduction. In the previous campaigns most of the results were time integrated, and the time dependent results on the forward annealing in protons do not show this behaviour. This feature might have been present in proton irradiated sensors but hidden by the slow temperature approach. We can appreciated a significant difference in the initial boost from 175 °C (20% recovery) to 150 °C (30% recovery) and a very large difference in the subsequent speed of recovery from 175 °C (10 h to R_d) to 150 °C (350 h to R_d), which might indicate an exponential dependence on the temperature. In this picture a low temperature of 100 °C can expect an initial boost of $\approx$ 9% (30% recovery, reduced by 1.5 every 25 °C) which is consistent with the first point (30 min) having a $\approx$ 20% recovery.

- **Forward annealing in protons versus forward annealing in neutrons (Reduction slope)**
  Another interesting feature that can be seen in the data is that, after a given time and up to measured points, the proton- and neutron-irradiated forward annealed curves overlap. This is quite an interesting result as one would assume the neutron-irradiated curve to converge to R_d slightly later, due to the head-start of the proton-irradiated of almost 90% recovery. This needs will need to be studied once the full measurements are available.

- **Forward annealing versus oven annealing (Time of recovery)**
  In the previous section, we postulated that the forward annealing procedure could have a recovery rate higher or equal to the one of the oven annealing. Here the comparison is unbiased and the message is much clearer: the forward annealing is much quicker when compared at the same conditions of irradiation and annealing time. In the last available point for the oven annealing, to reach the same f_d the oven annealing takes ≈ 10 times longer and in the same time the forward annealing has recovered ≈ 6% more.

- **Forward annealing versus oven annealing ($\mathrm{R_d}$)**
  The trend in the $175\,^\circ\mathrm{C}$ annealing highlights how the forward annealing trend in neutrons reaches the flat bottom $\mathrm{R_d}$. More annealing sessions are required to probe if the potential recovery can be more efficient for the neutron damage with respect to the proton damage.

The presented results are not complete, but already provide a very interesting picture for the annealing techniques and the radiation damage for protons and neutrons. Our measurements seem to go toward an equivalence of proton- and neutron-induced damage recovery for equal fluences, showing similar behaviours for annealing trends with time and temperature in both sets. The forward annealing still come out as the strongest candidate for an online efficient and quick annealing solution.

Characterisation of light response

After the 2022 start of light response measurements, the SiLab upgraded to a laser-based setup. The picosecond pulsed laser is still piloted with a pulser, provides a light of $401.4\,\mathrm{nm}$ wavelength with a $25\,\mathrm{ps}$ full width at half maximum, less than a $4\,\mathrm{ps}$ synchronisation jitter, up to $20\,\mathrm{MHz}$ repetition rate and a peak power over $2\,\mathrm{W}$. The laser is mounted on a z-axis linear translation stage, while the sensors are mounted on a x- and y-axis linear translation stage. The result is a fully automated XYZ movement of the sensors, installed in the climatic chamber and functioning down to $-40\,^\circ\mathrm{C}$.

The resolution is measured through the time distribution between the reference start of measurement (obtained by the pulser) and the time of arrival of the single photon onto the detector. The curve is fitted with a gaussian with an exponential tail, that is a feature yet to be understood.

The timing resolutions are shown in Figure 4.24 for all sensors at different bias voltages on the left panel. Reported is the gaussian sigma from the fit, which contains the laser-ALCOR synchronisation and the pulser reference time resolution. On the right a highlight for one voltage and one sensor is shown. The highlight shows the histogram used for the measurement. The peak presents a tail that is yet to be understood. The resolution contains contributions from the laser-ALCOR synchronisation and the time reference resolution. The best sensor for timing is the Hamamatsu 13360-3075 with a very good $100\,\mathrm{ps}$ resolution.

The next step will be to characterise an irradiated board to understand the radiation damage effect on the timing properties of the sensor.

Breakdown measurements in low current

The low temperatures at play and highly performant sensors resulted in a very low current. This is particularly the case for the Hamamatsu S13360-3050. This prevented, in the new sensors, a proper estimation of the $\mathrm{V_{bd}}$. The estimation was then

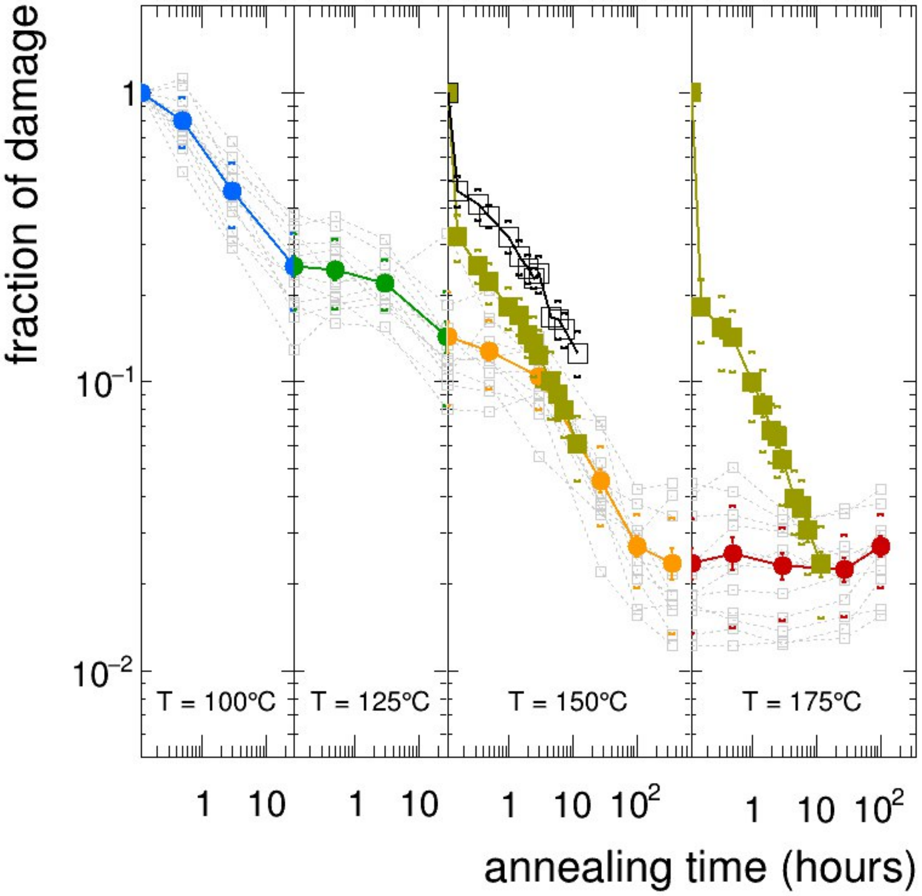

FIGURE 4.23: Fraction of damage as a function of annealing time and temperature. (blue, green, yellow, red) online annealing on proton irradiated at 10^9 $\mathrm{n_{eq}}$, (gold) online forward annealing on neutron irradiated at 10^9 $\mathrm{n_{eq}}$, (empty black) oven annealing on neutron irradiated at 10^9 $\mathrm{n_{eq}}$.

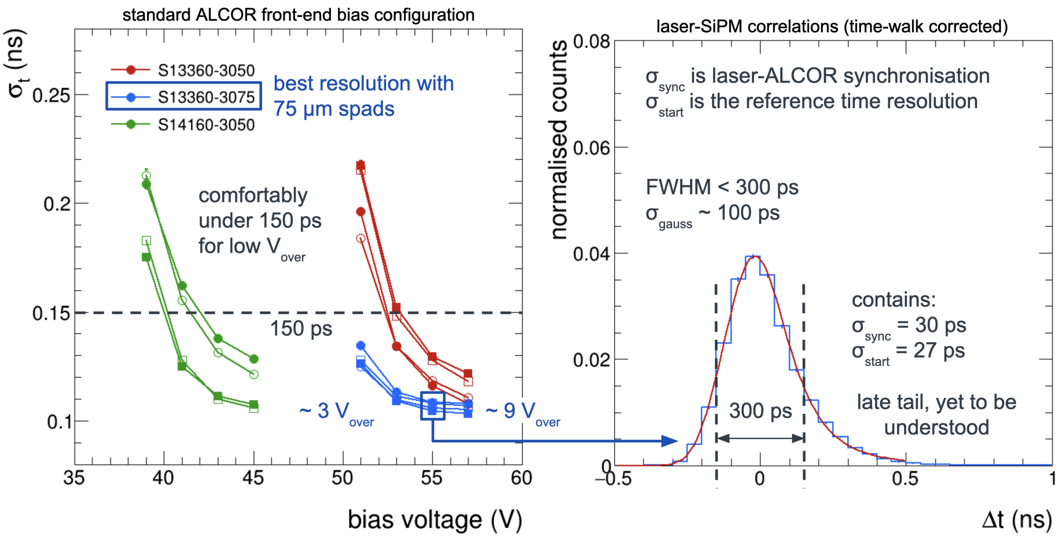

FIGURE 4.24: (left) timing resolution as a function of applied voltage (right) highlight of the timing shape of one voltage point.

performed on the irradiated sensors, where the current was a factor 100 higher. The comparison between the two measurements is shown in Figure 4.25. The temperature dependence clearly shows the measurement on the new sensors significantly deviates from the expected linear trend. For this reason, the irradiated sensor measurement of V_{bd} is taken as reference in the low temperature limit.

Characterisation of activation energy

The temperature scan measurements were also used to investigate the effects of radiation on the sensors' activation energy. Activation energy defines the amount of energy that needs to be delivered to generate an avalanche. In [233] an overview of three possible ways to measure this quantity are outlined, two of which can be done with the available data. Although the two methods are pointing to an incomplete picture, we make use of one to start an investigation on the effects of radiation damage on the activation energy. This line of research stems from the notion that the DCR is not going back to pre-irradiation levels (Section 4.4.5), so the suspicion is that an intrinsic characteristic is forever changed by the radiation damage and it cannot be recovered via the annealing procedures we explored so far.

The research [233] (Figure 4.26 top panel) indicates the existence of two main mechanisms for the DCR or dark current generation. The methods considered make use of the Arrhenius plot Figure (4.26) where the logarithm of the current at a certain (over)voltage is plotted against the inverse of the temperature times the Boltzmann constant. The activation energy is then measured as the slope of the linear trend of the data points. The threshold for one dominating over the other is $\approx 3\,^{\circ}\mathrm{C}$, which is consistent with our findings (Figure 4.26 bottom panel).

The main message we can take from the two different approaches is that there are many mechanisms that affect the DCR or dark current: some are linked to the absolute voltage applied and some are linked to the overvoltage applied. This can be seen from the quoted activation energies for the (low-)high-temperature regions, going from (0.42) 0.89 in the fixed voltage case to (0.47) 0.96 in the fixed overvoltage case. Then, a full picture is hard to infer from the two plots separately, and a new way for the measurement is proposed. In our case, being a pilot study, we start with these basic measurements. A preliminary result is shown in Figure 4.26 middle and bottom panels. The activation energy measurements do change after the radiation damage, reducing the energy of $\approx 30\%$ for both temperature regions. This effect is consistent across all sensors and show similar behaviours for the measurement in voltage and overvoltage. This indicates the need to extend this line of research to better understand the sensors different response to radiation damage and to explore the effects of annealing on the activation energies.

New prototype and 2023 test beam

In October 2023 a new prototype for the Photo Detection Unit (PDU) was developed (Figure 4.27 top panel). This new prototype was a first step toward a full integration of readout and services into a compact and light-weight solution. The PDU integrated 4 ALCOR dual boards, for a total of 8 ALCOR chips, water cooling, two coupled Peltier modules for sub-zero datataking, one temperature and humidity sensor. Each PDU carried 4 matrices of 256 SiPMs of roughly $3 \times 3\,\mathrm{mm}^2$, covering $\approx 50 \times 50\,\mathrm{mm}^2$.

The detector box used in the test beam consisted in 8 PDUs, four of which only

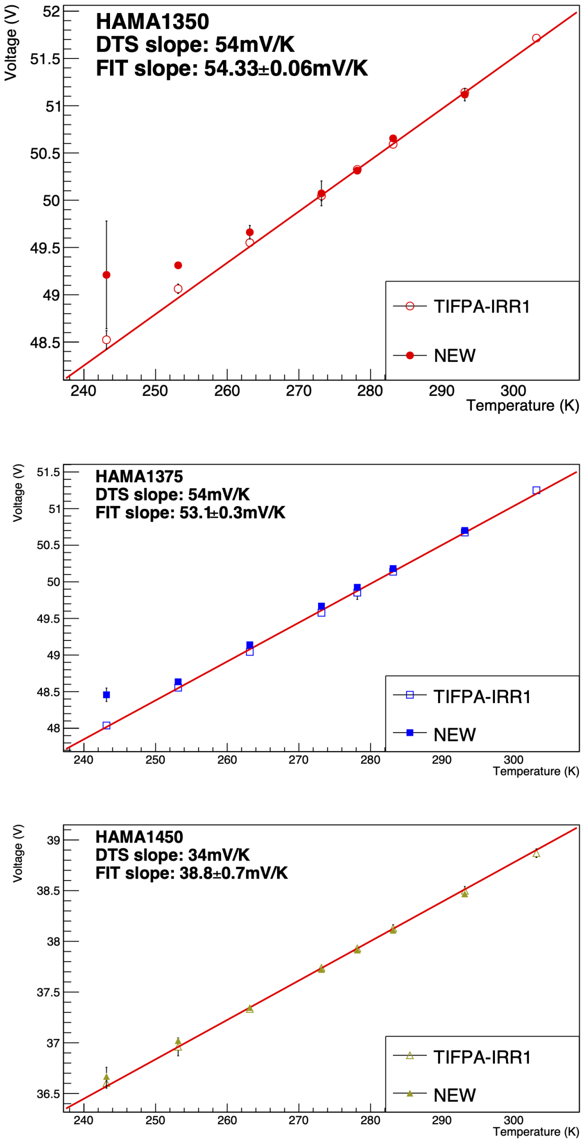

FIGURE 4.25: Breakdown voltage measurement as a function of temperature for new (NEW) and irradiated at TIFPA (TIFPA-IRR1) at a 10^9 n_{eq} sensors. The red line show the linear fit on the TIFPA-IRR1 data.

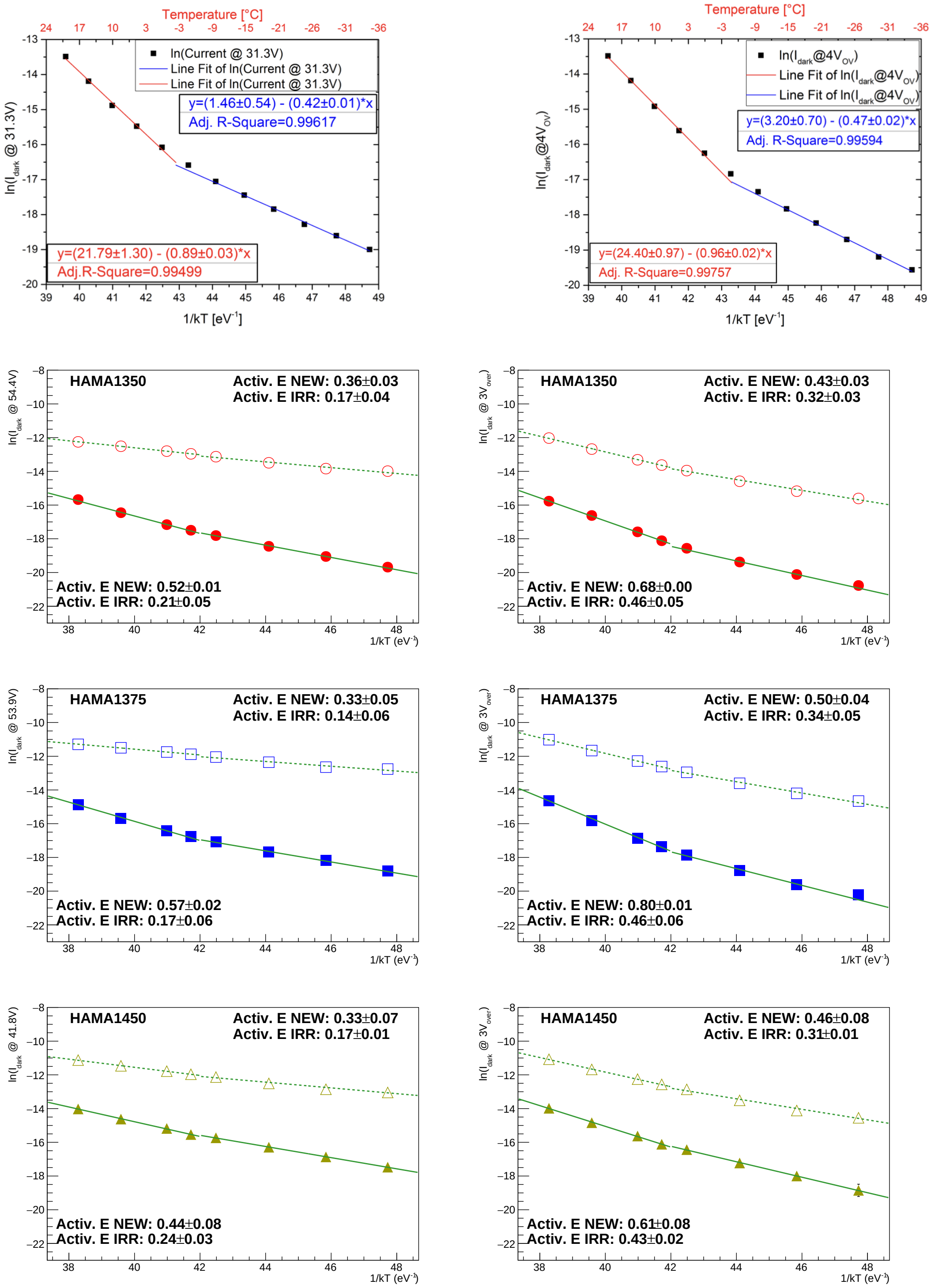

FIGURE 4.26: Evaluation of the activation energy with fixed voltage (left) and fixed overvoltage (right) in an Arrhenius plot. (top) Figure taken from [233]. (middle-top, middle-bottom, bottom) Measured sensors irradiated at 10^9 $\mathrm{n_{eq}}$ (empty) and for new sensors (full).

had a sensor matrix in one corner (Figure 4.27 middle panel). In Figure 4.27 bottom panel the result of the test beam succesful datataking: the detector box was installed in the dRICH prototype and the two rings correspond to light emitted in the aerogel and gas radiators for a negative beam of energy $10\,\mathrm{GeV}$.

This marked the first time the prototype measured the ring with such a high-precision and with almost full coverage. It is worth noting that this result was achieved with a prototype for the full readout chain, which is a further test of the art of the dRICH R&D for the full detector construction.

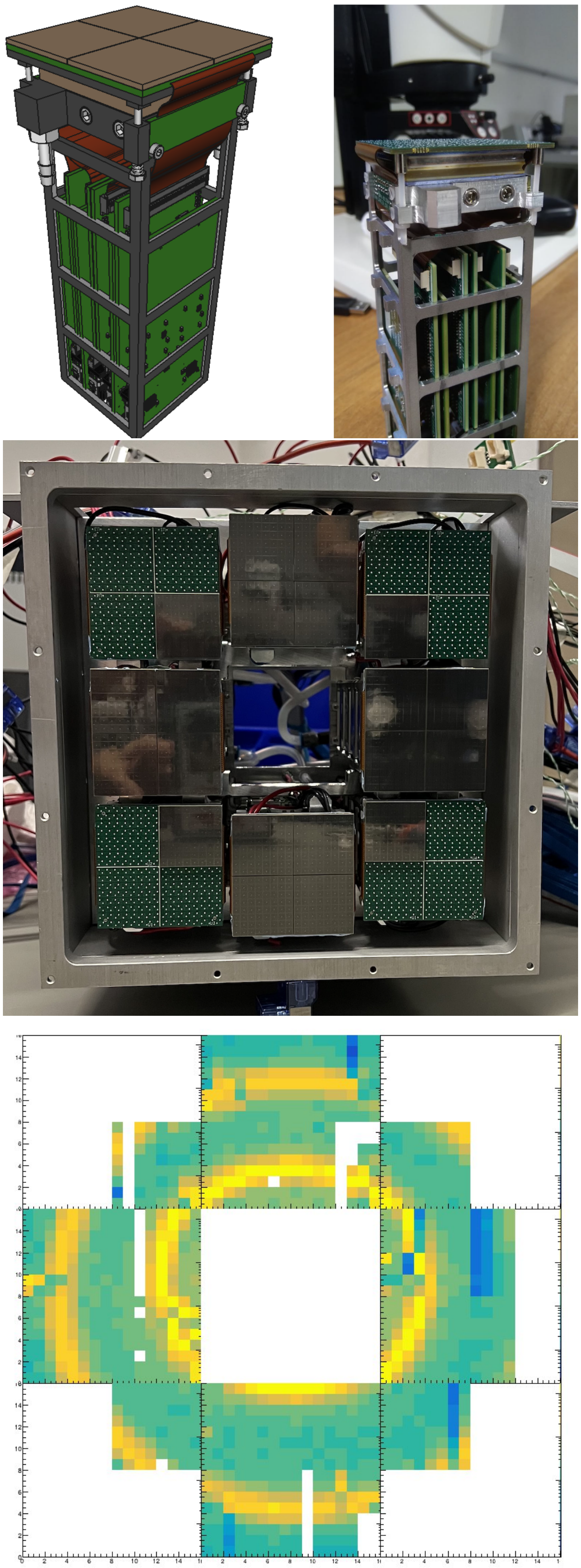

FIGURE 4.27: (top) schematics (left) and photo (right) of the PDU, (middle) detector box, (bottom) cherenkvov rings as measured with the SiPMs with the ALCOR full readout chain.

4.5 Conclusions

In this chapter a broad overview of the activities related to the SiPM characterisation, test of radiation tolerance, analysis of performance recovery via annealing was presented.

The preliminary results highlight how the new facility at the INFN Bologna is rapidly improving and scaling its potential for research on the SiPMs. In a three years time, many new results were achieved:

1. In laboratory I-V measurement of 32 sensors matrix is fully automated, for up to 2 boards in series with no operator intervention.
2. In laboratory DCR measurement of 32 sensors matrix is fully automated, for up to 2 boards in series with no operator intervention.
3. On-the-go IV measurement of 32 sensors matrix is fully automated, for up to 2 boards in series with no operator intervention.
4. On-the-go DCR measurement of 32 sensors matrix is fully automated, for up to 2 boards in series with no operator intervention.
5. In laboratory online forward (reverse) annealing of 32 sensors matrix is fully automated, with temperature monitoring.
6. Successful data taking capabilities for sensors use in test beams

On top of this rich hardware compendium, a number of software solutions for real time QA and data analysis have been developed. The ongoing R&D for the dRICH prototype has been greatly advanced and the preliminary results are very promising: the group managed to perform two gainful test beams testing the full readout chain.

On top of this, the last irradiation campaign was a success, providing a large plethora of exciting results. The repeated measurement of the fraction damage recovery limit ($R_d = 97\%$), the selection of the forward annealing method as a frontrunner for the online annealing solution, the equivalence of proton- and neutron-irradiated sensors response to annealing.

Conclusions

The analysis of the production of ϕ-meson pairs measured at the ALICE experiment in pp collision at $\sqrt{s} = 7$ TeV and $\sqrt{s} = 5.02$ was presented. It was shown how the unexpected observation of high-density QCD effects in small systems gave rise to a major shift in how these systems were perceived. They quickly went from a reference measurement for heavy-ion physics to a new thriving branch of research, where more and more effort was dedicated. In this context, the presented analysis was carried out as a novel addition to the investigation of the strangeness hadronisation and strangeness enhancement phenomena. The analysis relied on a careful check on the data quality. The signal extraction procedure was performed through a new method to access the ϕ-meson pair yield via a 2-dimensional invariant mass histogram. A generalisation of previous analysis procedures have been developed to extrapolated the measured spectra and access to the full yield. A thorough approach to the evaluation of the degree of correlation of systematics have been presented.

The measured ϕ-meson production gave us access to novel parameters that quantify the correlated or anti-correlated production with respect to a poissonian behaviour. The found excess was constant in multiplicity and ≈ 3.5%. On top of this, a number of results stemmed from the analysis, such as the p_{T} evolution of conditional spectra for the ϕ-meson.

An interesting take on the Monte Carlo predictions was also presented. As some previous results have suggested, the comparison to the full yields only show a fraction of the picture. In particular, considered PYTHIA models showed a discrepancy with the data when comparing multiplicity-dependent yields. Monash 2013 under predicts both yields by a factor ≈ 50%, whilst the Rope model under predicts by a factor ≈ 30%, failing to describe the absolute yield, but qualitatively describing the trend. The two different settings, when compared in γ_{ϕ} and R_{ϕ} , showed consistent predictions that are in agreement with the presented results within uncertainties. The agreement then does not appear to be affected by the effective string tension enhancement that the Rope model provides. This highlights the fact that the novel approach being put forward can have an impact in understanding the underlying mechanisms of hadronisation and in model discrimination.

The presented work is therefore a step forward in the understanding of the hadronisation of the ϕ meson and strangeness altogether. The excess in data was correctly reproduced in PYTHIA and now more comparison to new models are needed to understand how different phenomenological approaches behave in this context.

As discussed in Section 3.11.3, the presented analysis has many possible expansion that can be looked into. The Run 3 datataking currently undergoing in ALICE will provide a significantly larger dataset that will help reducing the dominant statistical uncertainty and open to the possibility of more differential studies using the presented technique.

The SiPM characterisation campaigns carried on by the INFN Bologna group were presented.

It has been presented how the SiPM sensors are an excellent candidate for photodetection in high energy physics experiments, their main drawback being their susceptibility to radiation damage.

Throughout the thesis a plethora of results have been presented for various ways of characterising the sensors. An analysis software for the study of the breakdown voltage was developed. The full readout chain with the ALCOR chip was developed and tested at two test beams, a start of investigation for the SiPM timing resolution yielded very promising result under $150\,\mathrm{ps}$, down to $100\,\mathrm{ps}$. An extensive study on the feasibility of the in situ annealing was carried on. Direct current is a strong candidate successfully demonstrating how a large fraction, over 90%, of radiation-induced (10^9 $1\text{-}\mathrm{MeV/cm^2}$ neutron equivalent) damage can be recovered in as little as $10\,\mathrm{h}$.

Even though many of the research lines are still ongoing, the understanding about SiPM as a technology and know-how about their behaviour after irradiation and annealing is fast growing in the Bologna SiLab.

Bibliography

[1] R. L. Workman and Others. "Review of Particle Physics". In: *PTEP* 2022 (2022), p. 083C01. DOI: 10.1093/ptep/ptac097.

[2] P. Skands. "Introduction to QCD". In: *Searching for New Physics at Small and Large Scales*. WORLD SCIENTIFIC, 2013. DOI: 10.1142/9789814525220_0008. URL: https://doi.org/10.1142%2F9789814525220_0008.

[3] Michael E. Peskin and Daniel V. Schroeder. *An Introduction to quantum field theory*. Reading, USA: Addison-Wesley, 1995. ISBN: 978-0-201-50397-5.

[4] Johan Alwall et al. "MadGraph 5: going beyond". In: *Journal of High Energy Physics* 2011.6 (2011). DOI: 10.1007/jhep06(2011)128. URL: https://doi.org/10.1007%2Fjhep06%282011%29128.

[5] Torbjorn Sjostrand. "Monte Carlo Generators". In: *2006 European School of High-Energy Physics*. Nov. 2006, pp. 51–74. arXiv: hep-ph/0611247.

[6] "The ALICE experiment - A journey through QCD". In: (Nov. 2022). arXiv: 2211.04384 [nucl-ex].

[7] A. Bazavov et al. "Chiral crossover in QCD at zero and non-zero chemical potentials". In: *Phys. Lett. B* 795 (2019), pp. 15–21. DOI: 10.1016/j.physletb.2019.05.013. arXiv: 1812.08235 [hep-lat].

[8] Jaroslav Adam et al. "Centrality Dependence of the Charged-Particle Multiplicity Density at Midrapidity in Pb-Pb Collisions at $\sqrt{s_{\mathrm{NN}}} = 5.02$ TeV". In: *Phys. Rev. Lett.* 116.22 (2016), p. 222302. DOI: 10.1103/PhysRevLett.116.222302. arXiv: 1512.06104 [nucl-ex].

[9] Shreyasi Acharya et al. "Centrality and pseudorapidity dependence of the charged-particle multiplicity density in Xe–Xe collisions at $\sqrt{s_{\mathrm{NN}}}$ =5.44TeV". In: *Phys. Lett. B* 790 (2019), pp. 35–48. DOI: 10.1016/j.physletb.2018.12.048. arXiv: 1805.04432 [nucl-ex].

[10] Kenneth Aamodt et al. "Centrality dependence of the charged-particle multiplicity density at mid-rapidity in Pb-Pb collisions at $\sqrt{s_{NN}} = 2.76$ TeV". In: *Phys. Rev. Lett.* 106 (2011), p. 032301. DOI: 10.1103/PhysRevLett.106.032301. arXiv: 1012.1657 [nucl-ex].

[11] Georges Aad et al. "Measurement of the centrality dependence of the charged particle pseudorapidity distribution in lead-lead collisions at $\sqrt{s_{NN}} = 2.76$ TeV with the ATLAS detector". In: *Phys. Lett. B* 710 (2012), pp. 363–382. DOI: 10.1016/j.physletb.2012.02.045. arXiv: 1108.6027 [hep-ex].

[12] Serguei Chatrchyan et al. "Dependence on pseudorapidity and centrality of charged hadron production in PbPb collisions at a nucleon-nucleon centre-of-mass energy of 2.76 TeV". In: *JHEP* 08 (2011), p. 141. DOI: 10.1007/JHEP08(2011)141. arXiv: 1107.4800 [nucl-ex].

[13] M. C. Abreu et al. "Scaling of charged particle multiplicity in Pb Pb collisions at SPS energies". In: *Phys. Lett. B* 530 (2002), pp. 43–55. DOI: 10.1016/S0370-2693(02)01353-9.

[14] B. I. Abelev et al. “Systematic Measurements of Identified Particle Spectra in pp, d^+ Au and Au+Au Collisions from STAR”. In: *Phys. Rev. C* 79 (2009), p. 034909. DOI: `10.1103/PhysRevC.79.034909`. arXiv: `0808.2041 [nucl-ex]`.

[15] B. Alver et al. “Phobos results on charged particle multiplicity and pseudorapidity distributions in Au+Au, Cu+Cu, d+Au, and p+p collisions at ultra-relativistic energies”. In: *Phys. Rev. C* 83 (2011), p. 024913. DOI: `10.1103/PhysRevC.83.024913`. arXiv: `1011.1940 [nucl-ex]`.

[16] K. Adcox et al. “Centrality dependence of charged particle multiplicity in Au - Au collisions at S(NN)**(1/2) = 130-GeV”. In: *Phys. Rev. Lett.* 86 (2001), pp. 3500–3505. DOI: `10.1103/PhysRevLett.86.3500`. arXiv: `nucl-ex/0012008`.

[17] I. G. Bearden et al. “Pseudorapidity distributions of charged particles from Au+Au collisions at the maximum RHIC energy”. In: *Phys. Rev. Lett.* 88 (2002), p. 202301. DOI: `10.1103/PhysRevLett.88.202301`. arXiv: `nucl-ex/0112001`.

[18] I. G Bearden et al. “Charged particle densities from Au+Au collisions at s(NN)**(1/2) = 130-GeV”. In: *Phys. Lett. B* 523 (2001), pp. 227–233. DOI: `10.1016/S0370-2693(01)01333-8`. arXiv: `nucl-ex/0108016`.

[19] Shreyasi Acharya et al. “Charged-particle pseudorapidity density at mid-rapidity in p-Pb collisions at $\sqrt{s_{\mathrm{NN}}}$ = 8.16 TeV”. In: *Eur. Phys. J. C* 79.4 (2019), p. 307. DOI: `10.1140/epjc/s10052-019-6801-9`. arXiv: `1812.01312 [nucl-ex]`.

[20] Betty Abelev et al. “Pseudorapidity density of charged particles in p + Pb collisions at $\sqrt{s_{NN}} = 5.02$ TeV”. In: *Phys. Rev. Lett.* 110.3 (2013), p. 032301. DOI: `10.1103/PhysRevLett.110.032301`. arXiv: `1210.3615 [nucl-ex]`.

[21] B. B. Back et al. “Pseudorapidity distribution of charged particles in d + Au collisions at s(NN)**(1/2) = 200-GeV”. In: *Phys. Rev. Lett.* 93 (2004), p. 082301. DOI: `10.1103/PhysRevLett.93.082301`. arXiv: `nucl-ex/0311009`.

[22] Albert M Sirunyan et al. “Pseudorapidity distributions of charged hadrons in proton-lead collisions at $\sqrt{s_{\mathrm{NN}}} = 5.02$ and 8.16 TeV”. In: *JHEP* 01 (2018), p. 045. DOI: `10.1007/JHEP01(2018)045`. arXiv: `1710.09355 [hep-ex]`.

[23] Jaroslav Adam et al. “Centrality dependence of the pseudorapidity density distribution for charged particles in Pb-Pb collisions at $\sqrt{s_{\mathrm{NN}}} = 5.02$ TeV”. In: *Phys. Lett. B* 772 (2017), pp. 567–577. DOI: `10.1016/j.physletb.2017.07.017`. arXiv: `1612.08966 [nucl-ex]`.

[24] Jaroslav Adam et al. “Pseudorapidity and transverse-momentum distributions of charged particles in proton–proton collisions at $\sqrt{s} = 13$ TeV”. In: *Phys. Lett. B* 753 (2016), pp. 319–329. DOI: `10.1016/j.physletb.2015.12.030`. arXiv: `1509.08734 [nucl-ex]`.

[25] Vardan Khachatryan et al. “Pseudorapidity distribution of charged hadrons in proton-proton collisions at $\sqrt{s}$ = 13 TeV”. In: *Phys. Lett. B* 751 (2015), pp. 143–163. DOI: `10.1016/j.physletb.2015.10.004`. arXiv: `1507.05915 [hep-ex]`.

[26] J. D. Bjorken. “Highly Relativistic Nucleus-Nucleus Collisions: The Central Rapidity Region”. In: *Phys. Rev. D* 27 (1983), pp. 140–151. DOI: `10.1103/PhysRevD.27.140`.

[27] Ehab Abbas et al. "Centrality dependence of the pseudorapidity density distribution for charged particles in Pb-Pb collisions at $\sqrt{s_{\mathrm{NN}}}$ = 2.76 TeV". In: *Phys. Lett. B* 726 (2013), pp. 610–622. DOI: `10.1016/j.physletb.2013.09.022`. arXiv: `1304.0347 [nucl-ex]`.

[28] Shreyasi Acharya et al. "System-size dependence of the charged-particle pseudorapidity density at sNN=5.02TeV for pp, pPb, and PbPb collisions". In: *Phys. Lett. B* 845 (2023), p. 137730. DOI: `10.1016/j.physletb.2023.137730`. arXiv: `2204.10210 [nucl-ex]`.

[29] Jaroslav Adam et al. "Measurement of transverse energy at midrapidity in Pb-Pb collisions at $\sqrt{s_{\mathrm{NN}}} = 2.76$ TeV". In: *Phys. Rev. C* 94.3 (2016), p. 034903. DOI: `10.1103/PhysRevC.94.034903`. arXiv: `1603.04775 [nucl-ex]`.

[30] Charles Gale et al. "Event-plane decorrelation of photons produced in the early stage of heavy-ion collisions". In: *PoS* HardProbes2020 (2021), p. 039. DOI: `10.22323/1.387.0039`. arXiv: `2009.07841 [nucl-th]`.

[31] Charles Gale et al. "Probing Early-Time Dynamics and Quark-Gluon Plasma Transport Properties with Photons and Hadrons". In: *Nucl. Phys. A* 1005 (2021). Ed. by Feng Liu et al., p. 121863. DOI: `10.1016/j.nuclphysa.2020.121863`. arXiv: `2002.05191 [hep-ph]`.

[32] T. Matsui and H. Satz. "J/ψ Suppression by Quark-Gluon Plasma Formation". In: *Phys. Lett. B* 178 (1986), pp. 416–422. DOI: `10.1016/0370-2693(86)91404-8`.

[33] Shreyasi Acharya et al. "Measurement of dielectron production in central Pb-Pb collisions at $\sqrt{s_{\mathrm{NN}}}$ = 2.76 TeV". In: *Phys. Rev. C* 99.2 (2019), p. 024002. DOI: `10.1103/PhysRevC.99.024002`. arXiv: `1807.00923 [nucl-ex]`.

[34] Hendrik van Hees, Charles Gale, and Ralf Rapp. "Thermal Photons and Collective Flow at the Relativistic Heavy-Ion Collider". In: *Phys. Rev. C* 84 (2011), p. 054906. DOI: `10.1103/PhysRevC.84.054906`. arXiv: `1108.2131 [hep-ph]`.

[35] O. Linnyk et al. "Hadronic and partonic sources of direct photons in relativistic heavy-ion collisions". In: *Phys. Rev. C* 92.5 (2015), p. 054914. DOI: `10.1103/PhysRevC.92.054914`. arXiv: `1504.05699 [nucl-th]`.

[36] Charles Gale et al. "Production and Elliptic Flow of Dileptons and Photons in a Matrix Model of the Quark-Gluon Plasma". In: *Phys. Rev. Lett.* 114 (2015), p. 072301. DOI: `10.1103/PhysRevLett.114.072301`. arXiv: `1409.4778 [hep-ph]`.

[37] Rupa Chatterjee, Pingal Dasgupta, and Dinesh K. Srivastava. "Anisotropic flow of thermal photons at energies available at the BNL Relativistic Heavy Ion Collider and at the CERN Large Hadron Collider". In: *Phys. Rev. C* 96.1 (2017), p. 014911. DOI: `10.1103/PhysRevC.96.014911`. arXiv: `1702.02378 [nucl-th]`.

[38] Jaroslav Adam et al. "Direct photon production in Pb-Pb collisions at $\sqrt{s_{NN}} = 2.76$ TeV". In: *Phys. Lett. B* 754 (2016), pp. 235–248. DOI: `10.1016/j.physletb.2016.01.020`. arXiv: `1509.07324 [nucl-ex]`.

[39] S. S. Adler et al. "Centrality dependence of direct photon production in s(NN)**(1/2) = 200-GeV Au + Au collisions". In: *Phys. Rev. Lett.* 94 (2005), p. 232301. DOI: `10.1103/PhysRevLett.94.232301`. arXiv: `nucl-ex/0503003`.

[40] A. Adare et al. "Enhanced production of direct photons in Au+Au collisions at $\sqrt{s_{NN}} = 200$ GeV and implications for the initial temperature". In: *Phys. Rev. Lett.* 104 (2010), p. 132301. DOI: 10.1103/PhysRevLett.104.132301. arXiv: 0804.4168 [nucl-ex].

[41] Shreyasi Acharya et al. "Direct photon elliptic flow in Pb-Pb collisions at $\sqrt{s_{\mathrm{NN}}} = 2.76$ TeV". In: *Phys. Lett. B* 789 (2019), pp. 308–322. DOI: 10.1016/j.physletb.2018.11.039. arXiv: 1805.04403 [nucl-ex].

[42] A. Adare et al. "Observation of direct-photon collective flow in $\sqrt{s_{NN}} = 200$ GeV Au+Au collisions". In: *Phys. Rev. Lett.* 109 (2012), p. 122302. DOI: 10.1103/PhysRevLett.109.122302. arXiv: 1105.4126 [nucl-ex].

[43] B. I. Abelev et al. "Neutral kaon interferometry in Au+Au collisions at s(NN)**(1/2) = 200-GeV". In: *Phys. Rev. C* 74 (2006), p. 054902. DOI: 10.1103/PhysRevC.74.054902. arXiv: nucl-ex/0608012.

[44] Michael Annan Lisa et al. "Femtoscopy in relativistic heavy ion collisions". In: *Ann. Rev. Nucl. Part. Sci.* 55 (2005), pp. 357–402. DOI: 10.1146/annurev.nucl.55.090704.151533. arXiv: nucl-ex/0505014.

[45] Thomas J. Humanic. "Hanbury-Brown-Twiss interferometry with identical bosons in relativistic heavy ion collisions: Comparisons with hadronic scattering models". In: *Int. J. Mod. Phys. E* 15 (2006), pp. 197–236. DOI: 10.1142/S0218301306003977. arXiv: nucl-th/0510049.

[46] R. Lednicky. "Correlation femtoscopy". In: *Nucl. Phys. A* 774 (2006). Ed. by T. Csorgo et al., pp. 189–198. DOI: 10.1016/j.nuclphysa.2006.06.040. arXiv: nucl-th/0510020.

[47] M. Herrmann and G. F. Bertsch. "Source dimensions in ultrarelativistic heavy ion collisions". In: *Phys. Rev. C* 51 (1995), pp. 328–338. DOI: 10.1103/PhysRevC.51.328. arXiv: hep-ph/9405373.

[48] K. Aamodt et al. "Two-pion Bose-Einstein correlations in central Pb-Pb collisions at $\sqrt{s_{NN}} = 2.76$ TeV". In: *Phys. Lett. B* 696 (2011), pp. 328–337. DOI: 10.1016/j.physletb.2010.12.053. arXiv: 1012.4035 [nucl-ex].

[49] Jaroslav Adam et al. "Centrality dependence of pion freeze-out radii in Pb-Pb collisions at $\sqrt{s_{NN}} = 2.76$ TeV". In: *Phys. Rev. C* 93.2 (2016), p. 024905. DOI: 10.1103/PhysRevC.93.024905. arXiv: 1507.06842 [nucl-ex].

[50] Wit Busza and Alfred S. Goldhaber. "NUCLEAR STOPPING POWER". In: *Phys. Lett. B* 139 (1984), p. 235. DOI: 10.1016/0370-2693(84)91070-0.

[51] S. V. Afanasiev et al. "Energy dependence of pion and kaon production in central Pb + Pb collisions". In: *Phys. Rev. C* 66 (2002), p. 054902. DOI: 10.1103/PhysRevC.66.054902. arXiv: nucl-ex/0205002.

[52] B. B. Back et al. "The Significance of the fragmentation region in ultrarelativistic heavy ion collisions". In: *Phys. Rev. Lett.* 91 (2003), p. 052303. DOI: 10.1103/PhysRevLett.91.052303. arXiv: nucl-ex/0210015.

[53] B. B. Back et al. "Charged-particle pseudorapidity distributions in Au+Au collisions at $s(NN)^{1/2}$ = 62.4-GeV". In: *Phys. Rev. C* 74 (2006), p. 021901. DOI: 10.1103/PhysRevC.74.021901. arXiv: nucl-ex/0509034.

[54] B. B. Back et al. "Transverse momentum and rapidity dependence of HBT correlations in Au + Au collisions at s(NN)**(1/2) = 62.4-GeV and 200-GeV". In: *Phys. Rev. C* 73 (2006), p. 031901. DOI: 10.1103/PhysRevC.73.031901. arXiv: nucl-ex/0409001.

[55] B. I. Abelev et al. “Pion Interferometry in Au+Au and Cu+Cu Collisions at RHIC”. In: *Phys. Rev. C* 80 (2009), p. 024905. DOI: `10.1103/PhysRevC.80.024905`. arXiv: `0903.1296 [nucl-ex]`.

[56] D. Adamová et al. “Beam energy and centrality dependence of two pion Bose-Einstein correlations at SPS energies”. In: *Nucl. Phys. A* 714 (2003), pp. 124–144. DOI: `10.1016/S0375-9474(02)01369-6`. arXiv: `nucl-ex/0207005`.

[57] C. Alt et al. “Bose-Einstein correlations of pi-pi- pairs in central Pb+Pb collisions at A-20, A-30, A-40, A-80, and A-158 GeV”. In: *Phys. Rev. C* 77 (2008), p. 064908. DOI: `10.1103/PhysRevC.77.064908`. arXiv: `0709.4507 [nucl-ex]`.

[58] A. Bazavov et al. “Equation of state and QCD transition at finite temperature”. In: *Phys. Rev. D* 80 (2009), p. 014504. DOI: `10.1103/PhysRevD.80.014504`. arXiv: `0903.4379 [hep-lat]`.

[59] Shreyasi Acharya et al. “Evidence of rescattering effect in Pb-Pb collisions at the LHC through production of $\mathrm{K}^*(892)^0$ and $\phi(1020)$ mesons”. In: *Phys. Lett. B* 802 (2020), p. 135225. DOI: `10.1016/j.physletb.2020.135225`. arXiv: `1910.14419 [nucl-ex]`.

[60] Shreyasi Acharya et al. “Pion-kaon femtoscopy and the lifetime of the hadronic phase in Pb−Pb collisions at $\sqrt{s_{\mathrm{NN}}}$ = 2.76 TeV”. In: *Phys. Lett. B* 813 (2021), p. 136030. DOI: `10.1016/j.physletb.2020.136030`. arXiv: `2007.08315 [nucl-ex]`.

[61] Adam Kisiel. “Pion-kaon femtoscopy in Pb–Pb collisions at $\sqrt{s_{\mathrm{NN}}} = 2.76$ TeV modeled in (3+1)D hydrodynamics coupled to Therminator 2 and the effect of delayed kaon emission”. In: *Phys. Rev. C* 98.4 (2018), p. 044909. DOI: `10.1103/PhysRevC.98.044909`. arXiv: `1804.06781 [nucl-th]`.

[62] S. Acharya et al. “Measurement of $\Lambda(1520)$ production in pp collisions at $\sqrt{s}$ = 7 TeV and p-Pb collisions at $\sqrt{s_{\mathrm{NN}}}$ = 5.02 TeV”. In: *Eur. Phys. J. C* 80.2 (2020), p. 160. DOI: `10.1140/epjc/s10052-020-7687-2`. arXiv: `1909.00486 [nucl-ex]`.

[63] Jaroslav Adam et al. “Enhanced production of multi-strange hadrons in high-multiplicity proton-proton collisions”. In: *Nature Phys.* 13 (2017), pp. 535–539. DOI: `10.1038/nphys4111`. arXiv: `1606.07424 [nucl-ex]`.

[64] Shreyasi Acharya et al. “Multiplicity dependence of light-flavor hadron production in pp collisions at $\sqrt{s}$ = 7 TeV”. In: *Phys. Rev. C* 99.2 (2019), p. 024906. DOI: `10.1103/PhysRevC.99.024906`. arXiv: `1807.11321 [nucl-ex]`.

[65] Shreyasi Acharya et al. “Multiplicity dependence of $\mathrm{K}^*(892)^0$ and $\phi(1020)$ production in pp collisions at $\sqrt{s}$ =13 TeV”. In: *Phys. Lett. B* 807 (2020), p. 135501. DOI: `10.1016/j.physletb.2020.135501`. arXiv: `1910.14397 [nucl-ex]`.

[66] Shreyasi Acharya et al. “Production of the $\rho(770)^0$ meson in pp and Pb-Pb collisions at $\sqrt{s_{\mathrm{NN}}}$ = 2.76 TeV”. In: *Phys. Rev. C* 99.6 (2019), p. 064901. DOI: `10.1103/PhysRevC.99.064901`. arXiv: `1805.04365 [nucl-ex]`.

[67] Jaroslav Adam et al. “$\mathrm{K}^*(892)^0$ and $\phi(1020)$ meson production at high transverse momentum in pp and Pb-Pb collisions at $\sqrt{s_{\mathrm{NN}}}$ = 2.76 TeV”. In: *Phys. Rev. C* 95.6 (2017), p. 064606. DOI: `10.1103/PhysRevC.95.064606`. arXiv: `1702.00555 [nucl-ex]`.

[68] Shreyasi Acharya et al. “Suppression of $\Lambda(1520)$ resonance production in central Pb-Pb collisions at $\sqrt{s_{\mathrm{NN}}} = 2.76$ TeV”. In: *Phys. Rev. C* 99 (2019), p. 024905. DOI: `10.1103/PhysRevC.99.024905`. arXiv: `1805.04361 [nucl-ex]`.

[69] Shreyasi Acharya et al. “Production of charged pions, kaons, and (anti-)protons in Pb-Pb and inelastic pp collisions at $\sqrt{s_{NN}} = 5.02$ TeV”. In: *Phys. Rev. C* 101.4 (2020), p. 044907. DOI: `10.1103/PhysRevC.101.044907`. arXiv: `1910.07678 [nucl-ex]`.

[70] Betty Abelev et al. “Centrality dependence of π, K, p production in Pb-Pb collisions at $\sqrt{s_{NN}} = 2.76$ TeV”. In: *Phys. Rev. C* 88 (2013), p. 044910. DOI: `10.1103/PhysRevC.88.044910`. arXiv: `1303.0737 [hep-ex]`.

[71] Betty Bezverkhny Abelev et al. “Multi-strange baryon production at mid-rapidity in Pb-Pb collisions at $\sqrt{s_{NN}} = 2.76$ TeV”. In: *Phys. Lett. B* 728 (2014). [Erratum: Phys.Lett.B 734, 409–410 (2014)], pp. 216–227. DOI: `10.1016/j.physletb.2014.05.052`. arXiv: `1307.5543 [nucl-ex]`.

[72] A. G. Knospe et al. “Hadronic resonance production and interaction in partonic and hadronic matter in the EPOS3 model with and without the hadronic afterburner UrQMD”. In: *Phys. Rev. C* 93.1 (2016), p. 014911. DOI: `10.1103/PhysRevC.93.014911`. arXiv: `1509.07895 [nucl-th]`.

[73] S. Wheaton, J. Cleymans, and M. Hauer. “THERMUS”. In: (Aug. 2011). arXiv: `1108.4588 [hep-ph]`.

[74] J. Cleymans et al. “Statistical model predictions for particle ratios at s(NN)**(1/2) = 5.5-TeV”. In: *Phys. Rev. C* 74 (2006), p. 034903. DOI: `10.1103/PhysRevC.74.034903`. arXiv: `hep-ph/0604237`.

[75] Giorgio Torrieri et al. “SHARE: Statistical hadronization with resonances”. In: *Comput. Phys. Commun.* 167 (2005), pp. 229–251. DOI: `10.1016/j.cpc.2005.01.004`. arXiv: `nucl-th/0404083`.

[76] G. Torrieri et al. “SHAREv2: Fluctuations and a comprehensive treatment of decay feed-down”. In: *Comput. Phys. Commun.* 175 (2006), pp. 635–649. DOI: `10.1016/j.cpc.2006.07.010`. arXiv: `nucl-th/0603026`.

[77] M. Petran et al. “SHARE with CHARM”. In: *Comput. Phys. Commun.* 185 (2014), pp. 2056–2079. DOI: `10.1016/j.cpc.2014.02.026`. arXiv: `1310.5108 [hep-ph]`.

[78] Michal Petrán et al. “Hadron production and quark-gluon plasma hadronization in Pb-Pb collisions at $\sqrt{s_{NN}} = 2.76$ TeV”. In: *Phys. Rev. C* 88.3 (2013), p. 034907. DOI: `10.1103/PhysRevC.88.034907`. arXiv: `1303.2098 [hep-ph]`.

[79] Volodymyr Vovchenko and Horst Stoecker. “Thermal-FIST: A package for heavy-ion collisions and hadronic equation of state”. In: *Comput. Phys. Commun.* 244 (2019), pp. 295–310. DOI: `10.1016/j.cpc.2019.06.024`. arXiv: `1901.05249 [nucl-th]`.

[80] Volodymyr Vovchenko, Mark I. Gorenstein, and Horst Stoecker. “Finite resonance widths influence the thermal-model description of hadron yields”. In: *Phys. Rev. C* 98.3 (2018), p. 034906. DOI: `10.1103/PhysRevC.98.034906`. arXiv: `1807.02079 [nucl-th]`.

[81] Peter Braun-Munzinger, Krzysztof Redlich, and Johanna Stachel. "Particle production in heavy ion collisions". In: (Apr. 2003). Ed. by Rudolph C. Hwa and Xin-Nian Wang, pp. 491–599. DOI: `10.1142/9789812795533_0008`. arXiv: `nucl-th/0304013`.

[82] A. Andronic, P. Braun-Munzinger, and J. Stachel. "Hadron production in central nucleus-nucleus collisions at chemical freeze-out". In: *Nucl. Phys. A* 772 (2006), pp. 167–199. DOI: `10.1016/j.nuclphysa.2006.03.012`. arXiv: `nucl-th/0511071`.

[83] Anton Andronic et al. "The thermal proton yield anomaly in Pb-Pb collisions at the LHC and its resolution". In: *Phys. Lett. B* 792 (2019), pp. 304–309. DOI: `10.1016/j.physletb.2019.03.052`. arXiv: `1808.03102 [hep-ph]`.

[84] F. Becattini et al. "Centrality dependence of hadronization and chemical freeze-out conditions in heavy ion collisions at $\sqrt{s_{NN}}$ = 2.76 TeV". In: *Phys. Rev. C* 90.5 (2014), p. 054907. DOI: `10.1103/PhysRevC.90.054907`. arXiv: `1405.0710 [nucl-th]`.

[85] Szabolcs Borsanyi et al. "QCD Crossover at Finite Chemical Potential from Lattice Simulations". In: *Phys. Rev. Lett.* 125.5 (2020), p. 052001. DOI: `10.1103/PhysRevLett.125.052001`. arXiv: `2002.02821 [hep-lat]`.

[86] D. H. Rischke et al. "Excluded volume effect for the nuclear matter equation of state". In: *Zeitschrift für Physik C Particles and Fields* 51.3 (1991), pp. 485–489. DOI: `10.1007/BF01548574`. URL: `https://doi.org/10.1007/BF01548574`.

[87] Betty Bezverkhny Abelev et al. "K^0_S and Λ production in Pb-Pb collisions at $\sqrt{s_{NN}}$ = 2.76 TeV". In: *Phys. Rev. Lett.* 111 (2013), p. 222301. DOI: `10.1103/PhysRevLett.111.222301`. arXiv: `1307.5530 [nucl-ex]`.

[88] Betty Bezverkhny Abelev et al. "$K^*(892)^0$ and (1020) production in Pb-Pb collisions at $\sqrt{sNN}$ = 2.76 TeV". In: *Phys. Rev. C* 91 (2015), p. 024609. DOI: `10.1103/PhysRevC.91.024609`. arXiv: `1404.0495 [nucl-ex]`.

[89] Jaroslav Adam et al. "Production of light nuclei and anti-nuclei in pp and Pb-Pb collisions at energies available at the CERN Large Hadron Collider". In: *Phys. Rev. C* 93.2 (2016), p. 024917. DOI: `10.1103/PhysRevC.93.024917`. arXiv: `1506.08951 [nucl-ex]`.

[90] Shreyasi Acharya et al. "Production of ^{4}He and $^4\overline{\mathrm{He}}$ in Pb-Pb collisions at $\sqrt{s_{\mathrm{NN}}}$ = 2.76 TeV at the LHC". In: *Nucl. Phys. A* 971 (2018), pp. 1–20. DOI: `10.1016/j.nuclphysa.2017.12.004`. arXiv: `1710.07531 [nucl-ex]`.

[91] Jaroslav Adam et al. "$^3_\Lambda\mathrm{H}$ and $^3_{\overline{\Lambda}}\overline{\mathrm{H}}$ production in Pb-Pb collisions at $\sqrt{s_{\mathrm{NN}}}$ = 2.76 TeV". In: *Phys. Lett. B* 754 (2016), pp. 360–372. DOI: `10.1016/j.physletb.2016.01.040`. arXiv: `1506.08453 [nucl-ex]`.

[92] Jan Steinheimer, Jörg Aichelin, and Marcus Bleicher. "Nonthermal p/π Ratio at LHC as a Consequence of Hadronic Final State Interactions". In: *Phys. Rev. Lett.* 110.4 (2013), p. 042501. DOI: `10.1103/PhysRevLett.110.042501`. arXiv: `1203.5302 [nucl-th]`.

[93] Francesco Becattini et al. "Hadron Formation in Relativistic Nuclear Collisions and the QCD Phase Diagram". In: *Phys. Rev. Lett.* 111 (2013), p. 082302. DOI: `10.1103/PhysRevLett.111.082302`. arXiv: `1212.2431 [nucl-th]`.

[94] Chun Shen et al. “Radial and elliptic flow in Pb+Pb collisions at the Large Hadron Collider from viscous hydrodynamic”. In: *Phys. Rev. C* 84 (2011), p. 044903. DOI: `10.1103/PhysRevC.84.044903`. arXiv: `1105.3226 [nucl-th]`.

[95] Vincenzo Minissale, Francesco Scardina, and Vincenzo Greco. “Hadrons from coalescence plus fragmentation in AA collisions at energies available at the BNL Relativistic Heavy Ion Collider to the CERN Large Hadron Collider”. In: *Phys. Rev. C* 92.5 (2015), p. 054904. DOI: `10.1103/PhysRevC.92.054904`. arXiv: `1502.06213 [nucl-th]`.

[96] Betty Bezverkhny Abelev et al. “Production of charged pions, kaons and protons at large transverse momenta in pp and Pb–Pb collisions at $\sqrt{s_{\mathrm{NN}}}$ =2.76 TeV”. In: *Phys. Lett. B* 736 (2014), pp. 196–207. DOI: `10.1016/j.physletb.2014.07.011`. arXiv: `1401.1250 [nucl-ex]`.

[97] Johann Rafelski and Berndt Muller. “Strangeness Production in the Quark - Gluon Plasma”. In: *Phys. Rev. Lett.* 48 (1982). [Erratum: Phys.Rev.Lett. 56, 2334 (1986)], p. 1066. DOI: `10.1103/PhysRevLett.48.1066`.

[98] Peter Koch, Berndt Müller, and Johann Rafelski. “From Strangeness Enhancement to Quark–Gluon Plasma Discovery”. In: *Int. J. Mod. Phys. A* 32.31 (2017), p. 1730024. DOI: `10.1142/S0217751X17300241`. arXiv: `1708.08115 [nucl-th]`.

[99] T. Alber et al. “Anti-baryon production in sulphur nucleus collisions at 200-GeV per nucleon”. In: *Phys. Lett. B* 366 (1996), pp. 56–62. DOI: `10.1016/0370-2693(95)01379-2`.

[100] M. Jacob and E. Quercigh, eds. *The CERN OMEGA spectrometer: 25 years of physics. Proceedings, Symposium, Geneva, Switzerland, March 19, 1997*. CERN Yellow Reports: Conference Proceedings. 1997. DOI: `10.5170/CERN-1997-002`.

[101] Claudia Ratti et al. “Are there hadronic bound states above the QCD transition temperature?” In: *Phys. Rev. D* 85 (2012), p. 014004. DOI: `10.1103/PhysRevD.85.014004`. arXiv: `1109.6243 [hep-ph]`.

[102] Rene Bellwied et al. “Is there a flavor hierarchy in the deconfinement transition of QCD?” In: *Phys. Rev. Lett.* 111 (2013), p. 202302. DOI: `10.1103/PhysRevLett.111.202302`. arXiv: `1305.6297 [hep-lat]`.

[103] Jean Cleymans et al. “Multiplicity dependence of (multi)strange baryons in the canonical ensemble with phase shift corrections”. In: *Phys. Rev. C* 103.1 (2021), p. 014904. DOI: `10.1103/PhysRevC.103.014904`. arXiv: `2009.04844 [hep-ph]`.

[104] Shreyasi Acharya et al. “D-meson azimuthal anisotropy in midcentral Pb-Pb collisions at $\sqrt{s_{\mathrm{NN}}} = \mathbf{5.02}$ TeV”. In: *Phys. Rev. Lett.* 120.10 (2018), p. 102301. DOI: `10.1103/PhysRevLett.120.102301`. arXiv: `1707.01005 [nucl-ex]`.

[105] S. Acharya et al. “Measurement of D^0, D^+, D^{*+} and D_s^+ production in Pb-Pb collisions at $\sqrt{s_{\mathrm{NN}}} = 5.02$ TeV”. In: *JHEP* 10 (2018), p. 174. DOI: `10.1007/JHEP10(2018)174`. arXiv: `1804.09083 [nucl-ex]`.

[106] Shreyasi Acharya et al. “Event-shape engineering for the D-meson elliptic flow in mid-central Pb-Pb collisions at $\sqrt{s_{\mathrm{NN}}} = 5.02$ TeV”. In: *JHEP* 02 (2019), p. 150. DOI: `10.1007/JHEP02(2019)150`. arXiv: `1809.09371 [nucl-ex]`.

[107] Albert M Sirunyan et al. “Measurement of prompt D^0 meson azimuthal anisotropy in Pb-Pb collisions at $\sqrt{s_{NN}} = 5.02$ TeV”. In: *Phys. Rev. Lett.* 120.20 (2018), p. 202301. DOI: 10.1103/PhysRevLett.120.202301. arXiv: 1708.03497 [nucl-ex].

[108] Albert M Sirunyan et al. “Nuclear modification factor of D^0 mesons in PbPb collisions at $\sqrt{s_{\mathrm{NN}}} = 5.02$ TeV”. In: *Phys. Lett. B* 782 (2018), pp. 474–496. DOI: 10.1016/j.physletb.2018.05.074. arXiv: 1708.04962 [nucl-ex].

[109] Shreyasi Acharya et al. “Prompt D^0, D^+, and D^{*+} production in Pb–Pb collisions at $\sqrt{s_{\mathrm{NN}}} = 5.02$ TeV”. In: *JHEP* 01 (2022), p. 174. DOI: 10.1007/JHEP01(2022)174. arXiv: 2110.09420 [nucl-ex].

[110] Shreyasi Acharya et al. “Transverse-momentum and event-shape dependence of D-meson flow harmonics in Pb–Pb collisions at $\sqrt{s_{NN}} = 5.02$ TeV”. In: *Phys. Lett. B* 813 (2021), p. 136054. DOI: 10.1016/j.physletb.2020.136054. arXiv: 2005.11131 [nucl-ex].

[111] Min He and Ralf Rapp. “Hadronization and Charm-Hadron Ratios in Heavy-Ion Collisions”. In: *Phys. Rev. Lett.* 124.4 (2020), p. 042301. DOI: 10.1103/PhysRevLett.124.042301. arXiv: 1905.09216 [nucl-th].

[112] Weiyao Ke, Yingru Xu, and Steffen A. Bass. “Modified Boltzmann approach for modeling the splitting vertices induced by the hot QCD medium in the deep Landau-Pomeranchuk-Migdal region”. In: *Phys. Rev. C* 100.6 (2019), p. 064911. DOI: 10.1103/PhysRevC.100.064911. arXiv: 1810.08177 [nucl-th].

[113] A. Beraudo et al. “Heavy flavors in heavy-ion collisions: quenching, flow and correlations”. In: *Eur. Phys. J. C* 75.3 (2015), p. 121. DOI: 10.1140/epjc/s10052-015-3336-6. arXiv: 1410.6082 [hep-ph].

[114] Andrea Beraudo et al. “Event-shape engineering and heavy-flavour observables in relativistic heavy-ion collisions”. In: *Eur. Phys. J. C* 79.6 (2019), p. 494. DOI: 10.1140/epjc/s10052-019-6996-9. arXiv: 1812.08337 [physics.data-an].

[115] Andrea Beraudo et al. “Rapidity dependence of heavy-flavour production in heavy-ion collisions within a full 3+1 transport approach: quenching, elliptic and directed flow”. In: *JHEP* 05 (2021), p. 279. DOI: 10.1007/JHEP05(2021)279. arXiv: 2102.08064 [hep-ph].

[116] Taesoo Song et al. “Tomography of the Quark-Gluon-Plasma by Charm Quarks”. In: *Phys. Rev. C* 92.1 (2015), p. 014910. DOI: 10.1103/PhysRevC.92.014910. arXiv: 1503.03039 [nucl-th].

[117] Marlene Nahrgang et al. “Influence of hadronic bound states above T_c on heavy-quark observables in Pb + Pb collisions at at the CERN Large Hadron Collider”. In: *Phys. Rev. C* 89.1 (2014), p. 014905. DOI: 10.1103/PhysRevC.89.014905. arXiv: 1305.6544 [hep-ph].

[118] Francesco Scardina et al. “Estimating the charm quark diffusion coefficient and thermalization time from D meson spectra at energies available at the BNL Relativistic Heavy Ion Collider and the CERN Large Hadron Collider”. In: *Phys. Rev. C* 96.4 (2017), p. 044905. DOI: 10.1103/PhysRevC.96.044905. arXiv: 1707.05452 [nucl-th].

[119] Salvatore Plumari et al. “Heavy - light flavor correlations of anisotropic flows at LHC energies within event-by-event transport approach”. In: *Phys. Lett. B* 805 (2020), p. 135460. DOI: 10.1016/j.physletb.2020.135460. arXiv: 1912.09350 [hep-ph].

[120] Shuang Li and Jinfeng Liao. “Data-driven extraction of heavy quark diffusion in quark-gluon plasma”. In: *Eur. Phys. J. C* 80.7 (2020), p. 671. DOI: `10.1140/epjc/s10052-020-8243-9`. arXiv: `1912.08965 [hep-ph]`.

[121] Roland Katz et al. “Sensitivity study with a D and B mesons modular simulation code of heavy flavor RAA and azimuthal anisotropies based on beam energy, initial conditions, hadronization, and suppression mechanisms”. In: *Phys. Rev. C* 102.2 (2020), p. 024906. DOI: `10.1103/PhysRevC.102.024906`. arXiv: `1906.10768 [nucl-th]`.

[122] S. Acharya et al. “Transverse momentum spectra and nuclear modification factors of charged particles in pp, p-Pb and Pb-Pb collisions at the LHC”. In: *JHEP* 11 (2018), p. 013. DOI: `10.1007/JHEP11(2018)013`. arXiv: `1802.09145 [nucl-ex]`.

[123] Alexander Rothkopf. “Heavy Quarkonium in Extreme Conditions”. In: *Phys. Rept.* 858 (2020), pp. 1–117. DOI: `10.1016/j.physrep.2020.02.006`. arXiv: `1912.02253 [hep-ph]`.

[124] S. Digal, P. Petreczky, and H. Satz. “Quarkonium feed down and sequential suppression”. In: *Phys. Rev. D* 64 (2001), p. 094015. DOI: `10.1103/PhysRevD.64.094015`. arXiv: `hep-ph/0106017`.

[125] M. Laine et al. “Real-time static potential in hot QCD”. In: *JHEP* 03 (2007), p. 054. DOI: `10.1088/1126-6708/2007/03/054`. arXiv: `hep-ph/0611300`.

[126] Robert L. Thews, Martin Schroedter, and Johann Rafelski. “Enhanced J/ψ production in deconfined quark matter”. In: *Phys. Rev. C* 63 (2001), p. 054905. DOI: `10.1103/PhysRevC.63.054905`. arXiv: `hep-ph/0007323`.

[127] Kai Zhou et al. “Medium effects on charmonium production at ultrarelativistic energies available at the CERN Large Hadron Collider”. In: *Phys. Rev. C* 89.5 (2014), p. 054911. DOI: `10.1103/PhysRevC.89.054911`. arXiv: `1401.5845 [nucl-th]`.

[128] A. Capella et al. “Charmonium dissociation and recombination at RHIC and LHC”. In: *Eur. Phys. J. C* 58 (2008), pp. 437–444. DOI: `10.1140/epjc/s10052-008-0772-6`. arXiv: `0712.4331 [hep-ph]`.

[129] Yukinao Akamatsu. “Quarkonium in quark–gluon plasma: Open quantum system approaches re-examined”. In: *Prog. Part. Nucl. Phys.* 123 (2022), p. 103932. DOI: `10.1016/j.ppnp.2021.103932`. arXiv: `2009.10559 [nucl-th]`.

[130] L. Maiani et al. “J / psi absorption in heavy ion collisions II”. In: *Nucl. Phys. A* 748 (2005), pp. 209–225. DOI: `10.1016/j.nuclphysa.2004.10.023`. arXiv: `hep-ph/0408150`.

[131] Jaroslav Adam et al. “Measurement of an excess in the yield of J/ψ at very low p_{T} in Pb-Pb collisions at $\sqrt{s_{\mathrm{NN}}}$ = 2.76 TeV”. In: *Phys. Rev. Lett.* 116.22 (2016), p. 222301. DOI: `10.1103/PhysRevLett.116.222301`. arXiv: `1509.08802 [nucl-ex]`.

[132] Shreyasi Acharya et al. “Measurements of inclusive J/ψ production at midrapidity and forward rapidity in Pb−Pb collisions at $\sqrt{s_{\mathrm{NN}}}$ = 5.02 TeV”. In: (Mar. 2023). arXiv: `2303.13361 [nucl-ex]`.

[133] B. Alessandro et al. “A New measurement of J/psi suppression in Pb-Pb collisions at 158-GeV per nucleon”. In: *Eur. Phys. J. C* 39 (2005), pp. 335–345. DOI: `10.1140/epjc/s2004-02107-9`. arXiv: `hep-ex/0412036`.

[134] Jaroslav Adam et al. “Measurement of inclusive J/ψ suppression in Au+Au collisions at $\sqrt{s_{NN}}$ = 200 GeV through the dimuon channel at STAR”. In: *Phys. Lett. B* 797 (2019), p. 134917. DOI: 10.1016/j.physletb.2019.134917. arXiv: 1905.13669 [nucl-ex].

[135] Anton Andronic et al. “Transverse momentum distributions of charmonium states with the statistical hadronization model”. In: *Phys. Lett. B* 797 (2019), p. 134836. DOI: 10.1016/j.physletb.2019.134836. arXiv: 1901.09200 [nucl-th].

[136] Xiaojian Du and Ralf Rapp. “Sequential Regeneration of Charmonia in Heavy-Ion Collisions”. In: *Nucl. Phys. A* 943 (2015), pp. 147–158. DOI: 10.1016/j.nuclphysa.2015.09.006. arXiv: 1504.00670 [hep-ph].

[137] A. Andronic et al. “Heavy-flavour and quarkonium production in the LHC era: from proton–proton to heavy-ion collisions”. In: *Eur. Phys. J. C* 76.3 (2016), p. 107. DOI: 10.1140/epjc/s10052-015-3819-5. arXiv: 1506.03981 [nucl-ex].

[138] Jean-Philippe Lansberg. “New Observables in Inclusive Production of Quarkonia”. In: *Phys. Rept.* 889 (2020), pp. 1–106. DOI: 10.1016/j.physrep.2020.08.007. arXiv: 1903.09185 [hep-ph].

[139] Roel Aaij et al. “Study of χ_{b} meson production in $\mathrm{p}\,\mathrm{p}$ collisions at $\sqrt{s} = 7$ and $8\,\mathrm{TeV}$ and observation of the decay $\chi_{\mathrm{b}}(3\mathrm{P}) \rightarrow \Upsilon(3\mathrm{S})\gamma$”. In: *Eur. Phys. J. C* 74.10 (2014), p. 3092. DOI: 10.1140/epjc/s10052-014-3092-z. arXiv: 1407.7734 [hep-ex].

[140] Shreyasi Acharya et al. “$\Upsilon productionandnuclearmodificationatforwardrapidityinPb\breve{\ }Pbcollisions$ $5.02TeV$”. In: *Phys. Lett. B* 822 (2021), p. 136579. DOI: 10.1016/j.physletb.2021.136579. arXiv: 2011.05758 [nucl-ex].

[141] Elena G. Ferreiro and Jean-Philippe Lansberg. “Is bottomonium suppression in proton-nucleus and nucleus-nucleus collisions at LHC energies due to the same effects?” In: *JHEP* 10 (2018). [Erratum: JHEP 03, 063 (2019)], p. 094. DOI: 10.1007/JHEP10(2018)094. arXiv: 1804.04474 [hep-ph].

[142] Xiaojian Du, Min He, and Ralf Rapp. “Color Screening and Regeneration of Bottomonia in High-Energy Heavy-Ion Collisions”. In: *Phys. Rev. C* 96.5 (2017), p. 054901. DOI: 10.1103/PhysRevC.96.054901. arXiv: 1706.08670 [hep-ph].

[143] Xiaojun Yao et al. “Coupled Boltzmann Transport Equations of Heavy Quarks and Quarkonia in Quark-Gluon Plasma”. In: *JHEP* 01 (2021), p. 046. DOI: 10.1007/JHEP01(2021)046. arXiv: 2004.06746 [hep-ph].

[144] Brandon Krouppa and Michael Strickland. “Predictions for bottomonia suppression in 5.023 TeV Pb-Pb collisions”. In: *Universe* 2.3 (2016), p. 16. DOI: 10.3390/universe2030016. arXiv: 1605.03561 [hep-ph].

[145] Nora Brambilla et al. “Bottomonium production in heavy-ion collisions using quantum trajectories: Differential observables and momentum anisotropy”. In: *Phys. Rev. D* 104.9 (2021), p. 094049. DOI: 10.1103/PhysRevD.104.094049. arXiv: 2107.06222 [hep-ph].

[146] Georges Aad et al. “Observation of Long-Range Elliptic Azimuthal Anisotropies in $\sqrt{s}$ =13 and 2.76 TeV pp Collisions with the ATLAS Detector”. In: *Phys. Rev. Lett.* 116.17 (2016), p. 172301. DOI: 10.1103/PhysRevLett.116.172301. arXiv: 1509.04776 [hep-ex].

[147] Betty Abelev et al. “Long-range angular correlations on the near and away side in p-Pb collisions at $\sqrt{s_{NN}} = 5.02$ TeV”. In: *Phys. Lett. B* 719 (2013), pp. 29–41. DOI: `10.1016/j.physletb.2013.01.012`. arXiv: `1212.2001 [nucl-ex]`.

[148] Vardan Khachatryan et al. “Observation of Long-Range Near-Side Angular Correlations in Proton-Proton Collisions at the LHC”. In: *JHEP* 09 (2010), p. 091. DOI: `10.1007/JHEP09(2010)091`. arXiv: `1009.4122 [hep-ex]`.

[149] Georges Aad et al. “Measurement of long-range pseudorapidity correlations and azimuthal harmonics in $\sqrt{s_{NN}} = 5.02$ TeV proton-lead collisions with the ATLAS detector”. In: *Phys. Rev. C* 90.4 (2014), p. 044906. DOI: `10.1103/PhysRevC.90.044906`. arXiv: `1409.1792 [hep-ex]`.

[150] Betty Bezverkhny Abelev et al. “Performance of the ALICE Experiment at the CERN LHC”. In: *Int. J. Mod. Phys. A* 29 (2014), p. 1430044. DOI: `10.1142/S0217751X14300440`. arXiv: `1402.4476 [nucl-ex]`.

[151] Volodymyr Vovchenko, Benjamin Dönigus, and Horst Stoecker. “Canonical statistical model analysis of p-p , p -Pb, and Pb-Pb collisions at energies available at the CERN Large Hadron Collider”. In: *Phys. Rev. C* 100.5 (2019), p. 054906. DOI: `10.1103/PhysRevC.100.054906`. arXiv: `1906.03145 [hep-ph]`.

[152] Shreyasi Acharya et al. “Multiplicity dependence of π, K, and p production in pp collisions at $\sqrt{s} = 13$ TeV”. In: *Eur. Phys. J. C* 80.8 (2020), p. 693. DOI: `10.1140/epjc/s10052-020-8125-1`. arXiv: `2003.02394 [nucl-ex]`.

[153] Betty Bezverkhny Abelev et al. “Multiplicity Dependence of Pion, Kaon, Proton and Lambda Production in p-Pb Collisions at $\sqrt{s_{NN}} = 5.02$ TeV”. In: *Phys. Lett. B* 728 (2014), pp. 25–38. DOI: `10.1016/j.physletb.2013.11.020`. arXiv: `1307.6796 [nucl-ex]`.

[154] Jaroslav Adam et al. “Multi-strange baryon production in p-Pb collisions at $\sqrt{s_{\mathrm{NN}}} = 5.02$ TeV”. In: *Phys. Lett. B* 758 (2016), pp. 389–401. DOI: `10.1016/j.physletb.2016.05.027`. arXiv: `1512.07227 [nucl-ex]`.

[155] Shreyasi Acharya et al. “$\mathrm{K}^*(892)^0$ and $\phi(1020)$ production in p-Pb collisions at $\sqrt{s_{\mathrm{NN}}} = 8.16$ TeV”. In: (Oct. 2021). arXiv: `2110.10042 [nucl-ex]`.

[156] Torbjörn Sjöstrand et al. “An introduction to PYTHIA 8.2”. In: *Comput. Phys. Commun.* 191 (2015), pp. 159–177. DOI: `10.1016/j.cpc.2015.01.024`. arXiv: `1410.3012 [hep-ph]`.

[157] Christian Bierlich et al. “Effects of Overlapping Strings in pp Collisions”. In: *JHEP* 03 (2015), p. 148. DOI: `10.1007/JHEP03(2015)148`. arXiv: `1412.6259 [hep-ph]`.

[158] Shreyasi Acharya et al. “Light-flavor particle production in high-multiplicity pp collisions at $\sqrt{s} = \mathbf{13}$ TeV as a function of transverse spherocity”. In: (Oct. 2023). arXiv: `2310.10236 [hep-ex]`.

[159] Shreyasi Acharya et al. “Production of pions, kaons, and protons as a function of the relative transverse activity classifier in pp collisions at $\sqrt{s} = 13$ TeV”. In: *JHEP* 06 (2023), p. 027. DOI: `10.1007/JHEP06(2023)027`. arXiv: `2301.10120 [nucl-ex]`.

[160] F. Ercolessi. “Study of strangeness production in pp collisions as a function of multiplicity and effective energy with ALICE”. In: *Nuovo Cim. C* 45.4 (2022), p. 65. DOI: `10.1393/ncc/i2022-22065-0`.

[161] Shreyasi Acharya et al. “Underlying Event properties in pp collisions at $\sqrt{s}$ = 13 TeV”. In: *JHEP* 04 (2020), p. 192. DOI: `10.1007/JHEP04(2020)192`. arXiv: `1910.14400 [nucl-ex]`.

[162] Tim Martin, Peter Skands, and Sinead Farrington. “Probing Collective Effects in Hadronisation with the Extremes of the Underlying Event”. In: *Eur. Phys. J. C* 76.5 (2016), p. 299. DOI: `10.1140/epjc/s10052-016-4135-4`. arXiv: `1603.05298 [hep-ph]`.

[163] Antonio Ortiz and Lizardo Valencia Palomo. “Universality of the underlying event in pp collisions”. In: *Phys. Rev. D* 96.11 (2017), p. 114019. DOI: `10.1103/PhysRevD.96.114019`. arXiv: `1710.04741 [hep-ex]`.

[164] Antonio Ortiz and Lizardo Valencia Palomo. “Probing color reconnection with underlying event observables at the LHC energies”. In: *Phys. Rev. D* 99.3 (2019), p. 034027. DOI: `10.1103/PhysRevD.99.034027`. arXiv: `1809.01744 [hep-ex]`.

[165] Shreyasi Acharya et al. “Charged-particle production as a function of the relative transverse activity classifier in pp, p−Pb, and Pb−Pb collisions at the LHC”. In: (Oct. 2023). arXiv: `2310.07490 [nucl-ex]`.

[166] T. Pierog et al. “EPOS LHC: Test of collective hadronization with data measured at the CERN Large Hadron Collider”. In: *Phys. Rev. C* 92.3 (2015), p. 034906. DOI: `10.1103/PhysRevC.92.034906`. arXiv: `1306.0121 [hep-ph]`.

[167] Jesper R. Christiansen. *Colour Reconnection - Models and Tests*. 2015. arXiv: `1510.04859 [hep-ph]`.

[168] Leif Lönnblad and Harsh Shah. “A spatially constrained QCD colour reconnection in pp, pA, and AA collisions in the Pythia8/Angantyr model”. In: *The European Physical Journal C* 83.7 (July 2023). ISSN: 1434-6052. DOI: `10.1140/epjc/s10052-023-11778-3`. URL: `http://dx.doi.org/10.1140/epjc/s10052-023-11778-3`.

[169] Meenakshi Sharma. “Strangeness production in p−Pb collisions at 8.16 TeV”. In: *Springer Proc. Phys.* 261 (2021). Ed. by Prafulla Kumar Behera et al., pp. 1019–1022. DOI: `10.1007/978-981-33-4408-2_148`. arXiv: `1911.04845 [hep-ex]`.

[170] URL: `https://home.cern/resources/faqs/facts-and-figures-about-lhc`.

[171] ALICE Collaboration. “The ALICE experiment at the CERN LHC”. In: *Journal of Instrumentation* 3.08 (2008), S08002.

[172] Felix Reidt. “Upgrade of the ALICE ITS detector”. In: *Nucl. Instrum. Meth. A* 1032 (2022), p. 166632. DOI: `10.1016/j.nima.2022.166632`. arXiv: `2111.08301 [physics.ins-det]`.

[173] Nicolo Jacazio. “Production and nuclear modification factors of pions, kaons and protons in pp and AA collisions at the LHC”. Presented 18 Mar 2019. 2018. URL: `https://cds.cern.ch/record/2672596`.

[174] J. Adolfsson et al. “The upgrade of the ALICE TPC with GEMs and continuous readout”. In: *JINST* 16.03 (2021), P03022. DOI: `10.1088/1748-0221/16/03/P03022`. arXiv: `2012.09518 [physics.ins-det]`.

[175] Jaroslav Adam et al. “Determination of the event collision time with the ALICE detector at the LHC”. In: *Eur. Phys. J. Plus* 132.2 (2017), p. 99. DOI: `10.1140/epjp/i2017-11279-1`. arXiv: `1610.03055 [physics.ins-det]`.

[176] Giacomo Volpe. "PID performance of the High Momentum Particle IDentification (HMPID) detector during LHC-Run 2". In: *Nucl. Instrum. Meth. A* 952 (2020), p. 161803. DOI: `10.1016/j.nima.2019.01.030`.

[177] Shreyasi Acharya et al. "Calibration of the photon spectrometer PHOS of the ALICE experiment". In: *JINST* 14.05 (2019), P05025. DOI: `10.1088/1748-0221/14/05/P05025`. arXiv: `1902.06145 [physics.ins-det]`.

[178] S. Acharya et al. "Performance of the ALICE Electromagnetic Calorimeter". In: *JINST* 18.08 (2023), P08007. DOI: `10.1088/1748-0221/18/08/P08007`. arXiv: `2209.04216 [physics.ins-det]`.

[179] Debasish Das. "Performance and First Physics Results of the ALICE Muon Spectrometer". In: *Nucl. Phys. A* 862-863 (2011). Ed. by Premomoy Ghosh, Tapan Nayak, and Raghava Varma, pp. 223–230. DOI: `10.1016/j.nuclphysa.2011.05.044`. arXiv: `1102.2071 [nucl-ex]`.

[180] Torbjorn Sjostrand, Stephen Mrenna, and Peter Z. Skands. "PYTHIA 6.4 Physics and Manual". In: *JHEP* 05 (2006), p. 026. DOI: `10.1088/1126-6708/2006/05/026`. arXiv: `hep-ph/0603175`.

[181] David Rohr et al. "Track Reconstruction in the ALICE TPC using GPUs for LHC Run 3". In: *4th International Workshop Connecting The Dots 2018*. Nov. 2018. arXiv: `1811.11481 [physics.ins-det]`.

[182] René Brun et al. "GEANT Detector Description and Simulation Tool". In: (Oct. 1994). DOI: `10.17181/CERN.MUHF.DMJ1`.

[183] Diego Casadei. "Estimating the selection efficiency". In: *JINST* 7 (2012), P08021. DOI: `10.1088/1748-0221/7/08/P08021`. arXiv: `0908.0130 [physics.data-an]`.

[184] Betty Abelev et al. "Production of $K^*(892)^0$ and $\phi(1020)$ in pp collisions at $\sqrt{s} = 7$ TeV". In: *Eur. Phys. J. C* 72 (2012), p. 2183. DOI: `10.1140/epjc/s10052-012-2183-y`. arXiv: `1208.5717 [hep-ex]`.

[185] Shreyasi Acharya et al. "$\mathrm{K}^*(892)^0$ and $\phi(1020)$ production at midrapidity in pp collisions at $\sqrt{s} = 8$ TeV". In: *Phys. Rev. C* 102.2 (2020), p. 024912. DOI: `10.1103/PhysRevC.102.024912`. arXiv: `1910.14410 [nucl-ex]`.

[186] Shreyasi Acharya et al. "Production of light (anti)nuclei in pp collisions at $\sqrt{s} = 5.02$ TeV". In: *Eur. Phys. J. C* 82.4 (2022), p. 289. DOI: `10.1140/epjc/s10052-022-10241-z`. arXiv: `2112.00610 [nucl-ex]`.

[187] Constantino Tsallis. "Possible Generalization of Boltzmann-Gibbs Statistics". In: *J. Statist. Phys.* 52 (1988), pp. 479–487. DOI: `10.1007/BF01016429`.

[188] Shreyasi Acharya et al. "Multiplicity and rapidity dependence of $\mathrm{K}^*(\mathbf{892})^0$ and $\phi(\mathbf{1020})$ production in p–Pb collisions at $\sqrt{s_{\mathrm{NN}}} = 5.02$ TeV". In: *Eur. Phys. J. C* 83.6 (2023), p. 540. DOI: `10.1140/epjc/s10052-023-11449-3`. arXiv: `2204.10263 [nucl-ex]`.

[189] Jaroslav Adam et al. "Production of K^* $(892)^0$ and ϕ (1020) in p–Pb collisions at $\sqrt{s_{\mathrm{NN}}}$ = 5.02 TeV". In: *Eur. Phys. J. C* 76.5 (2016), p. 245. DOI: `10.1140/epjc/s10052-016-4088-7`. arXiv: `1601.07868 [nucl-ex]`.

[190] Shreyasi Acharya et al. "Production of $\mathrm{K}^*(892)^0$ and $\phi(1020)$ in pp and Pb-Pb collisions at $\sqrt{s_{\mathrm{NN}}} = 5.02$ TeV". In: *Phys. Rev. C* 106.3 (2022), p. 034907. DOI: `10.1103/PhysRevC.106.034907`. arXiv: `2106.13113 [nucl-ex]`.

[191] B. I. Abelev et al. "Strange particle production in p+p collisions at s**(1/2) = 200-GeV". In: *Phys. Rev. C* 75 (2007), p. 064901. DOI: `10.1103/PhysRevC.75.064901`. arXiv: `nucl-ex/0607033`.

[192] Shreyasi Acharya et al. “Charged-particle production as a function of multiplicity and transverse spherocity in pp collisions at $\sqrt{s} = 5.02$ and 13 TeV”. In: *Eur. Phys. J. C* 79.10 (2019), p. 857. DOI: `10.1140/epjc/s10052-019-7350-y`. arXiv: `1905.07208 [nucl-ex]`.

[193] Alice Ohlson. “Measurements of the fluctuations of identified particles in ALICE at the LHC”. In: *PoS* CPOD2017 (2018), p. 031. DOI: `10.22323/1.311.0031`. arXiv: `1901.00709 [nucl-ex]`.

[194] Maitreyee Mukherjee. “Event-by-event multiplicity fluctuations in Pb-Pb collisions in ALICE”. In: *Acta Phys. Polon. Supp.* 9 (2016), p. 283. DOI: `10.5506/APhysPolBSupp.9.283`. arXiv: `1603.06824 [hep-ex]`.

[195] Peter Skands, Stefano Carrazza, and Juan Rojo. “Tuning PYTHIA 8.1: the Monash 2013 Tune”. In: *Eur. Phys. J. C* 74.8 (2014), p. 3024. DOI: `10.1140/epjc/s10052-014-3024-y`. arXiv: `1404.5630 [hep-ph]`.

[196] R. Abdul Khalek et al. “Science Requirements and Detector Concepts for the Electron-Ion Collider: EIC Yellow Report”. In: *Nucl. Phys. A* 1026 (2022), p. 122447. DOI: `10.1016/j.nuclphysa.2022.122447`. arXiv: `2103.05419 [physics.ins-det]`.

[197] R.L. Jaffe and Aneesh Manohar. “The g1 problem: Deep inelastic electron scattering and the spin of the proton”. In: *Nuclear Physics B* 337.3 (1990), pp. 509–546. ISSN: 0550-3213. DOI: `https://doi.org/10.1016/0550-3213(90)90506-9`. URL: `https://www.sciencedirect.com/science/article/pii/0550321390905069`.

[198] Johannes Blumlein. “The Theory of Deeply Inelastic Scattering”. In: *Prog. Part. Nucl. Phys.* 69 (2013), pp. 28–84. DOI: `10.1016/j.ppnp.2012.09.006`. arXiv: `1208.6087 [hep-ph]`.

[199] J. Ashman et al. “A Measurement of the Spin Asymmetry and Determination of the Structure Function g(1) in Deep Inelastic Muon-Proton Scattering”. In: *Phys. Lett. B* 206 (1988). Ed. by V. W. Hughes and C. Cavata, p. 364. DOI: `10.1016/0370-2693(88)91523-7`.

[200] Christine A. Aidala et al. “The Spin Structure of the Nucleon”. In: *Rev. Mod. Phys.* 85 (2013), pp. 655–691. DOI: `10.1103/RevModPhys.85.655`. arXiv: `1209.2803 [hep-ph]`.

[201] Dieter Müller et al. “Wave functions, evolution equations and evolution kernels from light ray operators of QCD”. In: *Fortsch. Phys.* 42 (1994), pp. 101–141. DOI: `10.1002/prop.2190420202`. arXiv: `hep-ph/9812448`.

[202] A. V. Radyushkin. “Scaling limit of deeply virtual Compton scattering”. In: *Phys. Lett. B* 380 (1996), pp. 417–425. DOI: `10.1016/0370-2693(96)00528-X`. arXiv: `hep-ph/9604317`.

[203] Xiang-Dong Ji. “Gauge-Invariant Decomposition of Nucleon Spin”. In: *Phys. Rev. Lett.* 78 (1997), pp. 610–613. DOI: `10.1103/PhysRevLett.78.610`. arXiv: `hep-ph/9603249`.

[204] Daniel Boer and P. J. Mulders. “Time reversal odd distribution functions in leptoproduction”. In: *Phys. Rev. D* 57 (1998), pp. 5780–5786. DOI: `10.1103/PhysRevD.57.5780`. arXiv: `hep-ph/9711485`.

[205] P. J. Mulders and R. D. Tangerman. "The Complete tree level result up to order 1/Q for polarized deep inelastic leptoproduction". In: *Nucl. Phys. B* 461 (1996). [Erratum: Nucl.Phys.B 484, 538–540 (1997)], pp. 197–237. DOI: `10.1016/0550-3213(95)00632-X`. arXiv: `hep-ph/9510301`.

[206] P. J. Mulders and J. Rodrigues. "Transverse momentum dependence in gluon distribution and fragmentation functions". In: *Phys. Rev. D* 63 (2001), p. 094021. DOI: `10.1103/PhysRevD.63.094021`. arXiv: `hep-ph/0009343`.

[207] S. Meissner, A. Metz, and K. Goeke. "Relations between generalized and transverse momentum dependent parton distributions". In: *Phys. Rev. D* 76 (2007), p. 034002. DOI: `10.1103/PhysRevD.76.034002`. arXiv: `hep-ph/0703176`.

[208] Francois Gelis et al. "The Color Glass Condensate". In: *Ann. Rev. Nucl. Part. Sci.* 60 (2010), pp. 463–489. DOI: `10.1146/annurev.nucl.010909.083629`. arXiv: `1002.0333 [hep-ph]`.

[209] John C. Collins, Davison E. Soper, and George F. Sterman. "Factorization of Hard Processes in QCD". In: *Adv. Ser. Direct. High Energy Phys.* 5 (1989), pp. 1–91. DOI: `10.1142/9789814503266_0001`. arXiv: `hep-ph/0409313`.

[210] J.J. Aubert et al. "The ratio of the nucleon structure functions F2N for iron and deuterium". In: *Physics Letters B* 123.3 (1983), pp. 275–278. ISSN: 0370-2693. DOI: `https://doi.org/10.1016/0370-2693(83)90437-9`. URL: `https://www.sciencedirect.com/science/article/pii/0370269383904379`.

[211] M. Arneodo et al. "The A dependence of the nuclear structure function ratios". In: *Nuclear Physics B* 481.1 (1996), pp. 3–22. ISSN: 0550-3213. DOI: `https://doi.org/10.1016/S0550-3213(96)90117-0`. URL: `https://www.sciencedirect.com/science/article/pii/S0550321396901170`.

[212] D F Geesaman, K Saito, and A W Thomas. "The Nuclear EMC Effect". In: *Annual Review of Nuclear and Particle Science* 45.1 (1995), pp. 337–390. DOI: `10.1146/annurev.ns.45.120195.002005`. eprint: `https://doi.org/10.1146/annurev.ns.45.120195.002005`. URL: `https://doi.org/10.1146/annurev.ns.45.120195.002005`.

[213] J. Gomez et al. "Measurement of the A dependence of deep-inelastic electron scattering". In: *Phys. Rev. D* 49 (9 1994), pp. 4348–4372. DOI: `10.1103/PhysRevD.49.4348`. URL: `https://link.aps.org/doi/10.1103/PhysRevD.49.4348`.

[214] J. Adam et al. "ATHENA detector proposal — a totally hermetic electron nucleus apparatus proposed for IP6 at the Electron-Ion Collider". In: *JINST* 17.10 (2022), P10019. DOI: `10.1088/1748-0221/17/10/P10019`. arXiv: `2210.09048 [physics.ins-det]`.

[215] E. Garutti and Yu. Musienko. "Radiation damage of SiPMs". In: *Nuclear Instruments and Methods in Physics Research Section A: Accelerators, Spectrometers, Detectors and Associated Equipment* 926 (2019), pp. 69–84. DOI: `10.1016/j.nima.2018.10.191`. URL: `https://doi.org/10.1016%2Fj.nima.2018.10.191`.

[216] Frank Simon. "Silicon photomultipliers in particle and nuclear physics". In: *Nucl. Instrum. Meth. A* 926 (2019), pp. 85–100. DOI: `10.1016/j.nima.2018.11.042`. arXiv: `1811.03877 [physics.ins-det]`.

[217] Pietro P. Calò et al. "SiPM readout electronics". In: *Nucl. Instrum. Meth. A* 926 (2019), pp. 57–68. DOI: `10.1016/j.nima.2018.09.030`.

[218] Claudio Piemonte and Alberto Gola. "Overview on the main parameters and technology of modern Silicon Photomultipliers". In: *Nucl. Instrum. Meth. A* 926 (2019), pp. 2–15. DOI: `10.1016/j.nima.2018.11.119`.

[219] Fabio Acerbi and Stefan Gundacker. "Understanding and simulating SiPMs". In: *Nucl. Instrum. Meth. A* 926 (2019), pp. 16–35. DOI: `10.1016/j.nima.2018.11.118`.

[220] S. España et al. "Performance Evaluation of SiPM Photosensors in the Presence of Magnetic Fields". In: *AIP Conf. Proc.* 1231.1 (2010). Ed. by J. A. Caballero et al., p. 171. DOI: `10.1063/1.3428910`.

[221] Fengbo Gu et al. "Achieving significant performance recovery of SiPMs' irradiation damage with in-situ current annealing". In: *Nucl. Instrum. Meth. A* 1053 (2023), p. 168381. DOI: `10.1016/j.nima.2023.168381`.

[222] Nicolas De Angelis et al. "Temperature dependence of radiation damage annealing of Silicon Photomultipliers". In: *Nucl. Instrum. Meth. A* 1048 (2023), p. 167934. DOI: `10.1016/j.nima.2022.167934`. arXiv: `2212.08474 [astro-ph.IM]`.

[223] Prof. Dr. Ivor Fleck Dr. Reimund Bayerlein. *SiPM Experiment Manual*. Uni Siegen.

[224] en:User:TheNoise. *P-n junction — Wikipedia, The Free Encyclopedia*. [Online; accessed 27-October-2023]. URL: `https://commons.wikimedia.org/wiki/File:Pn-junction-equilibrium-graphs.png`.

[225] Onsemi. *Introduction to the Silicon Photomultiplier (SiPM)*.

[226] Ferenc Nagy et al. "A model based DC analysis of SiPM breakdown voltages". In: *Nuclear Instruments and Methods in Physics Research Section A: Accelerators, Spectrometers, Detectors and Associated Equipment* 849 (2017), pp. 55–59. DOI: `10.1016/j.nima.2017.01.002`. URL: `https://doi.org/10.1016%2Fj.nima.2017.01.002`.

[227] Gunnar Lindström. "Radiation damage in silicon detectors". In: *Nuclear Instruments and Methods in Physics Research Section A: Accelerators, Spectrometers, Detectors and Associated Equipment* 512.1 (2003). Proceedings of the 9th European Symposium on Semiconductor Detectors: New Developments on Radiation Detectors, pp. 30–43. ISSN: 0168-9002. DOI: `https://doi.org/10.1016/S0168-9002(03)01874-6`. URL: `https://www.sciencedirect.com/science/article/pii/S0168900203018746`.

[228] H. J. Barnaby. "Total-Ionizing-Dose Effects in Modern CMOS Technologies". In: *IEEE Transactions on Nuclear Science* 53.6 (2006), pp. 3103–3121. DOI: `10.1109/TNS.2006.885952`.

[229] R. Kugathasan. "Integrated front-end electronics for single photon time-stamping in cryogenic dark matter detectors". In: *Journal of Instrumentation* 15.05 (2020), p. C05019. DOI: `10.1088/1748-0221/15/05/C05019`. URL: `https://dx.doi.org/10.1088/1748-0221/15/05/C05019`.

[230] Ferenc Nagy et al. "A model based DC analysis of SiPM breakdown voltages". In: *Nucl. Instrum. Meth. A* 849 (2017), pp. 55–59. DOI: `10.1016/j.nima.2017.01.002`. arXiv: `1606.07805 [physics.ins-det]`.

[231] Giulia Fazzino. *Study of a pulsed LED set-up to characterise the light response of SiPM sensors for the EIC dRICH detector*. URL: http://amslaurea.unibo.it/26376/.

[232] Chiara Fraticelli. “SiPM detector timing response study for the electron-ion collider”. MA thesis. URL: http://amslaurea.unibo.it/28847/.

[233] E. Engelmann et al. “Extraction of activation energies from temperature dependence of dark currents of SiPM”. In: *J. Phys. Conf. Ser.* 675.4 (2016), p. 042049. DOI: 10.1088/1742-6596/675/4/042049.